THE UNIVERSITY
OF BIRMINGHAM

Application of Microstructural Texture Parameters to Diffusional and Displacive Transformation Products

by

Dipl.-Ing. (FH) Alexander Fuchs

A thesis submitted to
The University of Birmingham
for the degree of
DOCTOR OF PHILOSOPHY

Metallurgy and Materials Science
School of Engineering
The University of Birmingham
May 2005

Acknowledgements

Thanks are given to my supervisor Dr. M. Strangwood for the discussion and his help during my PhD work. Professor I. R. Harris I thank for his support to make this work possible at the School of Metallurgy and Materials. I also want to thank all the students, research and support staff that helped me during my time at the University of Birmingham.

Thanks are also due to Professor G. Schneider who gave me the possibility to investigate this very exciting scientific topic. His team at the University of Applied Sciences Aalen helped me to do much of the practical but also theoretical work. Therefore I want to thank Mr. T. Bernthaler, his colleagues and the students that were involved in the research. Special thanks go to Mrs. B. Stahl who helped me not just with the scientific work.
Thanks go also to Professor U. Klauck who helped me with establishing the method regarding the computational and image analytical background.

I also want to thank the companies Alfing Kessler, Zahnradfabrik Friedrichshafen and Robert Bosch for the kind provision of samples. I also have to acknowledge Carl Zeiss for their support regarding image analytical questions but also provision of microscopes and the related equipment. Vicariously I want to thank Professor V. Smolej for his discussion and his help in writing and adjusting the KS macros for the various measurements.

Special thank are also due to my colleagues Dr. F. Groß and Mr. O. Friese who helped me with their honest friendship over all the time.

Finally I want to thank my parents for their patience and their unremitting support in every situation. Together with Mrs. J. Heitz they provide me the support that I needed to do this PhD thesis.

Abstract

The measurement of materials properties and the control of processing parameters is important for both materials development and quality control. Determination of these parameters is sometimes advantageous if done by means of microstructural characterisation as here additional information may be gained from the sample. These values, e.g. the grain size or the volume fraction of the present microconstituents, may allow the correlation with mechanical properties or processing properties.

Unfortunately, the diffusional and displacive transformation products, martensite and bainite, exhibit very fine microstructures with a low contrast, so that conventional microstructural image analysis cannot be applied readily to distinguish these structures.

As an alternative microstructural characterisation technique texture analysis based on Haralick parameters calculated from second order grey value statistics was successfully applied. It has been shown that the analysis of large sample areas can be done automatically enabling the correlation of the texture data with the respective local microhardness using a neural network.

The analysis is limited due to the dependence of the texture parameters on preparation and imaging conditions. A more detailed understanding of the individual Haralick parameters will be the basis to extend the method to a correlation with other properties of the sample that may be not easily accessible by physical testing, such as toughness.

actual contact details: alfuchs@gmx.de

Contents

1 Introduction

Steels have a very long history. They are used nowadays in a wide field of applications. Their variability in properties makes them versatile enough to fulfil various requirements of both structural and functional components. Their properties can be adjusted by mechanical deformation and/or heat treatments.
Due to increasing property demands the microstructures of steels have to be modified and for hardened steels this results in a very fine microstructure with comparatively low contrast.

The quality of thermo-mechanically processed steel can be characterised using mechanical testing of the components, e.g. by hardness testing, measurement of the wear resistance, measurement of the yield and tensile strength or measurement of the fatigue properties. These testing methods can either be local, i.e. the hardness testing or measurement of the wear resistance, or measure an overall value for the component, i.e. measurement of the tensile strength or the fatigue properties. Both methods have the limitation that a determination of the lateral distribution of the properties is either very time-consuming, as for the hardness measurement, or even not possible, as for the measurement of the fatigue properties.

An alternative way to characterise the properties of the component is through microstructure evaluation. This gives the possibility of a local characterisation, e.g. at mechanically highly loaded positions. A quantitative analysis of the microstructural features can be carried out using conventional image analysis, e.g. measurement of the volume fractions of the occurring phases or their size distribution. This is based on a grey value segmentation of the different phases. For the complex microstructures of hardened steels this is not possible due to the fine microstructure and the low contrast.
Instead of conventional image analysis the grey value statistics can be used to characterise the texture in micrographs. Texture describes the spatial distribution of the image intensities and discrete tonal features. To characterise the spatial distribution of the grey values in the image, the grey level cooccurrence matrix is calculated. Using measures computed from these second-order statistics, texture can be quantified and properties of the image or regions in this image such as the contrast, the variance or the entropy may be calculated. In this study a set of 11 texture parameters defined by Haralick was used to characterise micrographs.

To establish a correlation between these texture parameters and the processing parameters of the component or the resulting properties, the technology of neural networks was applied. These are self-learning mathematical constructs, i.e. they are presented a set of texture parameters together with corresponding properties or processing parameters with which the weights are being adjusted to give the desired correlation.

As the microstructures of hardened steels are most often too brittle for the application of the component, heat treatment is often limited to the surface of the component. This hard and wear resistive surface can be combined with a soft and ductile core. There are different ways to achieve this gradation in the microstructure, i.e. surface hardening, e.g. (i) case hardening, (ii) induction hardening, or (iii) laser hardening.
A fast method to determine the mapping of local properties gives the possibility to visualise not only the geometry of a hardened surface layer, but also makes it possible to use these data to predict the limiting loads, which the component can withstand. The correlation of the local microstructure with the corresponding microhardness is the easiest way to prove the method, its possibilities and its limits. It also gives the possibility to correlate the local microstructure to properties that are difficult to measure, e.g. fatigue properties.

Therefore the application of texture analysis was studied in the following way:

- Investigations of the mathematical background of the grey level cooccurrence matrix and the texture parameters were made to understand their response to different micrographs.
- Thermodynamic simulation for the investigated tool steel 100Cr6 to predict the phase balance in the investigated temperature range and comparison of these results with measured values.
- Measurement of the texture parameters after Haralick and correlation to the local microhardness for a Jominy end-quench specimen showing significant differences in the local microstructure to approve the basic functionality of the method.
- Characterisation of the complex microstructure of bainitised samples re-austenitised at different temperatures and correlation of the texture parameters with the re-austenitisation temperature to establish a quality control tool for the heat treatment process.

- Variations of the metallographical preparation, imaging technique, variation in the separation between pixels used for calculation of the grey level cooccurrence matrix, geometry of the neural network and the choice of representative data for the training of the neural network have been investigated to check their influence on the quality of the correlation to the properties or processing parameters of the component.
- The texture analysis was combined with conventional image analysis, i.e. the characterisation of coarse alloy carbides, to enhance the correlation.
- The practical usefulness was tested by calculation of the local hardness distributions from the texture parameters of three different surface hardened steel components.

2 Literature Review

2.1 Formation of microstructure and corresponding properties

In the history of mankind many different materials have been used to make tools and weapons. Since 2000 B.C. iron was used for that purpose in Egypt and Asia Minor. From this region, knowledge about this material spread over Greece, the Roman Empire to the Mediterranean area and Europe. Amongst other things, this may be related to the iron-containing compounds existing in abundant quantities within the earth's crust. Another important argument is that ferrous materials, i.e. steels, may be produced using relatively economical extraction, refining, alloying and fabrication techniques [Cal99, Hon00].

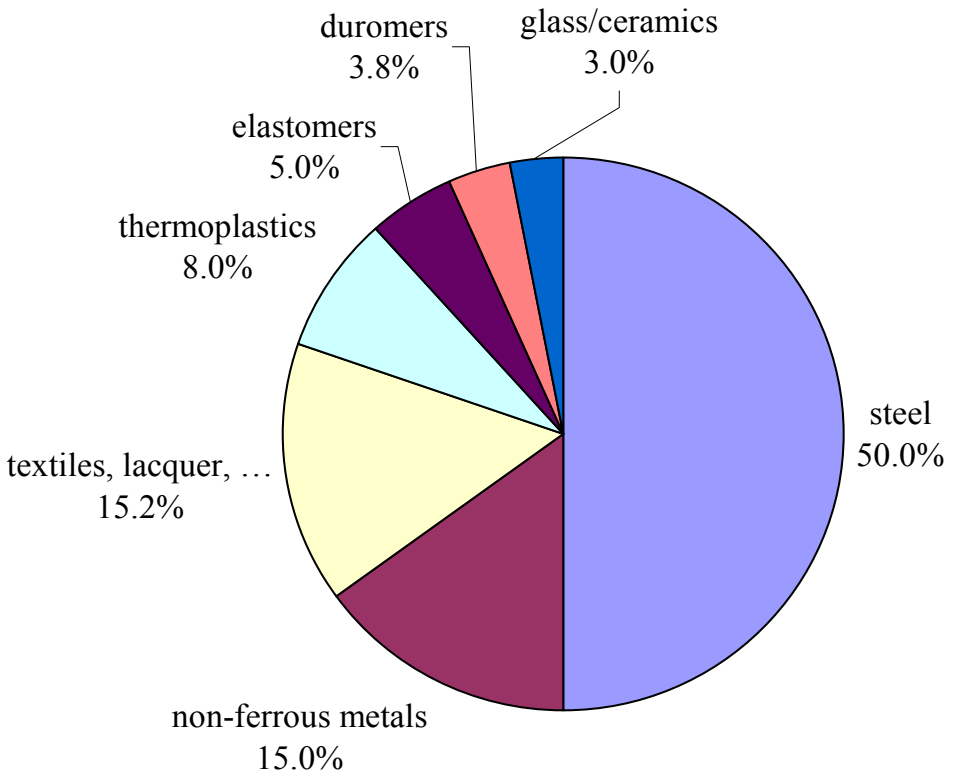

Figure 2-1 Fractions of the materials used for building a passenger car, all fractions in wt.-%, after [Kle04]

Over the years, iron has been substituted by steels, which fulfil the increasing demands on mechanical properties. Mechanical engineering, e.g. car manufacturers, has used steels for long time as the preferred material for structural components. With continuous improvements

in steelmaking, refining techniques and alloy composition, steels were developed with specially tailored properties. Today still half the weight of passenger cars is composed of steels (Figure 2-1).

Nowadays, high and ultra high strength steels are on the market with a tensile strength of up to 5500 MPa [Hon00] and a toughness of more than 200 MPa $m^{0.5}$ [Bha02]. For some applications other properties are demanded, such as fracture toughness or a high fracture strain. These requirements may be met by adjustment of the chemical composition, the mechanical processing and the heat treatment through (i) work hardening, (ii) grain refinement, (iii) solid solution strengthening by interstitial and/or substitutional atoms, and (iv) precipitation hardening [Hon00].

The influence of these parameters is well known and for the simulation of properties resulting from the variation of the microstructure mathematical descriptions were developed.

Work hardening

Work hardening describes the phenomenon whereby a ductile metal becomes harder and stronger as it is plastically deformed at temperatures low compared to the melting point. Due to an increase in the dislocation density and the interactions between the dislocations e.g. jogs, the motion of the dislocations is hindered. Thus the stress necessary for deformation increases with increasing cold work. The price of this enhancement of both yield and tensile strength is a decrease in ductility, Figure 2-2.

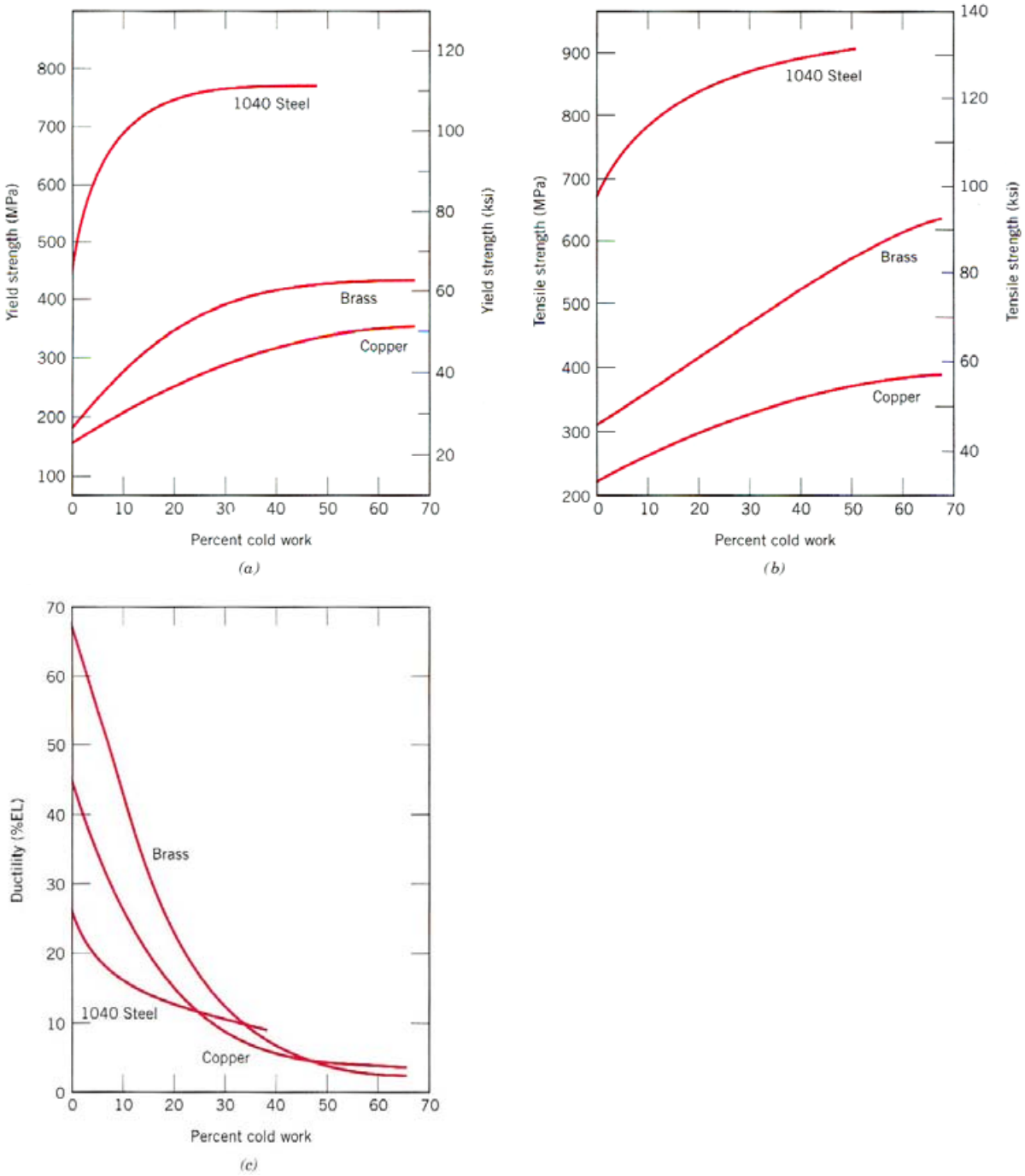

Figure 2-2 Increase in the yield (a) and tensile strength (b) together with the decrease in ductility (c) of 1040 steel, brass and copper for increasing amounts of cold work [Bar78]

Grain refinement

Most of the materials used for structural components are processed in the polycrystalline state. This means that adjacent grains are separated by a grain boundary that acts as a dislocation barrier during plastic deformation. If the stress concentration at the head of a slip plane is high enough, it may activate sources of new dislocations, even if that slip plane is not orientated to activate dislocation motion due to the externally applied force.

If this is considered when looking at different grain sizes, it can be said that for smaller grains the grain boundary area to impede dislocation motion is greater than for bigger grains. This is also expressed by the Hall-Petch equation [Cal99]:

$$\sigma_y = \sigma_0 + k_y d^{-1/2} \qquad \text{Eq. 2-1}$$

Here the yield strength, σ_y, can be calculated from the grain diameter, d, and two constants σ_0 and k_y for the particular material. The influence of the grain size on the yield strength of a 70Cu30Zn brass alloy is shown as an example in Figure 2-3.

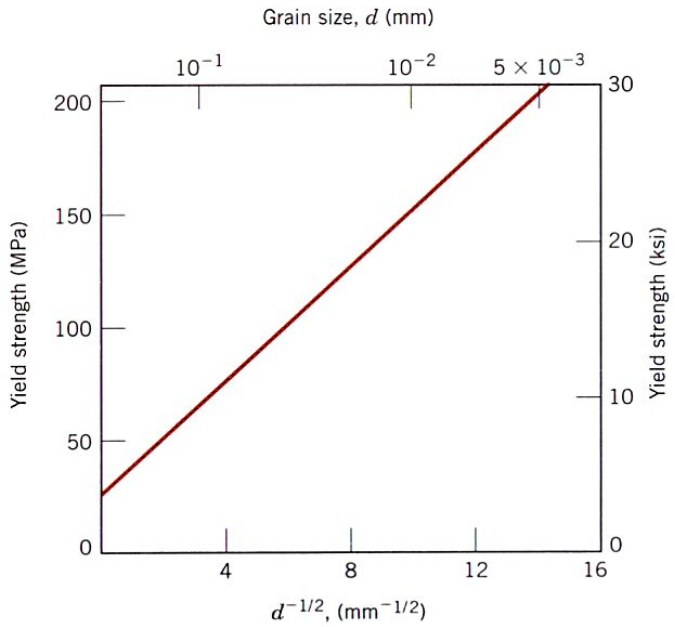

Figure 2-3 Influence of the grain size on the yield strength of a 70Cu30Zn brass alloy [Suz63]

It should also be mentioned that grain size reduction improves not only strength, but also the toughness. As this is also an important property for most structural components, grain refinement is used widely.

If this is applied to hardened microstructures the increase of strength can be partially explained. The lath- or plate-like structure of both martensite and bainite forms low-misorientation boundaries. These small crystallographic misorientations do not act as strong dislocation barriers, but, they can be combined with thin films of retained austenite or carbides, which give a much larger misalignment to the slip planes. Therefore the dislocations are hindered from moving and both strength and ductility of the material are increased. In these phases, however, high dislocation density, tetragonality, solid solution and precipitate strengthening also act to increase strength.

Solid solution strengthening

Steels are most often alloyed using different elements. Only a few of these elements have atoms that are small enough to go into solution in the iron interstitially. These are carbon, hydrogen and nitrogen. Other elements can be found in substitutional solid solution. Due to the difference in size between iron and these atoms, lattice strains are imposed by the substitutional atoms and the surrounding host atoms that can interact with and restrict the movement of dislocations. The resistance to slip is greater when interstitial atoms are present because the overall lattice strain must increase if a dislocation is torn away from them. Furthermore, the same lattice strain interactions will exist between solute atoms and dislocations that are in motion during plastic deformation. Thus, a greater applied stress is necessary to first initiate and then continue plastic deformation for solid-solution alloys, as opposed to pure metals; this is evidenced by the enhancement of strength and hardness [Cal99].

Precipitation hardening

The hardening using precipitates, also known as dispersion strengthening, is commonly used for steels. In steels carbides are the most common precipitate type due to the low solubility of carbon and these carbides often provide precipitate strengthening to the ferritic matrix. In plain carbon steels this carbide is normally cementite (Fe_3C). In alloy steels the iron carbide is

replaced by other carbides, which are thermodynamically more stable. Other dispersed phases which are encountered are nitrides, intermetallic compounds and, in cast irons, graphite.

As for the solid solution strengthening the precipitates induce lattice strains in the matrix increasing the strength necessary to move dislocations during plastic deformation. This increase in strength depends not only on the volume fraction of precipitates but also their diameter and therefore the size or number density respectively. For a constant volume fraction of precipitates and decreasing size both the number density and the strength are increasing [Ver84]. Dispersoids can act in the same way as grain boundaries in blocking slip planes to force the dislocations to bow around the particle (Orowan bowing). Strength in this case is increased by a larger volume fraction, but finer particle size. The behaviour for hard precipitates in a ferritic matrix is shown in Figure 2-4.

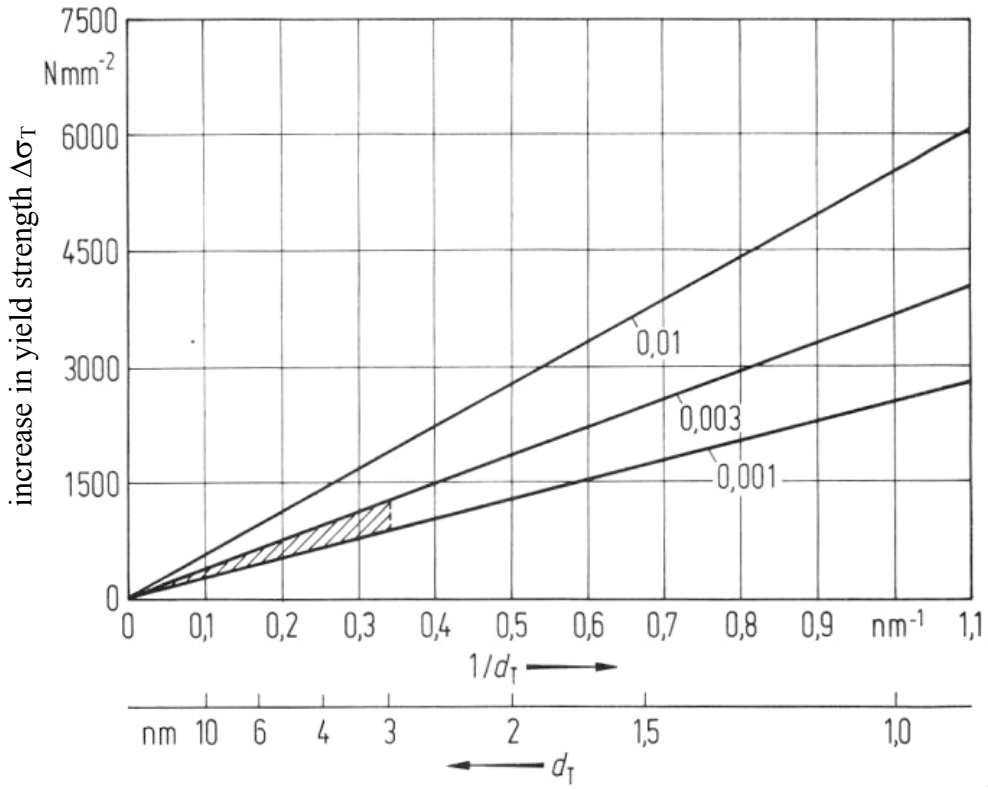

Figure 2-4 Calculated increase of the yield strength of ferrite $\Delta\sigma_T$ depending on the diameter of hard precipitates d_T and for different volume fractions of precipitates (0.1; 0.3; 1.0 vol.-%) [Hor79]

Prediction of material properties from alloy composition using linear regression

Different investigations have shown that material properties, e.g. the transformation temperatures such as the martensite or the bainite start temperature, may be derived from the alloy composition of the material using linear regression or as a more empirical attempt using a neural network [Kin97, Liu01, Ver96, Wan00, Hon00, Hor83, Ish95, Key04a]. The mathematical approach is shown in Eq. 2-2 [Bha99b].

$$y = \sum_j w_j x_j + \theta \qquad \text{Eq. 2-2}$$

where a material property, y, may be estimated from the wt.-% x_j of element j weighted respectively by w_j, and θ being a constant.

This mathematical description may also be used to simulate other material properties, e.g. the yield strength, which was shown by Singh and Bhadeshia [Sin98]. Here the yield strength of austenite was calculated from the chemical composition and the temperature.

Attempts have also been made to model the yield strength of pearlite from the chemical composition and the pearlite morphology, i.e. the interlamellar spacing, the pearlite colony size and the cementite plate thickness [Gla72]. Using a linear regression model it has been shown that strength and toughness not only depend on the chemical composition and therefore on the volume fraction of ferrite and pearlite but also on the morphology of the pearlite.

Hardening of steels

One of the very big advantages of steels is their allotropy, i.e. the prevailing crystal structure depends on composition, temperature and external pressure [Cal99]. At atmospheric pressure the crystal structure of pure iron changes from body-centred cubic (bcc) to face-centred cubic (fcc) form during heating up at 910 °C (A_3 point) [Hon00]. In this fcc structure, also known as austenite or γ iron, the solubility of carbon in iron has its maximum value of 2 wt.-% given at 1147 °C by far higher than in the bcc structure, also known as ferrite or α iron, with a maximum carbon solubility of 0.02 wt.-% at 723 °C [Hon00].

If a plain carbon steel is cooled slowly from the austenite phase field to ambient temperature it transforms to ferrite. The equilibrium solubility of carbon in ferrite is very low with only $3 \cdot 10^{-5}$ wt.-% C at 150 °C and even less at lower temperatures [Sch66a]. The excess carbon precipitates during the cooling process from the ferrite. This carbon generally forms the

metastable compound cementite (Fe_3C) according to the decreasing solubility of carbon in ferrite

$$\alpha_{\text{C rich}} \rightarrow \alpha_{\text{C depleted}} + Fe_3C \qquad \text{Eq. 2-3}$$

For the true equilibrium this cementite decomposes to ferrite and graphite according to the reaction [Cal99]

$$Fe_3C \rightarrow 3\,Fe + C \qquad \text{Eq. 2-4}$$

For the practical relevant heat treatments of steels the decomposition to graphite is not relevant, i.e. cementite can be found in the microstructure instead.

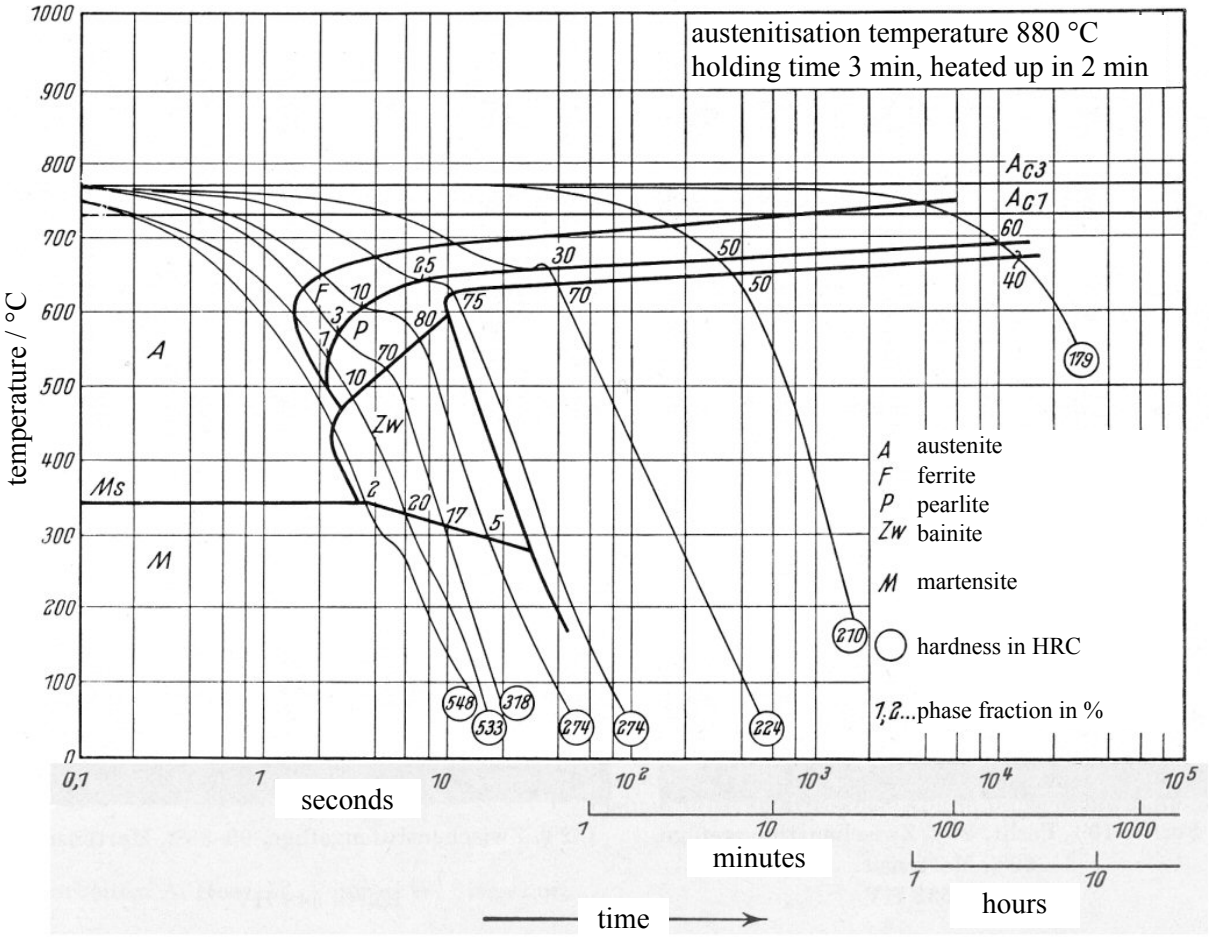

Figure 2-5 CCT diagram for continuous cooling of the plain carbon steel C45 for an austenitisation temperature of 880 °C [Ros61]

For technical purposes steels are not only cooled slowly to the metastable microstructure but they are often cooled more rapidly to generate a non-equilibrium microstructure, such as martensite and/or bainite. These transformations have either diffusional and/or displacive character. For the formation of bainite the redistribution of carbon is required and thus is diffusional, but not necessarily diffusion controlled. Formation of bainitic ferrite involves an invariant plane strain change of shape and is thus displacive [Mud02]. The latter is also the case for the transformation of austenite into martensite [Ver84, Ber89]. The resulting microstructural phases bainite and martensite are used widely in industrial applications. The possibility to control the resulting properties makes this material very versatile in use.

For the plain carbon steel C45 with 0.45 wt.-% C the continuous cooling transformation (CCT) diagram is presented in Figure 2-5. As can be seen, the resulting microstructure depends significantly on the rate of cooling. For cooling from an austenitisation temperature of 880 °C to ambient temperatures in 100 seconds or more the microstructure consists of ferrite and pearlite with varying fractions depending on the rate of cooling. For faster cooling rates the austenite will partially transform to bainite and fractions of martensite as the transformation to ferrite and pearlite is suppressed. For a critical cooling rate bainite will also be suppressed and the microstructure formed during quenching will only consist of martensite.

This dependence of transformation temperature and therefore the resulting microstructure on the rate of cooling is also shown in Figure 2-6. With increasing rate of cooling the metastable microstructures are replaced by the non-equilibrium microstructures bainite and/or martensite. The determining factor for these differences is the strong decrease of the diffusivity with increased rate of cooling.

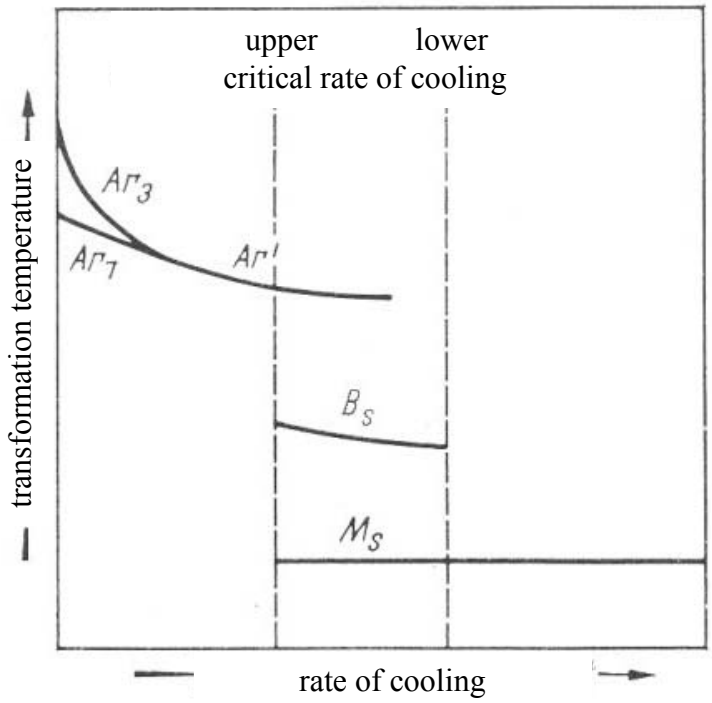

Figure 2-6 Influence of the rate of cooling on the transformation temperature and the microstructure of a hypoeutectoid steel [Hor92]

Also very common in industrial heat treatment is isothermal transformation of steels. For this heat treatment the samples are cooled from austenitisation temperature to the transformation temperature where they are held for a specific time before further cooling. As an example the TTT diagram for isothermal transformation of the plain carbon steel C45 with 0.45 wt.-% C is presented in Figure 2-7. With this method, similar microstructures can be obtained to those in continuously cooled samples, but, due to the differences in the transformation behaviour the morphology might differ [Sch66a]. As can be seen with decreasing transformation temperature the microstructure changes from ferritic-pearlitic to bainitic and then to a martensitic structure.

Also for isothermal transformation, complex microstructures can be found, which was shown for example for the steels Fe-4Mo-0.2C and Fe-10Cr-0.4C [Bee97]. As the transformation temperature is decreased, the decomposition products change from the disordered growth of nodular alloy pearlites to blocky ferrite structures containing fine dispersions of alloy carbide, and finally to acicular ferrite structures also containing alloy carbides.

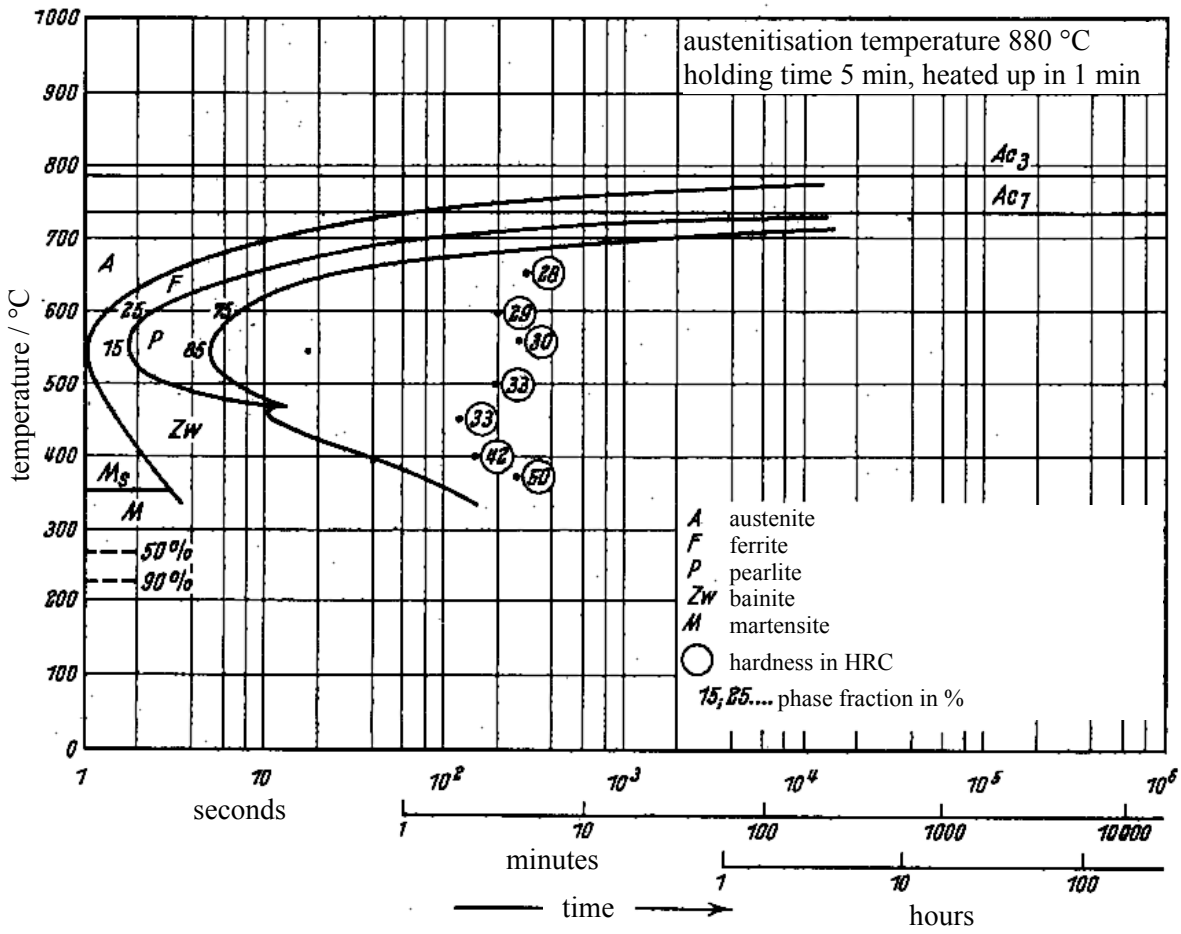

Figure 2-7 TTT diagram for the isothermal transformation of the plain carbon steel C45 for an austenitisation temperature of 880 °C [Ros61]

Bainitic microstructures

For ferritic-pearlitic microstructures carbon diffuses during the cooling to form ferrite and cementite phase at a common transformation front with the austenite. This contrasts with bainite, which occurs in separable stages, first the displacive formation of ferrite, followed by carbon redistribution and the precipitation of carbides [Bha01]. Nevertheless bainite is a eutectoid structure consisting of ferrite and carbides just like pearlite [Bor96]. Due to the difference in transformation temperature bainite can be categorised in (a) upper bainite for higher transformation temperatures and (b) lower bainite for lower transformation temperatures. Both of them have in common that they consist of aggregates of plates of ferrite, separated by untransformed austenite, martensite or cementite. The aggregates of plates are called sheaves. Lower bainite, which is obtained by transformation at relatively low

temperatures just above the martensite start temperature, shows carbides precipitated within the lower bainitic ferrite. This is due to the slower diffusion associated with the reduced transformation temperature. In contrast to this upper bainite formed at higher transformation temperatures consists of bainitic ferrite being free of precipitates and carbides growing from the carbon enriched residual austenite between the plates of ferrite [Bha01, Key04b].

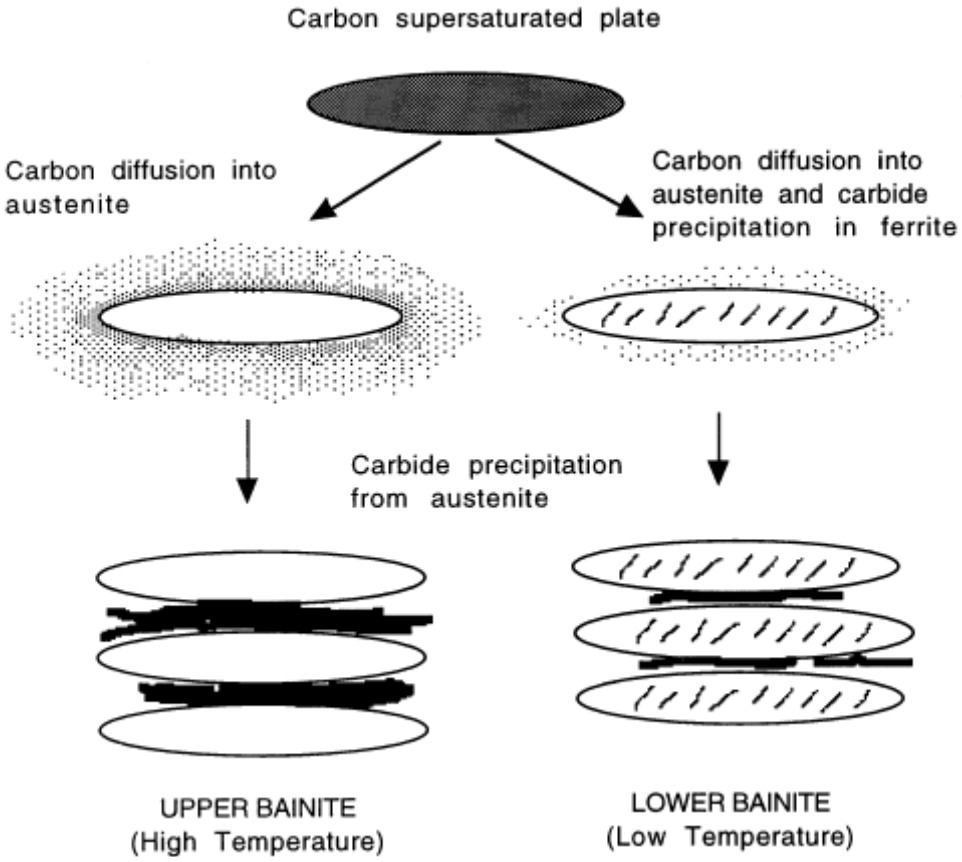

Figure 2-8 Growth of bainite and development of upper and lower bainite [Bha99c]

Due to the differences in the mechanism of formation upper and lower bainite have different microstructural appearances. While upper bainite most often appears feathery, lower bainite tends to have a plate-like structure [Kut99, Key04b]. Not only the appearances differ, but the mechanical properties also vary with the morphology of the bainite. As the plate size is finer and the dislocation density higher at lower transformation temperatures, the tensile strength is higher than for higher transformation temperatures [Bha01]. This means that, for upper bainite showing a coarser structure, a lower strength is expected than for the finer microstructure of lower bainite (Figure 2-9).

The toughness of upper bainite is limited by the presence of large carbides on grain boundaries [Bar95]. Lower bainite with smaller carbides inside the bainitic ferrite laths shows a higher toughness.

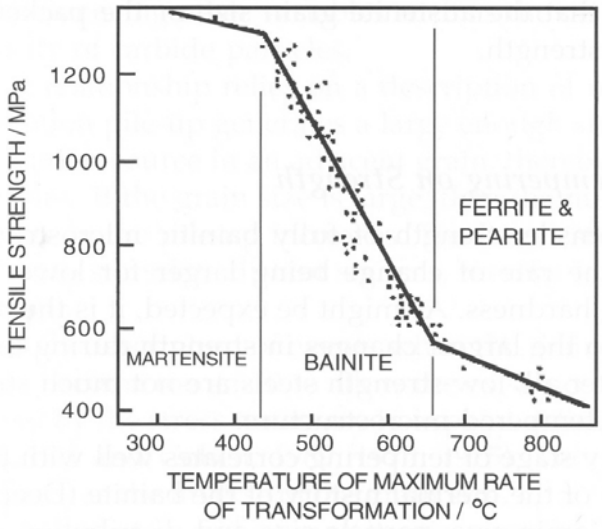

Figure 2-9 Variation of the tensile strength of structural steels as a function of the temperature at which the rate of transformation is greatest during continuous cooling heat treatment, after [Irv57]

As the morphology and therefore also the size of the microstructural features of the bainitic microstructure strongly depend on the chemical composition, i.e. mainly the carbon content, and on the heat treatment, this also affects the mechanical properties. For bainitic ferrite plates thinned to a width of only 20 nm the tensile strength can be in excess of 2.5 GPa [Cab04].

Martensitic microstructures

For higher cooling rates and therefore lower transformation temperatures than for the bainitic transformation the austenitic microstructure transforms completely or partially into martensite. This hard microconstituent of great technological importance can confer an outstanding combination of strength (> 3500 MPa) and toughness (> 200 MPa $m^{0.5}$) [Bha02]. At the temperatures at which martensite is formed, diffusion, even of interstitial atoms, is not conceivable over the time of the experiment. As the speed of growth of the martensite plates approaches that of sound in the metal diffusion during the transformation is impossible.

Therefore the chemical composition of the martensite is identical to that of the parent austenite.

The nucleation of martensite takes place heterogeneously on pre-existing embryos. These embryos are postulated to have a semicoherent dislocation interface with the austenite. This is most likely at grain boundaries, incoherent twin boundaries and inclusion particle interfaces [Hon00]. From these nuclei, for lower carbon contents (≤0.6 wt % C) laths develop forming lath (or massive) martensite. If the carbon content is higher, lenticular (or plate) martensite is generated with needle-like or plate-like martensitic grains [Cal99]. For lath martensite the laths are typically too small to be revealed by optical microscopy.

For the transformation of austenite to martensite three types of transformation can take place [Haa96]. The first type describes martensite forming in the absence of thermal activation, i.e. athermally, with increasing undercooling. A second type of transformation also involves athermal transformation, but the reaction commences suddenly with a burst phenomenon, which effectively causes a proportion of the austenite to transform isothermally. The third type is the true isothermal transformation but this has only been found in carbon-free iron-based alloys.

The athermal transformation implies that the fraction of martensite transformed is a function solely of the temperature [Hon00]. At a given temperature the transformed fraction is limited by the mechanical stabilisation of the austenite caused by the strain field of the already transformed martensitic regions. This can be derived from the increase of volume for the transformation from austenite to plate martensite of approximately 3 vol.-% [Ver84]. In addition to the volume change, the lattice deformation produces a shape change in the transformation region. This results in inhomogeneous slip or twinning of the martensitic plates to largely compensate the distortion of the matrix associated with the lattice deformation [Haa96].

Compared to bainitic microstructures martensite formation is entirely diffusionless. This means that carbon, as well as other alloying elements, remains in solid solution in the martensite decreasing the etching attack compared with bainite, which contains precipitates inside the bainitic ferrite. Martensite therefore appears brighter in the optical microscope as long as it is not tempered when submicroscopic precipitates would increase the etching attack and then a differentiation between lower bainite and tempered martensite would be

complicated. As, during heat treatment, auto-tempering of the martensite is not improbable, some fine particles can be found to increase the etching attack during chemical etching.

Martensitic microstructures are well known for their high strength. This property depends on (i) the tetragonality of the lattice given by the amount of interstitial carbon in the matrix, (ii) the high density of dislocations and twins, and (iii) the prior austenite grain size. The austenitic grain size determines the maximum size of a martensite plate and therefore limits the grain size of the martensitic microstructure, which, in turn, increases strength [Hon00]. The high dislocation density [Ver84] constrains the mobility of dislocations and the formation of additional dislocations during plastic deformation due to their induced strain field. A typical dislocation density for a 0.2 wt.-% carbon steel is between 0.3 and 1.0 * 10^{12} cm cm^{-3} [Hon00]. The tetragonality of the martensite is given by the amount of carbon being held in solid solution in the martensite. This was in solid solution in the austenite before quenching and due to the diffusionless transformation the carbon is restricted to these interstitial positions. The increasing difference in the lattice parameters of the body centred cubic crystal structure increases the hardness of the martensite [Sah02]. During the post-quenching heat treatment or even during autotempering this interstitial carbon may precipitate in the form of carbides, decreasing the tetragonality and therefore the strength. These precipitates are far too small to be resolved using optical microscopy. For the example of the high-strength steel HSLA100 precipitates are smaller than 60 nm even for tempering at 700 °C for 1.5 h [Wen96]. For the martensitic steel AerMet 100 the as-quenched condition showed MC with a size between 5 and 12 nm and $M_{23}C_6$-type carbides between 20 and 100 nm [Bha04]. But as these carbides precipitate the strength of the martensite deteriorates associated with an increase in ductility [Lee99, Liu04].

Mixed microstructures

As the transformation of steels during heat treatment is a competitive mechanism involving the formation of different microconstituents, the resulting microstructures very often consist of a mixture of these microconstituents. This can be observed both for continuous cooling and isothermal transformation of steels. The respective transformation diagrams show that, for many steels, most often a mixture of two or more microconstituents can be found (e.g. Figure 2-5 and Figure 2-7). This can be derived from the varying alloying contents of the different

microconstituents. For example, upper bainite may form in plain carbon steels with more than 0.32 wt.-% carbon during isothermal transformation and increase the carbon content in the residual austenite so much that the austenite transforms to lower bainite [Bha01]. In dual phase steels the microstructure can be adjusted using the alloying content and heat treatment schedules, i.e. the cooling rate and possibly the intercritical annealing temperature whereby the resulting microstructure may consist of martensite, allotriomorphic ferrite, pearlite, bainite or retained austenite [Erd03].

For dual phase steels a mixed microstructure is not always formed unintentionally. The combination of different microconstituents can give a good compromise between the strength and the toughness as demanded for a large variety of applications. For a multiphase microstructure containing ferrite, bainite and martensite monotonic cyclic strength even higher than that of a tempered martensitic steel could be found [San03]. Due to the different microconstituents and their varying etching activity new etchants have to be found to fulfil the demanding requirements for microscopy of dual phase steels [Gir98].

For high strength steels consisting of a mixture of martensite and bainite extensive investigations have been carried out regarding the influence of the volume fractions of the microconstituents on the mechanical properties. For mixtures of lower bainite in a martensitic matrix it was found that about 25 vol.-% of lower bainite in tempered martensite increases both the strength and the ductility of a martensitic microstructure while for increasing volume fractions of lower bainite the mechanical properties decrease [Tom83a, Tom83b, Tom85a, Tom85b]. In contrast to this upper bainite in a martensitic matrix has a very detrimental effect on both strength and ductility [Tom85a].

The ever-increasing demands for mechanical properties necessitate new steel compositions and respective thermomechnical treatments which very often result in complex microstructures. Due to the variety of microconstituents and their respective characteristics a quantitative characterisation of microstructure of modern steels has to be very sophisticated.

2.2 Quantitative characterisation of microstructure

The determination of the properties of components is not only essential for the development of new material grades with specifically tailored properties and their thermomechanical treatments to fulfil the needs in later application but it is also very important for the quality control of existing fabrication processes.

Some mechanical properties of components are readily accessible, such as hardness. Others are more difficult to measure, such as yield or tensile strength, when special samples have to be machined from the material to be analysed. Properties like the fatigue strength are far more difficult to determine since the testing needs several samples for each condition and testing can be time-consuming.

As already described in Section 2.1 the microstructure contains a large amount of information about the material and its processing history. Quantitative analysis of this microstructure therefore gives the possibility to perform on the one hand a quality control check of the processing of the material, and on the other hand it gives the possibility to establish correlations between microstructural features and related properties using quantitative image analysis of the micrographs (Figure 2-10). Microstructural analysis in combination with automated measurement using motorised microscopes and dedicated software for the measurement of the features of interest therefore allows description of the material not only qualitatively but also quantitatively. This again allows correlation of these features with processing parameters as well as resulting properties.

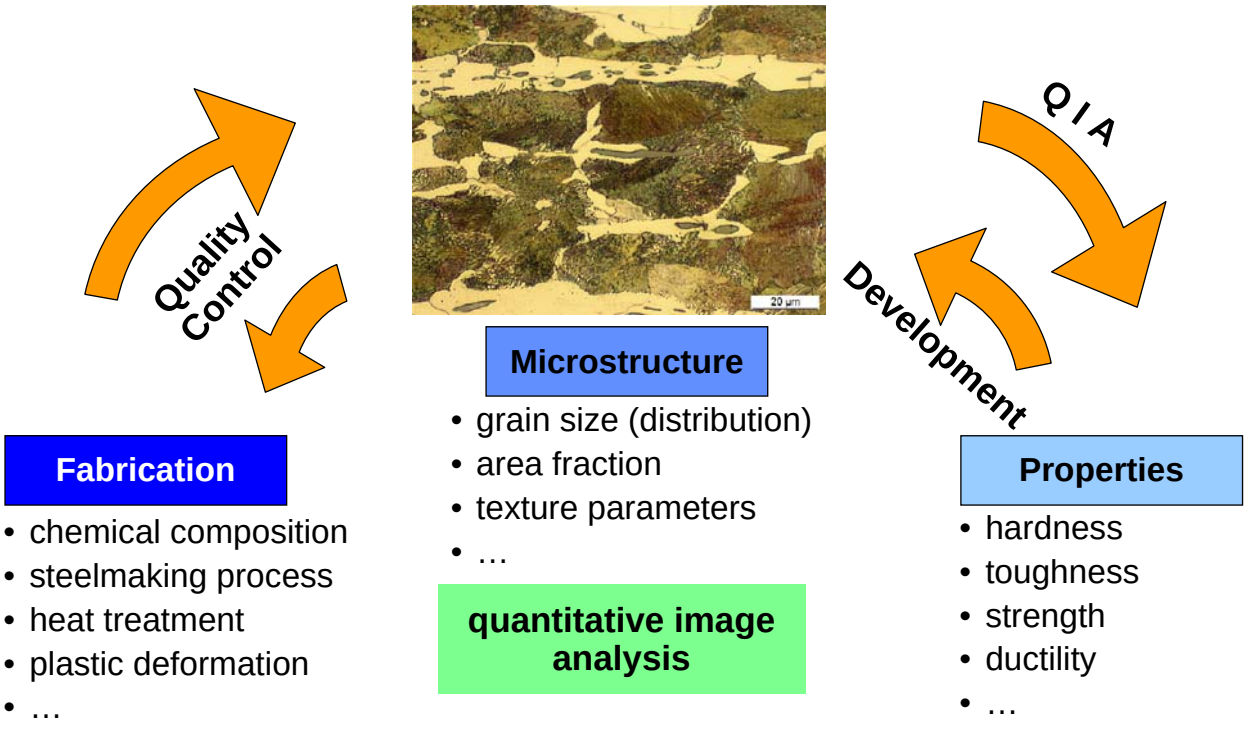

Figure 2-10 Microstructure as connection between the fabrication of components and their properties

Assessment of the grain size

Measurement of grain size is one example showing the effectiveness of quantitative image analysis. For a low carbon-manganese steel the quantitative dependence between ferrite grain size and the hardness, the yield and tensile strength and the elongation has been demonstrated [Byu01]. Higher strength and good toughness were found for the steel showing the smaller ferrite grain size.

With the increasing possibilities of image analysis using computers grain size measurement could be done automatically. Since manual determination is not only expensive in time and resources it is also very subjective, whereas automated quantitative image analysis promises reproducible results for repeated measurements of the same sample. Manual and automated intercept length analysis [Exn88] has been used for grain size determination. The manual method and the automated method based on the watershed algorithm were compared in [Lah96] for a measurement according to ASTM E112 [AST96]. It was shown that image analysis is an essential tool for reproducible evaluation of the microstructure. This was also confirmed for an austenitic steel where the results determined by image analysis proved to be highly consistent with high repeatability [Lat01].

For ferrite-pearlite high and extra high strength steels the grain size of the primary ferrite was measured using image analysis and correlated successfully with the impact transition temperature [Fro99]. For a nearly fully pearlitic structure of a 0.65 wt.-% C steel hardness and yield strength follow a Hall-Petch type relationship with the interlamellar spacing of the pearlite [Mod01].

It was also reported that the fracture toughness of a tempered martensitic steel does not depend on the prior austenite grain size [Les02]. Therefore other microstructural features have to be measured to correlate with this property.

Assessment of the precipitation hardening

Precipitates in steel can most often be found in form of carbides. The quantification of these carbides can be used to estimate the properties of the steel.

The carbides in steel can be used to control recrystallisation and grain growth resulting in both improved strength and toughness [Edm98]. For microalloyed steels a significant amount of very finely dispersed alloy carbide precipitates in the ferrite phase can contribute significantly to the strength of the steel.

Carbon can be found in steels either as interstitial atoms or in form of carbides. Both forms increase the strength of the steel. It has been shown for a ferritic-martensitic dual phase steel (0.11C–1.58Mn–0.4Si) that the amount of interstitial carbon increases the hardness and the tensile strength of both ferrite and martensite [Els02]. The amount of carbides can therefore be used as a measure of interstitial carbon and hence a measure of the strength.
For ferritic stainless steels a significant influence of the alloying elements and hence the chemical composition of the carbides has been found regarding the adhesive wear resistance of the steel [Aks01].

Methods for the microscopical image acquisition

Due to the sizes of the microstructural features needed to characterise the microstructure and be able to determine the correlation to the fabrication and/or the resulting properties, the structures have to be magnified to a reasonable size. Traditionally optical microscopy is commonly used in this field of characterisation. The resolution of optical microscopy is given by the wavelength of the light used to image the sample surface and can be calculated according to

$$d_{gr} = \frac{0.61 \cdot \lambda}{n \cdot \sin \sigma} = \frac{0.61 \cdot \lambda}{N.A.} \qquad \text{Eq. 2-5}$$

where d_{gr} represents the resolution limit, λ the wavelength of the light, n the refractive index of the medium between object and objective and σ the angle between the illuminating beam and the optical axis of the microscope [Sch90] where N.A. is also referred to as numerical aperture.
For air as a medium n reaches a value of about 1 and with illumination parallel to the optical axis resolutions of the order of the wavelength of light are obtained. This means that the resolution of an optical microscope is limited to about 476 nm for the longest wavelength in the spectral region, i.e. for red light with about 780 nm. The spatial resolution of an optical microscope is often given as approximately 1 µm as a rough approximation.
For the optimum theoretical conditions, i.e. a maximum aperture N.A. due to a high angular aperture of the immersion oil with a high refractive index as high as n=1.52 to fill the space between object and objective and the use of blue light with λ = 450 nm a resolution of 0.18 µm can be achieved [Hab68].

To resolve the very fine structures of hardened steels a higher resolution would be necessary. This can be achieved using electron microscopy. Due to the much lower wavelength of the electron beam of only 0.05 Å at an acceleration voltage of 60 kV compared to the wavelength of the optical light, theoretically 100,000 times the resolution of the optical microscope should be achievable [Hab68].

Nevertheless optical microscopy plays an important role in the quantitative image analysis. The outstanding advantages of optical microscopy over electron microscopes are

- lower price
- high availability in both scientific and industrial environments
- comparatively simple usability
- additional information from colour images
- possibility of high automation
- lower requirements for sample preparation

Since these reasons speak in the optical microscopy's favour this technique is still widely applied in both scientific and industrial environments. The disadvantage of limited resolution is compensated for by the high availability of optical microscopes or their low price respectively. As the microstructure cannot be resolved in form of the separate microstructural features alternative methods have to be found to characterise the complex microstructures of modern steels using optical microscopy.

2.2.1 Limits of the conventional image analysis for complex microstructures

Modern steels typically have both high strength and high ductility. To achieve these demands different strengthening mechanisms are applied. Grain sizes with a diameter of less than 5 µm are common [Hur01] and microalloying yields precipitates that are even smaller. Different groups of steels are affected by this decrease of the size of the microstructural features. For ferritic hot rolled strips a process is described to produce a ferritic microstructure with grains that are 2 µm or smaller [Hur01]. For the coarse grained heat affected zone of a structural steel the martensite laths showed a length between 1.4 and 4.3 µm [Bon04]. For bainitic microstructures plate sizes of about 10 µm in length and less than 0.5 µm in thickness are reported to be typical [Bar95]. A plate thickness down to 20 nm was reported due to high

carbon content and low transformation temperatures of the investigated steel 0.79C-1.59Si-1.94Mn-1.33Cr-0.30Mo-0.11V [Cab04].

For the quantitative characterisation of all the different very fine-grained hardened microstructures of steels sophisticated methods are required. As transformations in steel rarely occur in isolation, very often two or more phases are formed during quenching [Jon97]. These phases can then be found side by side forming the complex microstructure of the hardened steels. For the quenched microstructure of steels mainly martensite and bainite are the prevailing phases in their different forms, e.g. upper or lower bainite. The structures of the bainitic and the martensitic phases are mostly very fine and comparatively low in contrast. E.g. for low carbon martensite in lath- or plate-like morphology the width of the laths is about 0.5 µm and for upper bainite the width of the ferrite plates is reported to be about 0.2 µm with a length of about 10 µm [Hon00]. Often precipitates are contained in the microstructure that can hardly be resolved using optical microscopy directly but they increase the roughness of the sample surface due to the etching and therefore may give a slight colouring of this area if a significant number density of precipitates is present. The carbides precipitates inside lower bainitic ferrite are about 500 nm long [Hon00].
An example the microstructures of two modern steels are shown in Figure 2-11. For the tool steel 100Cr6 in (a) and (b) at the highest possible light optical magnification of 1000:1 the bainitised microstructure appears as a needle-like structure containing very small alloy carbides. A differentiation between adjacent needles is not always possible since the contrast is low and varies over the length of the needles. Also a variation of the etchant cannot reveal the microstructure sufficiently to allow measurement of single needles.
The same can be said for the high strength steel 300M used predominantly in structural aircraft components, e.g. in critical components of aircraft landing gear. Here also different etchants have been applied to reveal the martensitic microstructure of the quenched and tempered samples.

Resolving the morphology of the microstructure using optical microscopy is associated with a reasonable effort that has to be made due to the high magnifications used and the metallographic preparation needed. Due to the limitation of the light optical resolution and the insufficient contrast of these microstructures a separation of the microstructural features is not

possible, nor is automated image analysis. A separation of all the martensitic or bainitic laths or plates from each other using a grey value segmentation is therefore not possible (Figure 2-12 (c), (d)) in contrast to the segmentation of the pores in a cast aluminium component, which appear dark in the micrograph (Figure 2-12 (a)) and white in the corresponding binary image (Figure 2-12 (b)).

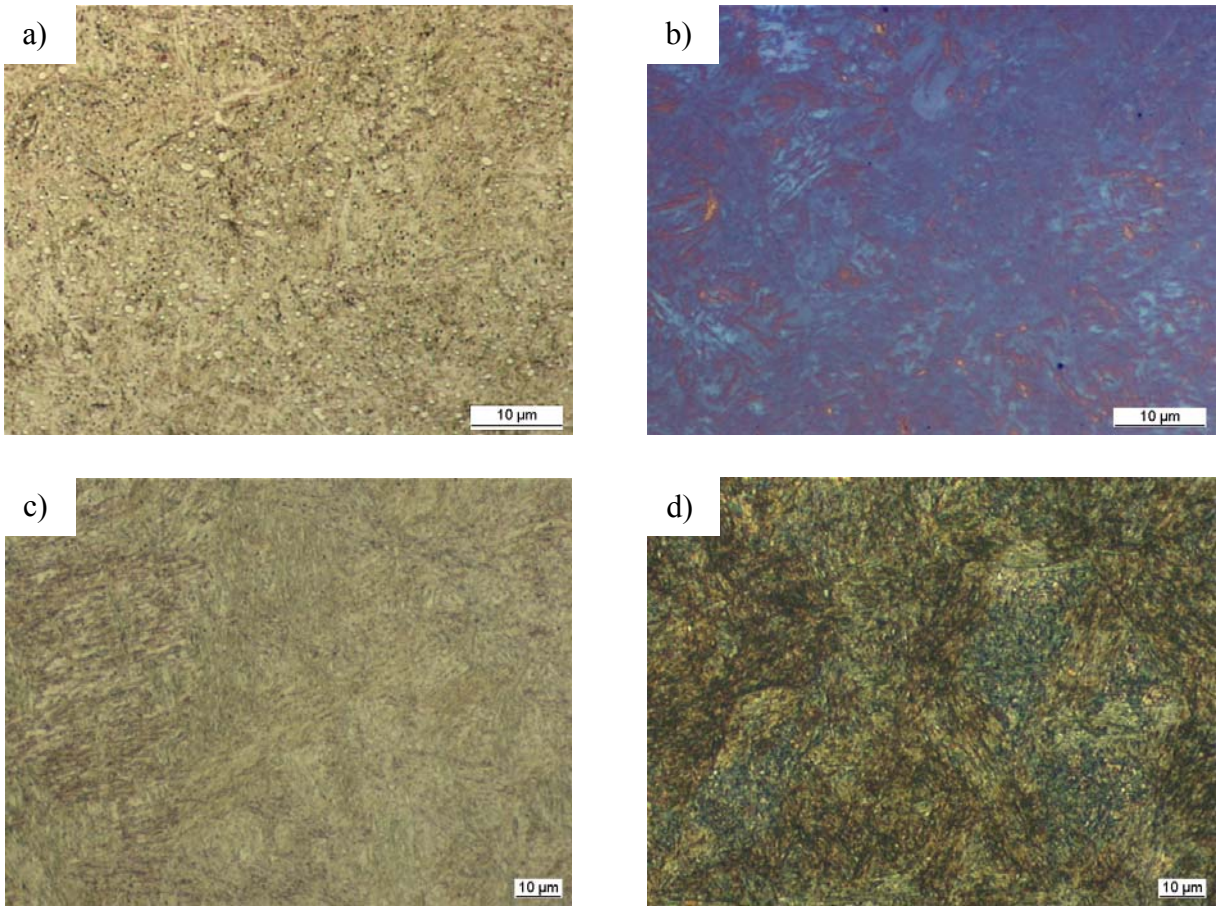

Figure 2-11 Examples for the fine, low-contrast microstructure of modern steels

a) tool steel 100Cr6, bainitised, 2 % nital, 1000:1

b) 100Cr6, bainitised, colour etch (Table 3-9, no. 4), 1000:1

c) high strength steel 300M, quenched and tempered, 2 % nital, 500:1

d) 300M, quenched and tempered, picric acid with 10 % xylene, 500:1

However, these complex microstructures can be characterised using automated image analysis. The microstructural features cannot be resolved and discriminated but the

macroscopic structure is characteristic for the respective microconstituent. Since lath martensites, that have overwhelming industrial significance due to their superior properties, have a tendency to align themselves parallel to one another in the major area of the parent grain, lath martensite exhibits a characteristic microstructure at the optical microscopic scale [Mor03]. These can be determined using automatic image analysis despite not being able to discriminate the single martensitic plates

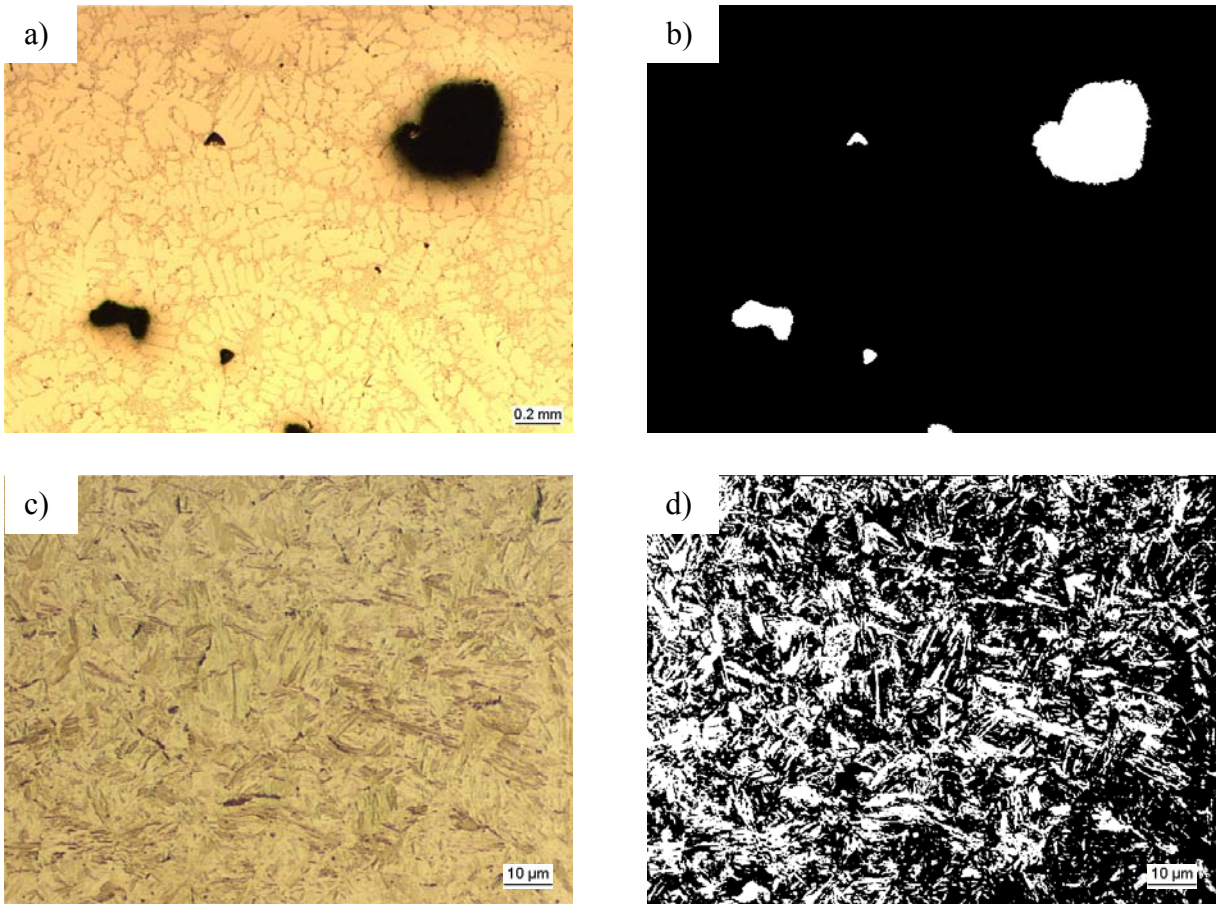

Figure 2-12 Grey value segmentation of different features in the microstructure

a) pores in a cast aluminium component at a magnification of 50:1

b) binary image after grey value segmentation of (c)

c) martensitic microstructure of a plain carbon steel with 0.45 wt.-% carbon micrograph at a magnification of 1000:1, etched with 2 % nital

d) binary image after grey value segmentation of (c)

For the pores in an aluminium component the size distribution or the aspect ratio of the pores may be determined easily using conventional image analysis. Due to the contrast between the pores and the surrounding microstructure, i.e. the difference in the intensities of the pores as the microstructural features to be measured and the surrounding microstructure, the pores can easily be segmentated from the microstructure using a grey value segmentation. The result of this segmentation is a binary image representing all the microstructural features to be measured by white pixels (grey value 255) and the surrounding represented by black pixels (grey value 0).

A quantitative characterisation of the complex microstructure of hardened steels is not possible with conventional image analysis. As the separation of the microstructural features using grey value segmentation is not feasible, features such as the length, the width, the aspect ratio or the volume fraction of the objects cannot be quantified. Nevertheless, quality control of these microstructures is essential but quantification of microstructural parameters using conventional quantitative microstructural analysis is not possible for these complex microstructures.

Alternative methods for the quantification of the complex microstructures of hardened steels have to be found to provide a tool for the development and the quality control of materials and their processing.

2.2.2 Characterisation of the microstructure

2.2.2.1 What is texture

As the analysis of single microstructural features is not possible using optical microscopy a new approach has to be found for fast, reproducible but also objective quantitative characterisation of the complex microstructures of hardened steels. The problem not only relates to complex microstructures of steels but can also be found for various image analysis tasks, e.g. sandstone [Har73], aerial photographs and satellite images [Har73], hair analysis [Ver02], iris recognition [Dau98], mammograms [Sol04] or food [Ber99, Du04]. The analysis of all these images has in common that the objects in the images cannot be separated, e.g. by grey value segmentation, to allow the measurement of the respective feature parameters of the conventional image analysis such as length or aspect ratio.

What all these images have in common is texture. Texture is concerned with the spatial distribution of the image intensities and discrete tonal features. This can also be seen in the example image of a cheetah presented in Figure 2-13. While the skin shows a very high contrast and dark regions formed irregularly in the brighter matrix, the grass in the background has a much lower contrast but, instead, shows a directed alignment. These differences in the texture together with the colour information make it possible for the human brain to differentiate the object ‘cheetah’ from the background ‘grass’.

Figure 2-13 Example image of a cheetah showing significant variations in the texture in different regions in the image

This subjective impression of the human brain may also be described using image analytical vocabulary. When a small area of the image has little variation of discrete tonal features, the dominant property of that area is grey tone. When a small area has wide variation of discrete tonal features, the dominant property of that area is texture [Har91]. Texture can simply also be described as a measure of spatial variability, random or non-random, within an area of interest [Fer98]. The two types of images that are termed non-textured can be roughly divided

in two classes: (i) noise-like images with very rapid grey-level variation and (ii) images containing distinguishable objects that are too large to be termed texture [Kar96].
The complex microstructures, i.e. for hardened steels as can be seen in Figure 2-12 (c), consist mostly of plates or laths. These may be arranged in packets where they are oriented parallel to a certain degree. Because of the three-dimensional arrangement and differences in the etching attack due to local chemical inhomogeneities or orientational differences the optical impression in the micrograph shows objects that are looking similar but not the same. The human brain treats these micrographs as textured images and allows a qualitative differentiation between different micrographs. For quantification using conventional image analysis a segmentation would be necessary which is not possible for these images because the objects can not be separated from each other by the grey value. Nevertheless the arrangement of the grey values in the micrographs contains a large quantity of information that may be accessible by texture analysis.

To characterise these structures in textured images quantitatively new approaches had to be found. For this feature extraction four different approaches have been established [Che98, Mat98]:

- geometrical (or structural)
- statistical
- model-based
- signal processing (or transform) methods

For the **geometrical** (or structural) approach the texture is represented by well-defined primitives and a hierarchy of spatial arrangements of these primitives [Mat98]. The texture may then be described by the choice of a primitive (from a set of primitives) and the probability of the chosen primitive to be placed at a particular location. This generates a very good symbolic description of the image. Problems arise with natural textures showing a wide variability in the primitives and their placement. This method will therefore not be suitable for the characterisation of complex microstructures.
The **statistical** methods are far more promising for the demands of microstructural analysis. These methods do not attempt to understand explicitly the hierarchical structure of the texture. Instead, they represent the texture indirectly by the non-deterministic properties that govern

the distributions and relationships between the grey levels of an image. The statistical methods can be separated according to the order of grey-level statistics that they are based on. The first-order statistical measures include the moments of the grey levels of a given region, typically the mean, the variance, the skewness and the kurtosis of the grey level histogram [Har91]. These values can be computed from the grey value histogram that represents the likelihood of observing a grey value at a randomly-chosen location in the image [Che98]. Using measures computed from the second-order statistics, properties of the image or regions in this image such as the contrast, the variance or the entropy may be calculated [Har73]. The statistical methods have proved to show better characterisation of the images than e.g. power spectrum of the transform-based methods [Wes76]. Therefore the second-order statistical description of the micrographs was chosen to characterise complex microstructure and therefore will be explained in detail below.

Model-based texture analysis methods are based on the construction of an image model that can be used not only to describe the texture, but also to synthesize it [Che98]. The model parameters capture the perceived qualities of texture. Markov and Gibbs random fields and Wold models [Zha02] belong just as well to this group of methods as do fractals. The random fields methods assume that the intensity at each pixel in the image depends on the intensities of only the neighbouring pixels. The Gibbs random field assigns a probability mass function to the entire lattice of pixels specifying cliques over neighbouring pixels.

Fractals also belong to the model-based texture analysis methods. The texture of an image is characterised using a deterministic fractal describing the self-similarity across scales [Che98]. As most of the natural surfaces are not that deterministic that they could be described using fractal methods but they rather show statistical variations.

The **signal processing** (or transform) methods can be divided into spatial domain filters, Fourier domain filters, Gabor and wavelet models. They all have in common that they characterise the spatial frequency content of the texture [Du04]. Spatial domain filters perform convolutions of the textured image with linear filter masks, e.g. for an unsharp masking or a local adaptive contrast enhancement [Smo01]. The Fourier transform has proved to perform poorly in practice due to its lack of spatial localisation [Mat98]. For Gabor and wavelet filters the spatial localisation is better, but the filters are orientation selective and therefore not orientation-invariant [Che98].

Due to the advantages and the disadvantages of the different texture analysis methods the statistical texture analysis of second-order statistics was chosen and combined with the analysis according to Haralick [Har73] in previous work where it turned out to be a very powerful and flexible tool for the characterisation of complex microstructures [The98, Sch99, Fuc00, Fuc01]. The steps of the texture analysis and the results obtained in previous work will be presented in the following.

2.2.2.2 Cooccurrence matrix

To characterise the spatial distribution of the grey values, the grey level cooccurrence matrix (GLCM) is used. This describes the second order histogram of the image. The matrix contains the relative frequencies with which two neighbouring pixels (separated by distance d with angle α) occur on the image, one with grey value i and the other with grey value j [Mar90]. In other words it can be said that the GLCM is an estimate of the joint probability of a "i" grey level pixel and of a "j" grey level pixel, for a given pixel spacing and direction [Any95].

For a rectangular image consisting of N_x pixels in horizontal direction and N_y in vertical direction, the grey values appearing in every pixel are quantized to N_g levels [Har73, Alj01]. With the horizontal spatial domain $L_x=\{1, 2, \ldots, N_x\}$, the vertical spatial domain $L_y=\{1, 2, \ldots, N_y\}$and the set of quantized grey values $G=\{1, 2, \ldots, N_g\}$, the image I can be represented as a function which assigns some grey values in G to each pixel or pairs or pair of coordinates in

$L_y \times L_x$; $I: L_y \times L_x \rightarrow G$. Eq. 2-6

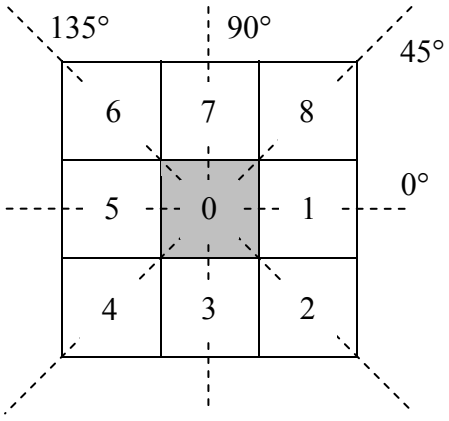

Figure 2-14 Spatial relationship of pixels adjacent to pixel 0 in horizontal (0°), vertical (90°) and the two diagonal directions (45° and 135°)

To be able to characterise the textural information contained in the image I, the spatial relationship of the grey values in the image is computed. Each pixel, excluding those on the periphery of the image, is considered to have 8 nearest neighbours (Figure 2-14).

For all of these four directions a GLCM can be computed with different distances d between the neighbouring pixels. For angles α quantized to 45° intervals the unnormalised frequencies P(i,j,d,α) are defined by

$$P(i,j,d,0°) = \#\left\{\begin{array}{l}((k,l),(m,n)) \in (L_y \times L_x) \times (L_y \times L_x) \,|\, k-m=0, |l-n|=d, \\ I(k,l)=i, I(m,n)=j\end{array}\right\} \quad \text{Eq. 2-7}$$

$$P(i,j,d,45°) = \#\left\{\begin{array}{l}((k,l),(m,n)) \in (L_y \times L_x) \times (L_y \times L_x) \,|\, (k-m=d, l-n=-d) \text{ or} \\ (k-m=-d, l-n=d), I(k,l)=i, I(m,n)=j\end{array}\right\} \quad \text{Eq. 2-8}$$

$$P(i,j,d,90°) = \#\left\{\begin{array}{l}((k,l),(m,n)) \in (L_y \times L_x) \times (L_y \times L_x) \,|\, |k-m|=d, l-n=0, \\ I(k,l)=i, I(m,n)=j\end{array}\right\} \quad \text{Eq. 2-9}$$

$$P(i,j,d,135°) = \#\left\{\begin{array}{l}((k,l),(m,n)) \in (L_y \times L_x) \times (L_y \times L_x) \,|\, (k-m=d, l-n=d) \text{ or} \\ (k-m=-d, l-n=-d), I(k,l)=i, I(m,n)=j\end{array}\right\} \quad \text{Eq. 2-10}$$

where # denotes the number of elements in the set [Har73], (k,l) the coordinate with grey value i and (m,n) the coordinate with grey level j [Alj01]. To obtain comparable results from different images all the elements of the matrix are normalised by dividing the number of elements by the number R of pixel pairs occurring in the image with distance d and angle α according to

$$p(i,j) = P(i,j)/R \quad \text{Eq. 2-11}$$

For the nearest neighbour the number R of nearest pixel pairs in an image may be calculated according to the expressions given in Table 2-1.

Table 2-1 Calculation of the number R of nearest pixel pairs in an image depending on the investigated angle

distance d	angle α	number R of pixel pairs
1	0°	$2 \cdot N_y \cdot (N_x - 1)$
1	45°	$2 \cdot (N_y - 1) \cdot (N_x - 1)$
1	90°	$2 \cdot N_x \cdot (N_y - 1)$
1	135°	$2 \cdot (N_x - 1) \cdot (N_y - 1)$

As an example for such a GLCM an example image showing 36 pixels with four different grey values labelled with the numbers 0 to 3 is presented in Figure 2-15 together with the respective GLCM for the direct horizontal neighbour (d=1 pixel, α=0°). For a better understanding only the direct right neighbour is analysed in this example and not both horizontal neighbour pixels. If the neighbouring pixels in the two opposite directions (direct left and right neighbouring pixels for d=1 pixel and α=0°) are investigated, the resulting GLCM is symmetric

$$P(i,j,d,\alpha) = P(j,i,d,\alpha) \qquad \text{Eq. 2-12}$$

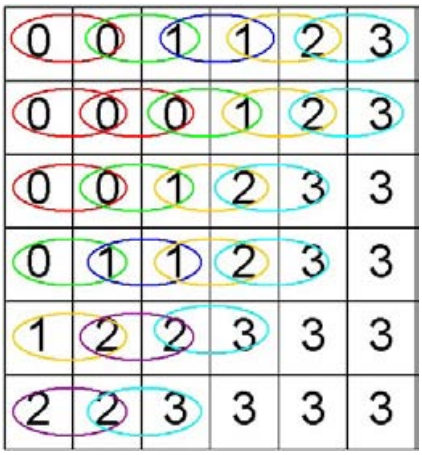

		grey value i of the examined pixel			
		0	**1**	**2**	**3**
grey value j of the neighbour pixel	**0**	4	0	0	0
	1	4	2	0	0
	2	0	5	2	0
	3	0	0	6	7

Figure 2-15 Schematic grey image (left) and corresponding cooccurrence matrix (right) for the direct, right neighbour (d=1, α=0°). The four grey values in the image are represented by the numbers 0 to 3

2.2.2.3 Parameters to characterise complex microstructures

The extraction of the texture information contained in the image can be done using different texture parameters based on the normalised GLCM. In different papers a set of 14 parameters have been suggested [Har73, Har74], which extract the textural features from the GLCM and therefore characterise the corresponding image quantitatively. The mathematical description of these parameters is as follows

1) Haralick 1 = Angular Second Moment

$$f_1 = \sum_i \sum_j \left[p(i,j)\right]^2 \qquad \text{Eq. 2-13}$$

2) Haralick 2 = Contrast

$$f_2 = \sum_{n=0}^{N_g-1} n^2 \left[\sum_{i=1}^{N_g} \sum_{\substack{j=1 \\ |i-j|=n}}^{N_g} p(i,j) \right] \qquad \text{Eq. 2-14}$$

3) Haralick 3 = Correlation

$$f_3 = \frac{\sum_i \sum_j (i \cdot j) \cdot p(i,j) - \mu_x \cdot \mu_y}{\sigma_x \cdot \sigma_y} \qquad \text{Eq. 2-15}$$

4) Haralick 4 = Sum of Squares: Variance

$$f_4 = \sum_i \sum_j (i - \mu)^2 \cdot p(i,j) \qquad \text{Eq. 2-16}$$

5) Haralick 5 = Inverse Difference Moment

$$f_5 = \sum_i \sum_j \frac{1}{1 + (i-j)^2} \cdot p(i,j) \qquad \text{Eq. 2-17}$$

6) Haralick 6 = Sum Average

$$f_6 = \sum_{i=2}^{2N_g} i \cdot p_{x+y}(i) \qquad \text{Eq. 2-18}$$

7) Haralick 7 = Sum Variance

$$f_7 = \sum_{i=2}^{2N_g} (i - f_8)^2 \cdot p_{x+y}(i) \quad \text{Eq. 2-19}$$

8) Haralick 8 = Sum Entropy

$$f_8 = -\sum_{i=2}^{2N_g} p_{x+y}(i) \cdot \log\left[p_{x+y}(i)\right] \quad \text{Eq. 2-20}$$

9) Haralick 9 = Entropy

$$f_9 = -\sum_i \sum_j p(i,j) \cdot \log(p(i,j)) \quad \text{Eq. 2-21}$$

10) Haralick 10 = Difference Variance

$$f_{10} = \text{variance of } \mathrm{p}_{\mathrm{x-y}} \quad \text{Eq. 2-22}$$

11) Haralick 11 = Difference Entropy

$$f_{11} = -\sum_{i=0}^{N_g-1} p_{x-y}(i) \cdot \log\left[p_{x-y}(i)\right] \quad \text{Eq. 2-23}$$

12) Haralick 12 = Information Measures of Correlation

$$f_{12} = \frac{HXY - HXY1}{\max(HX, HY)} \quad \text{Eq. 2-24}$$

13) Haralick 13 = Information Measures of Correlation

$$f_{13} = \left(1 - \exp\left[-2 \cdot \left(HXY2 - HXY\right)\right]\right)^{1/2} \quad \text{Eq. 2-25}$$

14) Haralick 14 = Maximal Correlation Coefficient

$$f_{14} = (\text{second largest eigenvalue of Q})^{1/2} \quad \text{Eq. 2-26}$$

Therefore the following abbreviations are used:

$p(i,j)$	$(i,j)^{th}$ entry in a normalised GLCM with distance d under angle α, $= P(i,j)/R$
$p_x(i)$	sum of the i^{th} column of the GLCM with $p_x(i) = \sum_{j=1}^{N_g} p(i,j)$
$p_{x+y}(k)$	$p_{x+y}(k) = \sum_{i=1}^{N_g}\sum_{\substack{j=1 \\ i+j=k}}^{N_g} p(i,j)$ $\quad k = 2, 3, ..., 2N_g$
$p_{x-y}(k)$	$p_{x-y}(k) = \sum_{i=1}^{N_g}\sum_{\substack{j=1 \\ \lvert i-j\rvert=k}}^{N_g} p(i,j)$ $\quad k = 0, 1, ..., N_g-1$
$\mu_x, \mu_y, \sigma_x, \sigma_y$	means and standard deviations of p_x and p_y
$\sum_i$ and $\sum_j$	$\sum_{i=1}^{N_g}$ and $\sum_{j=1}^{N_g}$ respectively
HX	entropy of p_x
HY	entropy of p_y
HXY	$HXY = -\sum_i \sum_j p(i,j) \cdot \log\big(p(i,j)\big)$
HXY1	$HXY1 = -\sum_i \sum_j p(i,j) \cdot \log\big(p_x(i) \cdot p_y(j)\big)$
HXY2	$HXY2 = -\sum_i \sum_j p_x(i) \cdot p_y(j) \cdot \log\big(p_x(i) p_y(j)\big)$
Q	$Q(i,j) = \sum_k \frac{p(i,k) \cdot p(j,k)}{p_x(i) \cdot p_y(k)}$

To generate a measure that is invariant under rotation the mean $f_{1,m}$ of every parameter under the four angles is calculated [Har73] as e.g. for the parameter Haralick 1

$$f_{1,m} = \frac{1}{4} \cdot \sum_{\alpha} f_1(\alpha) \qquad \text{Eq. 2-27}$$

2.3 Correlation of microstructure and properties

2.3.1 Correlation of the hardened microstructure with properties

As stated in section 2.2.1 the quantitative characterisation of hardened steel microstructures is not possible using conventional image analysis. This lack of quantification can be eliminated by the use of the texture analysis after Haralick [Har73]. These parameters describe image analytical features of the micrographs. Therefore they cannot be related directly to the processing or the properties of the respective sample, as e.g. the volume content of a phase may be related to the heat treatment or the chemical composition of the respective component. As these correlations are essential for both material development and the quality control in routine processes, the information has to be correlated with the relevant parameters (compare also section 2.2).

2.3.2 Correlation with material properties by neural networks

For the correlation of measured data with respective properties and/or process parameters various methods can be applied. The most common method is to analyse the processing parameters and/or the microstructural features influencing the (mechanical) properties and fit these data to a linear regression algorithm. This was shown for the prediction of mechanical material properties, such as. the hardness, yield and tensile strength, from alloy composition and/or heat treatment parameters using linear regression (see sections 2.1 and 2.2). This method however requires knowledge of which parameters may influence the respective property. For many problems in materials science the influencing parameters are numerous and are mostly not known or the knowledge of the interaction between different parameters is not well enough established [Bha99b, Guo03, Kus02]. For these problems showing overwhelming complexity alternative methods of correlation had to be found.

Neural networks have been shown in various applications that they are able to handle these problems [Bha99b], especially feed-forward networks have proved to be a helpful tool [Bis96], amongst other applications as well as for characterisation problems in materials science. The fundamental idea of these networks is taken from neurobiology and the computational theory of highly parallel, distributed information processing and systems [Jai96, Jor99]. The feed-forward networks, also known as ‘back-propagation’ neural networks, consist of units that have one-way connections to other units [Rip96]. The units,

also called neurons, are arranged in layers with weighted connections multiplying the signals contained in the neurons travelling along them by a certain factor. Using this tool a mathematical correlation between the data in the input layer and the value(s) in the output layer can be established. For a feed-forward neural network at least one hidden layer is needed to establish the correlation between input and output layer [Dui00]. The knowledge is stored in the structure of the topology and the weights of the weighted connections [Ge99]. Training with datasets with known output values allows the weights to be adjusted to give a correlation between the input and the output values. This training is based on the back-propagation of the errors from the output layer to the hidden layer [Krö96]. This learning ability is the key feature enabling this method to provide a correlation of microstructural features with corresponding mechanical properties without having to understand the underlying mechanisms.

2.4 Characterisation of complex microstructures

As the complex microstructures, e.g. of hardened steels, cannot be quantified using the methods of conventional image analysis (see section 2.2), the methods of the texture analysis after Haralick can be applied to quantify the microstructure and the neural networks to correlate these values with corresponding properties.

In previous work, experiments have first been made to characterise the complex microstructures using texture analysis after Haralick in combination with a neural network to establish a correlation with properties [The98]. This showed the capability of the method to characterise these micrographs.

2.4.1 Jominy end-quench specimen of the plain carbon steel C45

In later work texture analysis after Haralick was applied to characterise samples of the plain carbon steel C45 [Sch99]. Jominy end-quench specimens were generated showing the whole spectrum of microstructures that may appear during continuous cooling of the respective material. For samples of the plain carbon steel C45 with 0.45 wt.-% carbon, images were acquired along the axis of the sample representing the complete range of microstructures present in the sample. For all these images the texture parameters were acquired together with the respective microhardness H_{V1}. A neural network was trained with microhardness values as

output and the corresponding texture parameters as input values. For the texture parameters of micrographs not involved in the training process the hardness calculated by the neural network was compared with the mechanically measured values. A very good correlation between the texture parameters after Haralick and the corresponding microhardness could be established successfully (Figure 2-16). This is also proved by the low mean deviation between measured and calculated values, which was 17.6 H_{V1}.

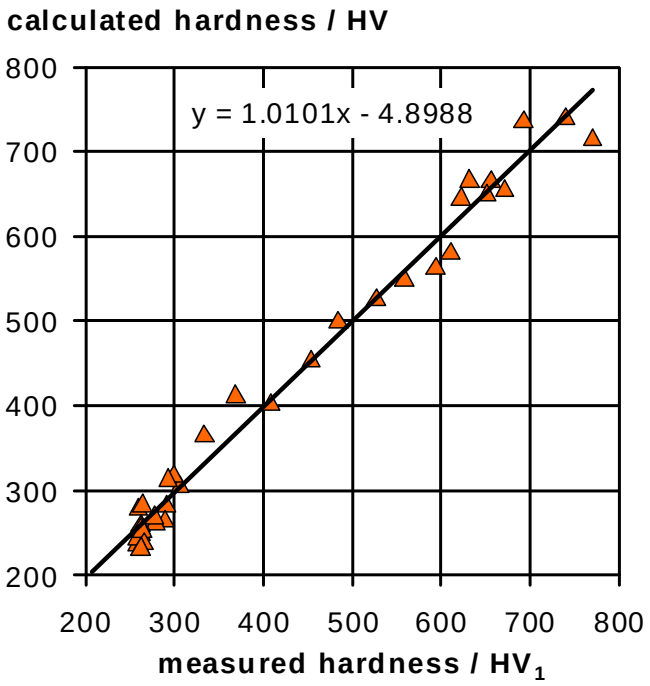

Figure 2-16 Correlation between the measured calculated microhardness, calculated from the texture parameters after Haralick for a Jominy end-quench specimen of the plain carbon steel C45 with 0.45 wt.-% carbon [Sch99]

3 Experimental procedure

3.1 Materials and processing

3.1.1 Material for testing of texture analysis and corresponding heat treatment

The investigations related to the basic properties of texture analysis have been made with the tool steel 100Cr6. This steel (material number 1.3505 according to EN 10027-2) [EN92] is comparable to AISI E 52100. The chemical composition is given in Table 3-1.

Table 3-1 Chemical analysis of the steel 100Cr6, measured by quantitative spectral analysis on two different samples, specified values according to [Weg01], all values in wt.-%

element	measured value	specified value
C	0.92	0.92 – 1.13
Si	0.24	0.12 – 0.38
Mn	0.33	0.21 – 0.49
P	0.012	< 0.035
S	0.002	< 0.008
Al	0.005	< 0.06
Cr	1.46	1.30 – 1.70
Mo	0.04	< 0.15
Ni	0.07	< 0.30
Cu	0.10	< 0.30
Ti	0.001	< 0.003

The material is an ultra clean steel used for heavily loaded steel parts, e.g. for fuel injectors. To obtain this quality the steel was vacuum arc remelted and vacuum degassed. This material was then cast into ingots, which where then hot rolled to bars with a diameter of 27 mm.

These bars were then soft annealed at 780 °C to enhance machinability for further mechanical treatment.

From such a bar discs were cut off according to Figure 3-1 using a Struers Discotom-50 cut-off machine. Additionally cylinders according to DIN 50191 [DIN87] with a length of 100 mm and a diameter of 25 mm were machined from the bar for Jominy end-quench tests.

For the investigations in the dilatometer cylindrical samples were machined. These had an inner diameter of 3 mm, an outer diameter of 5 mm and a length of 17 mm with the inner bore parallel to the rolling direction of the bar.

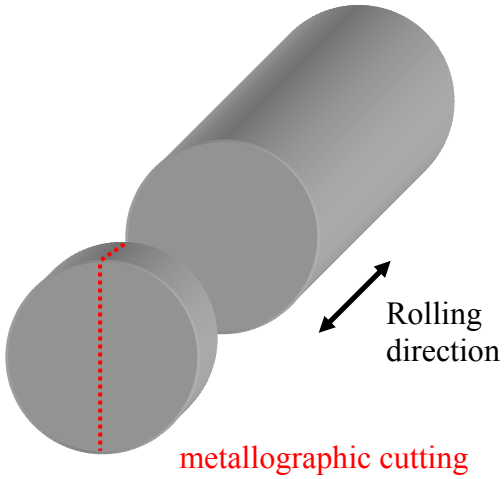

Figure 3-1 Scheme of the cutting of the sample discs from the received bar and the position of the cutting of the discs after the heat treatment

Jominy end-quench specimen

For determination of the hardenability of steels the widely utilised Jominy end-quench test was carried out with the available material. Cylinders, 100 mm long and 25 mm in diameter (Figure 3-2 (a)), of the tool steel 100Cr6 were heat treated according to DIN 50191 [DIN87] (Figure 3-2 (b)) over 20 minutes to a re-austenitisation temperature of 900 °C for a hold time of 30 minutes to ensure complete and homogeneous re-austenitisation of the sample prior to the cooling. The variation in carbide volume fraction with re-austenitisation for 100Cr6 is shown in Figure 3-3, from which a volume fraction of about 1 % of carbides during re-austenitisation can be predicted for the treatment described above. Hence, prior to cooling the

steel should be fully austenitic with an uniform carbon content and a distribution of a small fraction of fine carbides dispersed.

Following re-austenitisation the sample was rapidly transferred from the furnace to a special fixture to be quenched with water from one face while the other face is cooling in air, Figure 3-2 (b). This causes a variation in cooling rate along the specimen length and so a range of continuously cooled microstructures can be generated with this method in a single specimen. This microstructural differences are responsible for the variation in hardness along the bar length. From the water quenched martensitic face the hardness decreases due to slower cooling and therefore increasing carbon diffusion forming mixtures of martensite, bainite and, eventually, pearlite. After end quenching the specimens were characterised as described in Section 3.2.

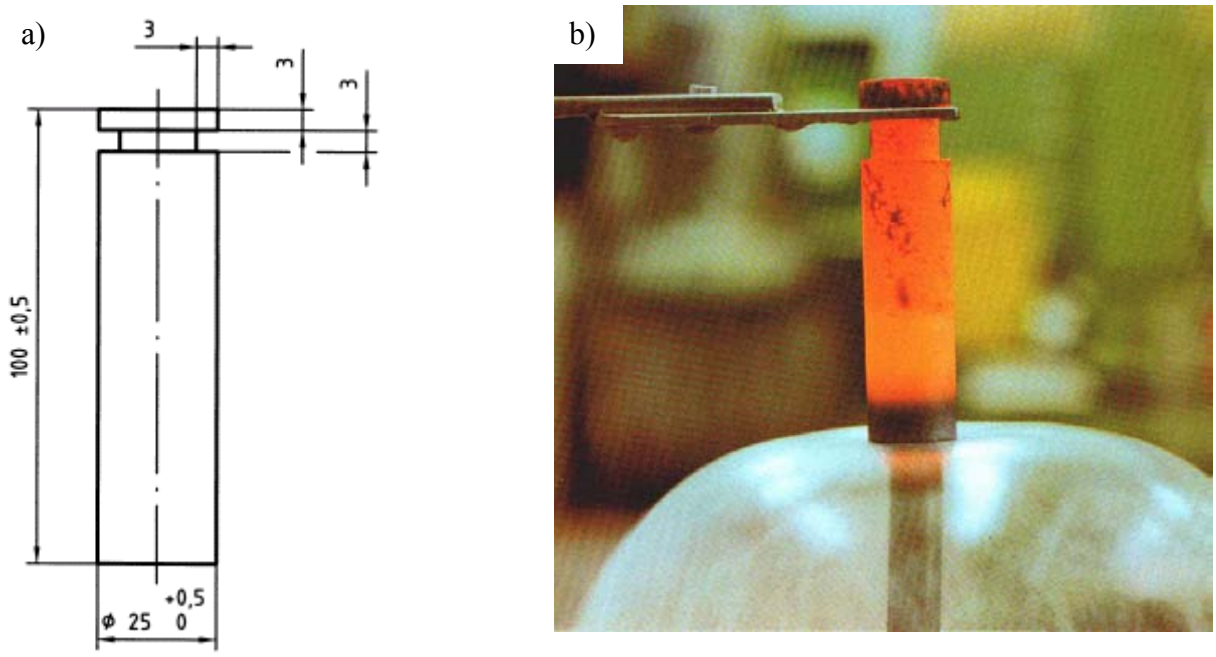

Figure 3-2 Dimensions of the Jominy end quench specimen (a) according to DIN 50191 [DIN87] (in millimetres) and illustration of the quenching after re-austenitisation (b) [Lie98]

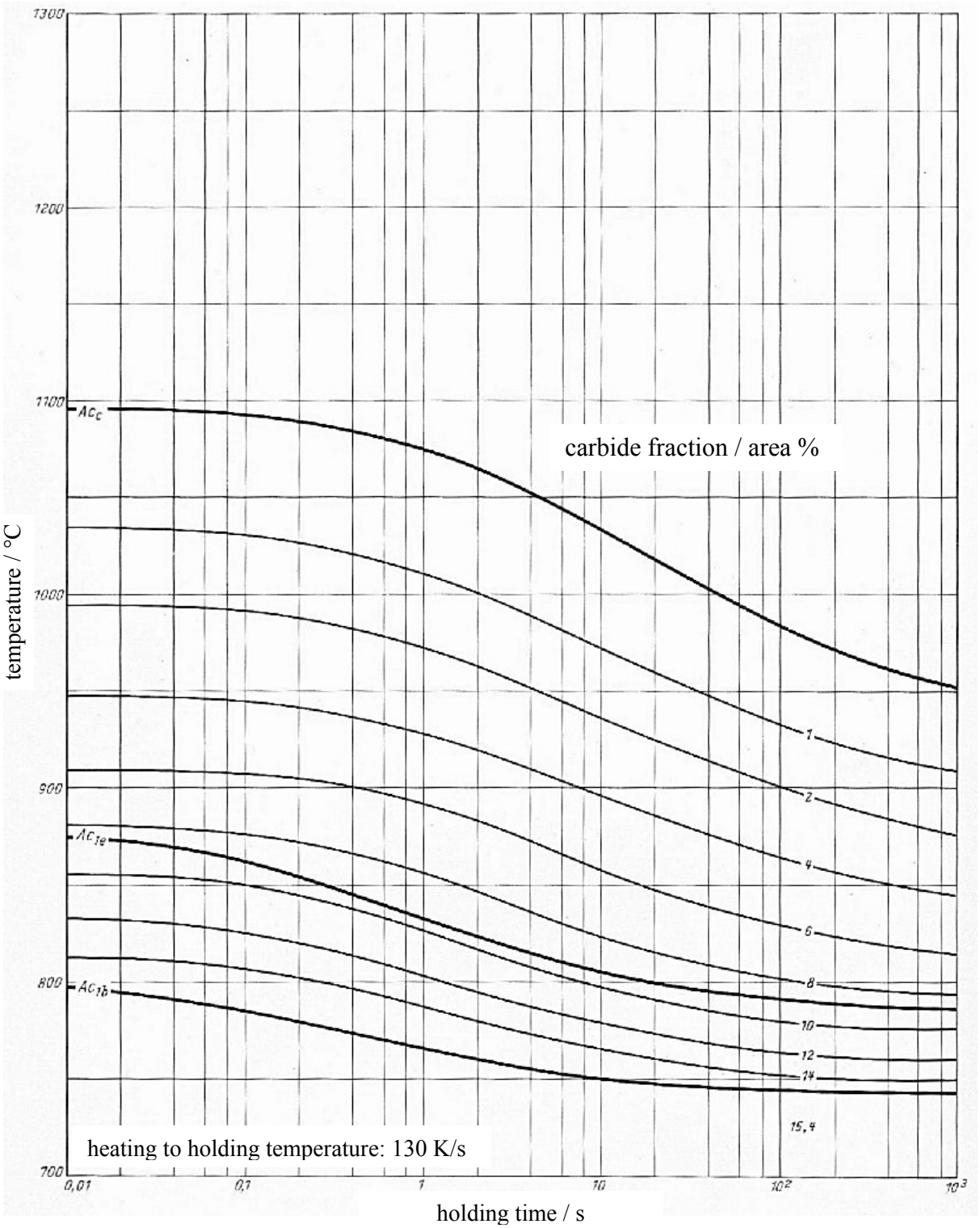

Figure 3-3 Isothermal carbide dissolution diagram for the tool steel 100Cr6 [Ros61]

Variation of re-austenitisation temperature

To determine the effect of re-austenitisation temperature on transformation behaviour and carbide distribution, samples of the steel 100Cr6 were austenitised at temperatures in the range between 780 °C and 930 °C (around the technically used temperature of 850 °C) with a holding time of 20 minutes and slowly cooled to room temperature. Using a Theta Industries quenching dilatometer samples were produced with closely controlled near-equilibrium heating/cooling rates (rate of 0.2 K s^{-1}) using RF heating and a helium gas quench. This heat treatment was chosen to control the extent of dissolution of carbides and re-distribution of carbon in solution during re-austenitisation.

For this heat treatment cylindrical specimen with a length of 17 mm, an inner diameter of 3 mm and an outer diameter of 5 mm have been machined from 100Cr6 (Figure 3-4).

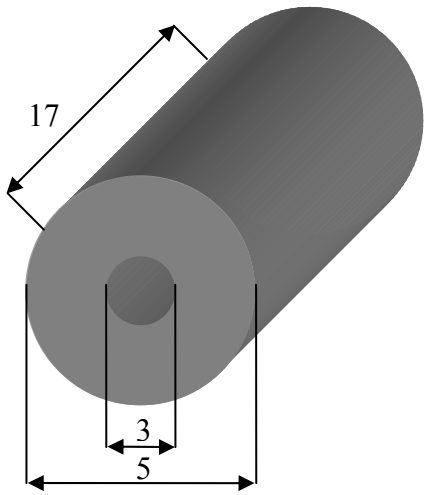

Figure 3-4 Sketch of the geometry for the samples heat treated in the dilatometer, all values in millimetres

The details of the heat treatment are given in Table 3-2. The re-austenitisation temperatures have been chosen around the technically applied temperature of 850 °C to simulate the influence of a variation in the heat treatment. Due to the relative slow continuous cooling the samples transformed into pearlite. Figure 3-5 shows the corresponding CCT diagram from an austenitising temperature of 860 °C with the approximate cooling rate being marked yielding a hardness of 289 H_V.

Table 3-2 Summary of heat treatments to produce the Jominy end-quench specimen, pearlitic and bainitic samples of the tool steel 100Cr6 together with the respective sample descriptions

heat treatment	**austenitisation temperature T_A, heating rate, holding time**	**bainitisation temperature T_B, holding time**	**cooling to room temperature**	***sample description***
Jominy end-quench specimen	900 °C, - , 50 min	-	water … air	*Jom100Cr6*
pearlitic samples	780 °C, 0.2 K s^{-1}, 20 min	-	0.2 K s^{-1}	*p100Cr6_780*
	800 °C, 0.2 K s^{-1}, 20 min	-	0.2 K s^{-1}	*p100Cr6_800*
	850 °C, 0.2 K s^{-1}, 20 min	-	0.2 K s^{-1}	*p100Cr6_850*
	900 °C, 0.2 K s^{-1}, 20 min	-	0.2 K s^{-1}	*p100Cr6_900*
	930 °C, 0.2 K s^{-1}, 20 min	-	0.2 K s^{-1}	*p100Cr6_930*
bainitic samples	780 °C, ≈ 0.2 K s^{-1}, 20 min	220 °C, 6 h	air	*b100Cr6_780*
	800 °C, ≈ 0.2 K s^{-1}, 20 min	220 °C, 6 h	air	*b100Cr6_800*
	850 °C, ≈ 0.2 K s^{-1}, 20 min	220 °C, 6 h	air	*b100Cr6_850*
	900 °C, ≈ 0.2 K s^{-1}, 20 min	220 °C, 6 h	air	*b100Cr6_900*
	930 °C, ≈ 0.2 K s^{-1}, 20 min	*220 °C, 6 h*	*air*	*b100Cr6_930*

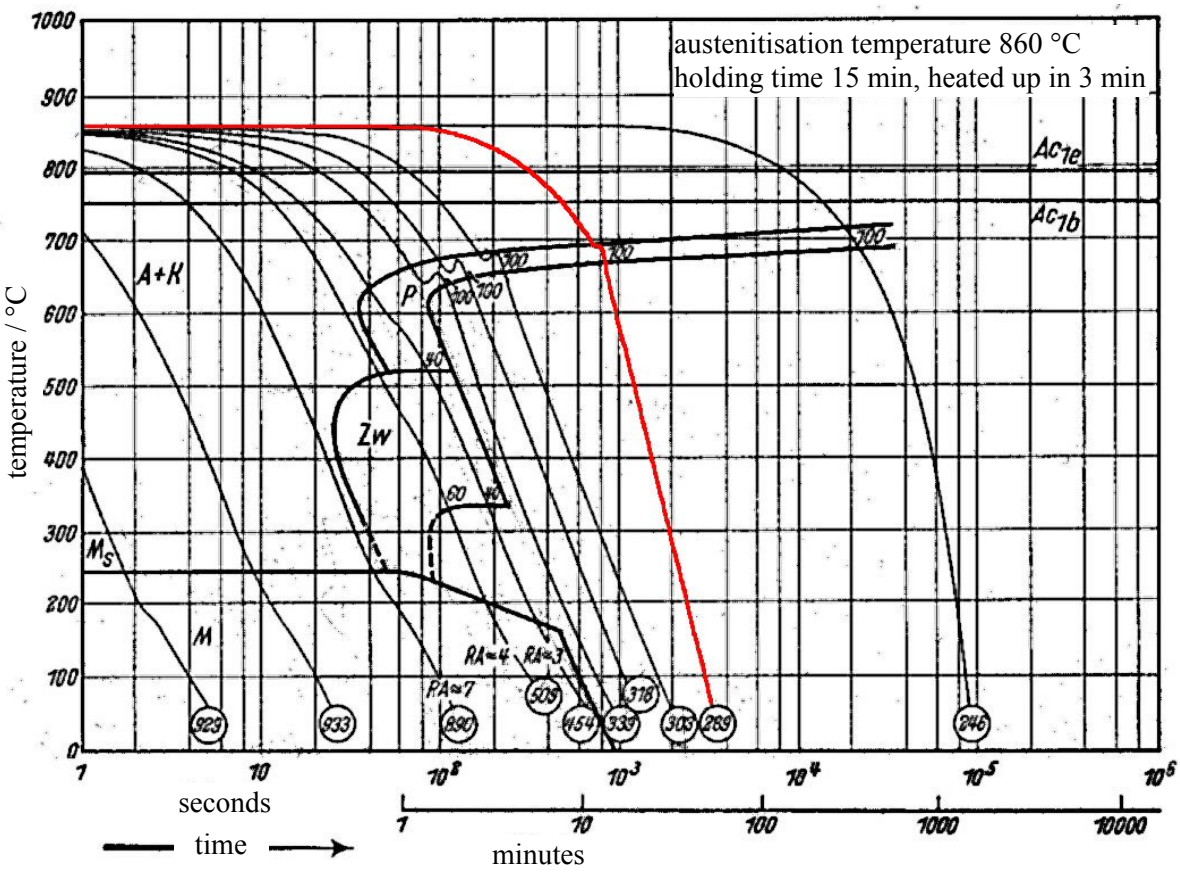

Figure 3-5 CCT diagram of the tool steel 100Cr6 for an austenitisation temperature of 860 °C [Ros61] with the constant cooling rate of approximately 0.2 K s^{-1} marked

Bainitic samples

To simulate complex bainitic microstructures, discs described in Figure 3-1 of the tool steel 100Cr6 were re-austenitised at different temperatures and transformed isothermally to bainite before cooling at air to room temperature. The schematic heat treatment for bainitisation is given in Figure 3-6.

To generate a variety of different bainitic microstructures, the same five re-austenitisation temperatures were chosen as for the pearlitic samples (Table 3-2). After a heating up at a rate of 0.2 K s^{-1} the samples were held at the re-austenitisation temperature for 20 minutes before they were transferred to a salt bath at a temperature of 220 °C for the isothermal transformation into bainite. After 6 hours the samples were then removed from the bath and air cooled to room temperature.

With the bainitisation temperature of 220 °C being close to the martensite start temperature of approximately 245 °C [Ros61] these samples should transform to lower bainite and possibly some martensite. As the austenitising temperature varies the carbon content in the austenite and therefore the martensite start temperature varies, which may change the percentage of martensite formed. As can be seen from Figure 3-3 the amount of dissolved carbides increases with both re-austenitisation time and temperature. Thus the carbon content in the austenite increases, which decreases the martensite start temperature [Bor95] and thereby decreases the amount of martensite formed during quenching in favour of retained austenite or fine bainitic carbides [Spe72]. The isothermal TTT diagram is shown in Figure 3-7.

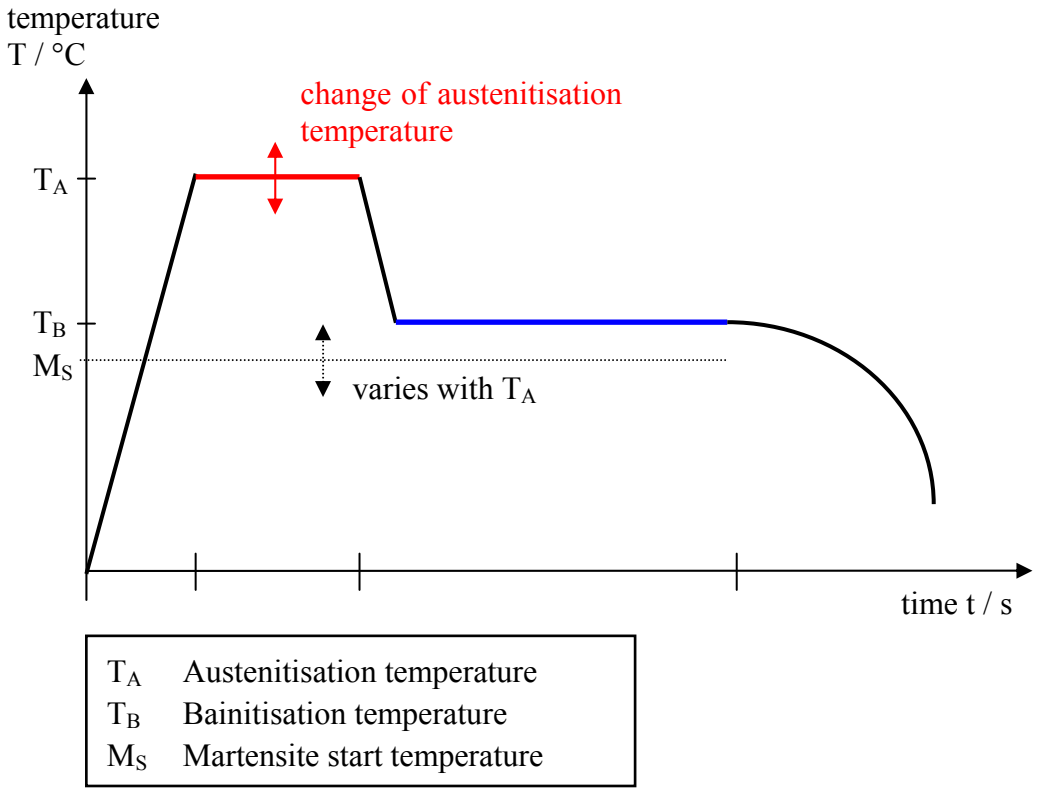

Figure 3-6 Schematic heat treatment for the isothermal transformation (bainitisation)

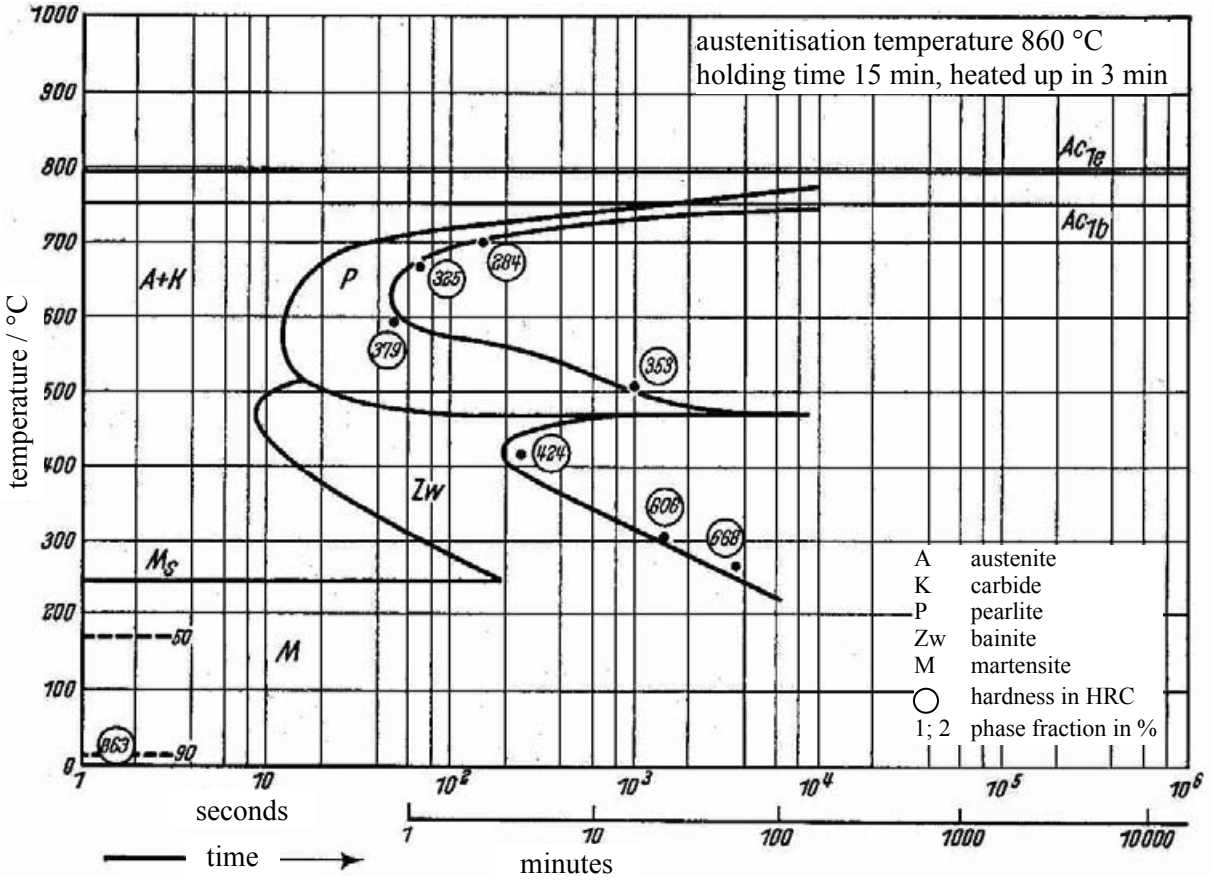

Figure 3-7 TTT diagram for the isothermal transformation of the tool steel 100Cr6 for an austenitisation temperature of 860 °C [Ros61]

3.1.2 Material for the determination of the lateral hardness distribution and corresponding heat treatment

For practical characterisation of the complex microstructure of surface hardened steel components and correlation of the quantitatively measured data with local mechanical properties, such as microhardness, different components have been chosen to apply the texture analysis.

Three components of different steels have been examined (i) laser hardened, (ii) induction hardened or (iii) case hardened, as stated in Table 3-3. For all the components the main aim of the heat treatment was to combine the ductile behaviour of the core with the wear resistance of the hard surface layer.

Table 3-3 Overview of the samples used to calculate the lateral hardness distribution from texture analysis data

hardening technique	steel	component
laser hardened	32CrB4	bearing surface
induction hardened	42CrMoS4	bearing surface of a crankshaft
case hardened	18CrNiMo 7-6 mod.	tooth of a steering column

Laser hardened steel component

The laser hardened steel component was made of the structural alloy steel 32CrB4 (material number 1.7076) and the chemical composition given in Table 3-4. A CCT diagram for this material is given in Figure 3-9.

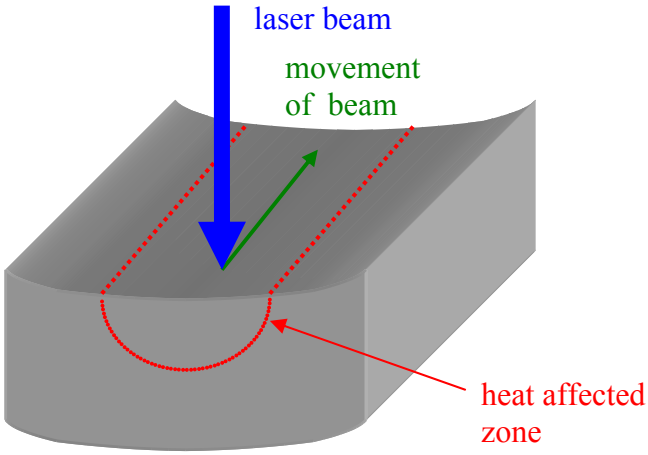

Figure 3-8 Scheme of the heat treatment of the laser hardened bearing surface

The initial microstructure of the material was soft annealed. The surface of the sample was heated up using a laser beam with a beam power of 1 kW and a beam diameter of approximately 1 mm (Figure 3-8). A continuous feed rate of 1 m/min was used, which gave an approximate residence time of 50 ms of the beam on every position of the sample surface. With a surface temperature of approximately 900 °C as aspired temperature the component was quenched in oil at room temperature to transform the austenitised surface into martensite while the core microstructure remained annealed.

Table 3-4 Chemical analysis of the steel 32CrB4 specified according to [Weg01], all values in wt.-%

element	C	Si	Mn	P	S	Cr	B
composition	0.29 – 0.36	≤ 0.40	0.60 – 0.90	≤ 0.035	≤ 0.035	0.90 – 1.20	0.0008 – 0.0050

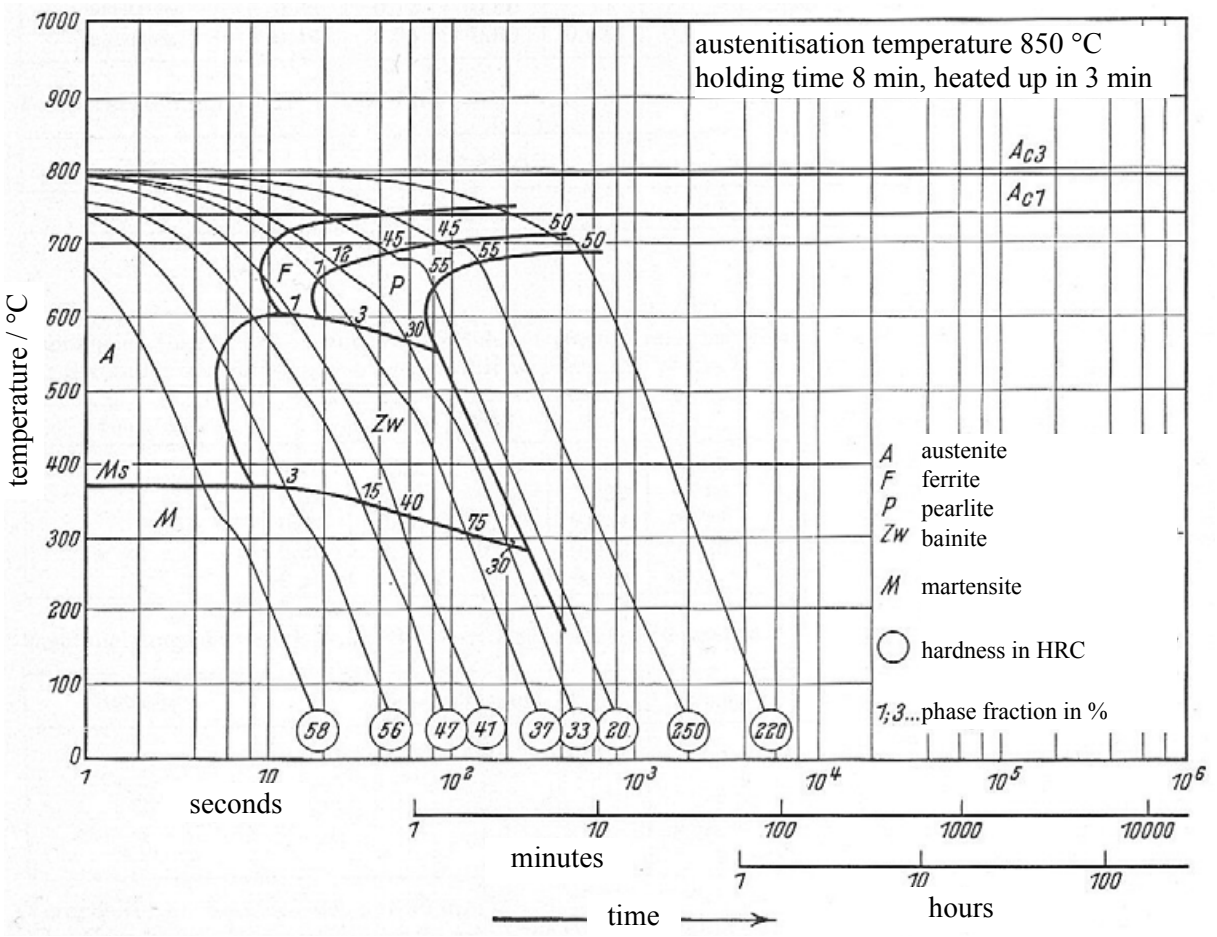

Figure 3-9 CCT diagram of the structural alloy steel 32CrB4 for an austenitisation temperature of 850 °C [Ros61]

Induction hardened steel component

For induction hardening the heat-treatable steel 42CrMoS4 (material number 1.7227) was used. The chemical composition of this steel is given in Table 3-5, and the respective CCT diagram in Figure 3-11.

Before surface treatment the crankshaft made of this material was hardened by water quenching from an austenitisation temperature of 840 °C and tempered at 630 °C for 2 hours to obtain a hardness of approximately 330 H_{V10}.

For surface hardening the sample was locally heated at the positions where the bearings will be placed afterwards using a specially designed induction coil. An aspired temperature of approximately 860 °C can be reached at the surface. After local surface heating the component was oil quenched to room temperature to transform the surface from austenite into martensite while the microstructure in the core is not changed and therefore remains in the quenched and tempered state.

After heat treatment the crankshaft was cut along the rotational axis through the crankpin bearing (Figure 3-10) for characterisation (Section 3.2).

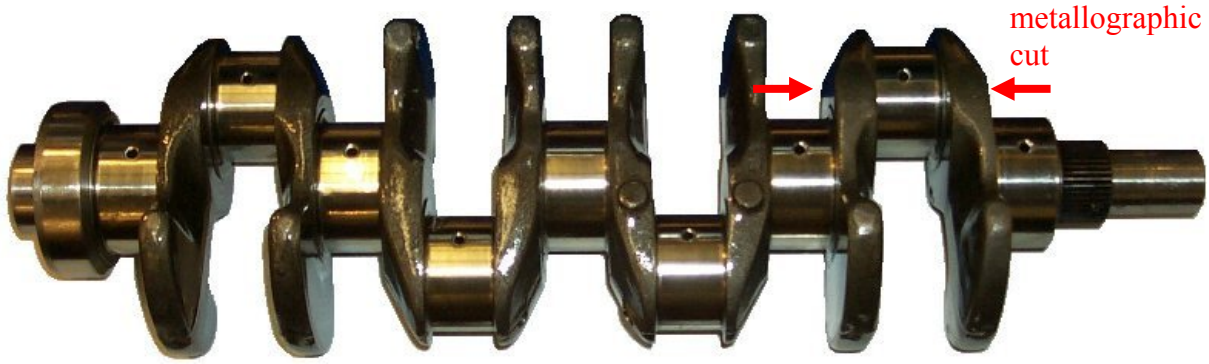

Figure 3-10 Scheme of a crankshaft and the position of the metallographic cut after the induction heat treatment

Table 3-5 Chemical analysis of the steel 42CrMoS4 specified according to [Weg01], all values in wt.-%

element	C	Si	Mn	P	S	Cr	Mo
composition	0.38 – 0.45	≤ 0.40	0.60 – 0.90	≤ 0.035	0.020 – 0.040	0.90 – 1.20	0.15 – 0.30

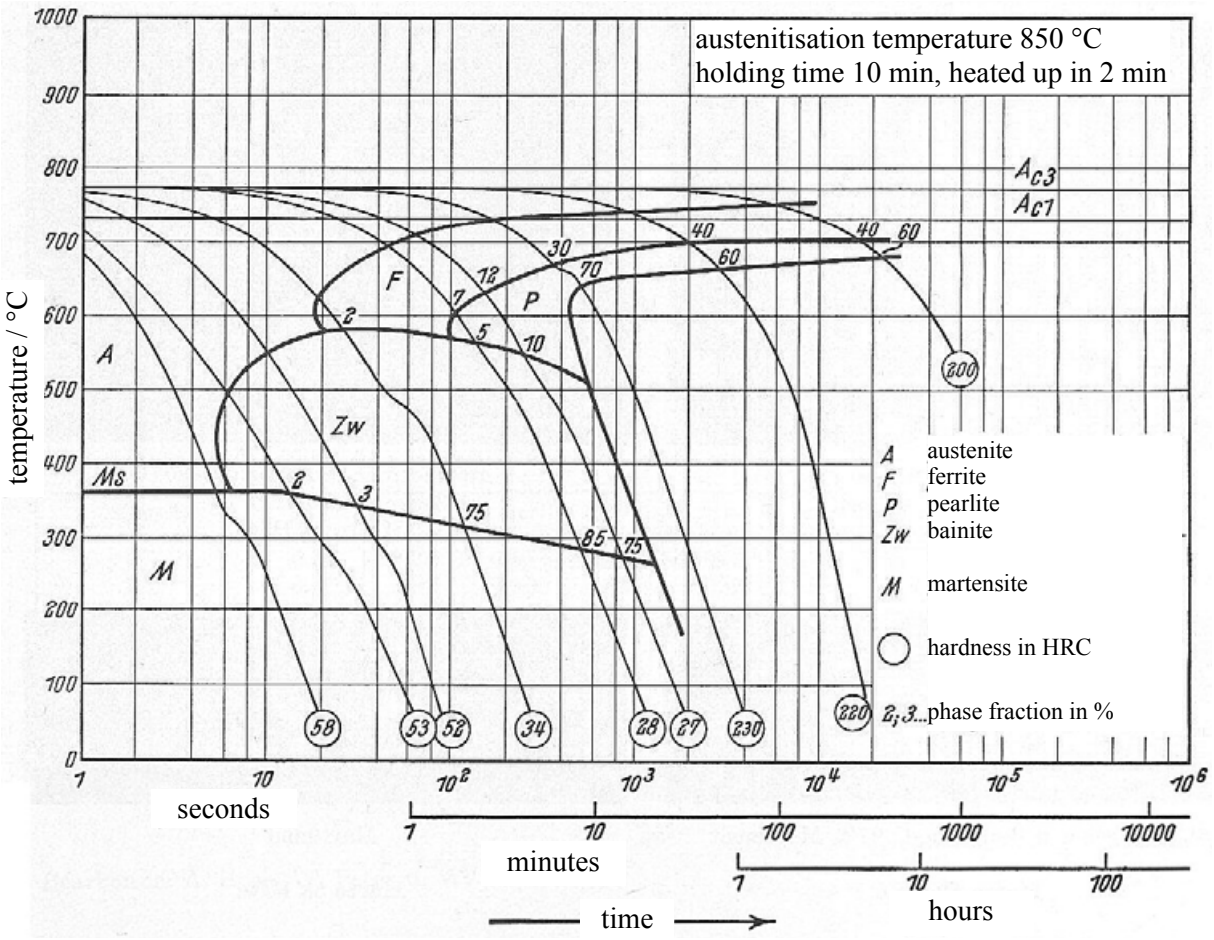

Figure 3-11 CCT diagram of the heat-treatable steel 42CrMo4 for an austenitisation temperature of 850 °C [Ros61]

Case hardened steel component

Parts of a 18CrNiMo 7-6 steel (material number 1.6587) steering column modified with the chemical composition given in Table 3-6 have been used to test the determination of lateral hardness distribution in the case hardened condition using texture analysis and a neural network.

This material was melted in an electric arc furnace and after subsequent ladle treatment cast to ingots. These were then hot rolled to bars. A ferritic-pearlitic microstructure was achieved by re-austenitisation at 950 °C and air cooling to room temperature.

For case hardening the components were then gas carburised at 930 °C for 12 hours to increase the carbon content at the surface to 0.65 – 0.85 wt.-%. After that the components were cooled to 600 °C and held for 2 hours at this temperature. For the hardening the

temperature was again raised to 830 °C where the components were held for 30 minutes before they were quenched in oil. By tempering at 180 °C for 2 hours a hardness of 59-63 HRC was achieved.

Table 3-6 Chemical composition of the case hardening steel 18CrNiMo 7-6 modified, all values in wt.-%

element	C	Si	Mn	P	Cr	Mo	Ni	Cu
composition	0.15 – 0.19	< 0.40	0.5 – 0.9	< 0.025	1.50 – 1.80	0.25 – 0.35	1.40 – 1.70	< 0.30

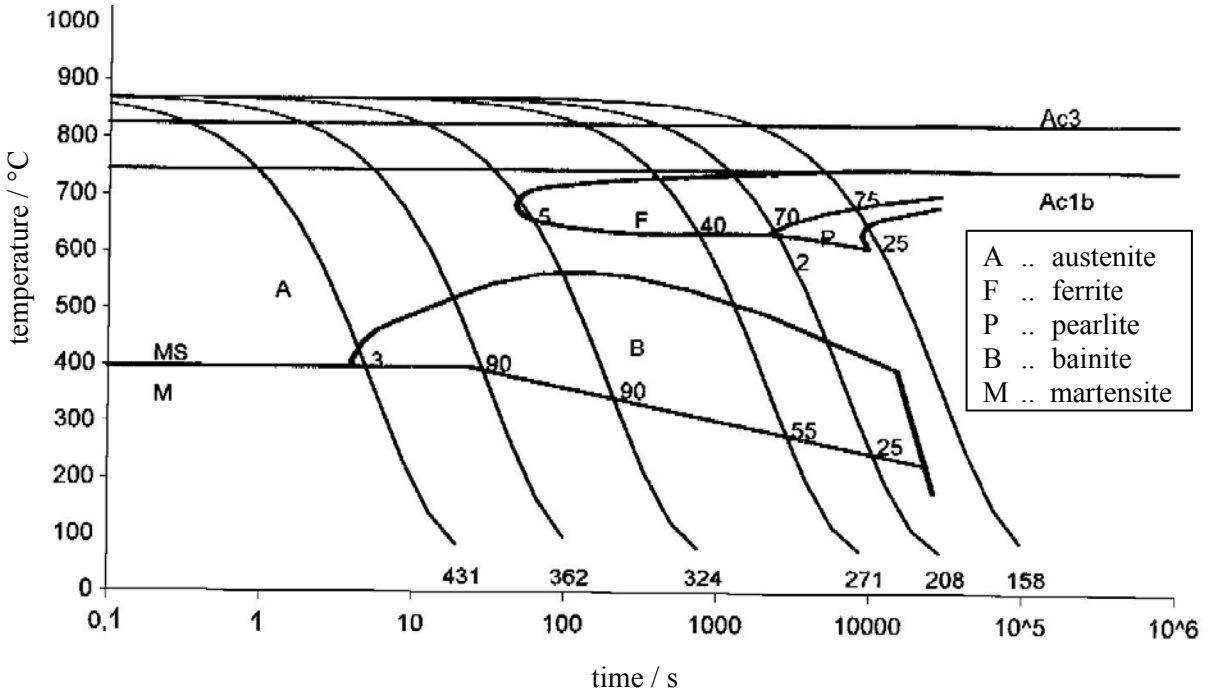

Figure 3-12 CCT diagram of the case hardening steel 18CrNiMo 7-6 mod. for 20 minutes austenitisation at 870 °C [Som02] showing the phase fractions and the Vickers hardness

For the texture analysis and the determination of the lateral hardness distribution three teeth forming the steering column have been cut after carburising and heat treatment and metallographically prepared on the face visible in Figure 3-13.

Figure 3-13 Illustration of the lower part of the steering column with the examined teeth cut from the shaft

3.2 Characterisation techniques

3.2.1 Thermodynamical simulation of transformation behaviour

To simulate the theoretical transformation behaviour of the tool steel 100Cr6 the equilibrium phase variation as a function of temperature was calculated. The chemical composition measured by quantitative spectral analysis (Table 3-1) was fed into Thermo-Calc and the phase stability calculated in the temperature range from 50 to 1000 °C based on total free energy minimisation on a sub-regular model. The parameters entered were temperature, atmospheric pressure and weight fractions of elements, namely Fe, C, Si, Mn, P, S, Al, Cr, Mo, Ni, Cu and Ti.

With these data the mass fractions of the different phases present at the respective temperatures were calculated. These were then converted to volume fractions and used to determine the content of carbides, which was later compared to the experimentally measured values.

3.2.2 Preparation of the samples

3.2.2.1 Cutting

All the samples have been cut to obtain a section showing the surface but also the core of the component to see local variations of the microstructure depending on the position inside the component.

For that reason the steel parts were metallographically cut using a Struers Discotom-5 with a 31TRE cut-off wheel. This wheel is 250 mm in diameter and 1.5 mm thick. It is intended for the cutting of extra hard ferrous metals (400 – 800 H_V) by using aluminium oxide particles in a resin bond. To avoid heating of the samples and mechanical deformation during cutting and therefore influencing the microstructure, a low feed speed of 0.2 mm/s was chosen along with use of the recirculation cooling unit to cool the samples during cutting.

For the Jominy end-quench specimen the samples (Figure 3-2 (a)) were cut along the axis of the bar to obtain two similarly sized halves. Both halves were mounted and metallographically prepared to increase the sample area that could be examined.

For the pearlitic samples the tubes were cut perpendicular to the axis of the samples so that the face visible in Figure 3-4 was parallel to the plane of sectioning. The bainitised discs were cut in two halves along the former bar rolling direction according to Figure 3-1.

The laser hardened sample has been cut in the middle of the sample parallel to the face visible in Figure 3-8. From the crankshaft the induction hardened positions of the crankpin bearings have been cut perpendicular to the shaft axis from which sections parallel to the shaft axis have been cut. From the case hardened steering column the teeth have been cut off and then cut again parallel to the face visible in Figure 3-13 through the centre of the tooth.

3.2.2.2 Mounting

To increase the handling and improve the quality of the metallographic preparation the samples were mounted. The discs of the bainitic samples and the dilatometer samples were hot mounted in epoxy resin using a Struers Prontopress electro-hydraulic mounting press with a 40 mm diameter mounting unit. The epoxy resin used provides edge retention and planeness of the samples, which is especially important for the surface hardened steel samples.

The Jominy end-quench specimens were cold mounted using EpoFix in mounting cups with the dimensions 40 mm x 40 mm x 80 mm.

3.2.2.3 Grinding and polishing

The mounted samples were mechanically ground and polished using a Struers RotoPol-31 automated grinding/polishing machine, equipped with a RotoForce-4 specimen mover and a Lupo automatic lubricant doser. The MD-Disc system was used to fix the grinding and polishing discs.

For all the samples the same procedure for metallographic preparation was used that is given in Table 3-7.

Table 3-7 Procedure for the metallographic preparation of the hardened steel samples

	grinding		**polishing**		
	1	2	3	4	5
disc	MD-Piano	MD-Allegro	MD-Largo	MD-DAC	MD-NAP
grit/grain size	220	9 µm	6 µm	3 µm	1 µm
lubricant	water	blue	blue	blue	blue
speed	300 rpm	150 rpm	150 rpm	150 rpm	150 rpm
pressure	150 N	150 N	150 N	150 N	60 N
time in min.	until flat	10	5	3	1.5

Table 3-8 Overview of the parameters changed for the electrolytic polishing and their influence on the revelation of the microstructure of the bainitised samples

parameter	**range of variation**	**influence**
electrolyte	Struers A2, A3	different etching response
polishing voltage	30 – 60 V	defines (local) polishing rate
polishing time	10 – 20 s	degree of etching attack
electrolyte temperature	12 °C / 22 °C	reaction kinetics, safety (electrolyte contain perchloric acid)

As an alternative to mechanical preparation the bainitised sample b100Cr6_850 was polished electrolytically. This was done using a Struers Lectropol-5 electropolisher. Several process parameters were adjusted to improve the homogeneity of the attack of etching over the sample surface. The range of variations of the parameters is given in Table 3-8. The best results were obtained with electrolyte A3, polishing for 10 s at 60 V with a flow rate of 13 and an electrolyte temperature of 22 °C.

3.2.2.4 Etching of the samples

Table 3-9 Etchants used for the revelation of the microstructure of the hardened steel samples and their effect on the microstructure

no.	etchant	application	effect on microstructure
1	1% - 3% nital: 1 – 3 ml nitric acid in 97 – 99 ml ethanol	submerge sample in etch for 20-30 s	reveals general structure
2	5 % nital: 5 ml nitric acid in 95 ml ethanol	submerge sample in etch for 10-20 s	reveals alloy carbides
3	etchant after A. Schrader [Hab68]: 0.3 ml picric acid, 0.2 ml nitric acid, 100 ml ethanol	submerge sample in etch for 30-60 s	reveals fine structures
4	colour etchant: 0.5g Na_2MoO_4 + 0.5g $Na_5S_2O_3$ in 100ml distilled water acidified with nitric acid (pH 3.5 – 4)	Pre-etch in 2 % nital, submerge in colour etch solution until the specimen surface has a blue appearance (30-60 s)	colour variation due to thickness of surface oxide layers which varies for different phases and composition
5	colour etchant after Klemm [Wec82]: stock solution: 1kg sodium thiosulphate dissolved in 300 ml distilled water at 30-40 °C 100 ml stock solution, 2 g potassium pyro-sulphite	submerge sample in etch for 1-2 min	colours martensite and bainite blue-brown, residual austenite remains white

Before etching the samples were cleaned thoroughly with ethanol in an ultrasonic bath, then etched to reveal the microstructure of the different steel samples. Afterwards the samples were again cleaned with ethanol in an ultrasonic bath to remove the remaining etchant. They were dried for about 10-15 s in hot air, then for at least 5 min in cold air. The etchants used are given along with their effects on the microstructure in Table 3-9.

For most of the investigations etching with nital in different concentrations was used (etchants 1 and 2). The etchant after Schrader (no. 3) was tested but did not show the expected contrast. The colour etchant (no. 4) was also tested but showed an etching attack that was not reproducible. Therefore this etchant was also not used for further investigations. However, Klemm's colour etchant (no. 5) showed a reproducible etching attack and this was used to contrast the bainitic samples for the texture analysis.

3.2.3 Microscopical methods

3.2.3.1 Optical microscopy

The optical microscopical investigations have been made using a Zeiss Axiophot microscope in brightfield reflected light. The microscope was equipped with a 3CCD colour video camera Sony MC-3249 and attached to a computer using a Matrox Meteor framegrabber for the digitisation and acquisition of micrographs. The samples were moved using a motorised scanning stage. An autofocus system was used to adjust the z position of the samples during scanning.

The procedure for automated measurement of the texture parameters using an optical microscope with motorised scanning stage is given in Figure 3-14.

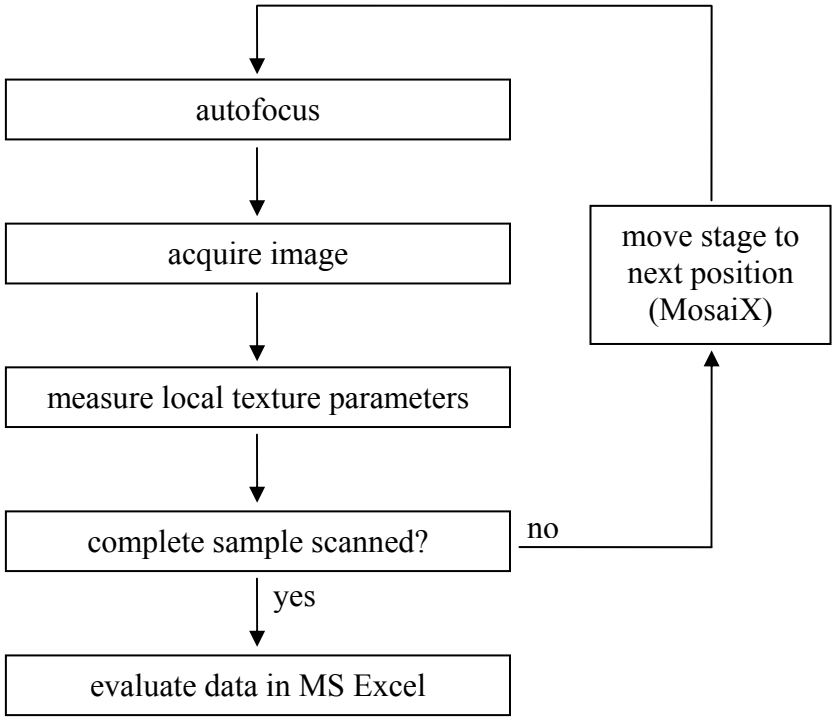

Figure 3-14 Flow diagram for automated measurement of texture parameters using a motorised scanning stage

3.2.3.2 Scanning electron microscopy (SEM)

SEM was used to investigate the very fine hardened microstructure and carbides in the pearlitic and the bainitic samples. This was carried out using a JEOL 5410 operating at 20 kV at a magnification of 7,500:1. To characterise the chemical composition of the microstructure EDS was applied.

All the samples were etched using 2 % nital. The acquired images were analysed as for the optical micrographs using the image analysis system KS400.

3.2.4 Software for image analysis

Control of the microscope, scanning stage, image acquisition, image processing and measurement of the microstructural features was done using the Carl Zeiss Vision image analysis software KS 400.

3.2.4.1 Measurement of volume fractions of phases

The volume fractions of the occurring phases were measured for the Jominy end-quench specimen. By quantitative analysis these contents were measured along the bar length. For the measurement the optical micrographs were segmented by a grey value segmentation in the KS400 image analysis software. To ensure a reliable measurement the segmentation was adjusted for every image to compensate for differences due to changes in the degree of etching or illumination. The segmentation is shown for the measurement of the bainite phase fraction in the martensitic matrix in Figure 3-15.

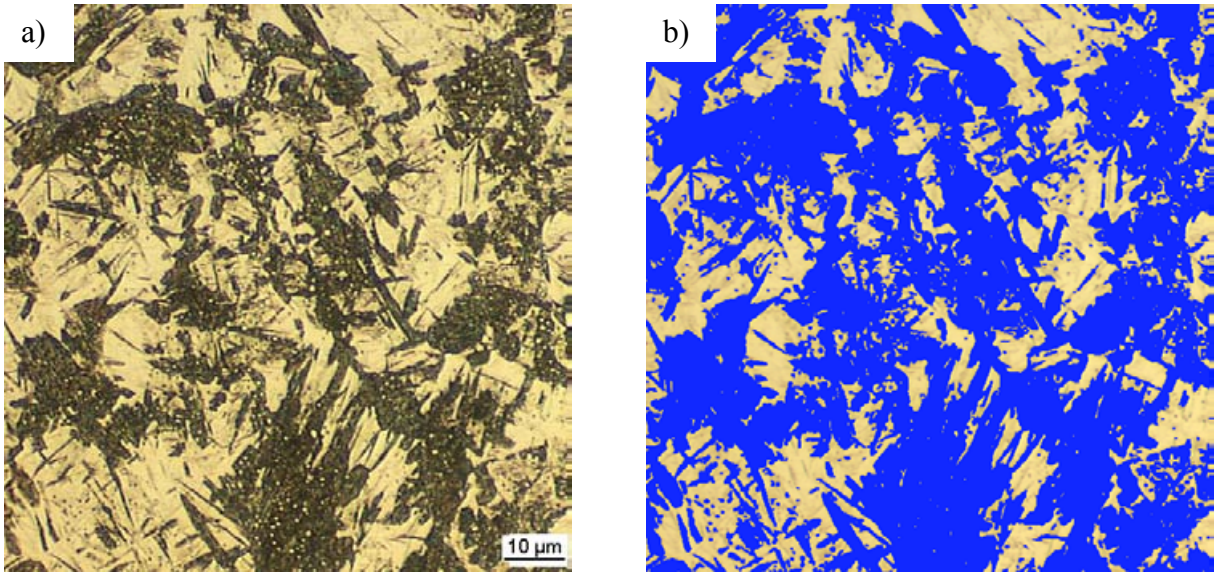

Figure 3-15 Micrograph of the Jominy end-quench specimen of the tool steel 100Cr6 showing martensite and bainite (a) and the same image with the bainitic regions marked blue (b)

3.2.4.2 Measurement of texture parameters

For the texture analysis the means of 11 of the texture parameters designated as Haram1 to Haram11 implemented in the image analysis system KS 400 [Car97] have been measured for the acquired images. To compute the grey level cooccurrence matrix (GLCM) based on the direct neighbouring pixels the pixel separation, d, was defined within the range of 1 to 64 pixels by the variable TEXDISPL in KS 400. This value was varied for the different experiments. The number of grey values may be chosen between 2 and 64 but was limited to

16 different values using the variable NTEXLEVEL for all the experiments. Additionally the standard deviation may be computed that is designated as Harar in KS 400.

For measurement of the carbides the images have been delineated after acquisition to enhance the edges. After grey value segmentation the perimeter (PERIMF), the area (AREA) and the form factor (FCIRCLE) were measured for every carbide and stored in a database together with the respective image name to be able to calculate the volume fraction of carbides for every single image.

The analysis of the texture parameters and the hardness was done using Microsoft Excel to generate diagrams showing the distribution of the parameters over the sample surface.

3.2.4.3 Characterisation of the coarse, alloy carbides

For optical micrographs of the bainitic samples the area fraction of the carbides has been measured at a magnification of 1,000:1 after etching with 5 % nital to enhance the contrast between the alloy carbides and the bainitic matrix. To quantify the local amount of carbides the distribution of the area fraction of the carbides was measured over the cross-section of the sample transverse to the rolling direction (Figure 3-16). Additionally the number density of carbides in every micrograph was measured.

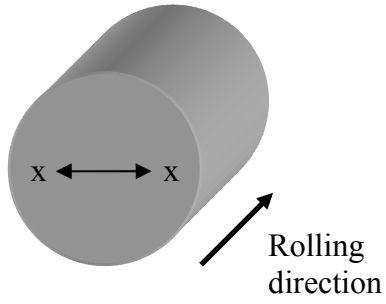

x ⟷ x Trace of carbide area fraction measurement

Figure 3-16 Sketch of the specimen and the position for the carbide area fraction measurement

From SEM secondary electron micrographs for both the pearlitic and the bainitic samples the area fraction and the size distribution of carbides have been measured for samples etched with

2 % nital at a magnification of 7,500:1. The carbides were then categorised in terms of area for 0.05 µm² steps. For every class the fraction of carbides from the total area of carbides in the examined samples was calculated together with the number density of carbides per micrograph.
The measurement of the carbides was done using KS400. After a grey value segmentation the area (AREA), the form factor (FCIRLCE) and the perimeter (PERIMF) were measured.

3.2.5 Software for the simulation of a neural network using a computer

The correlation between the microstructural features and the respective local properties has been established using a Stuttgart Neural Network Simulator (SNNS) version 4.2 neural network [SNN00]. Using supervised learning in a feed-forward network [Jor99] a correlation between the texture parameters after Haralick and mechanical properties and/or processing parameters can be established.
The organisation of such a network can be seen in Figure 3-17. As can be seen the neurons represented by blue/green squares are arranged vertically in three layers. On the left hand side the input layer consisting of 11 neurons can be found that take the texture parameters. The values of the texture parameters of an example data set are given right below the corresponding neuron. In the middle the 7 neurons of the hidden layer are arranged. On the right hand side the output layer consisting of a single neuron can be found. The lines between the neurons represent the weighted connections. Some of the weights are given with the lines representing the weighted connections but due to the huge number of connections not all the values can be shown.

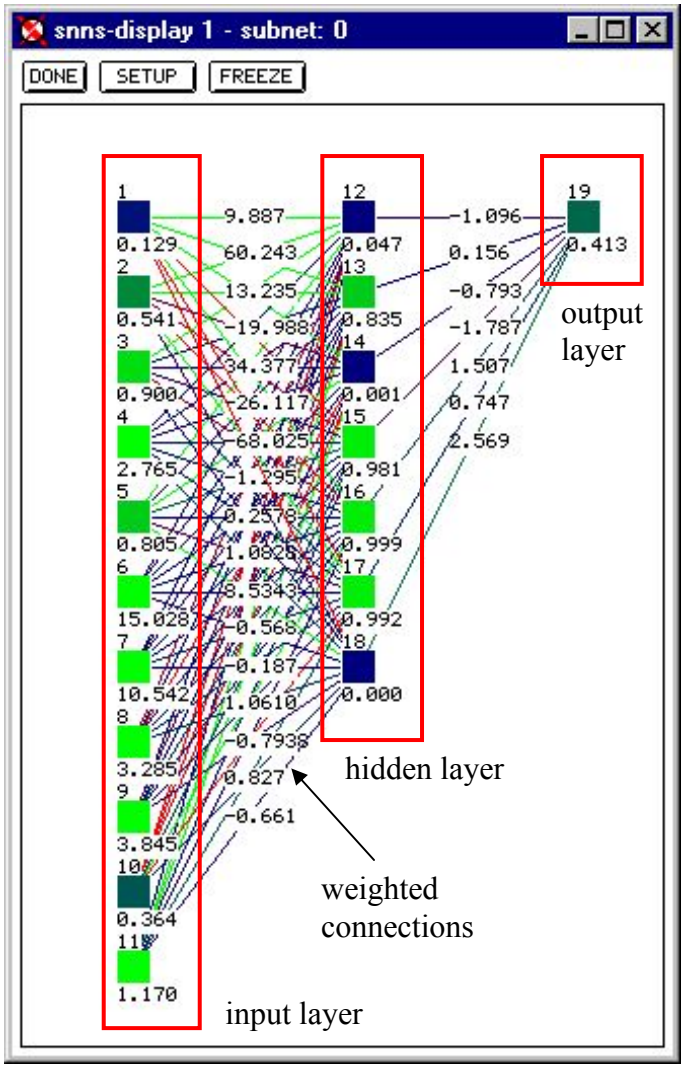

Figure 3-17 Organisation of a feed-forward network in the Stuttgart Neural Network Simulator [SNN00]

To initialise the neural network the weights were set to random values between -1.0 and 1.0. The updating was done in topological order, i.e. after setting up the neurons in the input layer the values of the neurons in the hidden layer are calculated using the respective weighted connections and so on. The network was trained with the adaptive learning scheme “resilient back propagation” for 10,000 cycles in shuffle mode, i.e. the order of the data set was changed to increase the training result. The resilient back propagation algorithm works in batch mode, i.e. the update of the weights of the connections is done after the complete set of data is computed [Hin99].

The network was trained using the local adaptive learning scheme "resilient back propagation" [SNN00]. Therefore the values of the neurons based on a set of input values and the actual weighted connections are calculated. After calculation of the derivatives $\frac{\partial E}{\partial w_{ij}}^{(t)}$ of each weight w_{ij} and its respective Error E in the training cycle t, this value is compared to the previously computed value $\frac{\partial E}{\partial w_{ij}}^{(t-1)}$ for the respective weight. If both of these derivatives show the same sign the change of the weights $\Delta w_{ij}^{(t)}$ are determined by a weight-specific, so-called 'update-value' $\Delta_{ij}^{(t)}$

$$\Delta w_{ij}^{(t)} = \begin{cases} -\Delta_{ij}^{(t)}, \ if \ \frac{\partial E}{\partial w_{ij}}^{(t)} > 0 \\ +\Delta_{ij}^{(t)}, \ if \ \frac{\partial E}{\partial w_{ij}}^{(t)} < 0 \\ 0, \ else \end{cases} \qquad \text{Eq. 3-1}$$

The new update-values are then computed based on a sign-dependent adaptation process

$$\Delta_{ij}^{(t)} = \begin{cases} \eta^{+} \cdot \Delta_{ij}^{(t-1)}, \ if \ \frac{\partial E}{\partial w_{ij}}^{(t-1)} \cdot \frac{\partial E}{\partial w_{ij}}^{(t)} > 0 \\ \eta^{-} \cdot \Delta_{ij}^{(t-1)}, \ if \ \frac{\partial E}{\partial w_{ij}}^{(t-1)} \cdot \frac{\partial E}{\partial w_{ij}}^{(t)} < 0 \\ \Delta_{ij}^{(t-1)}, \ else \end{cases} \qquad \text{Eq. 3-2}$$

$where \ 0 < \eta^{-} < 1 < \eta^{+}$

Every time the partial derivative of the corresponding weight w_{ij} changes its sign, which indicates that the last update was too big and the algorithm has jumped over a local minimum, the update-value $\Delta_{ij}^{(t)}$ is decreased by the factor η^{-}. If the derivative retains its sign, the update-value is slightly increased by the factor η^{+}. For all the experiments the factors are set to the fixed values $\eta^{+} = 1.2$ and $\eta^{-} = 0.5$ as proposed in [SNN00].

3.2.6 Format of the datasets

The texture parameters measured in the image analysis software KS 400 were initially saved in the proprietary Zeiss database format ‘d00’. For further processing these data were then imported into Microsoft Excel using an import function for the specific file format provided by Carl Zeiss. To create a dataset for the training of the neural network the hardness was added to the corresponding texture parameters and using a VBA macro a text file with the format necessary to be imported in the neural network software SNNS was created. These training files have to consist of a header giving the number of datasets contained in the file, the number of input units (texture parameters) and the number of output parameters (microhardness) (Figure 3-18). This header is followed by the respective data.

The files necessary for the testing of the neural network are formatted in the same manner with the only difference being that the number of output units is set to zero and therefore also the corresponding data (microhardness) is not contained in these training files. As the output values of the neural network have to lie between 0 and 1, the microhardness was divided by 1000 to obtain values in the required range.

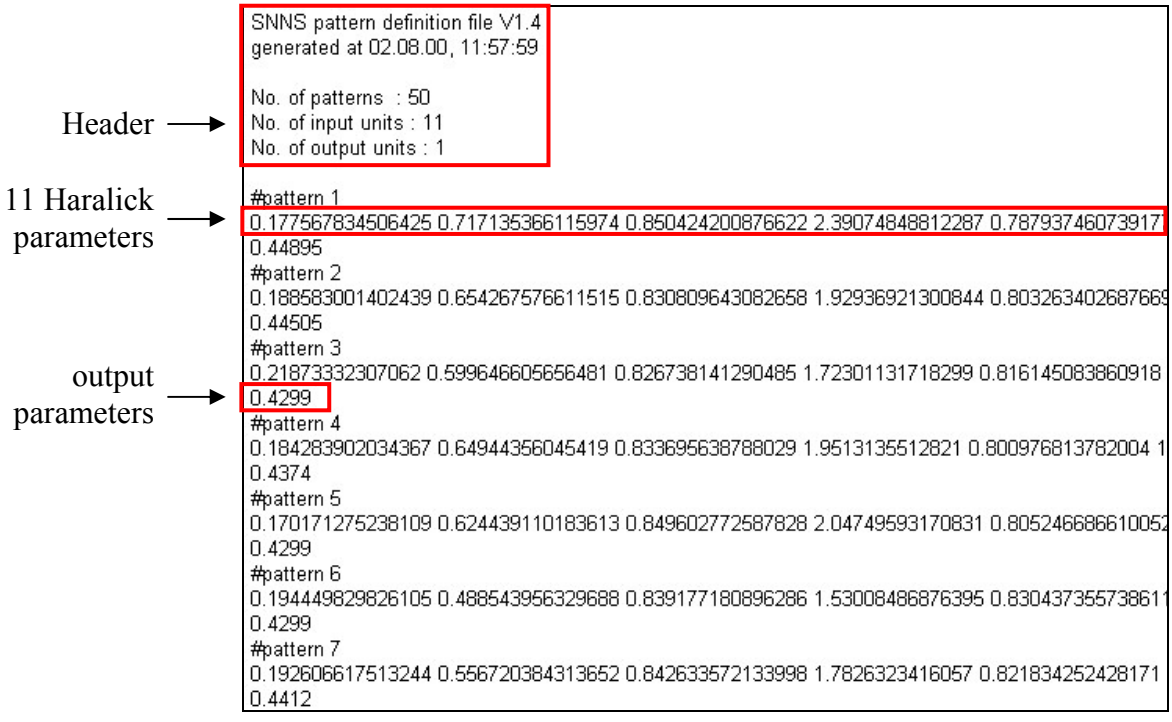

Figure 3-18 Structure of the dataset to train the neural network in the SNNS

The result files containing the values calculated by the trained neural network based on the test data are also formatted in the same way. The data consist of the texture parameters and the output value calculated with these data.

To visualise the resulting data files were imported into Microsoft Excel again using a VBA macro. The output values were multiplied with 1000 to obtain the microhardness and were then arranged according to the measurement of the texture parameters to be able to generate a distribution mapping of the parameters and the output values calculated by the neural network.

3.2.7 Evaluation of the lateral hardness distribution

To evaluate the lateral hardness distribution the texture parameters were scanned using a motorised scanning stage with the optical microscope over a large sample area and stored in a database. At specific position rows of hardness have been measured using microhardness at the positions representing the measured images to be able to correlate the texture parameters with the corresponding microhardness. The neural network was trained with this set of training data to establish a correlation between the texture parameters and the corresponding local microhardness. Subsequently for the whole scanned sample area the microhardness was calculated from the texture parameters and visualised using Microsoft Excel.

3.3 Mechanical characterisation

3.3.1 Hardness measurement

To measure the Vickers microhardness H_{V1} a Leitz Miniload was used with a load of 9.81 N at room temperature. For evaluation of the lateral hardness distribution these indentations were placed in the centre of the formerly acquired image to ensure the correlation between microhardness and image information represented by the texture parameters.

To characterise the bainitic samples the macrohardness H_{V30} was averaged from 5 indentations for every sample. Using a load of 294.3 N the indentations were made on a Reicherter hardness tester at room temperature.

For the measurement of the trend of hardness of the Jominy end-quench specimen the Knoop microhardness $H_{K0.2}$ was measured using a load of 1.96 N. Therefore a microhardness tester

MHT-4 from Anton Paar GmbH was used. With this hardness tester the indenter is fitted in the objective turret of the optical microscope to give the possibility to measure the local microhardness at the position of an acquired image. The indenter was calibrated to place the indentation in the centre of the acquired images. Using KS400 traces of hardness were placed along the Jominy end-quench specimen.

4 Results

4.1 Simulation of the microstructure for the calculation of the cooccurrence matrix

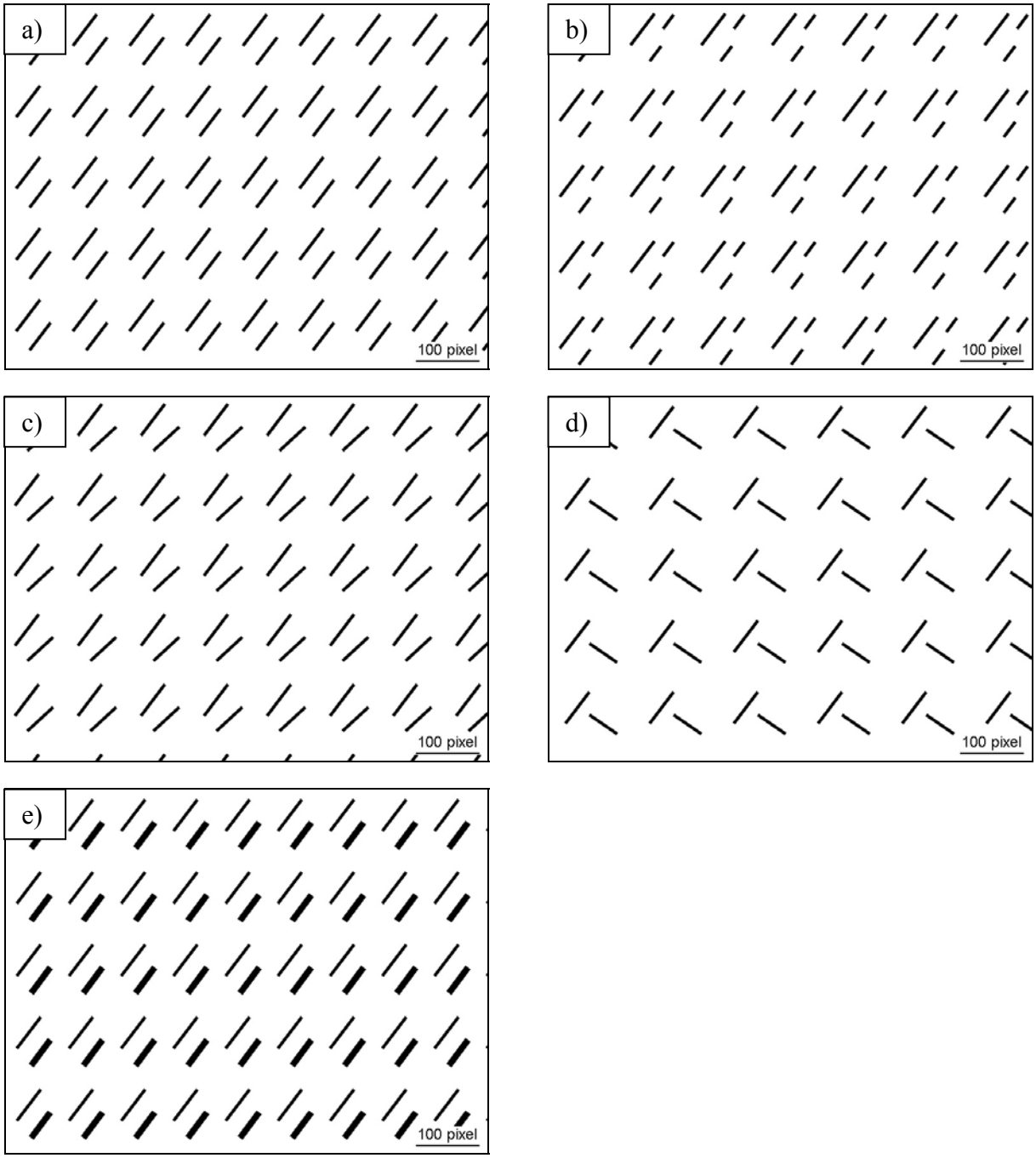

Figure 4-1 Example images to distinguish the influence of the separation between inspected pixels on the texture parameters

a) 5 pixel wide
b) 5 pixel wide, short
c) 5 pixel wide, not parallel
d) 5 pixel wide, perpendicular
e) 5+10 pixel wide

To simulate the needle-like structure of diffusional and displacive transformation products in steels, i.e. martensite and bainite, example images were created showing a simplified needle-like structure.

Calculation of the grey level cooccurrence matrix (GLCM) determines the variation in the separation between adjacent detected pixels (see section 2.2.2.2). This also allows adjustment to deal with different structure sizes in the images investigated. The use of this parameter to characterise needle-like structures typical of hardened steels microstructures was tested using the images in Figure 4-1. The same investigations were made on micrographs from the bainitic samples (Figure 4-18) to assess the practical usefulness of these parameters in characterising these structures.

The needle-like features represent the basic structures of the microstructure of hardened steels. The characteristics of the needle-like features were varied to incorporate varying lengths (Figure 4-1 (b)), orientations (Figure 4-1 (a), (c), (d)), and widths (Figure 4-1 (e)).

a)

		i	
		0	1
j	0	+	-
	1	-	+++

b)

		i	
		0	1
j	0	-	++
	1	++	+

c)

		i	
		0	*1*
j	0	++	+
	1	+	+

Figure 4-2 Schematic GLCMs for the horizontal neighbourhoods of the example image Figure 4-1 (a) transformed to a plain black and white image for 3 representative separations (i: grey value of examined pixel, j: grey value of neighbour pixel; 0: black, 1: white)

a) separation d ≈ 1 pixel b) separation d ≈ 10-30 pixels

c) separation d ≈ 37 pixels

- very low, + low, ++ high, +++ very high number of neighbourhoods

The schematic GLCMs for the horizontal neighbourhoods of Figure 4-1 (a) are presented for 3 representative separations between the examined pixels (Figure 4-2), one separation for adjacent pixels, one for a mean separation and one for a separation of approximately the

distance between the lines in the images. For these schematic GLCMs the image has been transformed to a plain black and white image to bring out the underlying effects.

The matrix in Figure 4-2 (a) representing the direct horizontal neighbourhood relationship shows that the image contains a very low number of pixels with a change in grey value from black to white or vice versa as would occur on crossing the object/matrix interface. The number of black pixels with black neighbours are also quite low but higher than the aforementioned type. This number characterises pixels within a black object. By far the highest number of neighbours were found for the white neighbouring white, i.e. pixels in the matrix between the black objects.

For a separation of approximately 10-30 pixels the proportions of the matrix are shifted significantly. The number of black-black neighbourships decreases to zero since the lines are 6 pixels wide and their horizontal separation is about 37 pixels. So there cannot be two pixels with this separation within a single object and the distance between two objects is larger than the separation applied for the examination. Instead the number of black-white neighbourships increases since the black pixels within an object have neighbours outside this object. The number of white pixels with white neighbours decreases in favour of the black-white combinations but a certain number still remains.

If the separation between the examined pixels is further increased to 37 pixels, which is equivalent to the distance between the black objects in the image, the number of black-black neighbourships increases again since pixels of adjacent objects are examined. Due to this the number of black pixels having a white neighbour is lowered since these have a neighbour in an adjacent object. The number of white-white neighbourships is slightly increased because the white pixels have neighbours behind the adjacent object. White pixels with neighbour black pixels will not occur.

In the following 3 of the Haralick parameters are presented together with their relation to the GLCM and microstructural features. The parameters Haram2, Haram4 and Haram5 have been chosen since this are the easiest to describe regarding the mathematical background.

Texture parameter Haram2

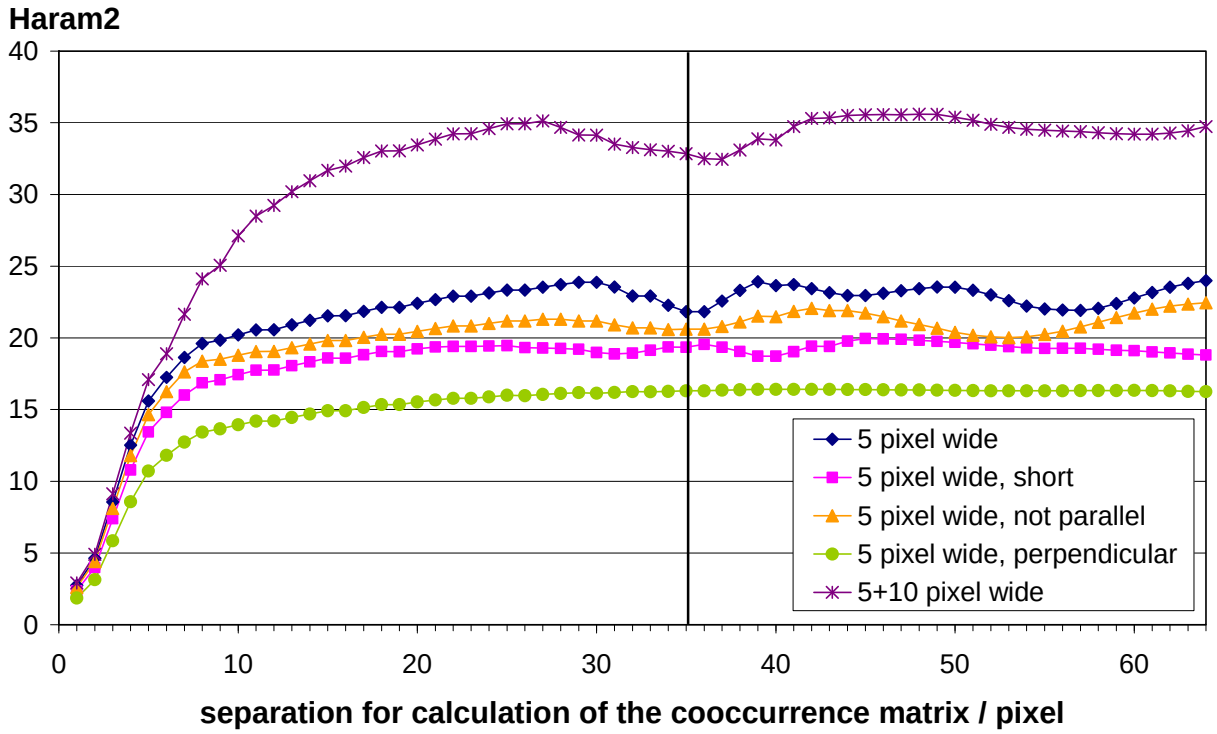

Figure 4-3 Influence of the variation of the separation between inspected pixels on the texture parameter Haram2 for the example images in Figure 4-1

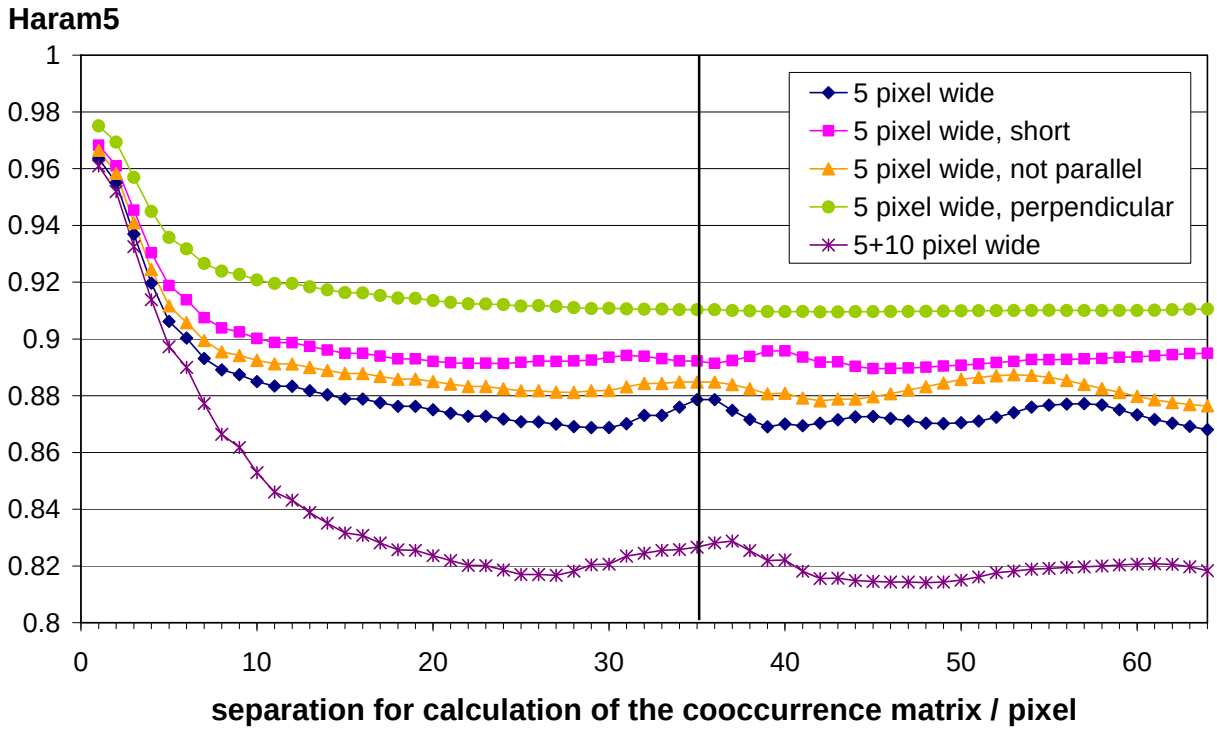

Figure 4-4 Influence of the variation of the separation between inspected pixels on the texture parameter Haram5 for the example images in Figure 4-1

For the example images the texture parameters were calculated with variation of measurement length between 1 and 60 pixels. The parameters Haram2 and Haram5 (Section 2.2.2.3) resulting from these example images are shown in Figure 4-3 and Figure 4-4 respectively.

For both parameters, influences of the variation of the separation can be found. While some parameters such as Haram2 show an increasing trend with increasing separation, other parameters such as Haram5 decrease with increasing spacing up to approximately 20-30 pixels. Beyond this value small variations can be found for the parameters. Especially for the image with the 5 pixel wide parallel lines local turning points exist for a measurement spacing of approximately 35 pixels. Similar features can also be seen, but less markedly in the analyses of Figure 4-1 (b) to (e).

The trends in the texture parameter values can also be explained theoretically by the difference due to the varied separations of the aforementioned GLCMs. The texture parameter Haram2, as defined in Section 2.2.2.3, is a measure for the contrast in the image.

$$Haram2 = \sum_{n=0}^{N_g-1} n^2 * \left\{ \sum_{i=1}^{N_g} \sum_{\substack{j=1 \\ |i-j|=n}}^{N_g} p(i,j) \right\} \qquad \text{Eq. 4-1}$$

According to the mathematical definition (Eq. 4-1), the numbers of occurrences p(i,j) for the grey values i and j of N_g grey values are summed along the main diagonal of the GLCM (n=0 in Figure 4-5) and their parallels for distances from the main diagonal n>0 respectively. These values are then weighted by the square of their distance n from the main diagonal in the GLCM and these weighted diagonal sums are again summed up.

If this is applied to the GLCMs obtained for different measurement lengths (Figure 4-2) of the example images (Figure 4-1), the effects visible in Figure 4-3 can be explained theoretically. In the following this is done exemplarily for the texture parameter Haram2 measured for the example image Figure 4-1 (a).

For low separations between the examined pixels, e.g. adjacent pixels with a separation of 1 pixel, the corresponding GLCM shows very high numbers of occurrences along the main

diagonal. As these values are weighted very low, or even are neglected if they fall directly on the main diagonal, the obtained texture parameter Haram2 is very low.

With increasing separation the number of pixels having a neighbour with the same grey value decreases and the numbers of black pixels with white neighbours and vice versa increase significantly. As these latter occurrences lie far away from the main diagonal in the GLCM they are weighted more highly and so they cause a rapid increase in the value of Haram2.

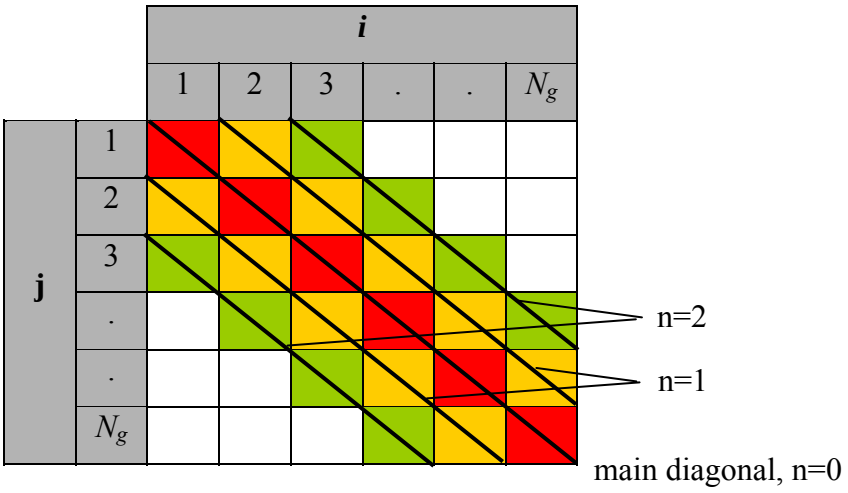

Figure 4-5 Schematic demonstration of a GLCM and the characteristic measures relevant to determine the texture parameter Haram2 (i: grey value of examined pixel, j: grey value of neighbour pixel; 0: black, 1: white)

With increasing separation the parameter Haram2 approaches a limiting value when a maximal fraction of black-white transitions is reached. The maximum value that may be reached depends on the area fraction of black and white pixels. For area fractions of 50:50 the number of black pixels having a white neighbour and vice versa is highest and therefore give a very high relative number of occurrences in the GLCM which then causes a high absolute value of the texture parameter Haram2.

In the case of separations around the distance between the objects in the image, which is 37 pixels in horizontal direction in the example image, the number of occurrences of black-white transitions between examined pixels are reduced in favour of more pixels having the same grey value as their examined neighbours. This means a slight shift of the values in the GLCM back towards the main diagonal causing a decrease of the parameter.

For further increasing separations the number of occurrences of black-white neighbourships increases again which increase the value of the parameter Haram2 again to the value it had for separations less than the distance between the objects in the image.

The aforementioned considerations were made for the horizontal relationships between the pixels. For the calculation of the texture parameters not only these horizontal neighbourships are brought into account but also the vertical and the two 45° diagonal neighbourships. Since in these directions the distances of the objects in the image may be different, the local extreme values are not as distinct as would be expected for the considerations for the horizontal direction. Taking the other directions into account may cause a broadening of these extreme values as may also be seen for the parameter Haram2 of the example image in Figure 4-3. There the extreme values cannot be found as a flat local minimum but instead a separation range is showing reduced values.

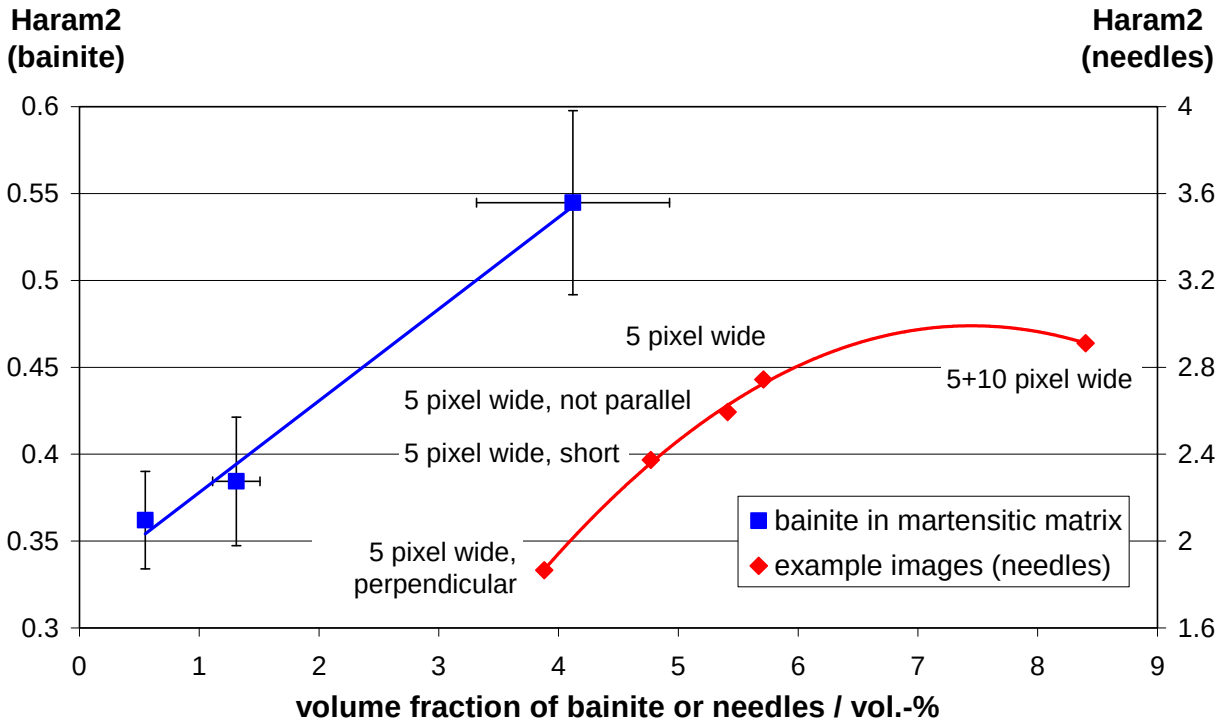

Figure 4-6 Correlation of the volume fraction of dark etching bainite in a martensitic matrix and the area fraction of the needles in the example images with the corresponding texture parameter Haram2 (separation 1 pixel) for the micrographs given in Figure 4-7 and Figure 4-1 together with according linear or polynomial trend lines

If the other example images are considered, similar effects can be observed. The differences in the widths and the distances between the single objects in the image are different and therefore give local extreme values at varying positions and with different broadenings. This effect will be discussed later (section 5.2.2).

In terms of relation to microstructural features the parameter Haram2 represents high values for a high number of pixel neighbourships with big differences in their respective grey values. For images showing only neighbourships with very low differences in the grey values the parameter Haram2 yields very low values. For the example images in Figure 4-1 the dependence of the texture parameter Haram2 on the volume fraction of needles in the image is shown in Table 4-1 and Figure 4-6. It can be seen that an increase in the volume fraction of needles yields an increase in Haram2, which is linear for the small volume fraction variations with a constant 5 pixel width. Changing the width to a mixture of 5+10 pixels causes the linearity to be lost.

For the micrographs of a hardened microstructure consisting of bainite in a martensitic matrix (Figure 4-7) both the volume fraction of bainite and the texture parameter Haram2 were measured. The bainite volume fraction was measured by a grey value segmentation with manual adoption of the grey levels. The results of the measurement are presented in Table 4-1 and Figure 4-6. A fully martensitic microstructure gives low values since the grey values in the image are all very similar. The micrograph Figure 4-7 (a) shows almost no bainite and therefore a nearly fully martensitic microstructure yielding a value of 0.36 for Haram2. For slower cooling rates bainite can be found in the samples with a volume fraction of 1.3 vol.-% as dark etching phase within the brighter martensitic regions (Figure 4-7 (b)) which gives an Haram2 of 0.38. With further decreasing cooling rate bainite increases to 4.1 vol.-% giving a Haram2 of 0.54 (Figure 4-7 (c)).
This effect of the texture parameter with the bainite volume fraction is consistent with the increase of the parameter with the volume fraction of needles in the example images. As the size of the bainitic regions changes, the number of bright-dark transitions is changed independent from the volume fraction of bainite in the microstructure. This will again cause a loss of linearity in the correlation as has be seen for the variation of the width of the lines in the example images.

Table 4-1 Volume fractions of needles for example images in Figure 4-1 and bainite in martensitic regions for images in Figure 4-7 together with respective texture parameters Haram2 at a separation of 1 pixel

image		vol. fraction of bainite or needles / vol.-%	Haram2
example images with needle-like structure	Figure 4-1 (a), 5 pixel wide	5.7	2.74
	Figure 4-1 (b), 5 pixel wide, short	4.8	2.37
	Figure 4-1 (c), 5 pixel wide, not parallel	5.4	2.59
	Figure 4-1 (d), 5 pixel wide, perpendicular	3.9	1.87
	Figure 4-1 (e), 5+10 pixel wide	8.4	2.91
bainite in martensitic matrix	Figure 4-7 (a)	0.55	0.36
	Figure 4-7 (b)	1.3	0.38
	Figure 4-7 (c)	4.1	0.54

For both an increasing volume fraction up to 50 % or a decreasing grain size at a constant volume fraction of dark etching phase in a bright matrix or vice versa the texture parameter Haram2 shows increasing values because more neighbourships with transitions from bright to dark grey values and vice versa are contained in the image. This means that a higher number of small particles will increase the contrast since more neighbourships can be found having a big difference in the respective grey values. Therefore microstructural features like the size distribution of the grains or the width of the needles influences the contrast. As the dimensions (length and width) of the bainitic regions vary along with the volume fraction a straight line relationship may not be expected as for the variation of the width of the lines in the example images.

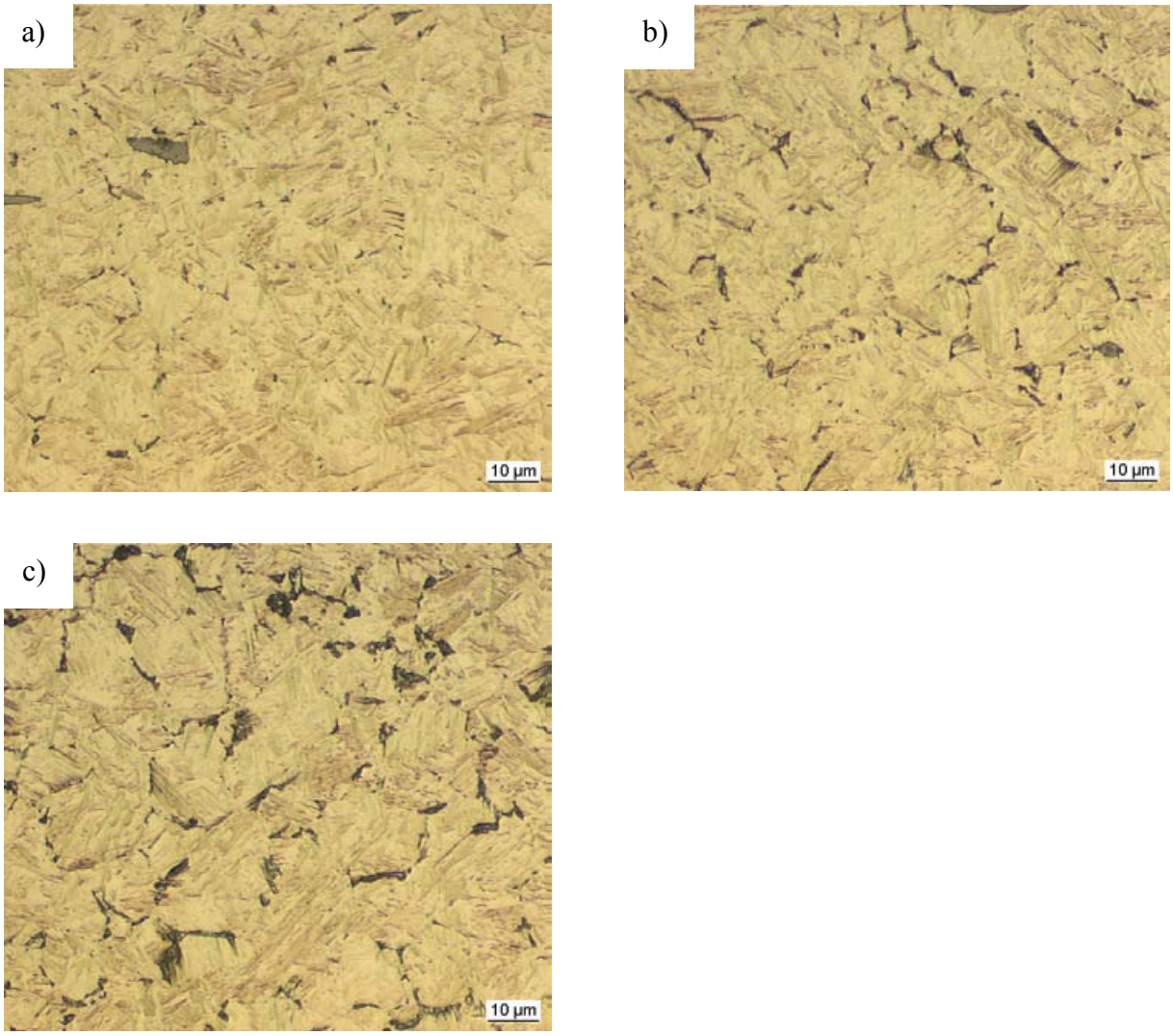

Figure 4-7 Microstructure and corresponding texture parameter Haram2 (separation 1 pixel) of the heat-treatable plain carbon steel C45 with 0.45 wt.-% C showing a martensitic matrix and different volume fractions of bainite after continuous cooling at different cooling rates

a) 0.55 vol.-% bainite, H2=0.36 b) 1.3 vol.-% bainite, H2=0.38

c) 4.1 vol.-% bainite, H2=0.54

Texture parameter Haram5

For the parameter Haram5 (Inverse Difference Moment of the image) values inversely proportional to those of the Parameter Haram2 can be measured. This can also be explained by the mathematical description of the parameter (Eq. 4-2).

$$Haram5 = \sum_{i=1}^{N_g} \sum_{j=1}^{N_g} \frac{1}{1+(i-j)^2} \cdot p(i,j) \qquad \text{Eq. 4-2}$$

To calculate the value of this parameter, the entries p(i,j) of the GLCM are weighted and summed up. This weight depends on the difference between the involved grey values i and j of the number of grey values N_g present in the image. The bigger the difference is, the lower the weighting. This means that values of the GLCM lying on their main diagonal are weighted highest, while values in the corners of the GLCM representing very large differences in the grey values are weighted very low (Figure 4-5). This is the opposite weighting distribution from that for parameter Haram2 but, due to the similarities of the principle of the calculation, the parameters show similar but complementary results.

For the relation of the values to microstructural features the same can be said as for the parameter Haram2. A large number of pixel pairs in the investigated separation with very similar or even identical grey values will yield high values for the parameter. In contrast combinations of pixels with very high differences in grey values give low values. This means that a fully martensitic microstructure showing very few differences in contrast yields high values. If portions of bainite are contained in this microstructure, the parameter will decrease. With both increasing number density and decreasing grain size the trend will be amplified since the number of pixel combinations showing similar grey values will be reduced.

Texture parameter Haram4

As a parameter showing a different dependence on separation the texture parameter Haram4 is presented in Figure 4-8 for the example images showing a needle-like structure. According to Haralick [Har73] this parameter represents the sum of squares as a measure of the variance of the image.

The trend of the parameter Haram4 is much more homogeneous with variation of separation than for the previously described parameters. All the parameters go through a maximum with increasing separation at different separation values. Only for the 5 pixel wide, perpendicular needles does the parameter not show a maximum but is increasing with increasing separation.

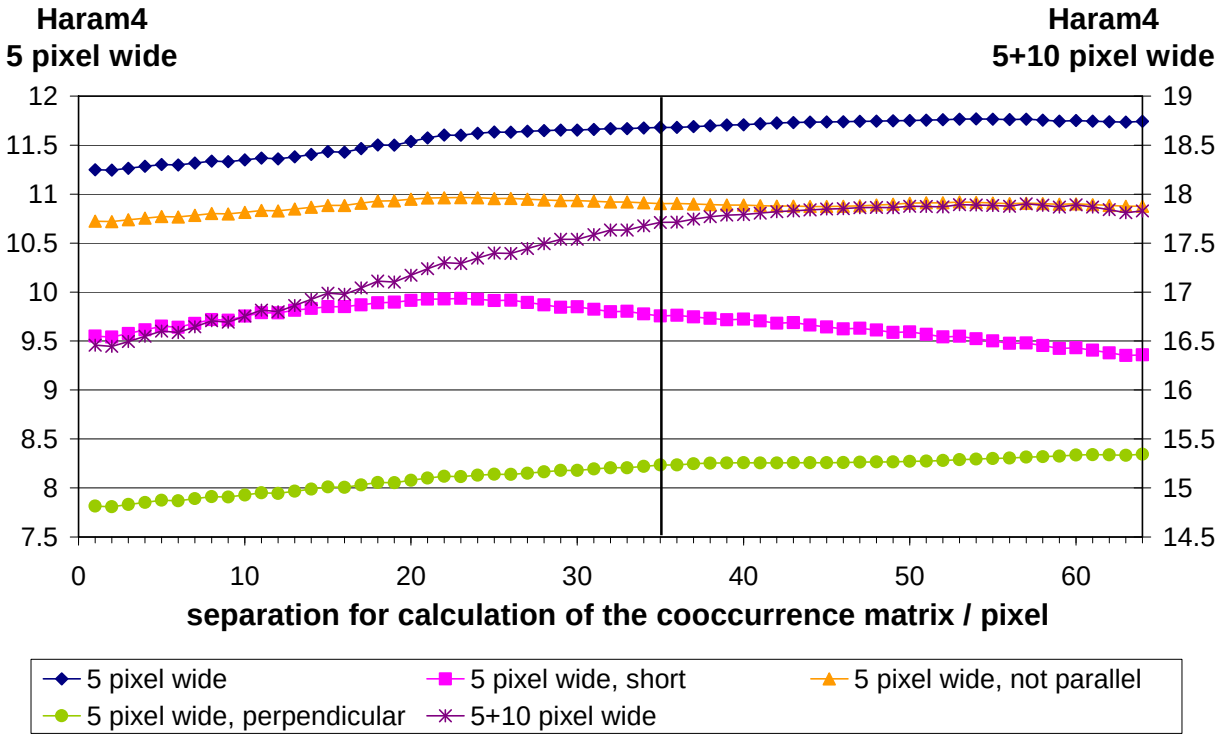

Figure 4-8 Influence of the variation of the separation between inspected pixels on the texture parameter Haram4 for the example images in Figure 4-1

For the image with lines that are 5 and 10 pixels wide, the parameter is starting at about 16.5 and reaches a maximum of ~18 at 45-55 pixels separation. The absolute values for the other images are significantly lower. The parameter for the image “5 pixel wide” shows increasing values for low separations. The parameter starts for values about 11.25 and reaches a limit of about 11.75 for a separation of approximately 40 pixels. For increasing separations the values remain nearly constant.

For the non-parallel lines the parameter shows very small variations. Only a faint maximum can be found at a separation of about 23 pixels followed by a minimum at about 45 pixels. The values are always in the range between 10.7 and 11.

The image showing the short lines yields a parameter that increases from about 9.5 to nearly 10 at a separation of approximately 23 pixels. For increasing separations a nearly linear decrease to a value of 9.3 at a separation of 65 pixels can be found.

For the image showing the perpendicular lines the value of Haram4 is constantly increasing with separation from a value of approximately 7.8 to a value just above 8.3.

For the parameter Haram4 comparable theoretical considerations can be made as for the parameter Haram2. This parameter expresses the mean square deviation of the grey values of the image. The mathematical description of the parameter is given as

$$Haram4 = \sum_{i=1}^{N_g}\sum_{j=1}^{N_g}(i-\mu_y)^2 \cdot p(i,j) \qquad \text{Eq. 4-3}$$

with μ_y being the mean of $p_y(j) = \sum_{i=1}^{N_g} p(i,j)$.

To explain the mathematical background of the parameter, again a schematic GLCM with the relevant features being marked is given in Figure 4-9 together with the corresponding marginal-probability matrix.

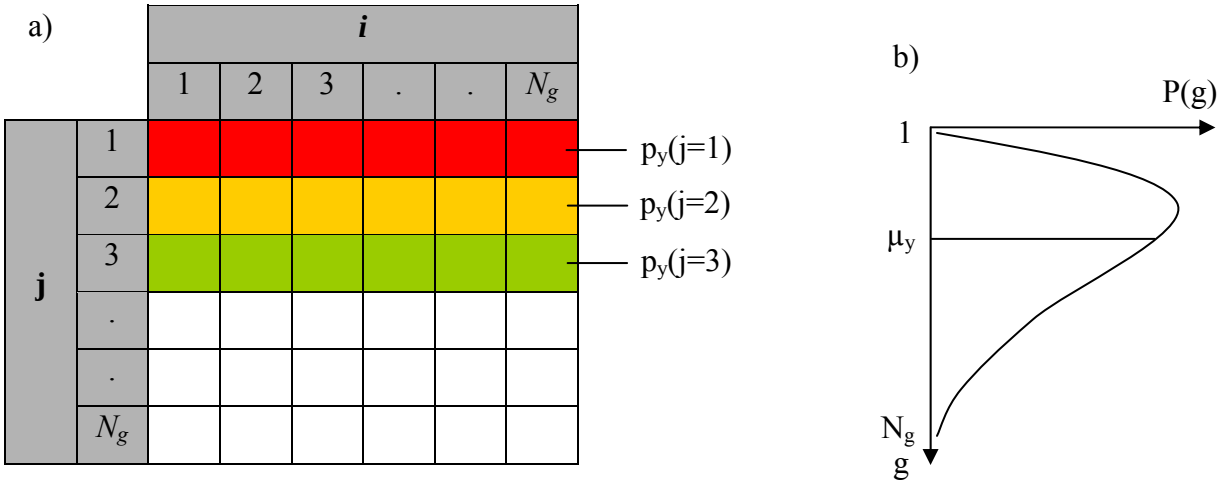

Figure 4-9 Schematic demonstration of a GLCM (a) together with the corresponding marginal-probability matrix (b) for the calculation of the texture parameter Haram4 (i: grey value of examined pixel, j: grey value of neighbour pixel, g: grey value; 0: black, 1: white)

To calculate the parameter Haram4, the marginal-probability matrix $p_y(j)$ is calculated from the GLCM by summing the entries of the matrix of the specific traces. This marginal-probability matrix is shown schematically for a specific grey value j in Figure 4-9 (b) where g represents the grey values numbered from 1 to the number of distinct grey levels N_g and P(g) their respective probability of occurrence in the quantized image. From this distribution the mean value μ_y of the marginal-probability matrix is calculated for a specific grey value j. This

mean value is then compared with the respective grey value of the examined element of the GLCM. The square of the difference of these two values is used as a weight for the summation over the existing grey values. This means that relatively high weights are put on the elements that differ most from the mean grey value μ_y of the marginal-probability matrix so that a widespread distribution will give a high value for the texture parameter Haram4. A narrow distribution instead will yield very low values.

Table 4-2 Volume fractions of needles for example images in Figure 4-1 and bainite in martensitic regions for images in Figure 4-7 together with respective texture parameters Haram4

image		**vol. fraction of bainite or needles / vol.-%**	**Haram4**
example images with needle-like structure	Figure 4-1 (a), 5 pixel wide	5.7	11.25
	Figure 4-1 (b), 5 pixel wide, short	4.8	9.55
	Figure 4-1 (c), 5 pixel wide, not parallel	5.4	10.72
	Figure 4-1 (d), 5 pixel wide, perpendicular	3.9	7.81
	Figure 4-1 (e), 5+10 pixel wide	8.4	16.46
bainite in martensitic matrix	Figure 4-7 (a)	0.55	1.05
	Figure 4-7 (b)	1.3	1.37
	Figure 4-7 (c)	4.1	2.22

To demonstrate the influence of the objects in the image on the absolute value of the parameter Haram4, the most demonstrative case regarding direct neighbours, i.e. a separation of 1 pixel, has been chosen. As μ_y is a function of the volume fraction of the black lines in the example images according to

$$\mu_y = V_F(black) + (1 - V_F)(white) \qquad \text{Eq. 4-4}$$

a linear relationship between the volume fraction of black pixels and the corresponding value of the texture parameter Haram4 can be expected for images showing a high contrast, i.e. only black or white pixels are contained in the image as for the example images, Figure 4-1.
This can be explained by a shift of the GLCM from white-white to black-black transitions if the area fraction of black objects is increased. For a volume fraction of more than 50% black phase the parameter would decrease again since the number of black-black transitions will increase significantly narrowing the distribution.
The volume fraction of black lines in the example images (Figure 4-1) and the volume fraction of bainite in the martensitic region (Figure 4-7) have been measured using a KS400 system. The results of the measurement of the volume fractions have been correlated to the texture parameter Haram4 of the corresponding images (Table 4-2 and Figure 4-10).

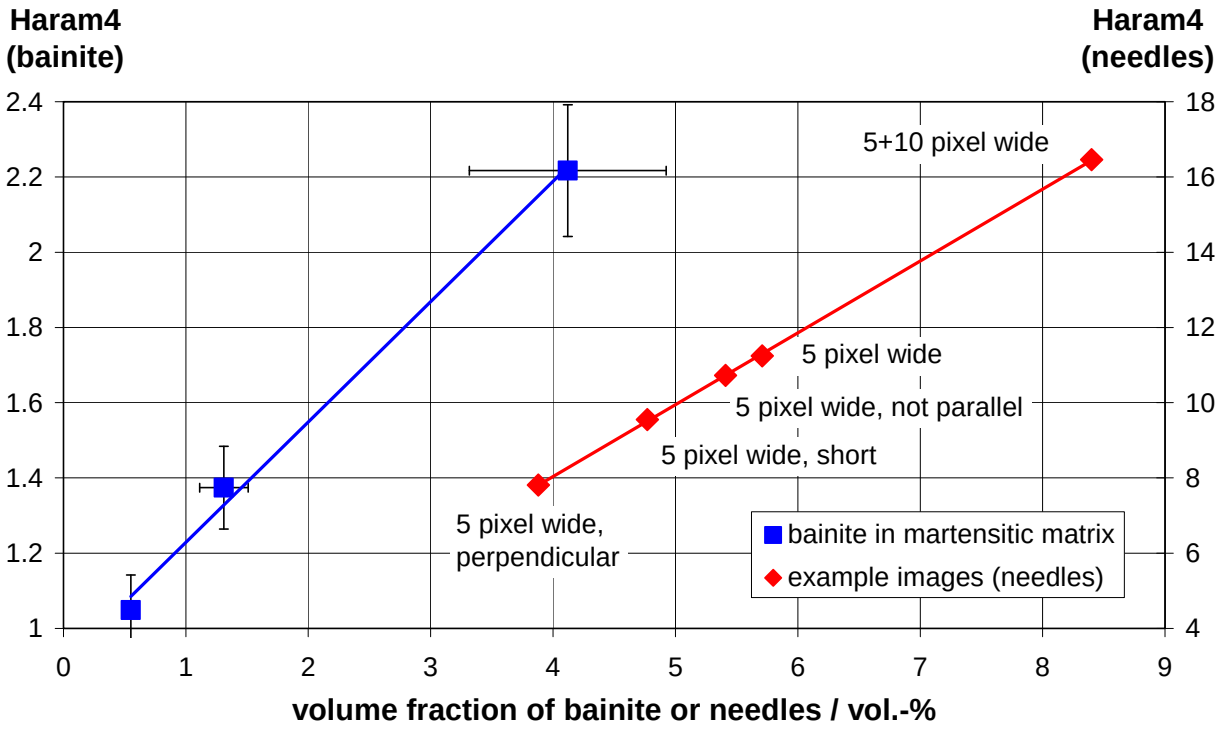

Figure 4-10 Correlation of dark etching bainite in martensitic matrix and the area fraction of black pixels contained in the example images with the texture parameter Haram4 at a separation of 1 pixel

The correlation shows a very good linear fit of the values for the different images as already expected from Eq. 4-4. With increasing area fraction of black pixels the texture parameter

Haram4 increases proportionally. This can be explained by the differences in the GLCM. For an image with a low area fraction of black objects, as for example the example images with the thin lines, Figure 4-1 (d), there is a high probability of sampling a white pixel and therefore a high number of neighbourships containing a white pixel. Due to this the marginal-probability matrix shows a distinct maximum in the range of the white grey values. The number of pixels with grey values differing much from the mean value will be very low and so the texture parameter Haram4 will show a very low value.
For an increasing area fraction of black pixels in the image the corresponding numbers in the GLCM are also increased, as e.g. for the image containing the lines with widths of 5 and 10 pixels, Figure 4-1 (e). This gives a wide distribution of the marginal-probability matrix. For the example images showing very discrete black and white pixels the distribution will show two maxima. Since the mean grey value is located between the two maxima of the distribution, many pixels show a big difference to this mean grey value. This yields a significantly higher value for the texture parameter.
For the micrographs showing different amounts of bainite in a martensitic region (Figure 4-7) the texture parameter Haram4 has also been measured and correlated to the respective volume fraction of bainite (Figure 4-10). Hereby also a clear correlation of the values can be found showing an increase of the texture parameter with an increasing amount of bainite.

For the variation of the separation between the adjacent pixels only a very small influence can be seen on the texture parameter Haram4. This can be explained if the influence of the variation of the separation on the GLCM is regarded. As the grey value of the examined pixel is independent of the applied separation, the values will just be shifted in this row of the GLCM if the separation is varied. For the marginal-probability matrix this means, that the distribution of the values will be the same for different separations. Hence, Haram4 is a good parameter for determining volume fraction as it is largely independent of the distribution of that phase. Figure 4-10 does indicate however, that its absolute value depends on the grey levels of the phases being investigated and so it may be etch-sensitive.

Regarding the microstructural features this parameter yields a high value if the image shows both bright and dark areas. The highest value will be achieved for a volume fraction of 50 % white pixels and the rest black pixels. Both the area fraction and the differences in grey value

of the bright and dark areas influence the parameter Haram4 whereas the local distribution of the pixels does not change the parameter. So, for example, a martensitic microstructure (Figure 4-7 (a)) yields a relatively low parameter Haram4 due to the homogeneously bright microstructure. For an increasing volume fraction of bainite (Figure 4-7 (b) and (c)) that shows up as dark etching phase in contrast to the martensite, the parameter increases with the area fraction of bainite. For an area fraction of 50 % a maximum will be reached and the parameter will decrease again with further increasing amount of bainite. However the size of the objects in the image will have no influence on the variance so that parameters such as grain size cannot be differentiated by this parameter. For other combinations of microconstituents similar considerations can be made.

Remaining texture parameters

The other texture parameters give of course different values and trends for varying separations which can be attributed to their mathematical description and so the kind of information they gather from the GLCM.

4.2 Jominy end-quench specimen of the tool steel 100Cr6

For characterisation of complex microstructures, samples of the tool steel 100Cr6 have been heat-treated in previous work to produce the complex range of microstructures that can occur in hardened steels [Fuc00, Fuc01]. Representative micrographs at varying distances from the face (water quenched end) of the sample and the corresponding microhardness values are given in Figure 4-11. The trend of the Knoop microhardness along the sample axis is presented in Figure 4-12.

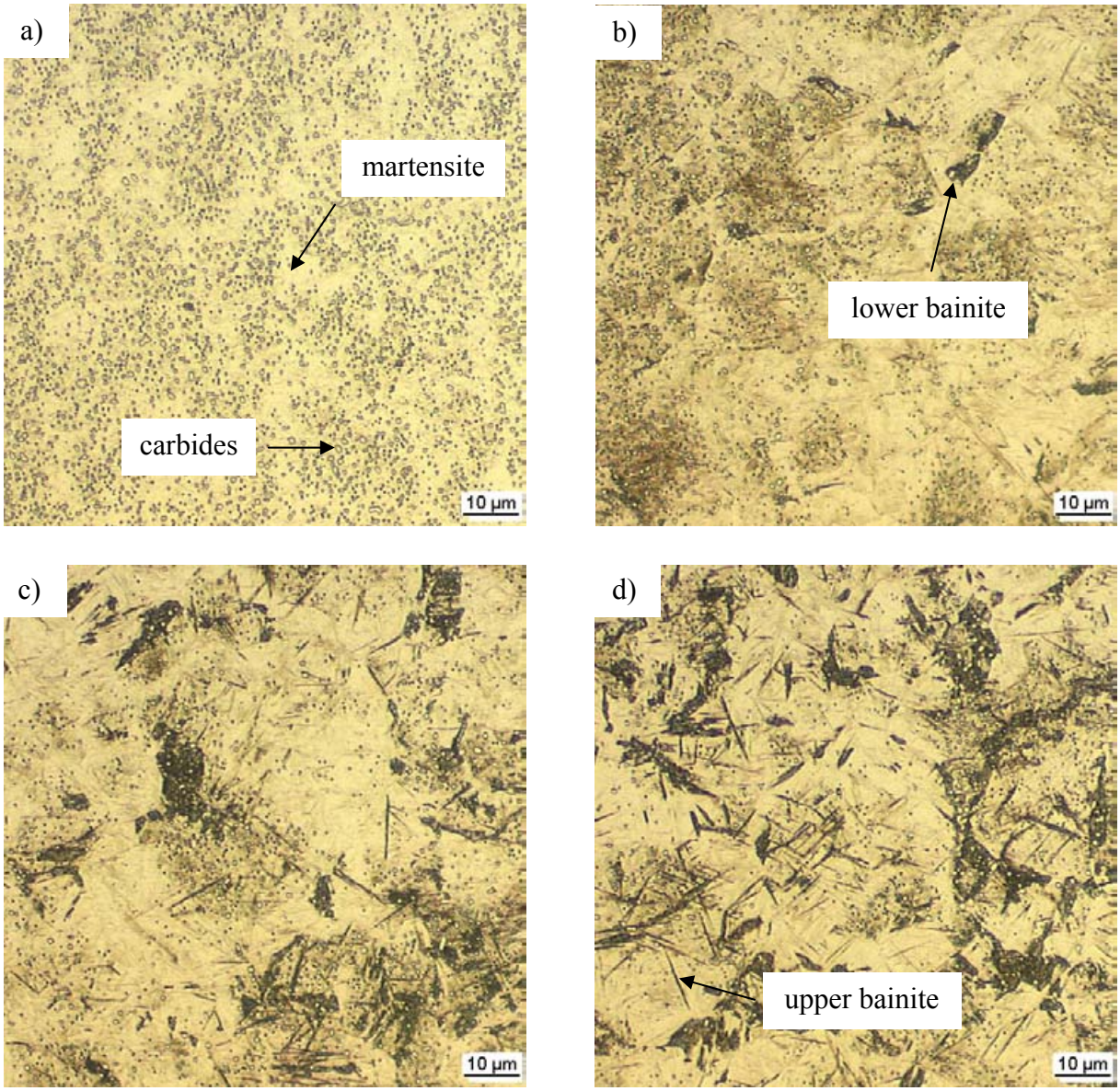

Figure 4-11 Micrographs of the Jominy end-quench specimen of the tool steel 100Cr6 austenitised at 850 °C with the corresponding distance from the face and the microhardness after Knoop (etched with 2 % nital) [Fuc00]

a) 0 µm; 964 $HK_{0.2}$ b) 7,770 µm; 838 $HK_{0.2}$

c) 9,990 µm; 791 $HK_{0.2}$ d) 11,100 µm; 784 $HK_{0.2}$

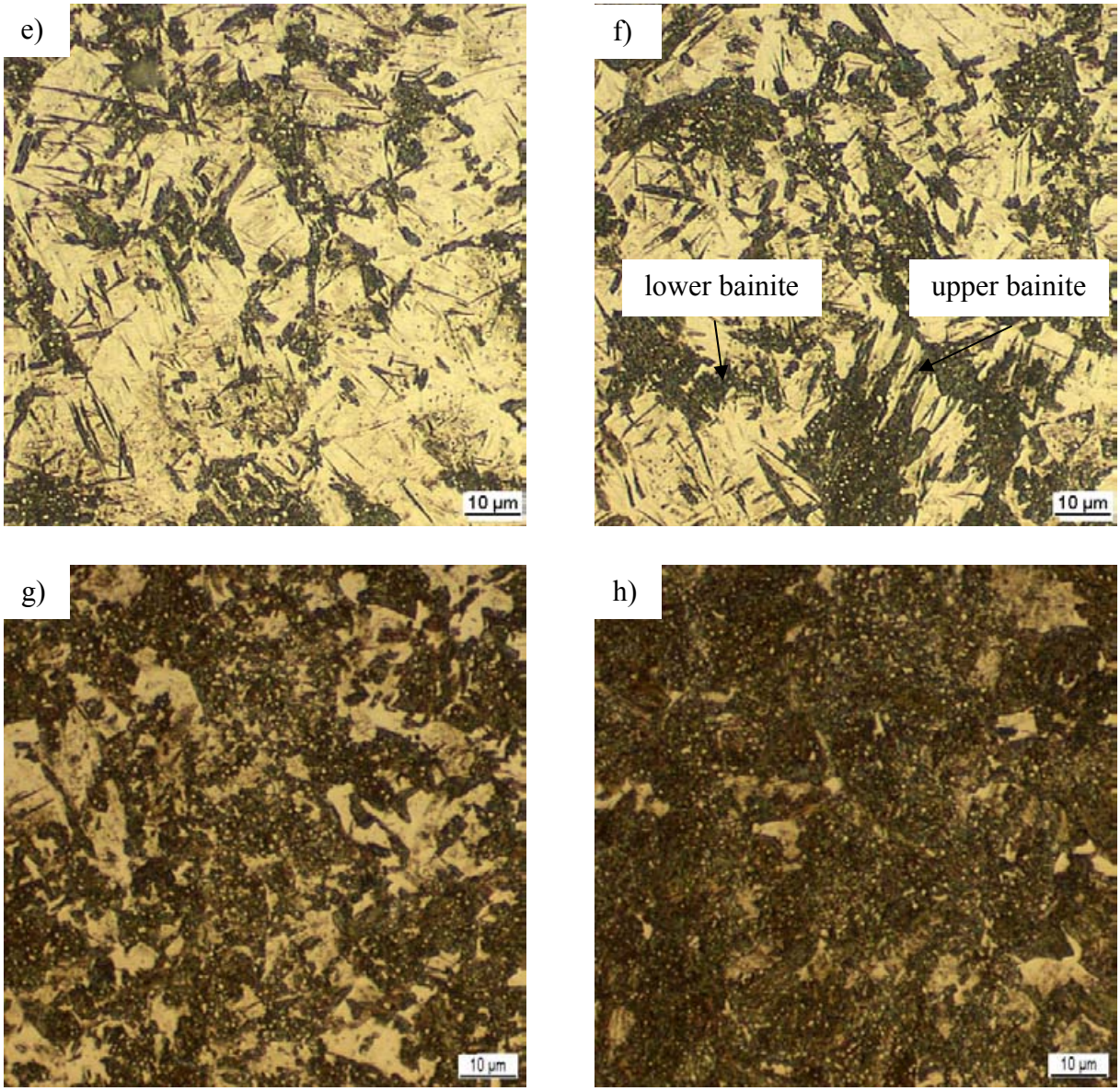

Figure 4-11 Micrographs of the Jominy end-quench specimen of the tool steel 100Cr6 austenitised at 850 °C with the corresponding distance from the face and the microhardness after Knoop (etched with 2 % nital) [Fuc00]

e) 11,840 µm; 691 $HK_{0.2}$ f) 12,580 µm; 604 $HK_{0.2}$

g) 14,060 µm; 473 $HK_{0.2}$ h) 16,280 µm; 421 $HK_{0.2}$

Directly at the water-quenched face of the specimen the microstructure consists of martensite with embedded spherical particles. To identify these particles their EDS spectrum was obtained in the SEM (Figure 4-17 and Figure 4-19). Through this the particles could be identified as chromium-rich carbides. From thermodynamical calculations a volume fraction

of 10.2 vol.-% for the cementite, 1.8 vol.-% of the Cr_3C_2 and vanishing amounts of MoC and TiC was determined for the metastable condition at a temperature of 100 °C of the tool steel 100Cr6 with the chemical composition given in Table 3-1.

The martensite in the region of the water-quenched face is very fine and the needle-like structure is hard to resolve due to the faint etching of the sample in this area. Because of the range of microstructures present along the sample length a compromise for etching has to be found in order not to etch the pearlitic microstructure too intensely, whilst still revealing as much of the structure of the martensite as possible. The carbides that can be found using optical microscopy are spherical and very homogeneous in their size distribution, which is shown for samples of the same heat in Section 4.5.7.

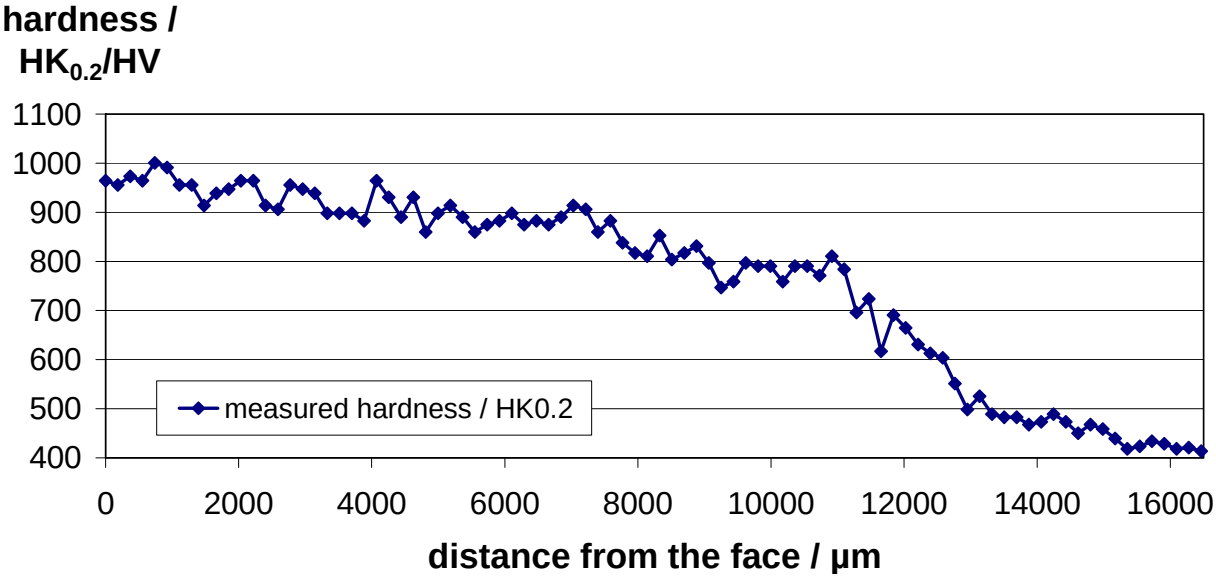

Figure 4-12 Trend of Knoop microhardness along the sample axis for the Jominy end-quench specimen of the tool steel 100Cr6

With increasing distance from the face of the sample lower bainite is appearing within the martensitic matrix. This bainite can be distinguished from the martensite by its darker appearance in optical microscopy according to the increased etching attack. With further increasing distance and thereby decreasing cooling rate of the sample upper bainite is also appearing in the microstructure. This microconstituent can be characterised by its acicular occurrence and the darker etching compared to the martensite.

What can be found with further increasing distance from the water-quenched face of the sample is an increasing amount of pearlite that is also coloured darker in the micrograph than the martensite but showing a more globular structure. With increasing distance the volume fraction of pearlite is increasing at the expense of the martensite. This can be seen in Figure 4-13 where the microstructure of the Jominy end-quench specimen is shown. There are regions in the microstructure showing pearlite in a very nodular form with very fine lamellae (Figure 4-13 b).

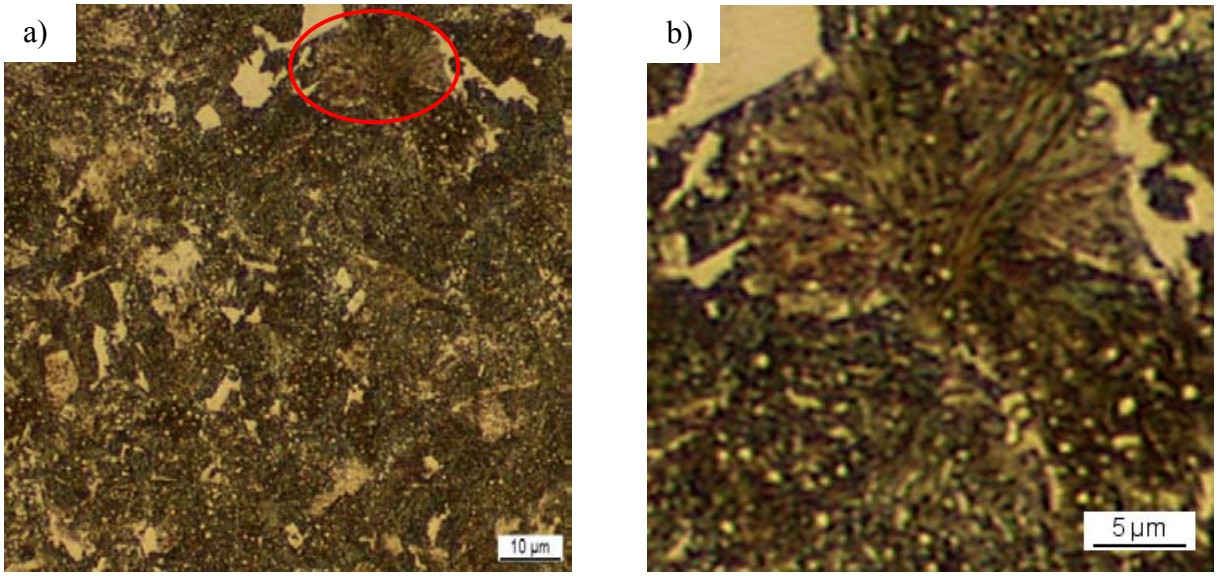

Figure 4-13 Microstructure of the Jominy end-quench specimen of the tool steel 100Cr6 at a distance of 15,910 µm from the face showing regions of pearlite in the microstructure (etched with 2 % nital)

a) overview image b) magnified region from (a)

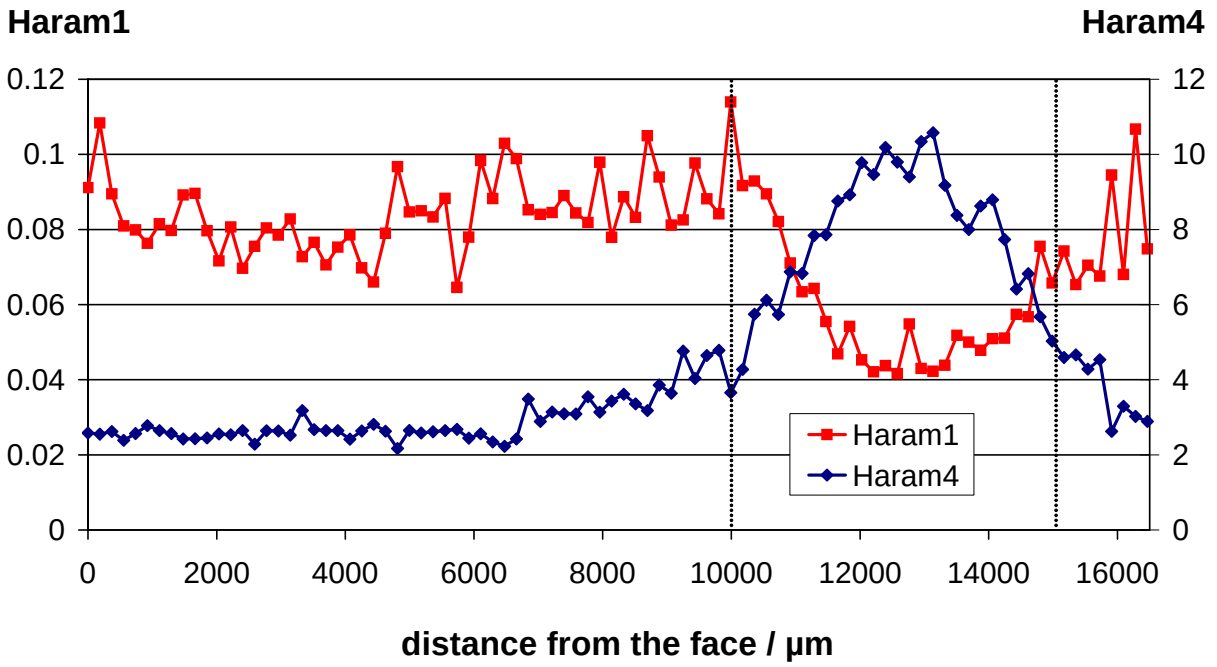

Figure 4-14 Trend of the texture parameters Haram1 and Haram4 alongside the Jominy end-quench specimen of the tool steel 100Cr6 (Figure 4-11)

For the same images of the end-quench specimen (Figure 4-11) the texture parameters have been measured. The trends of the parameters Haram1 and Haram4 are presented as examples with increasing distance from the water-quenched face of the sample in Figure 4-14.

For these two parameters a clear dependence of the position on the sample surface can be seen. The parameter Haram1 shows values between 0.7 and 1.1 for distances of up to approximately 10,000 µm. For larger distances from the face the values are significantly lower showing a local minimum at about 13,000 µm with a value of 0.42 increasing again for greater distances to comparable values as near the face.
The parameter Haram4 shows the inverse trend. For distance of up to 10,000 µm the values lie between 2 and 4, increasing significantly to over 10 at about 13,000 µm from the face, decreasing again at about 15,000 µm back to values between 2 and 4.

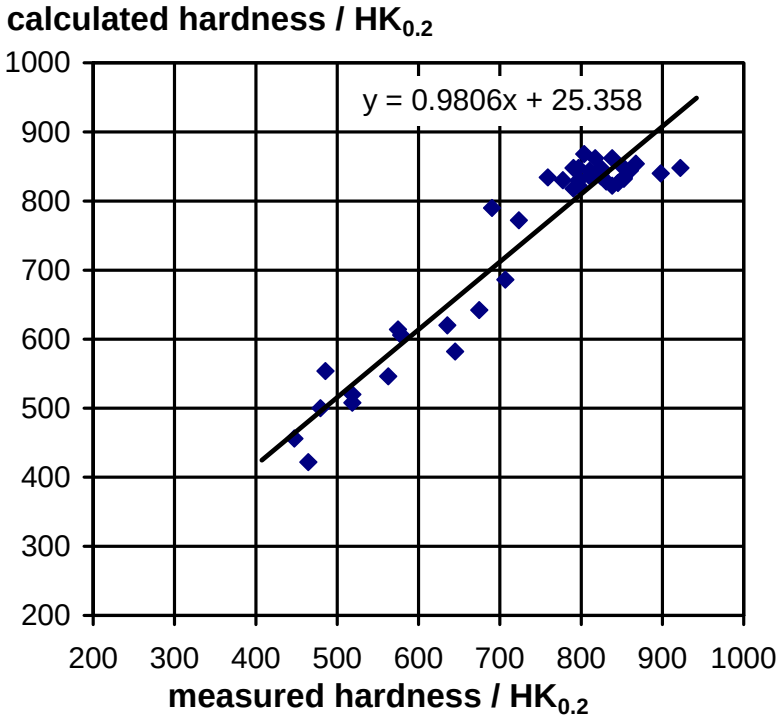

Figure 4-15 Correlation between the measured and the calculated hardness $HK_{0.2}$ for optical micrographs of the Jominy end-quench specimen of the tool steel 100Cr6, hardness calculated by the texture parameters Haram1 to Haram11 using a neural network, trained with texture parameters and the corresponding hardness [Fuc00]

To establish a correlation between the microstructure represented by the texture parameters and the hardness, every tenth micrograph was used to train a neural network by means of the 11 texture parameters as input values and the hardness as output value. The images were taken at equal distances to ensure that a representative amount of the sample is used to train the neural network. After training, the hardness at the position of the remaining micrographs was calculated from the texture parameters. As for all the micrographs the hardness was measured, these values can be correlated with those calculated from the texture parameters by the neural network. The result of this correlation is presented in Figure 4-15.

As can be seen the overall correlation for the Jominy end-quench specimen of the tool steel 100Cr6 yields only low differences between the measured values and the calculated ones. This is obvious by the data points lying very close to the best fit line in the diagram. The

difference between the measured values and the best fit line calculated on the basis of the calculated values yields a mean value of -0.01 with a standard deviation of 37.4.

The potential of these methods has been shown and it is the aim of this project to expand the understanding of these techniques in their application to model and real industrial steel microstructures.

4.3 Microstructure of the heat treated samples

Pearlitic samples

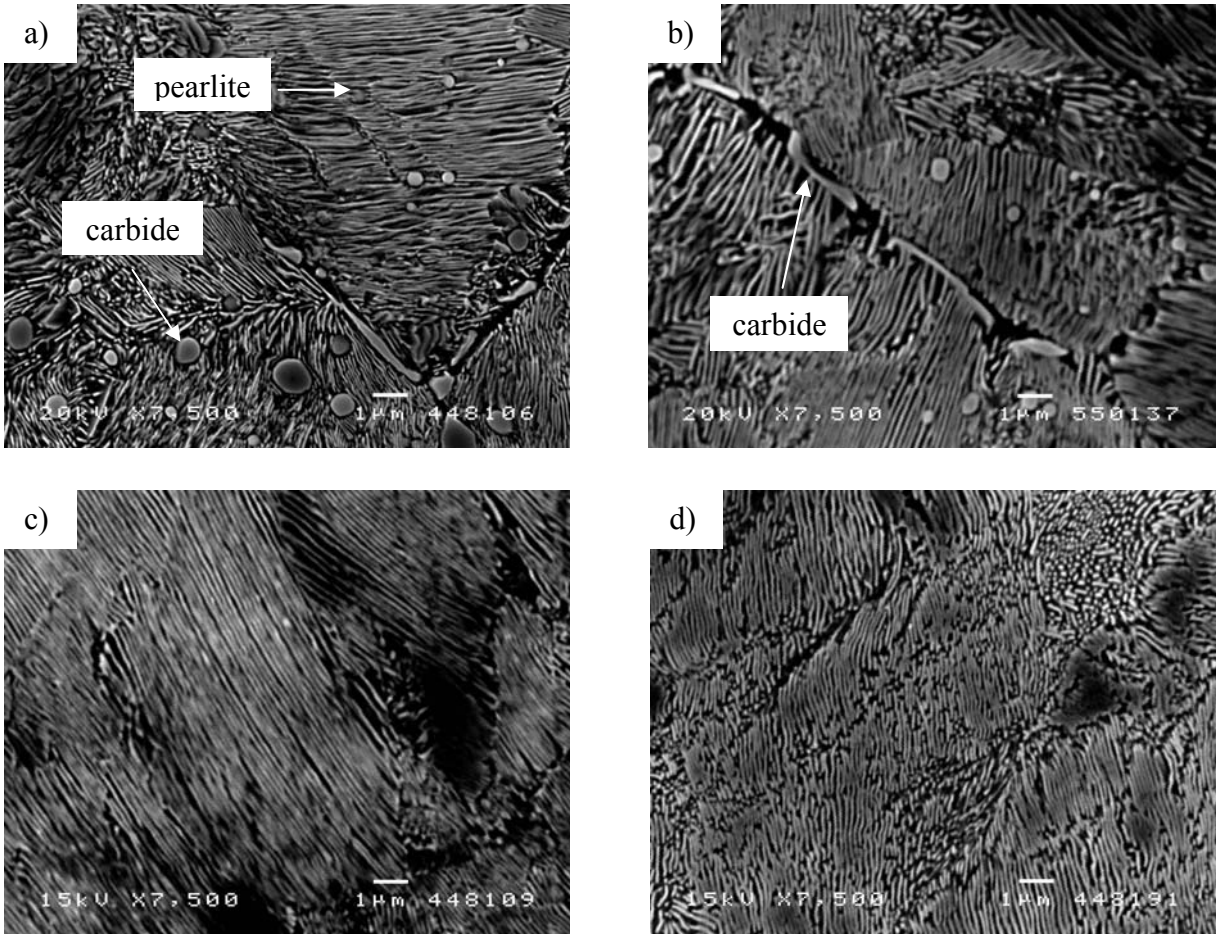

Figure 4-16 SEM secondary electron micrographs of the pearlitic samples of the tool steel 100Cr6 austenitised at different temperatures, together with respective sample designation (continuously cooled at 0.2 K s^{-1}, etched with 2 % nital)

a) 780 °C, p100Cr6_780 b) 800 °C, p100Cr6_800

c) 850 °C, p100Cr6_850 d) 900 °C, p100Cr6_900

SEM secondary electron micrographs of the pearlitic samples are shown in Figure 4-16 for a magnification of 7,500:1, continuously cooled from the austenitising temperature to ambient at 0.2 K s^{-1}.

The slow cooling rate of 0.2 K s^{-1} results in a matrix that is fully pearlitic with carbides present depending on the re-austenitising temperature. These particles are characterised as carbides and compared to the pearlitic matrix using EDS as shown in Figure 4-17. Compared to the matrix the carbides are enriched in chromium and manganese, especially chromium, as would be expected for carbides in this steel [Sch66a]. The carbon peaks for matrix and carbides are similar in Figure 4-17 (c)-(e), but this may indicate carbon contamination during preparation.

For the lowest re-austenitising temperature of 780 °C (Figure 4-17 (a)) the carbides are comparatively coarse with Cr-rich carbides found on the grain boundaries.

For the next higher temperature of 800 °C not only the number but also the size of the carbides decreases as can be seen qualitatively from the micrographs, Figure 4-17 (b). Quantitative measurements of the size distribution and area fraction of carbides will be presented in section 4.5.7.2. Also for this sample carbides can be found on the grain boundaries.

For the austenitising temperature of 850 °C only very few carbides can be found in the microstructure. Also the amount of carbides along the grain boundaries decreases significantly. This agrees to the Thermo-Calc simulations, section 4.4, that predict that for this temperature all the Cr-rich carbides and most cementite are fully dissolved in the matrix.

The same can be seen for the sample austenitised at 900 °C where hardly any carbides can be found on the grain boundaries. Again the number and the size of the carbides both decrease if compared to those in the sample heat treated at 850 °C.

a)

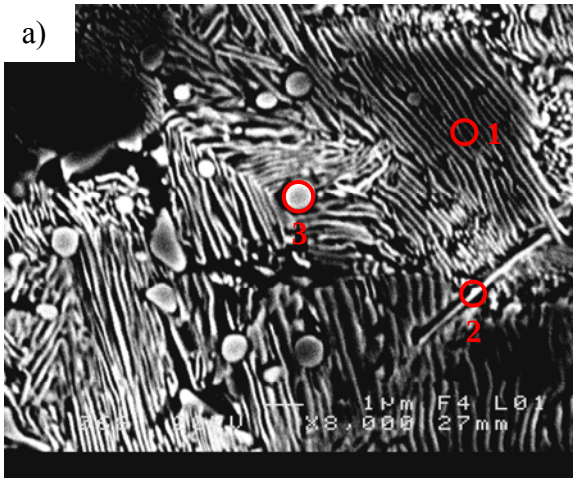

b) 1 - pearlitic matrix

element	at.-%	wt.-%	wt.-% error (1-Sigma)
Mn	0.48	0.47	± 0.14
Cr	1.54	1.44	± 0.09
Fe	97.68	97.94	± 0.79
Si	0.30	0.15	± 0.05

2 - grain boundary carbide

element	at.-%	wt.-%	wt.-% error (1-Sigma)
Mn	0.78	0.77	± 0.18
Cr	8.28	7.77	± 0.24
Fe	90.58	91.28	± 0.81
Si	0.36	0.18	± 0.06

3 - carbide

element	at.-%	wt.-%	wt.-% error (1-Sigma)
Mn	0.95	0.94	± 0.17
Cr	6.31	5.91	± 0.22
Fe	92.40	92.98	± 0.81
Si	0.34	0.17	± 0.06

Figure 4-17 SEM micrograph of the pearlitic sample p100Cr6_800 of the tool steel 100Cr6 austenitised at 800 °C (etched with 2 % nital) (a), quantitative analysis (b) at a matrix and two carbide positions together with corresponding EDS spectra (c, d and e) of the positions marked in (a)

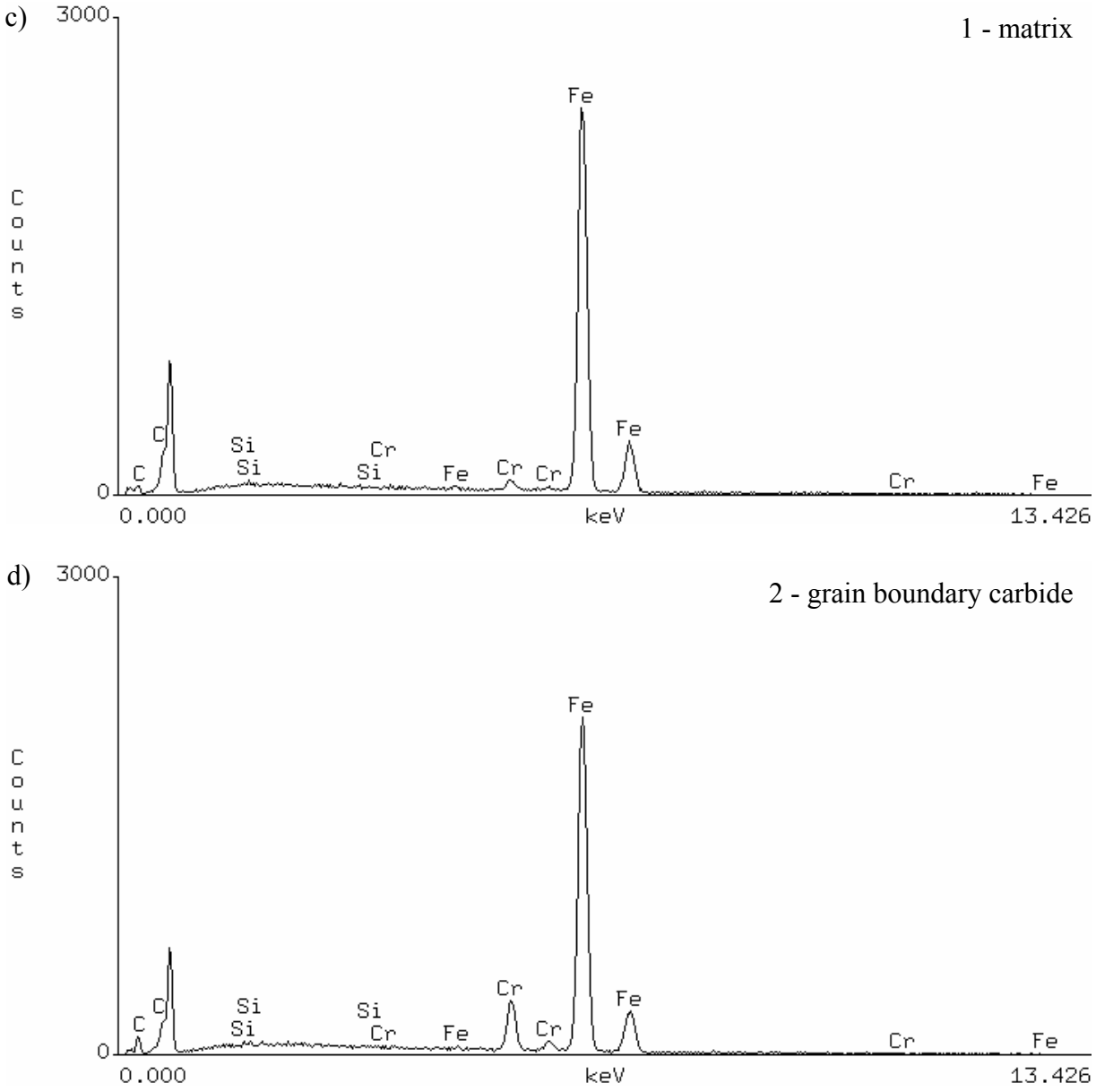

Figure 4-17 SEM micrograph of the pearlitic sample p100Cr6_800 of the tool steel 100Cr6 austenitised at 800 °C (etched with 2 % nital) (a), quantitative analysis (b) at a matrix and two carbide positions together with corresponding EDS spectra (c, d and e) of the positions marked in (a)

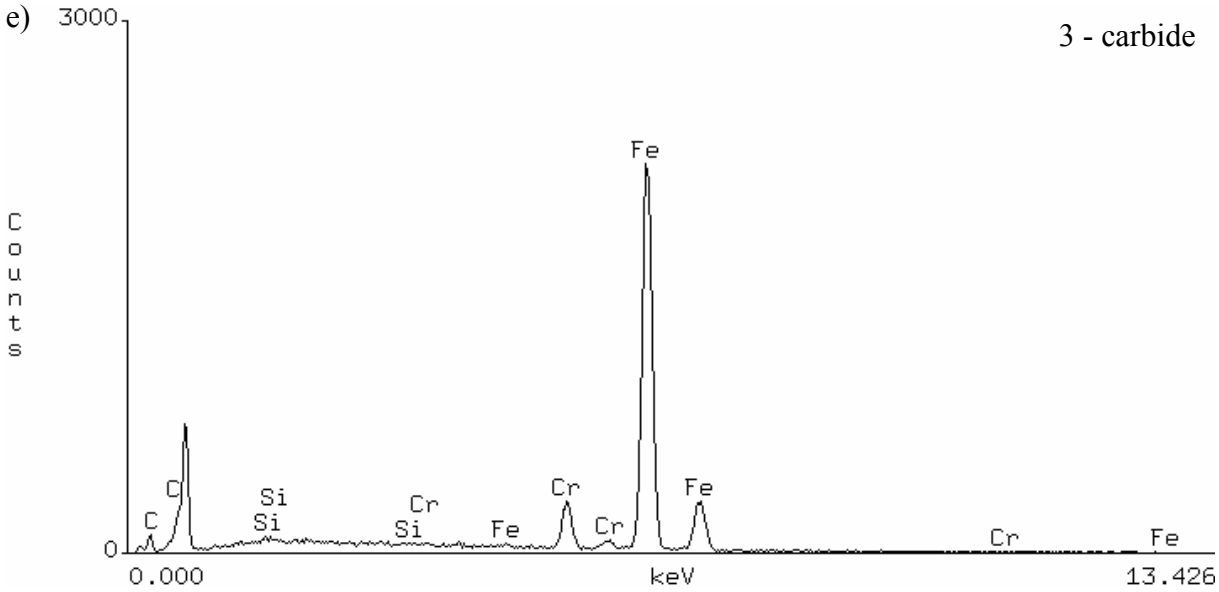

Figure 4-17 SEM micrograph of the pearlitic sample p100Cr6_800 of the tool steel 100Cr6 austenitised at 800 °C (etched with 2 % nital) (a), quantitative analysis (b) at a matrix and two carbide positions together with corresponding EDS spectra (c, d and e) of the positions marked in (a)

Bainitic samples

Optical Micrographs

Optical micrographs of these samples and the corresponding Vickers hardness values measured are shown in Figure 4-18 at a magnification of 500:1. To identify the carbides, SEM-EDS of the samples has been carried out, the results of which are presented in Figure 4-19.

The material was received in a spheroidised condition. The microstructure given in Figure 4-18 (a) shows a large number of relatively small carbides up to about 3 µm diameter, which are mostly rounded. These carbides are embedded in a ferritic matrix as typical for the spheroidised state of hypereutectoid steels. These particles can be characterised as carbides by EDS which is presented in Figure 4-19. There it can be seen that the carbides are enriched in Mn and Cr compared to the matrix. Although carbon contamination is again expected, the carbides in these specimens exhibit larger carbon peaks (relative to iron), Figure 4-19 (d) than the matrix, Figure 4-19 (c).

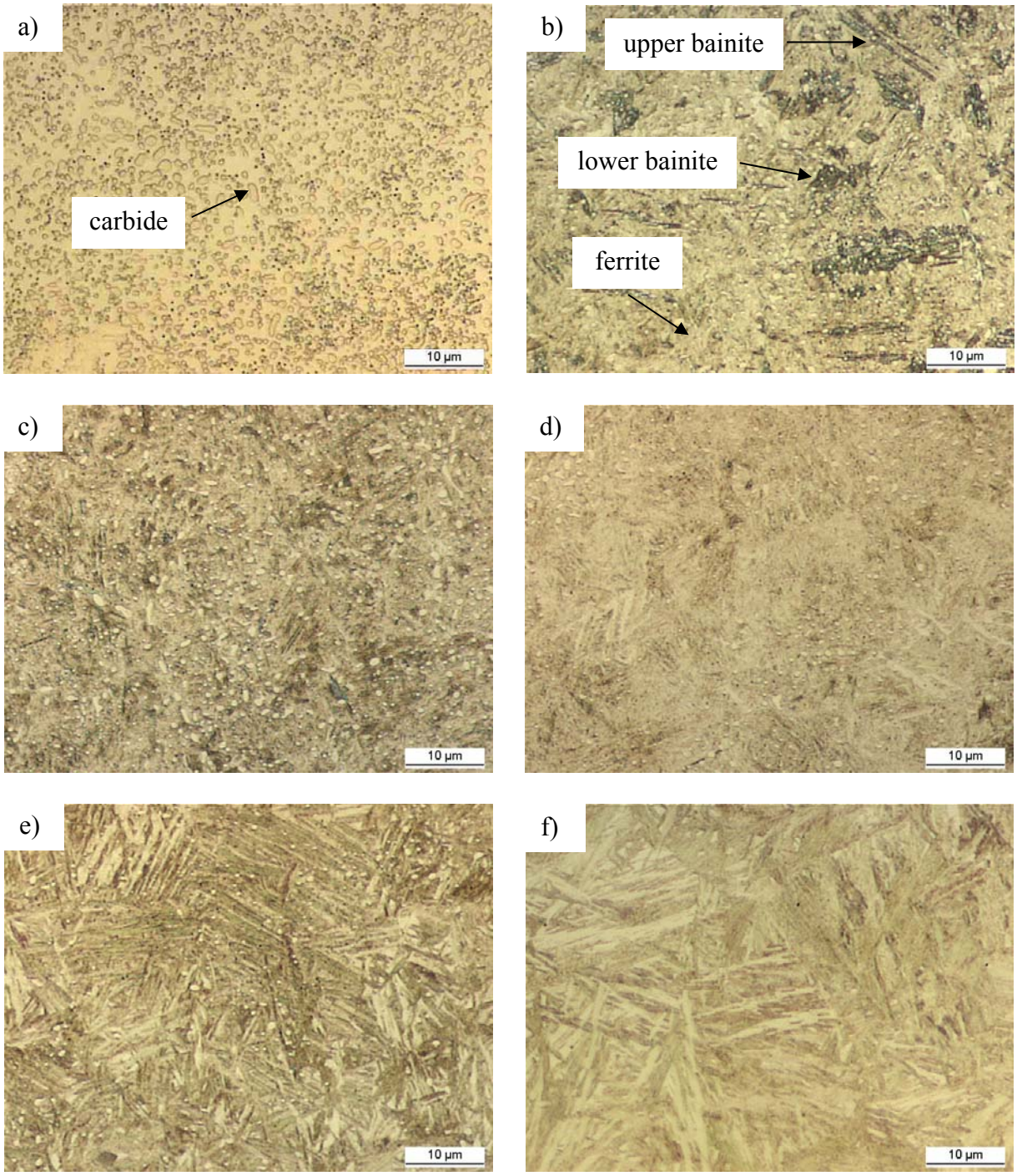

Figure 4-18 Optical micrographs of the bainitised samples of the tool steel 100Cr6, re-austenitised at different temperatures, T_A, with corresponding Vickers hardness values and the sample designation (etched with 2 % nital)

a) as-received, 204 H_{V30}, b100Cr6_rec
b) 780 °C, 656 H_{V30}, b100Cr6_780
c) 800 °C, 672 H_{V30}, b100Cr6_800
d) 850 °C, 755 H_{V30}, b100Cr6_850
e) 900 °C, 757 H_{V30}, b100Cr6_900
f) 930 °C, 747 H_{V30}, b100Cr6_930

a)

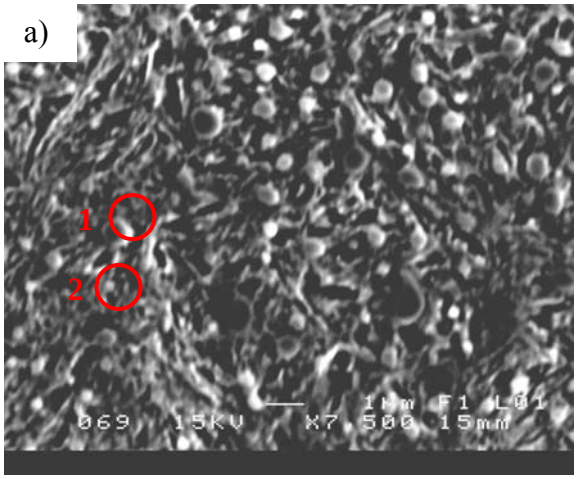

b) 1 - matrix

element	at.-%	wt.-%	wt.-% error (1-Sigma)
Mn	0.34	0.34	± 0.19
Cr	1.06	0.99	± 0.11
Fe	98.05	98.40	± 0.99
Si	0.55	0.28	± 0.05

2 - carbide

element	at.-%	wt.-%	wt.-% error (1-Sigma)
Mn	1.14	1.13	± 0.23
Cr	8.09	7.60	± 0.30
Fe	90.28	91.02	± 1.03
Si	0.49	0.25	± 0.06

Figure 4-19 SEM micrograph of the bainitic sample b100Cr6_800 of the tool steel 100Cr6 austenitised at 800 °C (etched with 2 % nital) (a), quantitative analysis (b) at a matrix and a carbide position together with corresponding EDS spectra (c and d) of the positions marked in (a)

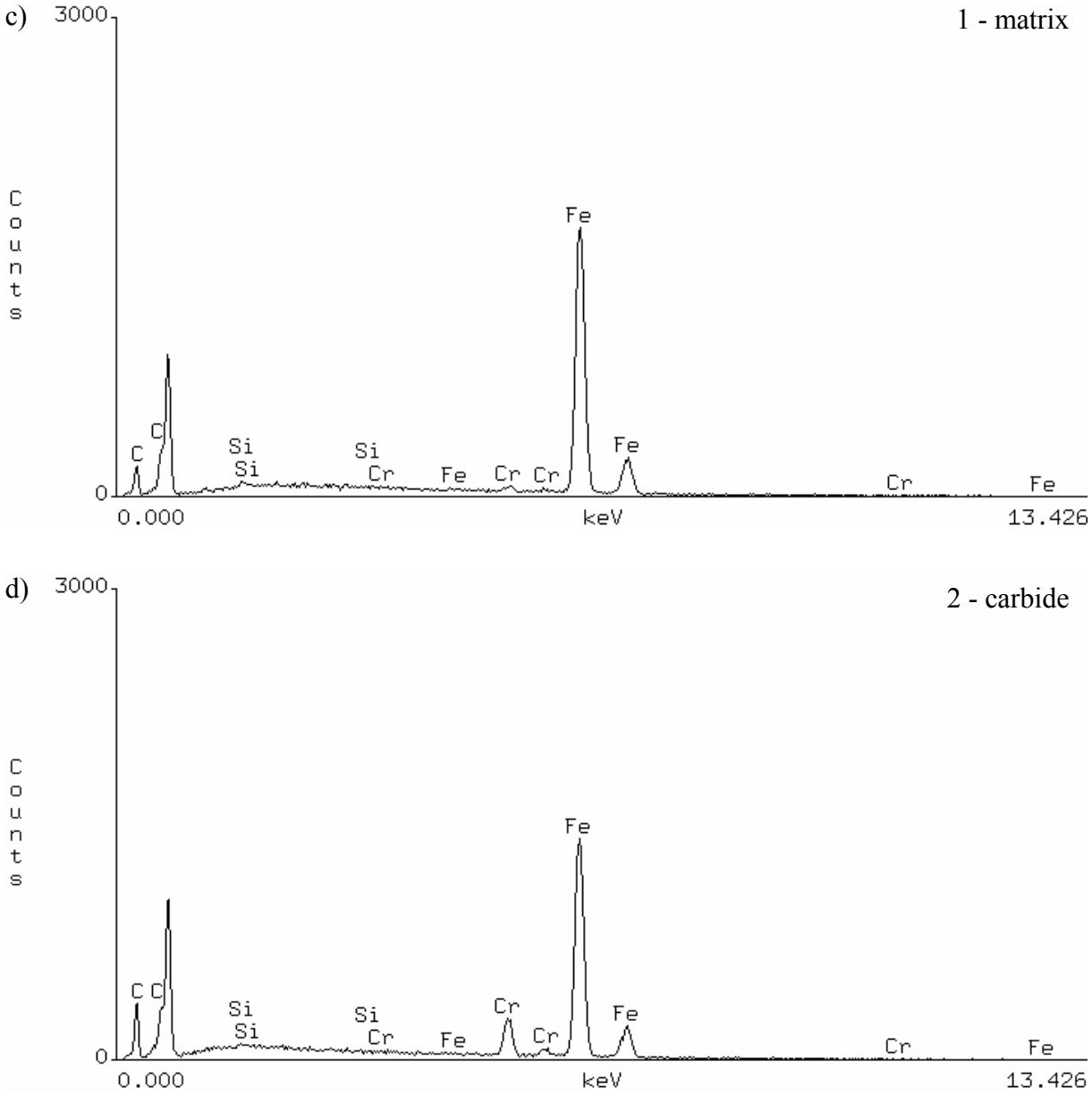

Figure 4-19 SEM micrograph of the bainitic sample b100Cr6_800 of the tool steel 100Cr6 austenitised at 800 °C (etched with 2 % nital) (a), quantitative analysis (b) at a matrix and a carbide position together with corresponding EDS spectra (c and d) of the positions marked in (a)

The sample austenitised at 780 °C, Figure 4-18 (b), shows a mixed microstructure of carbides in a mixed matrix. Ferrite, upper bainite and lower bainite are found due to incomplete re-austenitisation at the low temperature. The hardness is, at 656 H_{V30}, much higher than the 204 H_{V30} in the spheroidised as-received condition.

The sample austenitised at 800 °C, Figure 4-18 (c), shows a microstructure consisting of carbides in a bainitic matrix. The bainite is granular and hardly resolvable in the optical microscope even at a magnification of 1000:1. The hardness is, at 672 H_{V30}, slightly higher than for the sample austenitised at 780 °C

The re-austenitisation temperature of 850 °C is mostly used for heat treatment of this alloy in industrial processes. The microstructure obtained at this temperature, Figure 4-18 (d), shows fewer carbides, which are 1 µm or smaller and so are smaller than those in the samples austenitised at lower temperatures. The microstructure of the matrix is fine bainite with sporadic plates that are about 10 µm long. The hardness of 755 H_{V30} is significantly higher than for the other samples.

For the sample austenitised at 900 °C, Figure 4-18 (e), the carbides are again 1 µm or smaller. The matrix microstructure now shows very clear plates with a length of 10 µm and more. The plates are arranged in clusters also called sheaves. The hardness is 757 H_{V30}, the same as for the sample austenitised at 850 °C.

For the highest temperature of 930 °C, Figure 4-18 (f), almost no carbides can be found. The few carbides left are smaller than 0.5 µm and therefore hard to resolve in the optical microscope. The bainitic microstructure now shows very distinct plates with a length of 20 µm and more. The plates are again arranged in sheaves. The hardness is, at 747 H_{V30}, nearly the same as for the samples austenitised at 850 °C and 900 °C.

SEM micrographs

For the 5 different austenitising temperatures SEM secondary electron micrographs of the bainitised samples of the tool steel 100Cr6 have been made at a magnification of 7,500:1 and are presented in Figure 4-20. The same samples have been investigated by optical microscopy, as presented in Figure 4-18.

The microstructure of the sample austenitised at 780 °C (Figure 4-20 (a)) is very fine and needle-like consisting of a mixture of bainite, ferrite and carbides. The number density and the size (up to 2 µm) of the carbides are high compared to the other heat treatments. To identify these particles as carbides the EDS spectrum was obtained in the SEM (Figure 4-19). Through this the particles could be identified as chromium-rich and probably carbides.

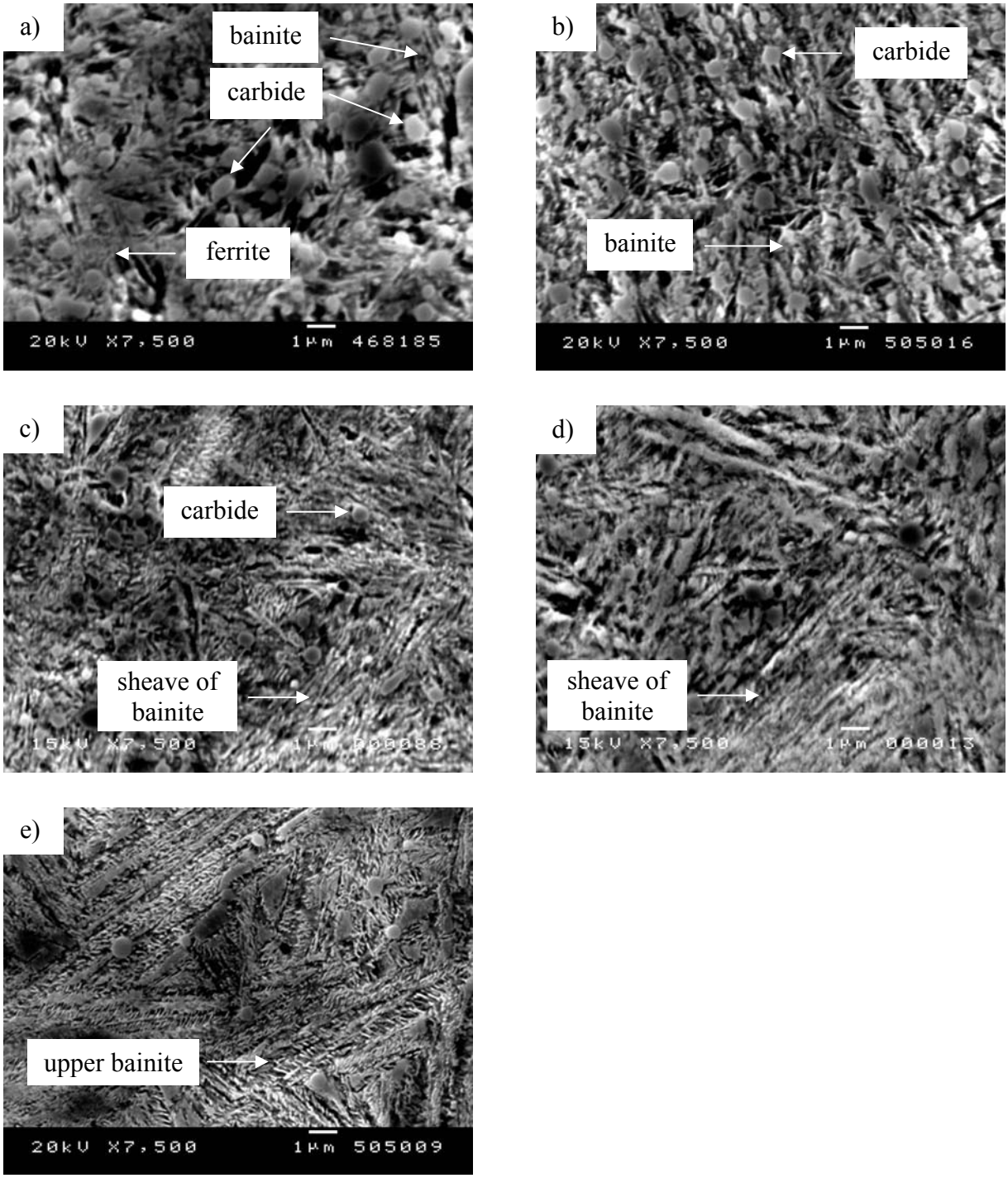

Figure 4-20 SEM secondary electron micrographs of the bainitised samples of the tool steel 100Cr6, re-austenitised at different temperatures, T_A, with corresponding Vickers hardness and the sample designation (etched with 2 % nital)

a) 780 °C, 656 H_{V30}, b100Cr6_780 b) 800 °C, 672 H_{V30}, b100Cr6_800
c) 850 °C, 755 H_{V30}, b100Cr6_850 d) 900 °C, 757 H_{V30}, b100Cr6_900
e) 930 °C, 747 H_{V30}, b100Cr6_930

With increasing re-austenitising temperature the carbide dissolution increases putting more Cr and C in solution. This increases the hardenability giving more lower bainite and then martensite (with high C level) which in turn, results in a higher hardness.
The sample re-austenitised at 800 °C shown in Figure 4-20 (b) shows finer but also needle-like microstructure consisting of lower bainite. The number and size of the carbides is comparable to that of the sample heat treated at 780 °C.
For a temperature of 850 °C (Figure 4-20 (c)) the microstructure looks much more lath-like than for the lower temperatures. The laths are arranged in sheaves as typical for lower bainitic microstructures. For this heat treatment the apparent number density of carbides is lower than for the previously discussed samples.

If the austenitising temperature is further increased to 900 °C (Figure 4-20 (d)) the same lath-like microstructure can be found as for the 850 °C sample. The laths of the bainite are bigger in both width and length. It is also obvious that the number density of the carbide is significantly lower than at 850 °C.
The microstructure of the sample austenitised at 930 °C shown in Figure 4-20 (e) differs from that of the samples austenitised at all the lower temperatures. The lath-like structure can still be found and these laths are also still arranged in sheaves. The laths have a feathery appearance and therefore can be identified as upper bainite. The number density of carbides again decreases in comparison to the 900 °C sample.

4.4 Modelling methods

4.4.1 Thermodynamical simulations of the phase composition of the analysed material

The equilibrium phase balance and compositions at different austenitisation temperatures were calculated using Thermo-Calc [The04] (see section 3.2.1) and extended over the temperature range 50 – 1300 °C. These data were used to compare the calculated content of carbides with the quantitatively measured values. The calculated mass fractions were converted to volume fractions using literature values for the corresponding densities as given in Table 4-3.

Table 4-3 Predicted stable phases (Thermo-Calc) and their densities occurring during the heat treatment of the tool steel 100Cr6

phase	density / g/cm³	reference for density
ferrite	7.88	[Cal99]
austenite	7.90	[Cun00]
Ti(C,N)	4.92	[Gog03]
MnS	4.05	[Vil91]
Fe_3C	7.4	[Gog03, Sch90]
MoC	8.8	[Gog03]
Cr_3C_2	6.68	[Gog03]
$(Fe,Cr,Mo)_{23}C_6$	7.92	calculated from lattice parameters, [Lee00], [Nem03]

These predictions are compared with quantitative carbide measurements in section 4.5.7.

The equilibrium volume fractions that have been calculated for the range of temperatures are presented in Figure 4-21 and in Figure 4-22. It can be seen that up to a temperature of 725 °C most of the microstructure consists of ferrite (approximately 87 vol.-%) and cementite (approx. 11 – 14 vol.-%) with smaller amounts of carbides such as M_3C_2 with a volume fraction of less than 2 vol.-%. For temperatures of 750 °C and above the matrix consist mainly of austenite with 95 vol.-% and more. The volume fraction of cementite decreases significantly with increasing temperatures to disappear between 850 and 900 °C. Manganese sulphide is present with a volume fraction of approximately 0.01 vol.-% up to a temperature of 1100 °C. With increasing temperature the volume fraction of manganese sulphide decreases and at about 1300 °C it is fully in solution.

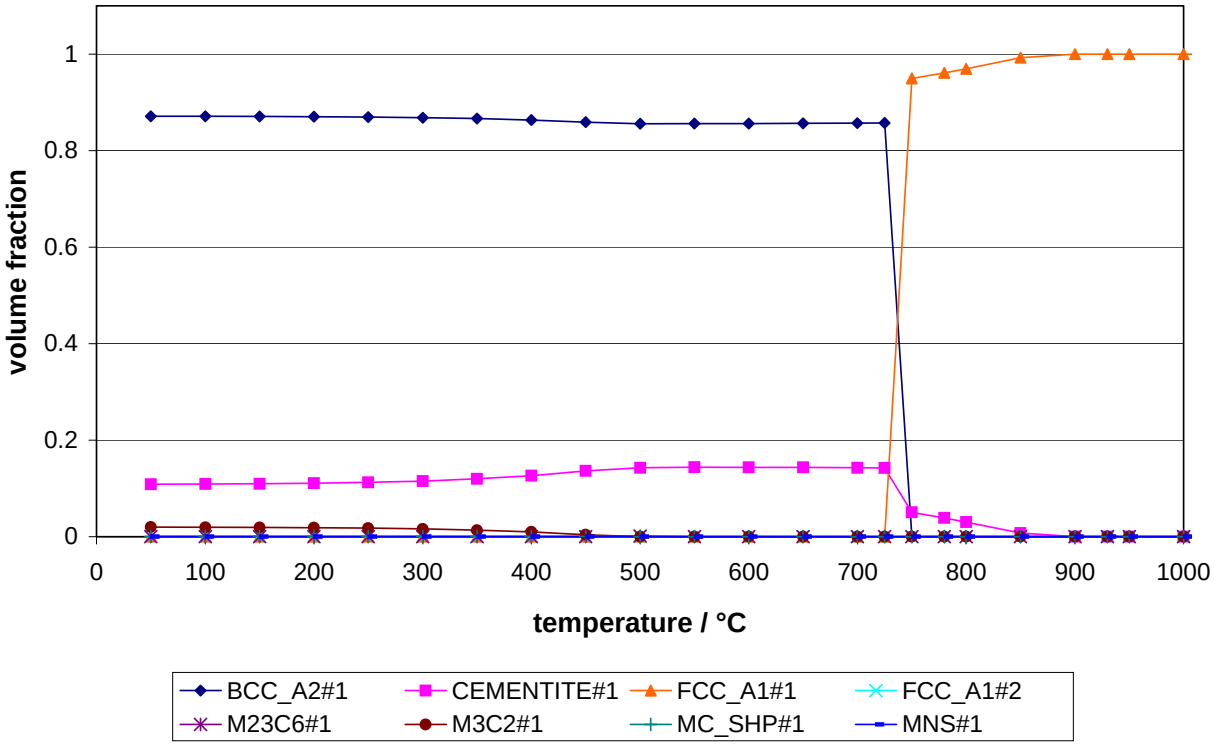

Figure 4-21 Influence of the temperature on the equilibrium phase balance for the tool steel 100Cr6 with the chemical composition given in 3.1.1

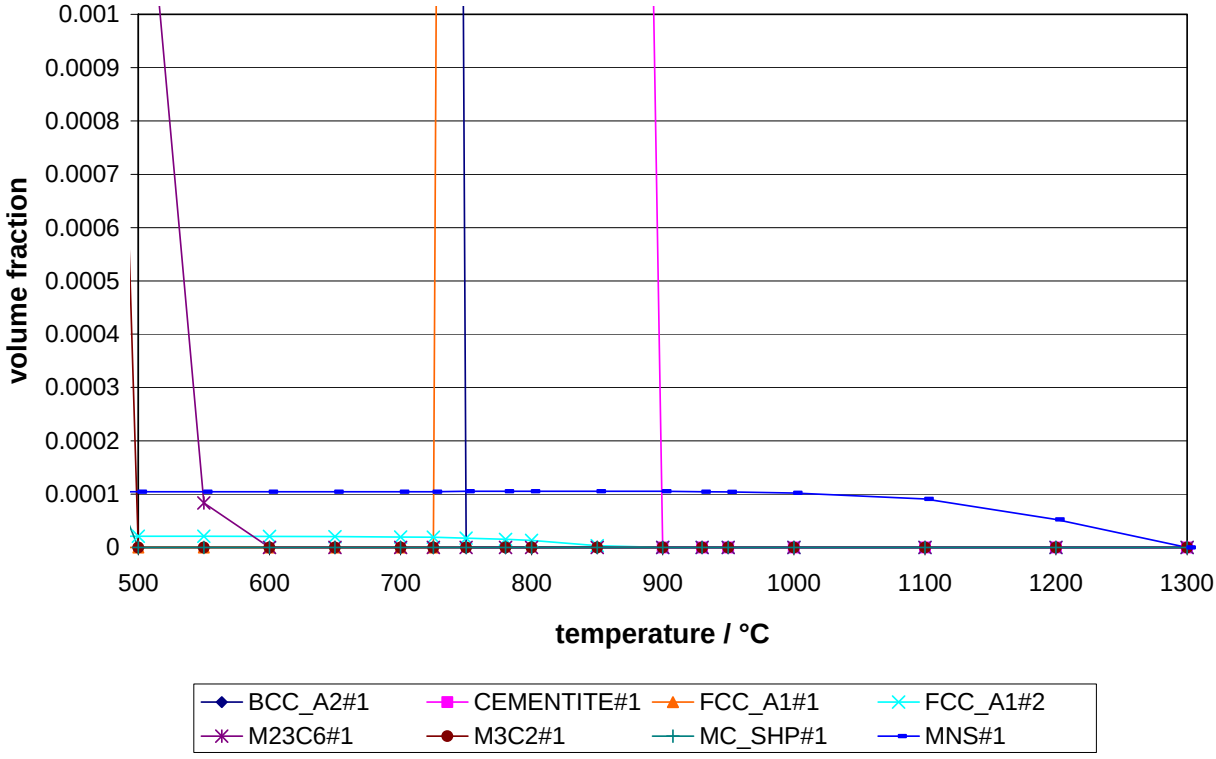

Figure 4-22 Section of the equilibrium phase balance of the tool steel 100Cr6 in the temperature range 500 – 1300 °C for lower volume fractions

4.4.2 Prediction of the hardness for a Jominy end-quench specimen

Giving large differences in the microstructure, a Jominy end-quench specimen has been chosen to show the possibilities of the prediction of the microhardness from data obtained by quantitative image analysis.

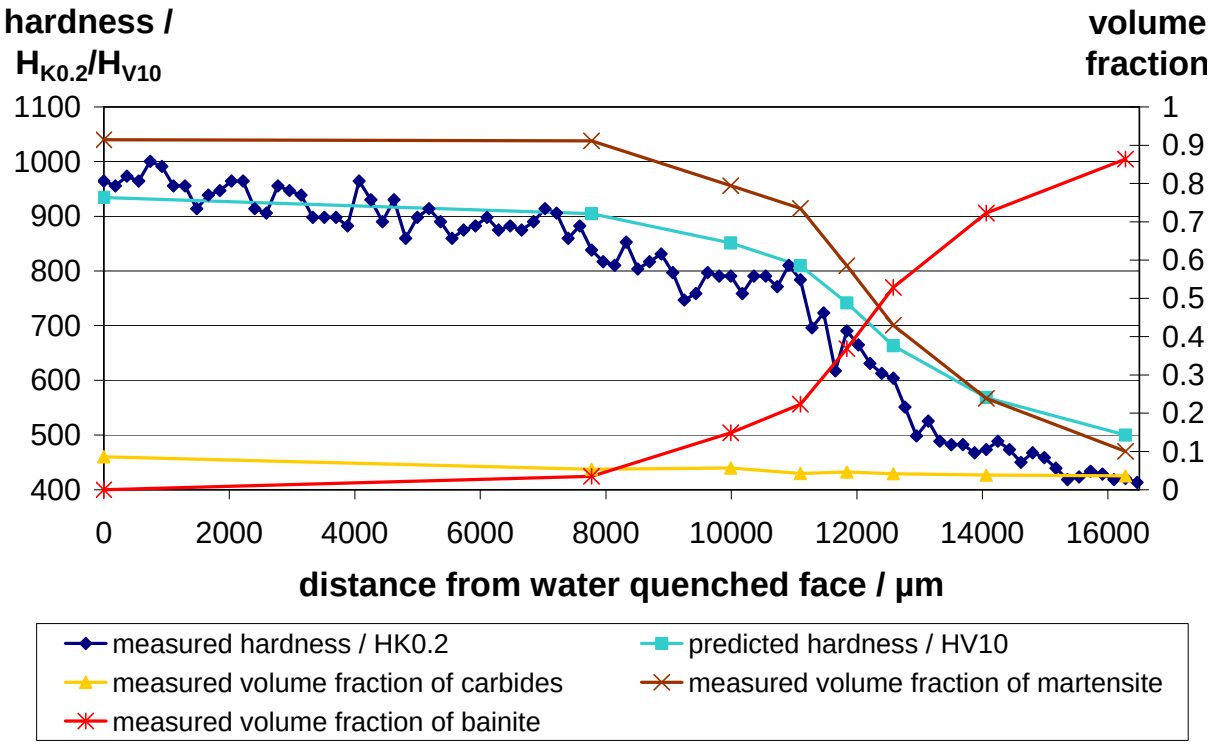

Figure 4-23 Distribution of Knoop microhardness along the length of the Jominy end-quench specimen Jom100Cr6 compared with the Vickers hardness predicted from the phase balance measured by quantitative optical microscopy from the micrographs given in Figure 4-11

To simulate the influence of the microstructural variations on hardness, the volume fractions of the microconstituents have been measured by quantitative optical microscopy and are presented in Figure 4-23 for the micrographs presented in Figure 4-11 together with the trend of the microhardness after Knoop along the sample axis given in Figure 4-12. The law of mixtures according to Gladman [Gla72] was used to calculate the yield strength σ_y of a mixed microstructure according to

$$\sigma_y = \sum f_\alpha^n \cdot \sigma_\alpha \qquad \text{Eq. 4-5}$$

from the volume fractions and their respective yield strengths. The index n allows a correlation in a non-linear manner if set to values different from 1.

Eq. 4-6 was used with the volume fractions of the different phases to predict the local Vickers hardness in order to compare these values with the measured values (Figure 4-23). This law of mixtures was used with an index n=1 to obtain linear dependencies and was expanded to cover all the phases occurring in the Jominy end-quench specimen of the tool steel 100Cr6.

$$hardness = V_f(m) \cdot h(m) + V_f(b) \cdot h(b) + V_f(p) \cdot h(p) + V_f(f) \cdot h(f) + V_f(c) \cdot h(c) \qquad \text{Eq. 4-6}$$

m ... martensite
b ... (upper and lower) bainite
p ... pearlite
f … ferrite
c ... carbide
$V_f(x)$ ... volume fraction of phase x
h(x) ... hardness of phase x

According to the equation the hardness of the single phases is weighted by the corresponding volume fraction and then summed up for the microstructure to be analysed. The hardness values for the phases used in this prediction are given in Table 4-4. The hardness values have been chosen that best represent the conditions of the experiments. Comparative values are given that show the hardness values for similar conditions.
The measured volume fractions of the occurring phases are given in Figure 4-23 and in Table 4-5. At the water quenched face of the sample about 91.4 vol.-% martensite and 8.6 vol.-% carbides can be found (Figure 4-23). The volume fraction of martensite stays nearly constant to a distance of 8,000 µm from the face. For the carbides a value of 5.4 vol.-% and for the bainite 3.5 vol.-% were determined at this distance. The amount of martensite decreases to 10.0 vol.-% at a distance of 16,000 µm with the bainite increasing its volume fraction to 86.4 vol.-%. The volume fraction of carbides is showing a slight decrease with increasing distances from the face. At a distance of 16,000 µm a volume fraction of 3.6 vol.-% can be found.

Table 4-4 Hardness of the phases occurring in the Jominy end-quench specimen of the tool steel 100Cr6

phase x	hardness h(x) / H_{V10}	conditions	reference	comparative values
martensite	900	for plain carbon steel with 1 wt.-% C	[Kra99]	tensile strength 2797 MPa [Els02], equals 843 H_V by extrapolation [DIN76], 500-1010 H_V [Dum03]
bainite	420	steel with 1.01 wt.-% C, 0.4 wt.-% Mn, 1.36 wt.-% Cr	[Atk77]	484 H_V for isothermal transformation at 329 °C [Shi97], 435 H_V for lower bainite [Bha99a], 250-450 H_V [Dum03]
pearlite	270	for interlamellar spacing S_0=1µm and 0.25 wt.-% Si	[Bal99]	320 H_V for 41Cr4 [Kul03], 300-460 H_V [Dum03]
carbide	1300	hardness of Fe_3C > 4.5 GPa, extrapolation to H_V	[Web95]	1330-1700 H_V [Dum03]

Table 4-5 Volume fraction of the phases at different distances from the water quenched face of the Jominy sample of the tool steel 100Cr6

phase	distance from water quenched face		
	0 µm	**8,000 µm**	**16,000 µm**
martensite	91.4 vol.-%	91.1 vol.-%	10.0 vol.-%
bainite	0 vol.-%	3.5 vol.-%	86.4 vol.-%
carbides	8.6 vol.-%	5.4 vol.-%	3.6 vol.-%
total	**100 vol.-%**	**100 vol.-%**	**100 vol.-%**

The predicted values show a hardness of 940 H_{V10} at the water quenched face of the sample with a slight decrease for increasing distances from this face. At about 8,000 µm from the face a hardness of 900 H_{V10} is reached. At this position the volume fraction of bainite increases at

the expense of martensite. With further distance from the face and constantly increasing volume fraction of bainite the hardness decreases significantly. At a distance of 16,000 µm a predicted hardness of 500 H_{V10} is reached. The actual hardness at this distance from the water quenched face is about 420 $H_{K0.2}$.
As can be seen from the values in Table 4-5 is the measured carbide volume fraction decreasing with the distance from the water quenched face. From theory the values should be constant since the sample was re-austenitised at the same temperature. The measured variations show the experimental scatter that is based on the differences in the recognisability of the carbides in the surrounding matrix. As e.g. the volume fraction of bainite increases the contrast between martensite and carbides decreases what yields decreasing values.

The effect of the change in the microstructure can also be seen in the distribution of the measured hardness along the axis of the sample (Figure 4-23). Therefore the Knoop hardness was measured with a load of 200 g. These values can be compared directly to Vickers hardness values. For loads of 150 g and more, variations of only about 5 % can be found if comparing Vickers and Knoop hardness values [Mot56].
It can be seen that the hardness is highest near the face of the sample with a hardness between 950 and 1000 $H_{K0.2}$ showing a slight decrease till about 11 mm distance from the face where a hardness between 750 and 800 $H_{K0.2}$ is reached. Then the hardness decreases more significantly with increasing distance from the face. At about 15 mm distance the hardness approaches a value of approximately 420 $H_{K0.2}$ showing very little variations.
If the measured and the predicted hardness are compared, a very similar trend along the bar length can be seen. As the values are determined according to different standards, they cannot be compared by their absolute value. From the face to a distance of approximately 11,000 µm the values show nearly the same absolute value. For larger distances the predicted values are slightly higher than the measured values. According to the slower cooling at this position autotempering can occur, which changes the microstructure and therefore can reduce the hardness. The prediction does not include this effect and therefore yields higher values.

The Haralick texture parameters have been calculated for every image along the sample. A neural network was then trained to obtain a correlation between the parameters and the corresponding microhardness using every tenth micrograph to provide a representative

spectrum of the microstructure occurring along the sample axis. From the data calculated by the neural network for all positions a hardness trace was established and compared with both the measured hardness values and the values predicted on the basis of phase balance (Figure 4-24). The comparison shows that the values predicted from the phase fractions show a good correlation in the range of the hard microstructure to a depth of approximately 10,000 µm from the face. For higher distances the predicted values are higher than the measured values. As stated above this can be due to autotempering.

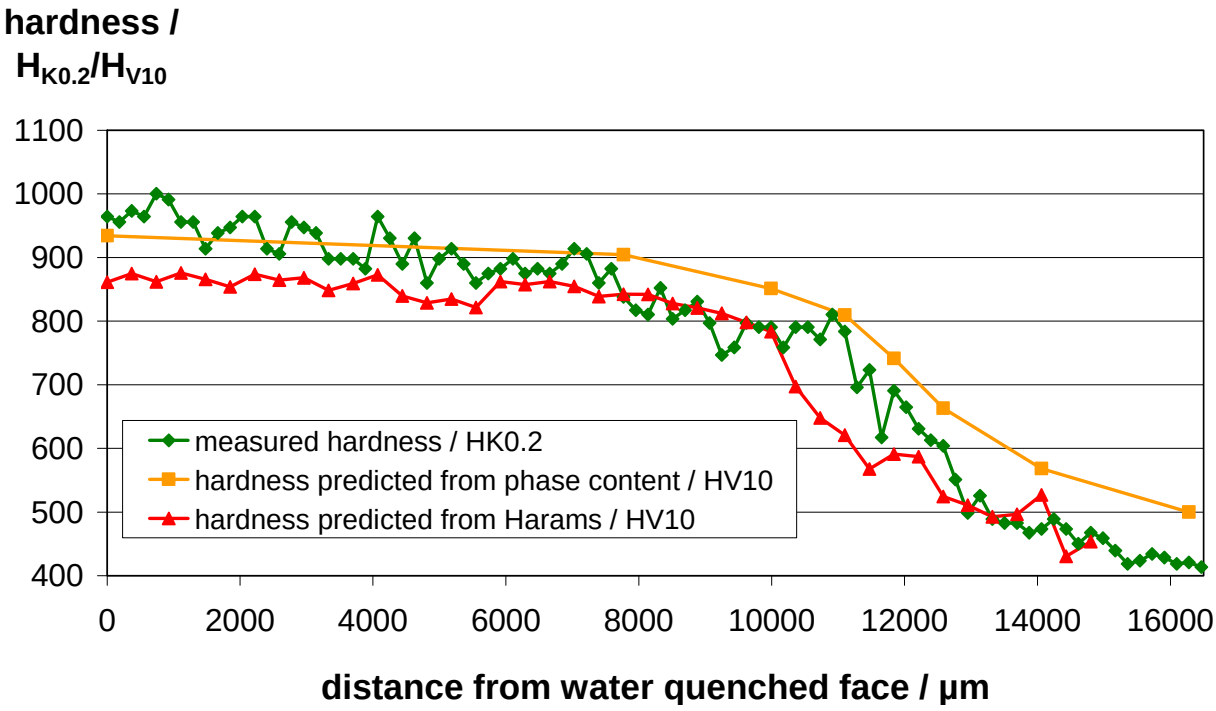

Figure 4-24 Comparison of microhardness variation along the Jominy end-quench specimen Jom100Cr6; measured Knoop hardness; predicted from the phase contents measured by quantitative optical microscopy; and predicted from the texture parameters using a trained neural network

For the values predicted from the 11 texture parameters according to Haralick described in section 2.2.2.3 it can be seen that in the range of the hard microstructure the values are slightly lower than the measured ones. From a distance of approximately 7,000 µm to 10,000 µm and from 13,000 µm and further from the face these value show a very good correlation with the measured values. Between 10,000 µm and 13,000 µm the predicted values are again lower than the measured values. In this range the micrographs show only

little variations in the volume fractions of the different phases while the hardness values show considerable variations. This range might therefore be represented too few in the data used for the training of the neural network compared to the changes in the corresponding hardness values what yields an insufficient correlation.
As the texture parameter can be measured automatically without user interaction this is a method giving a good possibility for a reproducible and objective prediction of mechanical properties.

4.5 Characterisation of steel microstructures using texture analysis

To simulate the complex microstructure of hardened steels often used in technical applications, samples have been bainitised (Figure 4-18). To produce differences of technical relevance in the microstructure, the re-austenitisation temperature has been varied. The aim is to establish this method for quality control of existing heat treatment processes or for the development of new processes.

4.5.1 Influence on the re-austenitisation on the microstructure

The variation in re-austenitisation temperature yields differences in the formation of austenite. As the re-austenitisation temperature increases the volume fraction of carbides and cementite left in the austenitic matrix decreases. This increases the amount of alloying elements (mainly carbon and chromium) in the austenite. These alloying elements increase the hardenability of the austenite making the formation of martensite rather than bainite more likely. As all this yields significant differences in the resulting mechanical properties, a quantification of these microstructures is essential. Due to the complex microstructure of hardened steels this is not possible with conventional methods of quantitative image analysis and makes other techniques necessary. The texture analysis after Haralick has therefore been tested for characterisation of these microstructures.

4.5.2 Influence of the microstructure on the Haralick parameters

The parameter Haram2 should show decreasing values with increased re-austenitisation temperature as more carbides dissolve. As has been seen in section 4.1 this parameter

decreases with a decreasing number density of bright phases, such as carbides, in a darker matrix. This is the case for increasing re-austenitisation temperatures where the number density and volume fraction of the optically resolvable carbides decreases. This can be seen for the Thermo-Calc predictions of this steel presented in Figure 4-21 and Figure 4-22 that above the eutectoid temperature the volume fraction of carbides decreases with increasing temperature. Additionally, with increasing temperature the austenite grain size will increase, increasing the hardenability by reducing the number of nucleation sites for bainite. The decreasing number of dark etching bainite sheaves in a bright matrix yields smaller differences in the grey values of adjacent pixels. Both effects give rise to a decrease in the parameter Haram2 with increasing re-austenitisation temperature. The same reasons cause the parameter Haram5 to increase with increasing re-austenitisation temperature.
The texture parameter Haram4 is expected to give the same trend as Haram2 with the re-austenitisation temperature. As re-austenitisation temperature increases, the volume fraction of coarse, light carbides present in the darker etched matrix decreases, the marginal-probability matrix is narrowed and therefore the value for the parameter is decreasing. Additionally the increased hardenability makes the formation of martensite than dark etching bainite more likely what decreases the value of the texture parameter Haram4. For a larger prior austenite grain size again the variation of the grey values in the micrograph decreases narrowing the marginal-probability matrix giving rise to a decrease of the parameter. But as stated before the parameter is etch-sensitive so that this effect superimposes the variations in the microstructure.

For the bainitic samples austenitised at different temperatures with the microstructure given in Figure 4-18 the texture parameters according to Haralick were measured. For 56 micrographs the parameters Haram2, Haram4 and Haram5 are shown exemplarily in Figure 4-25 together with the corresponding standard deviation.

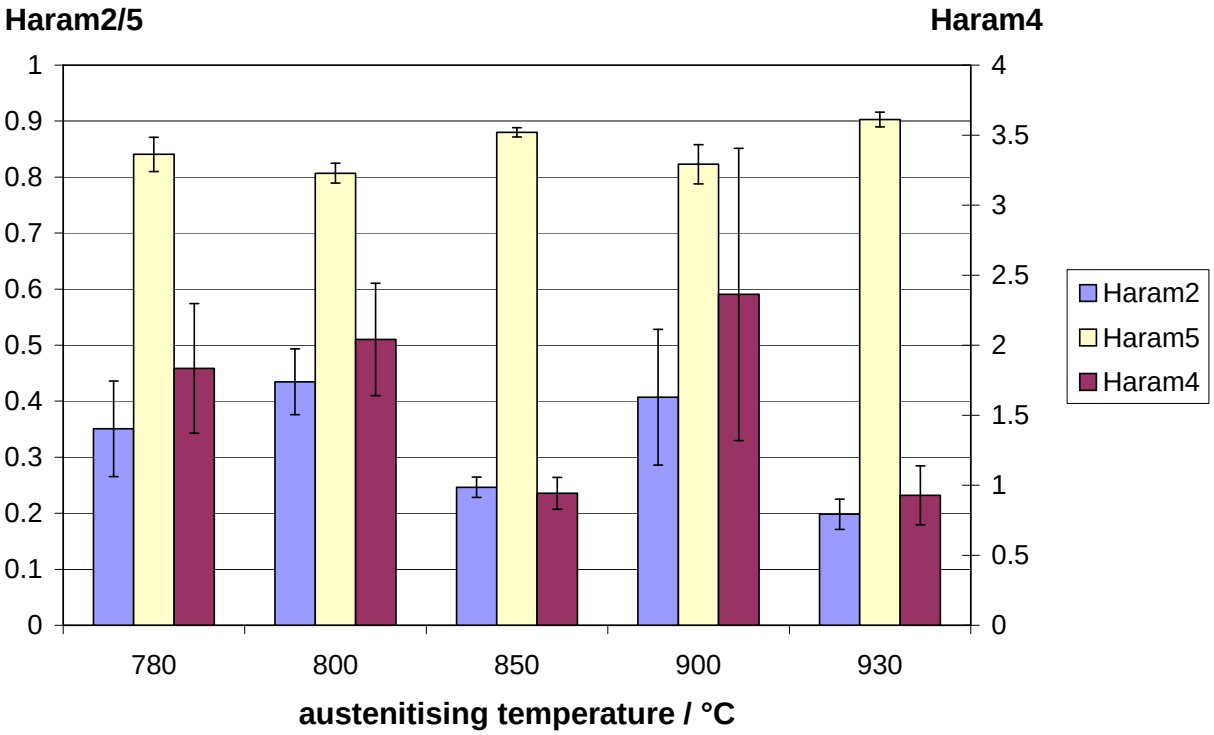

Figure 4-25 Influence of the austenitising temperature and therefore the microstructure on the texture parameters and the corresponding standard deviation at the example of Haram2, Haram4 and Haram5, measured at 56 optical micrographs of the bainitised 100Cr6 given in Figure 4-18; no direct correlation between the texture parameters and the austenitising temperature can be found

The parameters show variations with the austenitising temperature. However the trends of the parameters do not show a monotonic dependence of the parameters on the microstructure obtained by the bainitisation from different austenitising temperatures.

The parameter Haram2 does show an increase from the austenitising temperature 780 °C to 800 °C. Although the sample austenitised at 780 °C shows regions of dark etching upper and lower bainite in a brighter matrix, the number of bright-dark transitions between adjacent pixels is lower than for the 800 °C sample. In the latter sample a large number of darker etched positions can be found in the matrix together with a large number of very bright carbides.

For the sample austenitised at 850 °C the parameter decreases again. The matrix of the sample is etching much more homogeneously than the 800 °C sample as the needle-like structure is hardly resolvable in the optical microscope. Also the grey value difference to the carbides is

smaller, which results in a very large number of bright-bright pixel combinations in the GLCM and a lower contrast, i.e. lower texture parameter Haram2.
The value for 900 °C is increasing again to approximately the value that was found for 800 °C. This is also obvious for the microstructure. It is etching with higher contrast, i.e. the needles are much larger than for the 850 °C sample and show big differences in the grey levels of adjacent needles. The coarse alloy carbides remaining at this austenitising temperature are again clearly resolvable as they are significantly brighter than the matrix as is the case for the sample austenitised at 800 °C. The resulting contrast is the cause for the increase of the parameter Haram2.
The value at 930 °C is decreasing again and nearly as high as the value for 850 °C. Comparing the two microstructures shows similarities. Again the etching attack is relatively low compared to the other samples. The very large needles show only small differences in grey levels. Additionally almost no coarse alloy carbides can be found in the microstructure that could increase the contrast. This homogeneous distribution of the grey levels brings out the low value of the texture parameter Haram2.

A very similar trend can be found for the parameter Haram4. The most significant difference is that the absolute values are almost all higher than for Haram2.
The parameter Haram5 shows the opposite trend. It decreases with the austenitising temperature from 780 °C to 800 °C and increases again for 850 °C. The value for 900 °C is again lower than that for 850 °C. The value for 930 °C is again higher and comparable to the value at 850 °C.
From the standard deviations it can be said that significantly different values for the parameters Haram2 and Haram4 exist with the lowest values for the samples austenitised at 850 °C and the highest for the samples austenitised at 900 °C. Regarding the parameter Haram5 comparably low standard deviations can be found. Again for the 850 °C sample the lowest values can be found while for the 900 °C sample the highest values were measured.

4.5.3 Distribution of the texture parameters within a micrograph

For the local variations in the microstructure either due to chemical inhomogeneities or due to differences in the cooling conditions the variations of the texture parameters within a single micrograph were investigated. At a high magnification of 1000:1 a small area of 63 by 48 µm²

was investigated, which shows differences in the microstructure (i) in the carbide distribution, (ii) in the needles lengths, and (iii) in the bainite volume fraction. At this magnification several adjacent austenite grains are basis for the present microstructure. The characterisation of the small differences to be expected shall be tested to see if the method is capable of distinguishing these variations.

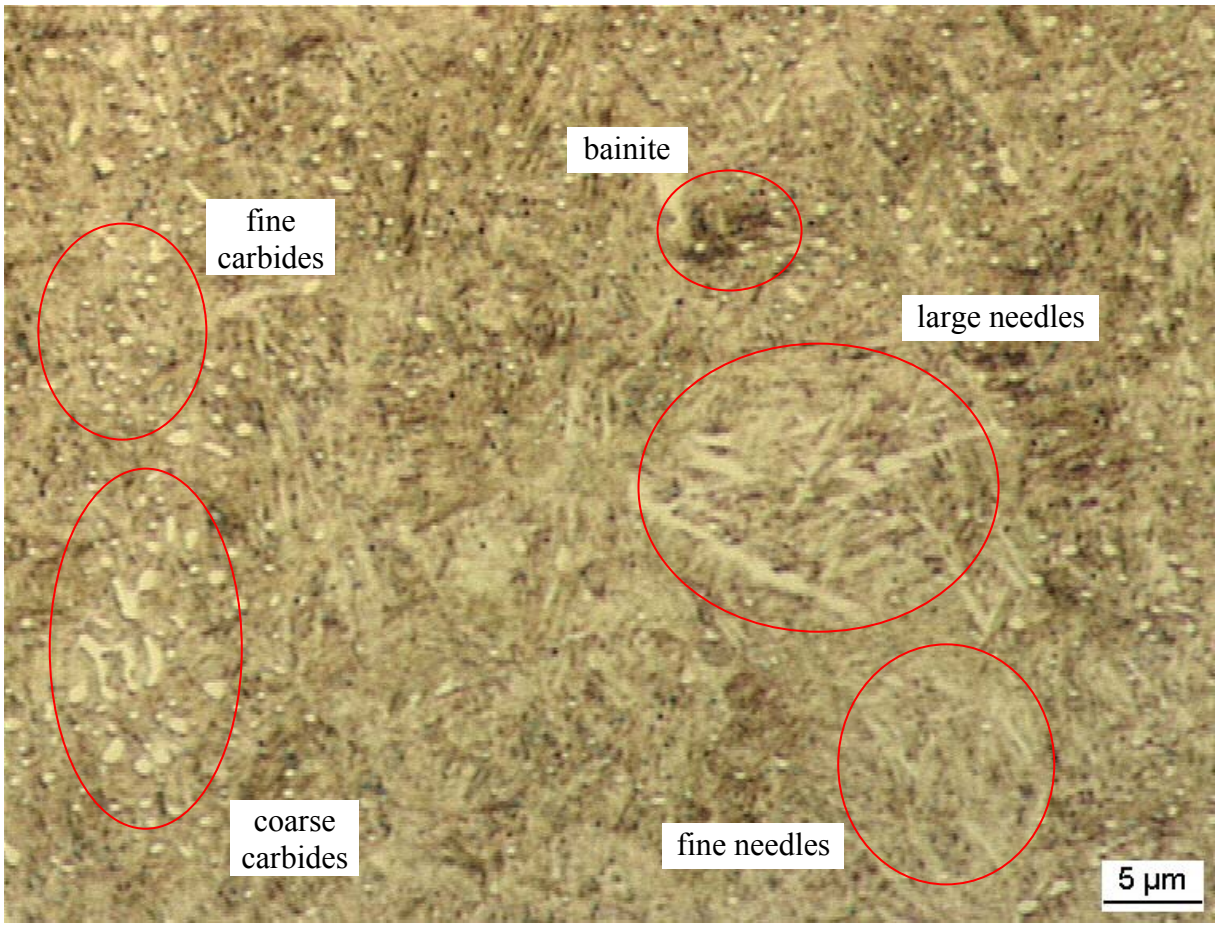

Figure 4-26 Micrograph of the sample b100Cr6_850 used to determine the variation of the texture parameters within a single micrograph, divided into 432 square regions (etched with 2 % nital)

To check the local variations of the texture parameters the distribution of the Haralick parameters within a single micrograph was determined by dividing the image into rectangular sections. This was done for 3 characteristic micrographs. As an example a micrograph taken at a magnification of 1000:1 of the bainitic sample b100Cr6_850 in Figure 4-26 is presented. As can be seen the microstructure is not totally homogeneous over the micrograph, which

give differences in the texture parameters that may allow differentiation of different microstructural features in the image. The Haralick parameters were measured using the image analysis system KS400 for each of the 432 regions in the image at a separation of 1 pixel and the distribution was plotted.

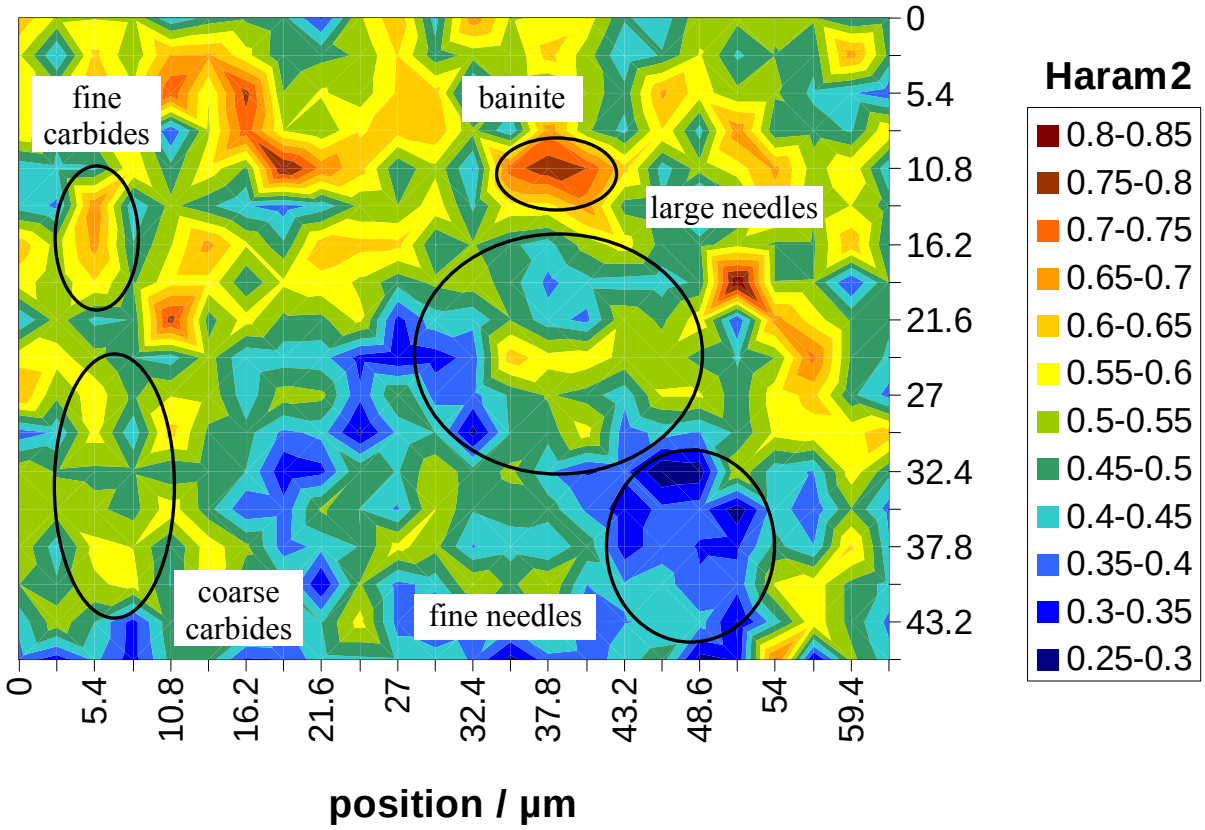

Figure 4-27 Distribution of the texture parameter Haram2 with a separation of 1 pixel over 432 sections of the micrograph shown in Figure 4-26

The micrograph used for this investigation shows local variations of the microstructure, which are representative of the available samples. There are sections in the lower left area that show the presence of very large carbides whilst towards the middle left there is a higher number density of finer carbides. In the other sections of the micrograph the bainitic matrix shows a more plate-like microstructure again with varying sizes and number densities.

All the texture parameters showed variations in their value over the examined image. The spatial distribution of the texture parameters is exemplarily shown for the parameter Haram2 in Figure 4-27 for the micrograph in Figure 4-26.

For the parameter Haram2 a strong dependence of the parameter on the microstructural features can be found. Especially the dark etching regions showing bainite in the martensitic matrix yield relatively high values due to the large differences in grey values between the adjacent microstructural features. The measurement gives a relatively low parameter for the region showing the fine needles. This is due to the weak development of the details in this region. The nearly uniform grey value shows only very small differences between adjacent pixels, which in turn results in a comparably low value for Haram2. The regions rich in both fine and coarse carbides show an intermediate value for this parameter. The differences in grey value of the very bright carbides to the matrix are huge, so that the corresponding GLCM shows more entries far away from the main diagonal than is measured for the matrix.

All the 11 texture parameters show a more or less pronounced correlation to local variations of various microstructural features.

4.5.4 Influence of the metallographic preparation on the texture parameters

The standard method for the metallographic preparation of the samples for texture analysis was by mechanical grinding and polishing together with chemical etching in 2 % nital. To verify if the quality of the etching required for texture analysis may be achieved by electrolytical polishing these two methods were compared in their results. Therefore, a sample of 100Cr6 re-austenitised at 850 °C and bainitised (b100Cr6_850) was metallographically prepared using the two different techniques.

Mechanical preparation

Mechanical preparation, which includes grinding and polishing, was carried out according to the method described in Section 3.2.2.3. An overview image of the microstructure is given in Figure 4-28 together with two representative micrographs.

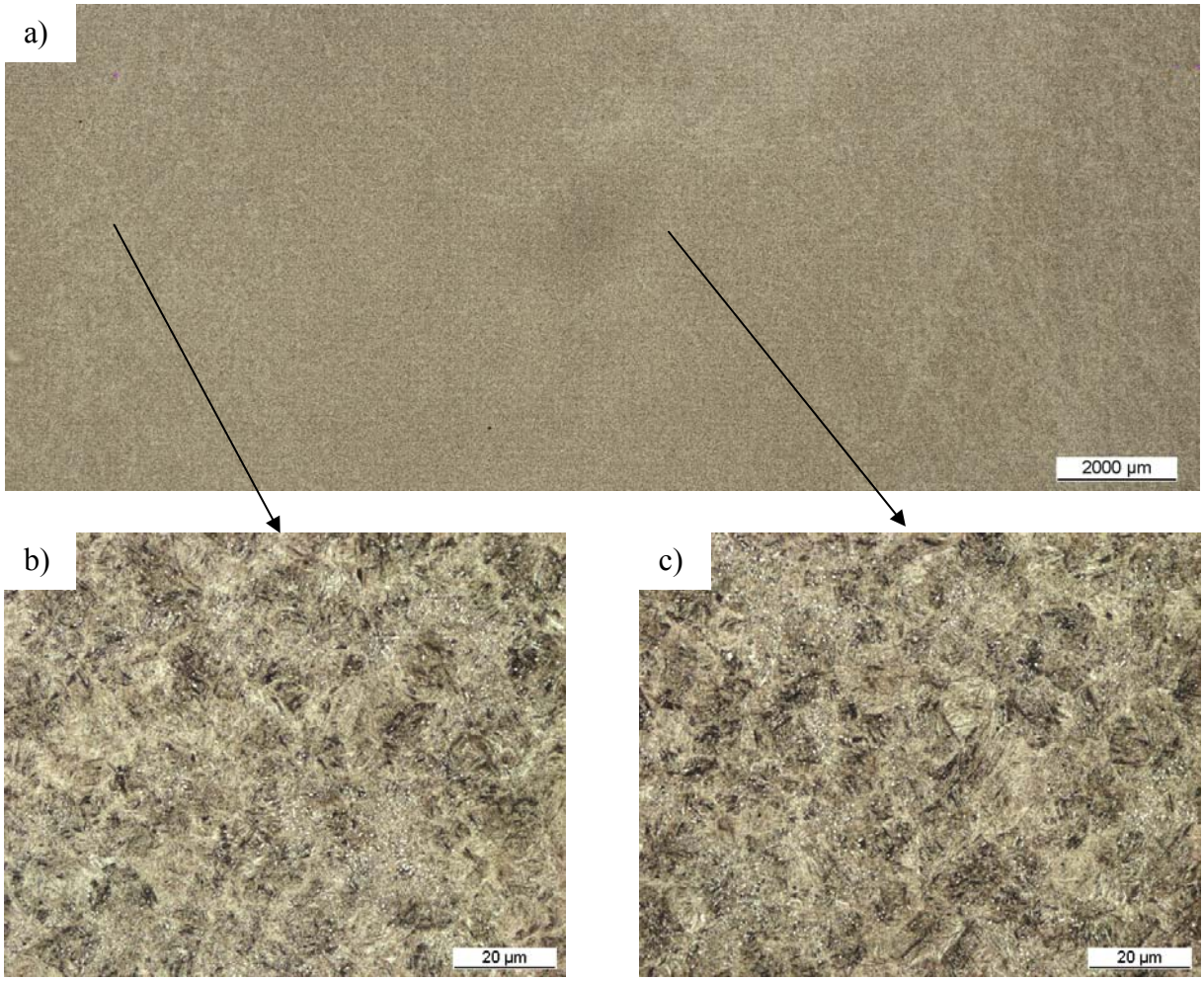

Figure 4-28 Result of the mechanical grinding and mechanical polishing of the bainitised sample b100Cr6_850 at a magnification of 500:1, etched with 2 % nital

a) overview image obtained by the Mosaix function of KS400

b) micrograph from the edge of the sample

c) micrograph from the core of the sample

From the overview image in Figure 4-28 (a) can be seen that both the microstructure and the preparation show only very limited variation over the examined sample area. This also proves to be true if the micrographs (b) and (c) are compared. Almost no difference in the appearance of the microstructure can be found over the surface of the sample. Neither a variation in the absolute grey level can be found, nor a variation in the grey level differences as would both influence the texture parameters.

Electrolytical preparation

For electrolytical polishing the sample was ground using SiC paper to 1200 grade and thoroughly cleaned with ethanol. Right after this cleaning the sample was polished electrolytically with the electrolyte A3 [Str04b, Str04c] for 10 s at 60 V with a flow rate of 13 and an electrolyte temperature of 22 °C. Subsequently the sample was again cleaned with ethanol and then etched with 2 % nital to reveal the microstructure.

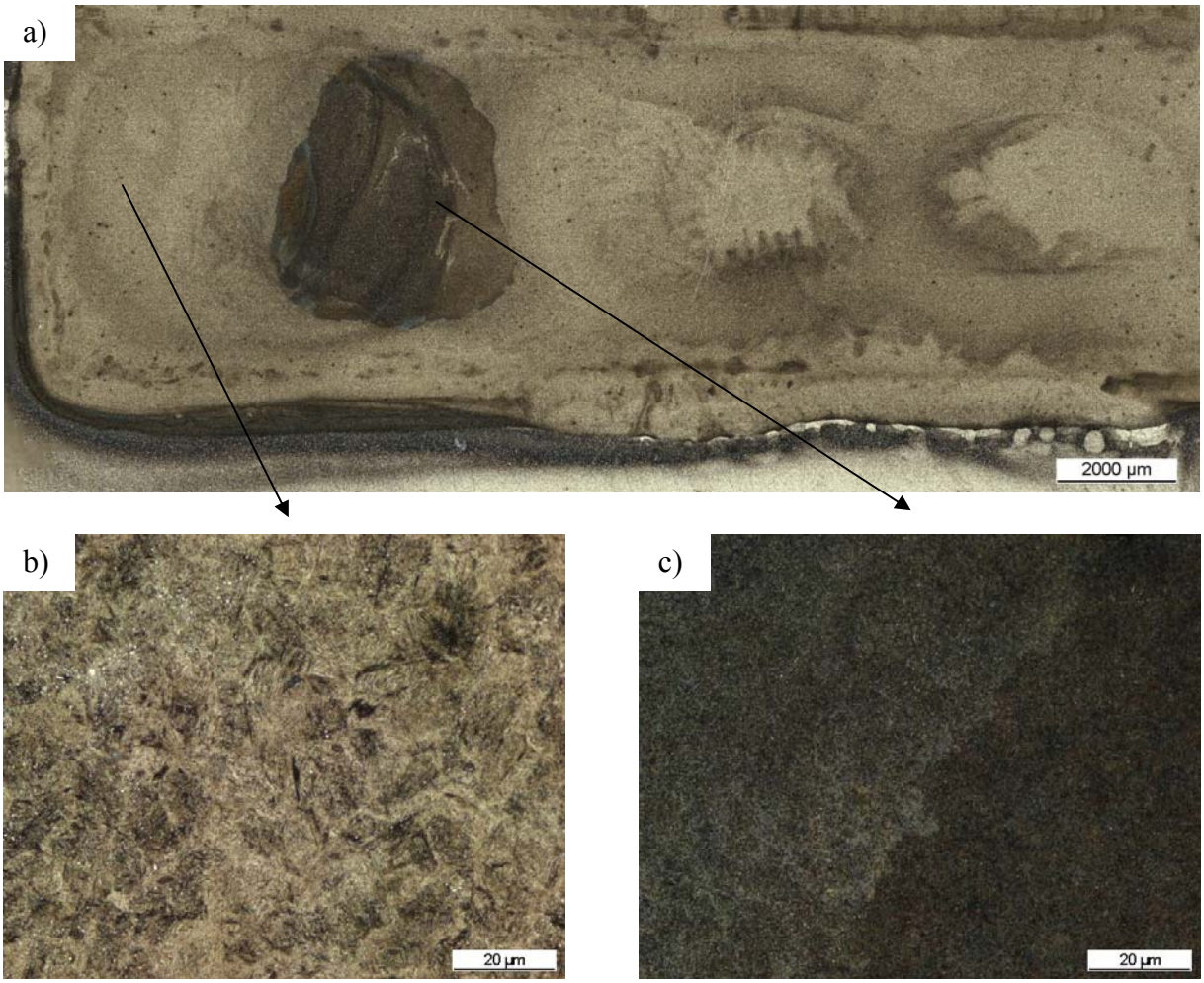

Figure 4-29 Result of mechanical grinding and electrolytical polishing of the bainitised sample b100Cr6_850 at a magnification of 500:1, etched with 2 % nital

a) overview image obtained by the Mosaix function of KS400

b) micrograph from the edge of the sample

c) micrograph from the core of the sample

As can be seen from the micrographs obtained after electrolytical preparation, this method is more heterogeneous than mechanical polishing and etching and therefore is not suitable for the quantitative analysis of the microstructure. The following experiments have all been made using mechanically prepared samples.

4.5.5 Variation of the separation

Optical micrographs

Haram texture calculations were carried out on the bainitic images in the same way as for the example images. The separation for determination of the texture parameters was varied in the same way. The results of the measurement for the micrographs presented in Figure 4-18 are shown exemplarily for the parameter Haram2 in Figure 4-30.

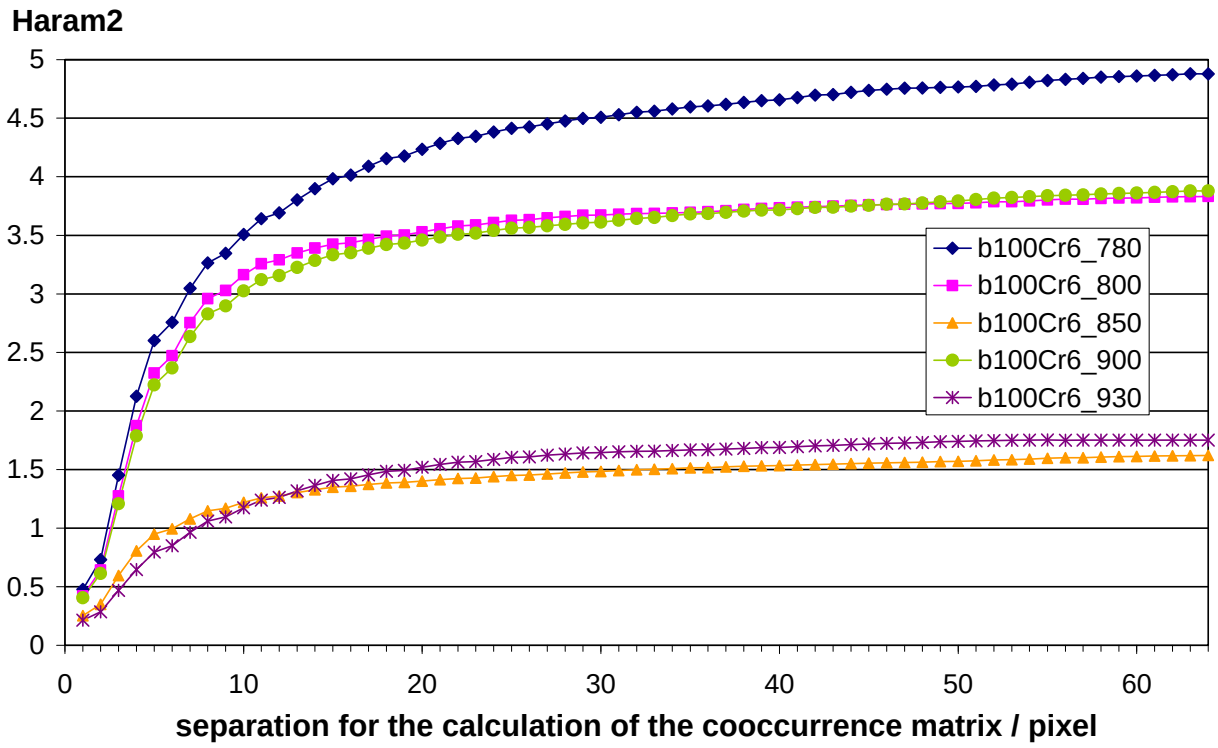

Figure 4-30 Influence of the variation of the separation between inspected pixels on the texture parameter Haram2 for the optical micrographs of the bainitic samples in Figure 4-18

For these bainitic micrographs basically the same trend can be found as for the example images. For the parameter Haram2 (Figure 4-30) the values are increasing with increasing separation approaching a constant value at a separation of about 20 to 30 pixels. The trend of the values are very similar showing small deviations as can be found for the examples image with the perpendicular lines (Figure 4-3). The only differences between the micrographs can be found in the absolute values. While the micrograph of the sample b100Cr6_780 produces the highest values for the parameter Haram2, the samples b100Cr6_850 and b100Cr6_930 show nearly the same relatively low values. The other two samples show nearly the same, intermediate values.

These values can be related to microstructural features. For the 780 °C sample a high volume fraction of dark etching bainite can be found in a relatively bright martensitic matrix. In this bainitic regions bright alloy carbides can be found. Due to the large differences in grey values that can be found for many neighbourships between the examined pixels the value is very high for this micrograph. There are many neighbourships of pixels in the black and pixels in the white region, which means that there are a high number of transitions far away from the main diagonal of the GLCM, which causes a high value of the parameter Haram2.

For the micrographs of the samples austenitised at 800 °C and 900 °C the microstructure consists of bainite with a needle-like structure. Due to differences in etching behaviour these show different grey values in the micrograph but the differences are much smaller than for the 780 °C sample. This means that the elements in the GLMC are located in the region of white-white transitions. The carbides that are still brighter than the matrix and therefore give some high contrast transitions in the images. But more important is that most of the transitions are located quite close to the main diagonal of the GLCM and therefore yield a low contrast.

For the micrographs b100Cr6_850 and b100Cr6_930 the obtained contrast expressed by the texture parameter Haram2 is even less. The micrographs show again a needle-like structure but the range of grey values occurring in the image is even smaller than for the previous two images. Also carbides can hardly be differentiated from the matrix. This means that the values can be found in the region of the white-white transitions of the GLCM and are all located very close to the main diagonal of the GLCM giving a very low texture parameter Haram2.

As has been seen for the example images, the absolute values of the parameters depend on the grey value characteristics. A shift in the histogram will cause changes in most of the texture

parameters. Since the micrographs are quite different in their brightness and so in their histogram, the GLCM will also show differences, which will then influence the texture parameters. This can also be seen in section 4.5.3 where the local variations of the texture parameters within a micrograph are presented.

For the other 10 Haralick texture parameters the same analysis was performed. For most of the parameters a strong dependence of their absolute value on the separation can be found. For all of them only very small variations can be found with separation. This can already be seen for the parameter Haram2 in Figure 4-30. Like this parameter none of them shows very distinct local extreme values.
The parameter Haram2 representing the contrast after Haralick [Har73] shows a strong correlation with the overall grey level in the image, which is linked to the volume fraction of dark etching phases. This is due to the differences in the grey values occurring between the respective images. Other parameters show different absolute values that are linked to other microstructural features.
For the parameter Haram4 for example very few differences can be found in the micrograph with varying separation whereas the absolute value shows a strong correlation to the respective image and is linked to the contrast as the parameter Haram2 is. This behaviour could also be seen for the example images in Figure 4-8.
For the parameter Haram5 a decreasing trend can be found for increasing separations. Unlike the example images (Figure 4-4) this parameter for the bainitised samples shows a very uniform trend with nearly no local extreme values. Again the absolute values differ between respective micrographs and, as for parameter Haram2, they are linked with the contrast in the micrograph.
A totally different correlation to the absolute value can be found for other parameters, e.g. Haram3 (correlation), which is not directly linked to the overall grey level in the image.

To investigate the influence of the variation of separation on the correlation with the heat treatment parameters, the texture data with and without the carbide information was used to predict the austenitising temperature of the bainitised samples using a neural network. For calculation of the variation with separation a neural network was used with 11x64 neurons in the input layer and a hidden layer of 7 neurons as also used for the data with a separation of 1

pixel. This geometry of the neural network was proved in previous work and showed good results for the correlation of texture data with processing parameters or mechanical properties [The98, Sch99].

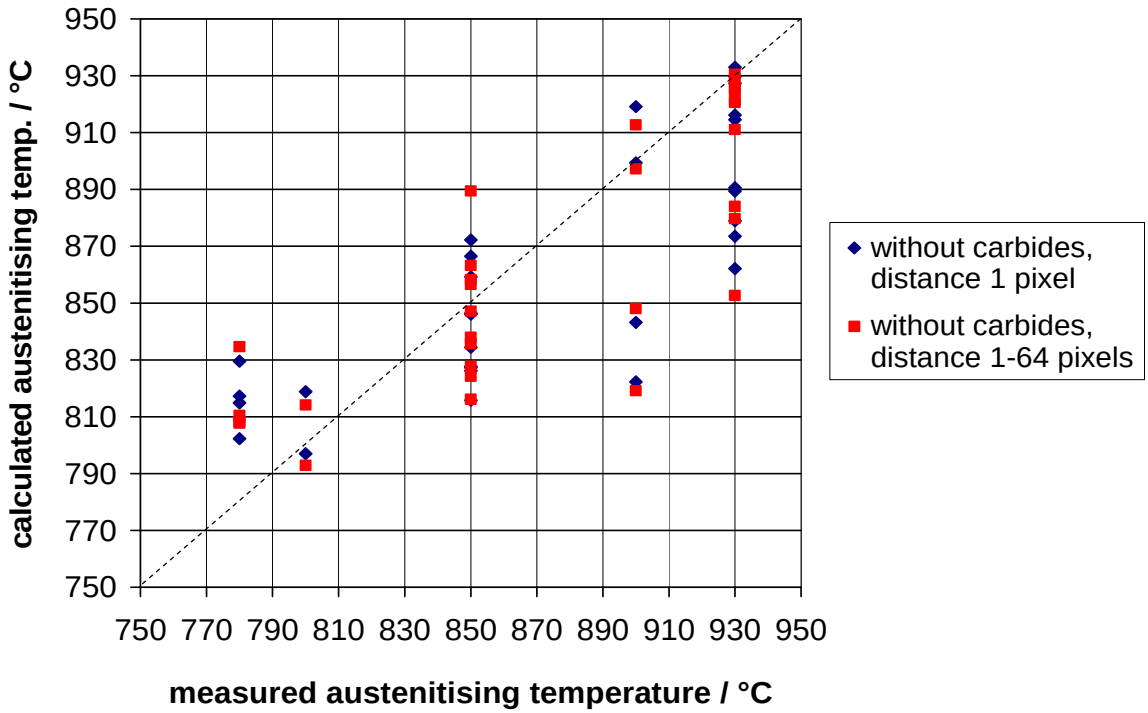

Figure 4-31 Correlation of the measured austenitising temperature and the temperature calculated from the texture parameters with a separation of 1 pixel using a neural network; 30 micrographs analysed

In Figure 4-31 the correlation of the measured austenitising temperature is shown with the values calculated by the neural network. To train the network the texture parameters of 31 micrographs were used together with the corresponding austenitising temperature. The calculation was done with 30 micrographs of the same samples not involved in training the network. Initially, only the texture parameters for a separation of 1 pixel were used in the calculation. In the second run for all 31 micrographs the 11 texture parameters for separations between 1 and 64 pixels were used to train the neural network. Again for the same 30 micrographs the austenitising temperature was calculated as before and is presented along with the other values in the diagram.

Table 4-6 Mean value and standard deviation of the difference between the calculated values and the nominal values of the correlation of the austenitising temperature with a constant separation of 1 pixel and with the information of the separations between 1 and 64 pixels together with the respective geometry of the neural network

separation	geometry of neural network			mean value	standard deviation
	neurons in input layer	neurons in hidden layer	neurons in output layer		
1 pixel	11 x 1	7	1	-10.6	32.2
1-64 pixels	11 x 64	7	1	-8.0	31.6

Regarding the correlation it is obvious that for both measurements the values calculated for the austenitisation at 780 °C are too high while for 930 °C as the highest temperature the calculated values are too low. In Table 4-6 the characteristic values of the two analyses presented in Figure 4-31 can be found. As the mean values are both negative that means that most of the calculated values are lower than they nominally should be. Regarding the two variants the analysis with a separation of 1 pixels shows the lower value and therefore the higher variation between the measured and the calculated values. For the standard deviation the effect is the same. While for a separation of 1 pixel the standard deviation is 32.2; this value decreases to 31.6 for the analysis with various separations.

The fact that for the lowest re-austenitisation temperature of 780 °C the values calculated from the neural network are higher as the measured values can be attributed to the microstructural constituents present for this heat treatment. Compared to the higher re-austenitisation temperatures ferrite is present additionally to bainite and carbides which can also be found for the higher re-austenitisation temperatures.

SEM micrographs

The variation in separation for the calculation of the texture parameters was carried out for the SEM micrographs in the same way as for the optical micrographs in the previous section. The secondary electron micrographs of the bainitic specimen given in Figure 4-20 were used for the following examinations.

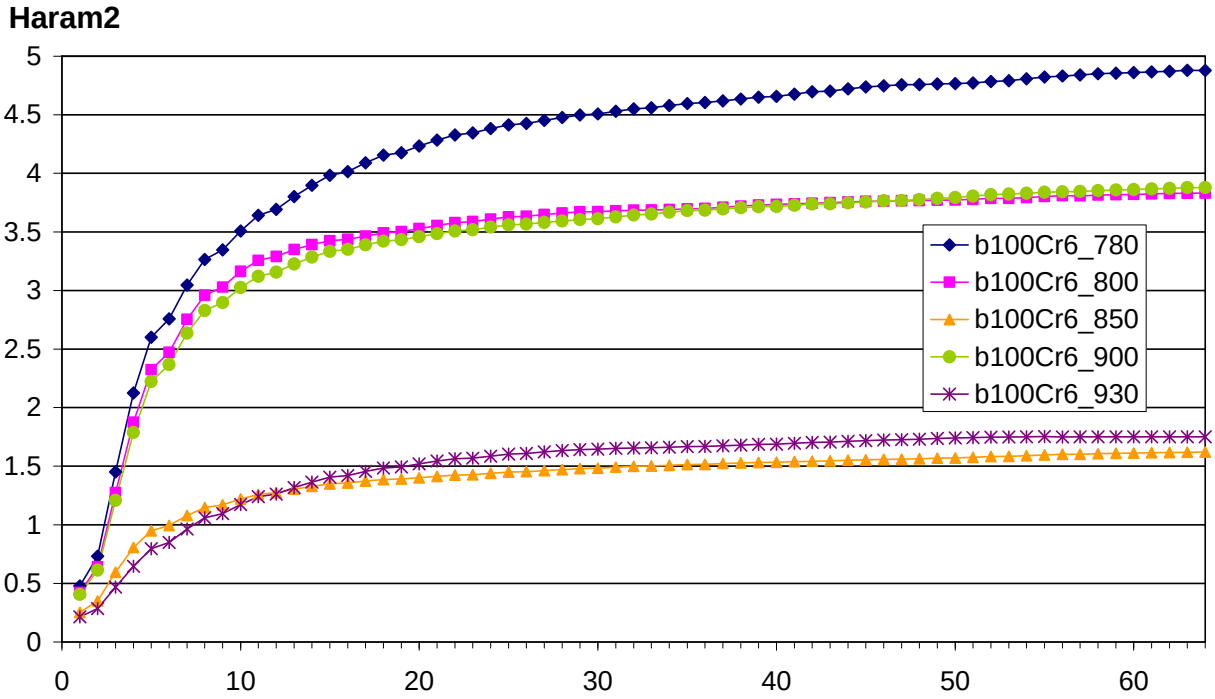

a)

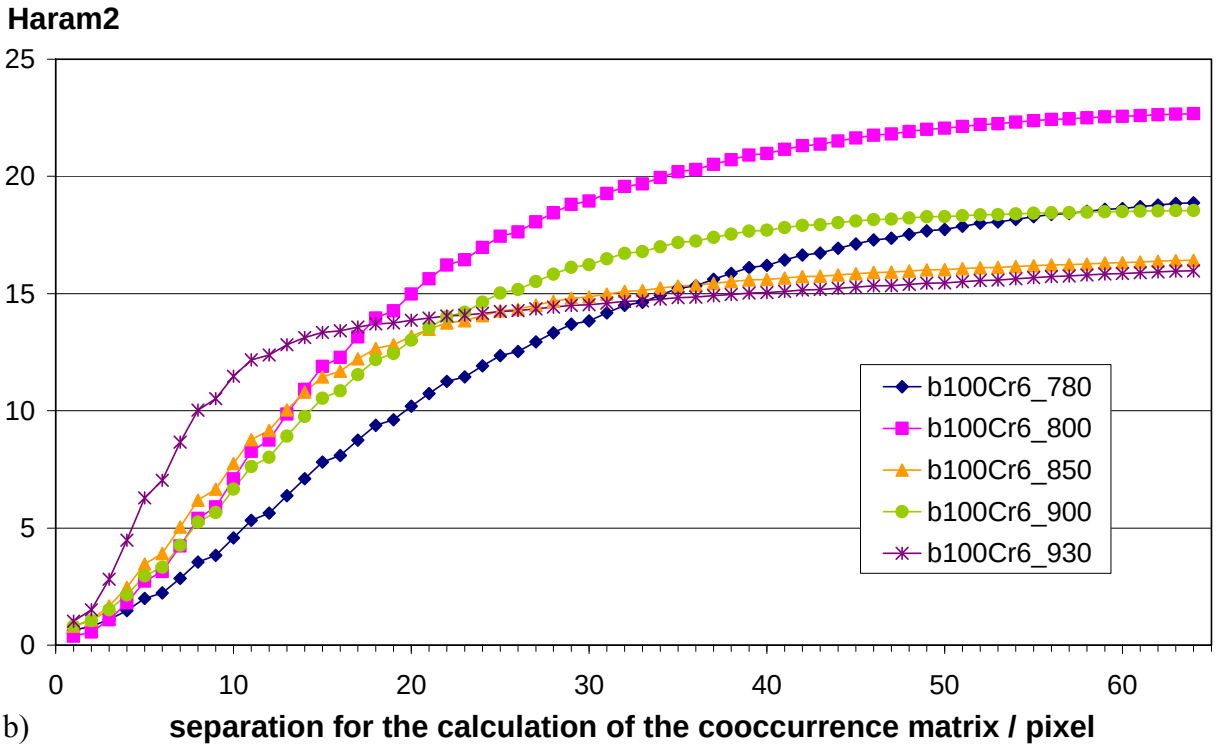

b)

Figure 4-32 Influence of the variation of the separation between inspected pixels on the texture parameter Haram2 for micrographs of the bainitic samples obtained from

a) the optical microscope (Figure 4-18)

b) the SEM (Figure 4-20)

These images were analysed with a variation in separation of the inspected pixels as in section 4.1 for the example images and the optical micrographs of the same samples. The separation was also varied over the same range to obtain comparable results from the two measurements. As an example the results of the measurement are shown for the parameter Haram2 in Figure 4-32.

The trend of the values for the SEM micrographs is similar to that of the optical micrographs. One difference is that the curves of the SEM measurements cross, whilst the curves of the optical micrographs do not. A differences in the source of contrast can be found for optical and SEM micrographs. These differences are discussed along with the scale of the images, i.e. different pixel sizes, in section 5.2.5.

For low separations low values can be found. With increasing separation the values are increasing significantly approaching a constant value. What is obvious is that the values obtained from the SEM micrographs are significantly higher in their absolute values compared to the values obtained from the optical micrographs (Figure 4-30). Additionally the shape, i.e. the slope, is also different for optical and SEM micrographs.

The micrograph of the sample austenitised at 780 °C shows the lowest values for separations up to about 30 pixels. For bigger separations the slope decreases slowly but the value is still increasing. For the higher temperatures very similar trends for the parameter Haram2 can be found that are only different in the increasing absolute values for the different austenitising temperatures, namely in the order b100Cr6_850, b100Cr6_800 and b100Cr6_900. The 930 °C sample shows a fast rise with the separation. For separations in the range between 10 and 15 pixels the slope is decreasing significantly but values are still increasing with increasing separation. Compared to the measurements for the optical micrographs do the curves cross for the SEM micrographs. This is due to the additional details that are revealed using the SEM what in turn causes more local variations of the texture parameters with increasing separation of the adjacent pixels for the calculation of the GLCM. As comparable structures in the SEM micrographs are bigger in terms of pixels, the texture parameters show an increase of the values up to higher pixel separations than for the optical micrographs.

For the micrograph of the sample austenitised at 780 °C (Figure 4-20 (a)) comparatively low values can be found for the parameter Haram2 at low separations. This indicates that the outlines of the objects in the image are blurred as a blurring yields a homogenisation of the

grey value distribution in the image. The respective GLCM shows an increased number of pixels with adjacent pixels in the same or very similar grey values. Therefore the parameter Haram2 yields lower values than it would for images that are in focus and therefore would show increased contrast. This assumption proves true when the micrograph is regarded (Figure 4-20 (a)). The microstructure is comparatively coarse and appears blurred. Also within the objects, e.g. the carbides, a gradient of the grey value can be found, i.e. some of the carbides show a bright margin around the darker core. Surely this would increase the value of Haram2 and offset the effects of lack of focus to some extent.

For the sample b100Cr6_800 the micrograph appears much sharper (Figure 4-20 (b)). Additionally the microstructure is much finer and therefore shows more bright-dark transitions in the GLCM leading to higher contrast value, which result in a higher parameter Haram2 for separations over 20 pixels. For smaller separations the measured values are comparatively low since a large number of pixels with neighbours in a similar grey value can be found. With increasing separation, pixels within an object and neighbouring pixels in the matrix are taken to calculate the GLCM which yields an increasing contrast due to the different grey values of object and matrix and hence an increase of the parameter Haram2.

The micrograph of the sample austenitised at 850 °C (Figure 4-20 (c)) again shows a finer microstructure than for the previously discussed samples. This has resulted in a smaller difference in grey value between adjacent objects than for the 800 °C sample, e.g. the carbides appear quite dark compared to the surrounding matrix whereas for the 800 °C sample at least some carbides are clearly brighter than the matrix.

For the 900 °C sample (Figure 4-20 (d)) the microstructure is again coarser showing an acicular structure. Between these needles very dark areas can be found so that the needles can be separated easily. This also enhances the number of bright-dark transitions in the GLCM, which then yields an increase in the texture parameter Haram2. The micrograph of the 930 °C (Figure 4-20 (e)) shows a very fine and feathery microstructure. This gives very high numbers of bright-dark transitions for short separations, which results in a sharp increase of the parameter Haram2 for separations up to 10 pixels. This is about the size of the feathery structure of the bainite in the micrograph. For larger separations the probability of finding a combination of pixels with such high grey value differences decreases. As for the 850 °C sample the microstructure shows only small differences in the overall variation of the grey value, i.e. the carbides have a grey value very similar to that of the matrix. Since in this case

the probability of finding pixels with high grey value differences is very low for large separations, the parameter Haram2 shows very low values at large separations.

Regarding the slope, the variation of the separation yields a slower increase of the texture parameter Haram2 for the SEM micrographs than for the optical micrographs except for the 930 °C sample that show a steeper slope for the SEM images and the 850 °C sample that shows a comparable slope. The lower slope depends on the differences in the image acquisition method and the resulting revelation of the microstructural features. The discussion above outlines the variation in overall grey level and its variation with separation. As well as the long range difference in grey level for the same specimens imaged optically and by SEM, Figure 4-27 shows more rapid rises in the value of Haram2 as the re-austenitisation temperature increases so that the curves in Figure 4-32 (b) cross, whilst they are parallel for the optical images (Figure 4-32 (a)). This may be due to the different resolution and contrast generation for the two techniques. The use of higher re-austenitisation temperatures causes a decrease in the scale of the microstructure, which can be resolved at the pixel level by SEM, but not by optical techniques. In addition, the scale of the carbides is also reduced by increased re-austenitisation temperatures, which can be detected more readily by SEM than by optical techniques. Combining these, the parameter Haram2 will rise more rapidly for samples re-austenitised at higher temperatures at low separations for SEM images, before plateauing out at a lower overall value, when the same behaviour is shown between the relative parameter values for optical and SEM techniques.

Parameter Haram4 is sensitive to volume fraction, but not the distribution of the phases, which is borne out as there were only very small differences in this parameter with variation in the separation as already seen for the optical micrographs and the example images (Figure 4-8). The absolute values for Haram4 derived from SEM results are much higher than those obtained from optical techniques. For optical micrographs the values of the parameter Haram4 are in the range between 0.85 and 2.6, whilst the values for the SEM micrographs are in the range between 10.05 and 12.2. For the SEM micrographs (Figure 4-20) very large differences in the grey levels of the microstructure can be found. While the alloy carbides are in general relatively bright, the bainitic matrix consist of both bright and very dark regions with the bright regions representing the bainitic ferrite and the dark regions the retained austenite /

martensite or carbides between the sub-units [Bha01]. The micrograph of the sample austenitised at 800 °C shows the highest value of Haram4, which is related to the high fraction of very bright microstructural features combined with very dark regions, i.e. a relatively high volume fraction of carbides remaining in a fine bainitic matrix. This causes a widespread marginal-probability matrix and therefore high values for the parameter Haram4. The micrograph of the 780 °C sample shows comparable values, which would be expected as the microstructure contains a high volume fraction of undissolved carbide, which increases the proportion of light pixels. However, this will be offset by the retention of ferrite and the lower proportion of bainite in the matrix. The effect of the change in matrix is to reduce the proportion of light-dark pixel combinations and so reduces the value of Haram4. The micrographs for the other re-austenitisation temperatures show lower maximal grey values.

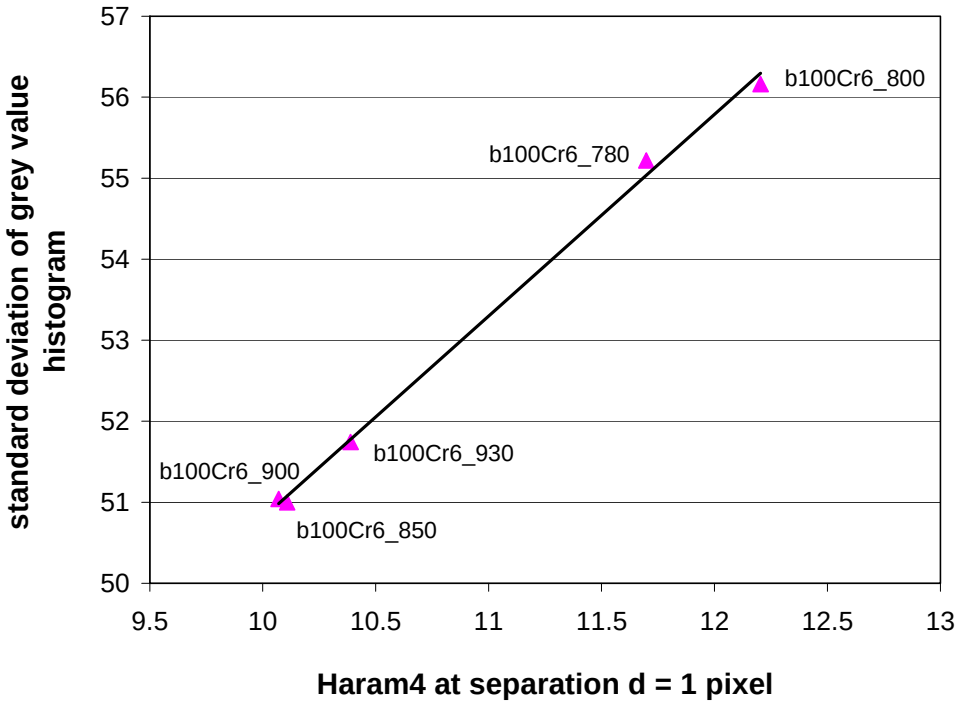

Figure 4-33 Correlation of the texture parameter Haram4 at a separation of 1 pixel with the standard deviation of the respective grey value distribution for the SEM micrographs of the bainitised 100Cr6 (Figure 4-20)

This narrows the marginal probability matrix and therefore produces a lower Haram4 value. This can also be seen clearly in the standard deviation of the grey value distribution of the micrographs. If these values are correlated with the texture parameter Haram4, a linear

relation between the values can be found (Figure 4-33). Thus the highest measured Haram4 of 12.2 correlates with a standard deviation of 52.2 of the corresponding grey value distribution. In contrast to this the lowest Haram4 of 10.1 correlates with a standard deviation of 51.0. The general trend would suggest that Haram4, in this case, is following the volume fraction of carbide, subject to the comment above regarding re-austenitisation at 780 °C.

For the parameter Haram5 a decreasing trend with increasing separation was measured for the SEM micrographs as for the optical micrographs and the example images (Figure 4-4). Compared to the optical micrographs the absolute values are slightly lower but they also do not show significant local extreme values as can be found for the example images.

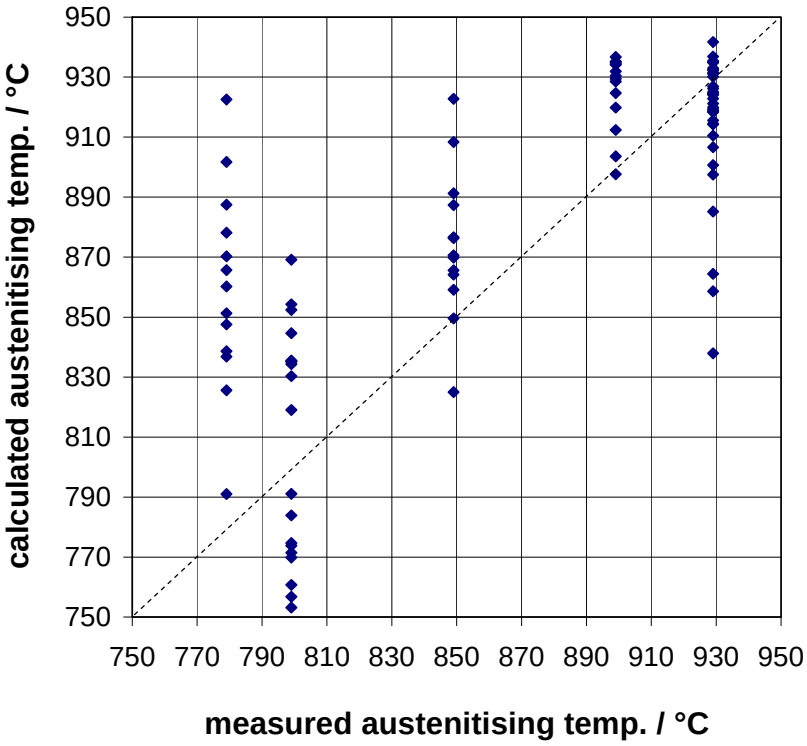

Figure 4-34 Correlation between the austenitising temperature applied during heat treatment and calculated from the texture parameters at a separation of 1 pixel determined from the SEM images presented in Figure 4-20; 103 micrographs analysed

The analysis of the SEM micrographs using the texture parameters as input values and the corresponding austenitising temperature as output value to train the neural network gives a correlation (Figure 4-34) with greater scatter than that obtained for the same analysis using

optical micrographs (Figure 4-31). To characterise the correlation the difference between the measured and the corresponding calculated values was analysed. The mean value of this difference yields a value of 4.0 and therefore shows a good overall congruence of the values. The standard deviation however is comparably high with a value of 59.7. This means that over all the values the fit is relatively poor due to the high scatter of the values.

4.5.6 Influence of the geometry of the neural network

To test the influence of the geometry of the neural network on the correlation with properties, the same data were used with different networks. The data from the optical micrographs given in Figure 4-18 were used in the form of the texture parameters measured at different separations between 1 and 64 pixels. The networks contain 704 neurons in the input layer for the texture parameters (11 texture parameters at 64 different separations each). The output neuron in both cases contains the austenitising temperature. The difference between the networks is the hidden layer containing 7 neurons in the first case and a matrix of 7x7 neurons in the second case. The correlation obtained by the different neural networks is presented in Figure 4-35.

Comparing the results of the two networks shows only small differences. For the lowest temperature the calculated temperature is higher than the measured one, but, as commented on above, the different microstructural mix for this sample results in different behaviour with respect to the values of the Haram parameters. The lowest two fully re-austenitised samples give scatter bands for the calculated temperatures which are centred around the measured value.

For the two highest temperatures the scatter bands for the calculated values are centred around values below the measured values. Both networks show considerable scatter, which is lower for the two lowest re-austenitisation temperatures, but shows little dependence on the neural network geometry. This is shown in the mean values of -8.0 and -8.7 for the difference between the calculated and the corresponding nominal values (Table 4-7). The standard deviation also shows only slight differences.

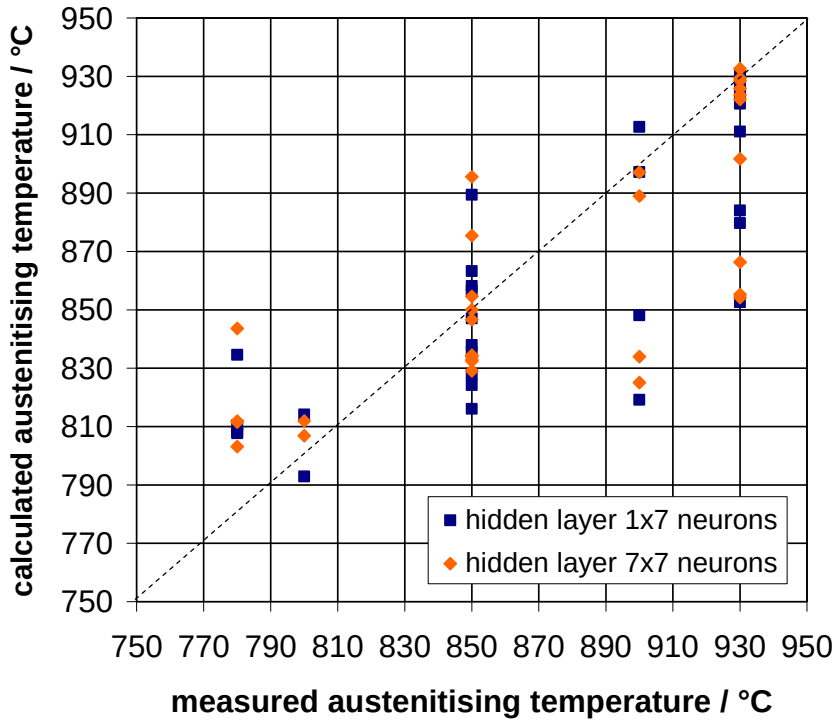

Figure 4-35 Influence of the geometry of the neural network on the correlation of the texture parameters measured at separations between 1 and 64 pixels for the optical micrographs of the bainitised 100Cr6 with the austenitising temperature; 30 micrographs analysed

Table 4-7 Mean value and standard deviation of the difference between the calculated values and the nominal values of the correlation of the austenitising temperature with separations between 1 and 64 pixels and neural networks with different hidden layers

hidden layer	mean value	standard deviation
1x7 neurons	-8.0	31.6
7x7 neurons	-8.7	34.9

4.5.7 Combination of the texture analysis with the characterisation of coarse, alloy carbides

As seen in section 4.5.2 the characterisation of bainitised microstructures is not always possible by texture analysis due to the similarity in the Haram parameters (Figure 4-25)

obtained from different microstructures. Therefore a method has to be found to be able to characterise even these very complex microstructures reliably. For the hypereutectoid steel 100Cr6 coarse alloy carbides are a good quantitative means to describe the prior heat treatment and especially the re-austenitising temperature. In addition to the texture analysis these data could help to clearly quantify and therewith characterise the microstructure.

4.5.7.1 Characterisation of coarse, alloy carbides

To investigate the dependence of the carbides on the austenitising temperature, the dilatometer samples with pearlitic microstructures were characterised along with the bainitic samples. To characterise the carbides EDS has used to determine the chemical composition. This was already presented in Figure 4-17 and Figure 4-19.

After analysis of these SEM micrographs of the pearlitic samples represented by Figure 4-16 the SEM micrographs of the bainitic samples from Figure 4-20 were characterised. For the image acquisition in the SEM the samples were etched in 2 % nital.

Analysis of optical micrographs of the samples has proved difficult since, on the one hand, the maximal applicable magnification for the optical microscope is just enough to be able to resolve the larger carbides in the microstructure. On the other hand, the contrast between the carbides and the matrix microstructure is not high enough to unambiguously segment the carbides. Therefore the samples were etched with 5 % nital to increase contrast whilst still being able to characterise the matrix microstructure by the texture analysis (Figure 4-36).

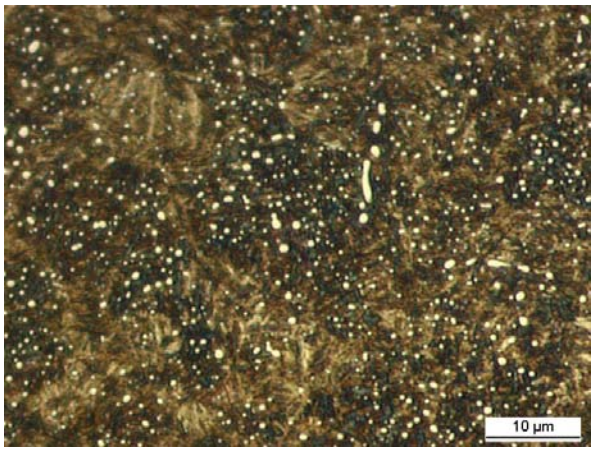

Figure 4-36 Optical micrographs of the bainitised samples of the tool steel 100Cr6, re-austenitised at 850 °C, etched with 5 % nital

To characterise the carbides in the different micrographs an automated segmentation and measurement sequence was programmed using a KS400 macro. With this macro the mean values per image of the perimeter, the area and the form factor of the single carbides were measured. Additionally the volume fraction and the number of carbides were measured per image.

4.5.7.2 Measurement of the carbides and relation to the austenitisation temperature

The number density, size and volume fraction of alloy carbides strongly depend on the prior heat treatment (Section 3.1.1). Additional information from the carbide distribution may be used to characterise the microstructure in addition to the texture parameters.

4.5.7.2.1 Number density

Using the image analysis software the number of carbides per image and the area of each carbide in the image were determined for the secondary electron SEM micrographs of both the pearlitic (Figure 4-16) and the bainitic samples (Figure 4-20). From these numbers the number density per mm² and the volume fraction of carbides were calculated (Table 4-8).

Table 4-8 Number densities of the pearlitic and the bainitic samples re-austenitised at different temperatures

re-austenitisation temperature	**number density / number/mm²**	
	pearlitic samples	**bainitic samples**
780 °C	0.089	0.091
800 °C	0.053	0.077
850 °C	0.004	0.030
900 °C	0.003	0.014
930 °C	–	0.014

The values show a decrease of the number densities with increasing re-austenitisation temperature not only for the pearlitic but also for the bainitic samples. For the lowest

temperature 780 °C very similar values have been measured for both samples. With increasing temperature higher values can be found for the bainitic samples than for the corresponding pearlitic samples. For the highest temperature 930 °C of the pearlitic sample the number density was not measured due to an insufficient number of micrographs.

4.5.7.2.2 Volume fraction

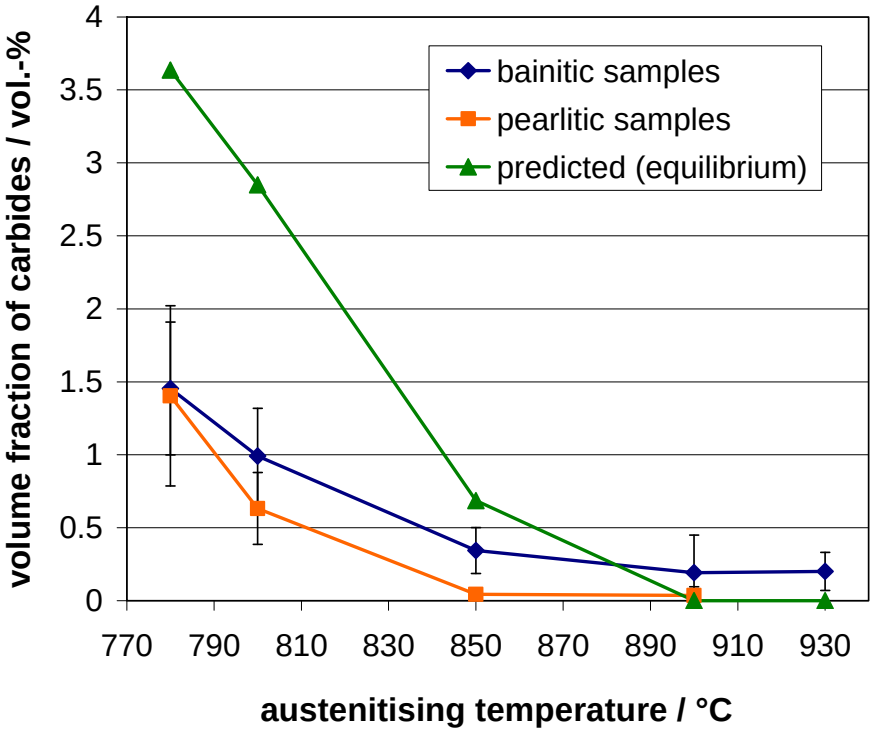

Figure 4-37 Influence of the austenitising temperature on the volume fraction of the carbides for the SEM micrographs of the pearlitic and bainitic samples of the steel 100Cr6 from Figure 4-16 and Figure 4-20 respectively with corresponding error bars as well as the predicted volume fractions for the equilibrium at austenitising temperatures for that steel; 16 to 52 micrographs analysed per temperature

For both the pearlitic (Figure 4-16) and the bainitic samples (Figure 4-20) the area of carbides was detected for the SEM micrographs. From these data the area fraction per micrograph has been calculated. As the carbides are spheroidal in shape and do not show a preferred orientation this area fraction equals the respective volume fraction of the carbides. The values are averaged for every sample to eliminate the influence of local inhomogeneities in the

distribution of the carbides. The measured values are presented in Figure 4-37 for both the pearlitic samples and the bainitic samples together with the corresponding error bars. Additionally the values predicted by the thermodynamical simulation using Thermo-Calc are included (Figure 4-21).

For the pearlitic samples, the volume fraction of carbides decreases rapidly with increasing re-austenitisation temperature from 780 °C to 850 °C above which the volume fraction does not vary significantly. Quantitatively, at the lowest austenitising temperature the value of the carbide volume fraction is about 1.40 vol.-%, it decreases for the austenitising temperature of 800 °C to 0.63 vol.-%. For a temperature of 850 °C the volume fraction is again decreasing to 0.043 vol.-%. The lowest value can be found for the highest investigated temperature of 900 °C where the volume fraction is only 0.036 vol.-%. Due to an insufficient number of micrographs and therefore carbides to be evaluated the volume fraction of the sample austenitised at 930 °C is not presented here.

For the bainitised samples a comparable trend of the volume fraction can be found with the variation of the austenitising temperature but with higher absolute values than were measured for the pearlitic samples. For the 780 °C sample a value of 1.45 vol.-% was found. For the 800 °C sample the value decreases to 0.99 vol.-%. Another decrease in the value can be found if the temperature for the austenitisation is raised to 850 °C with a volume fraction of 0.34 vol.-%. The volume fraction for the austenitisation at 900 °C is again lower with 0.19 vol.-% and nearly the same for the 930 °C sample with 0.20 vol.-%. The greater carbide volume fractions measured for the bainitised samples compared with the pearlitic samples is unlikely to be due to continued dissolution during the slower cooling of the latter samples, but probably indicates that carbides are more easily resolved against a bainitic matrix rather than a pearlitic one.

For the five investigated austenitising temperatures the volume fractions of the carbides at equilibrium at the austenitising temperatures was predicted using Thermo-Calc (see also chapter 4.4.1). The predicted values of the volume fractions of the carbides differ significantly from the measured values of the pearlitic and also the bainitic samples. For the three lower austenitising temperatures of 780 °C to 850 °C the values are higher than the measured values.

For 780 °C a volume fraction of 3.64 vol.-% was predicted, which is more than twice the value measured for the respective bainitised sample. The Thermo-Calc predictions are equilibrium values and so do not indicate any size of the carbides so that it is likely that the bainitic and pearlitic samples contain fine carbides below the detection limit of the optical microscope, which are not included in the measured values, but would be included in the predicted values. For an austenitising temperature of 800 °C the volume fraction decreases to 2.85 vol.-% still being significantly higher than measured values. Increasing the temperature to 850 °C gives only 0.69 vol.-% of carbides. For the two highest temperatures of 900 °C and 930 °C the carbides should go completely into solution in equilibrium condition. Experimental values at these higher temperatures could also include some spheroidised cementite, which gives a higher volume fraction than predicted.

4.5.7.2.3 Size distribution

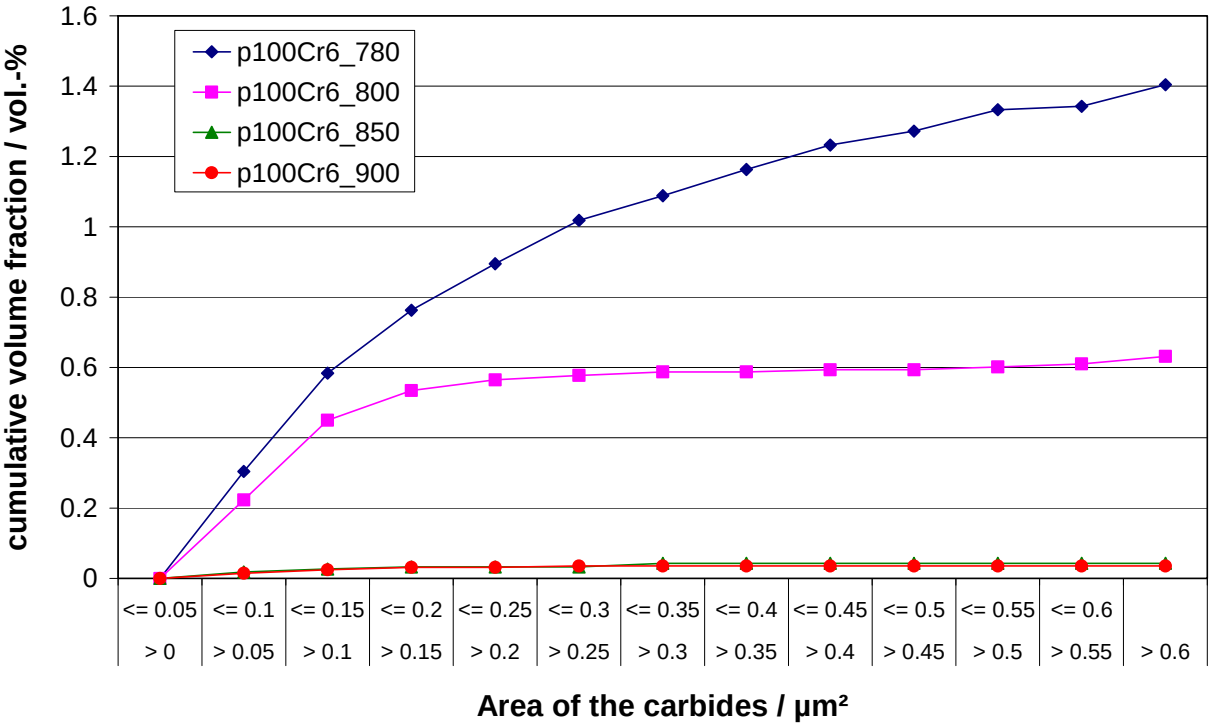

Figure 4-38 Distribution of the size of the carbides in the pearlitic samples from Figure 4-16 of the steel 100Cr6, measured for the SEM images

The carbide size distribution was determined for the SEM micrographs of the pearlitic and the bainitic samples. For the pearlitic samples only, the samples for the four lower austenitising

temperatures were analysed since for the 930 °C sample not enough images were available to ensure good statistics. For the bainitic samples, samples from all five re-austenitisation temperatures were analysed. The results of the measurement are shown in Figure 4-38 for the pearlitic samples and for the bainitic samples in Figure 4-39.

The size distribution of the pearlitic samples shows as expected significant differences in the volume fraction of carbides between the samples austenitised at different temperatures. The cumulative volume fraction of carbides increases with increasing area of carbides and with decreasing re-austenitising temperature.
The two highest investigated austenitising temperatures 850 °C and 900 °C gave very similar volume fractions and size ranges of carbides. For the 850 °C sample a volume fraction of 0.043 vol.-% was measured, for the 900 °C sample only 0.036 vol.-% with the biggest carbides having an area of 0.35 µm² or 0.3 µm² respectively.
The sample austenitised at 800 °C shows an overall volume fraction of 0.63 vol.-% for the carbides. The majority of carbides have areas of less than 0.3 µm². This can be seen by the strong increase of the cumulative volume fraction for carbides up to this size. For areas up to 0.6 µm² the distribution does not increase significantly. For carbides with 0.6 µm² and more an additional increase was measured.
The 780 °C sample shows the highest volume fractions of carbides by far. The cumulative volume fraction is increasing continuously with the carbide size. This represents a very wide spread distribution of the carbide sizes. A total volume fraction of 1.40 vol.-% can be found with a huge increase for carbides of 0.6 µm² and bigger.

For the bainitic samples significant differences between the different austenitising temperatures can be found. For the highest temperatures of 900 °C and 930 °C very similar trends for the cumulative volume fraction of carbides can be found. For both a total volume fraction of carbides of 0.2 vol.-% was measured. While the 930 °C sample shows higher volume fractions for carbide areas up to 0.6 µm², the 900 °C sample catches up for carbides larger than this size. Both samples have the majority of carbides in the size range of up to 0.3 µm². This size range is similar to that for the pearlitic samples, Figure 4-38, but the volume fraction detected for the bainitic samples is much greater (roughly six times more). This behaviour would support the hypothesis above that detection is easier against a bainitic

matrix as continued dissolution during cooling would be expected to give a smaller upper size in the pearlitic samples.

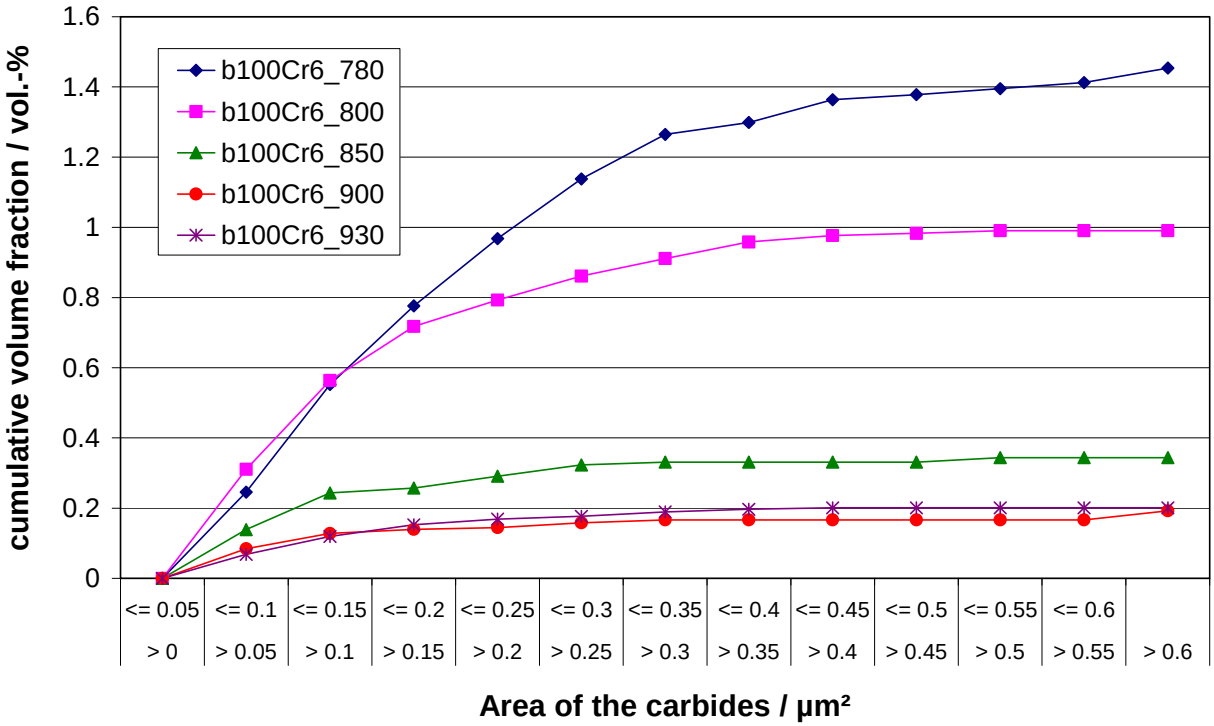

Figure 4-39 Distribution of the size of the carbides in the bainitic samples from Figure 4-20 of the steel 100Cr6, measured for the SEM images

The sample austenitised at 850 °C shows a higher volume fraction with up to 0.34 vol.-%. For this sample also most of the carbides show areas up to 0.3 µm².

For the 800 °C sample the volume fraction of carbides is again increasing significantly to 0.99 vol.-%. This sample also shows an increasing number of bigger carbides with the majority of particles having an area up to 0.45 µm².

The sample austenitised at 780 °C, as the lowest temperature, shows by far the highest amount of carbides with a value of 1.45 vol.-%. It is also obvious that this sample contains carbides of all sizes. Also a considerable number of carbides with a size of more than 0.6 µm² can be found. The size values for the lower re-austenitisation temperature samples are, again, comparable between bainitic and pearlitic samples reinforcing the theory that the volume fraction difference is due to detection differences.

4.5.7.2.4 Local inhomogeneities in the carbide distribution

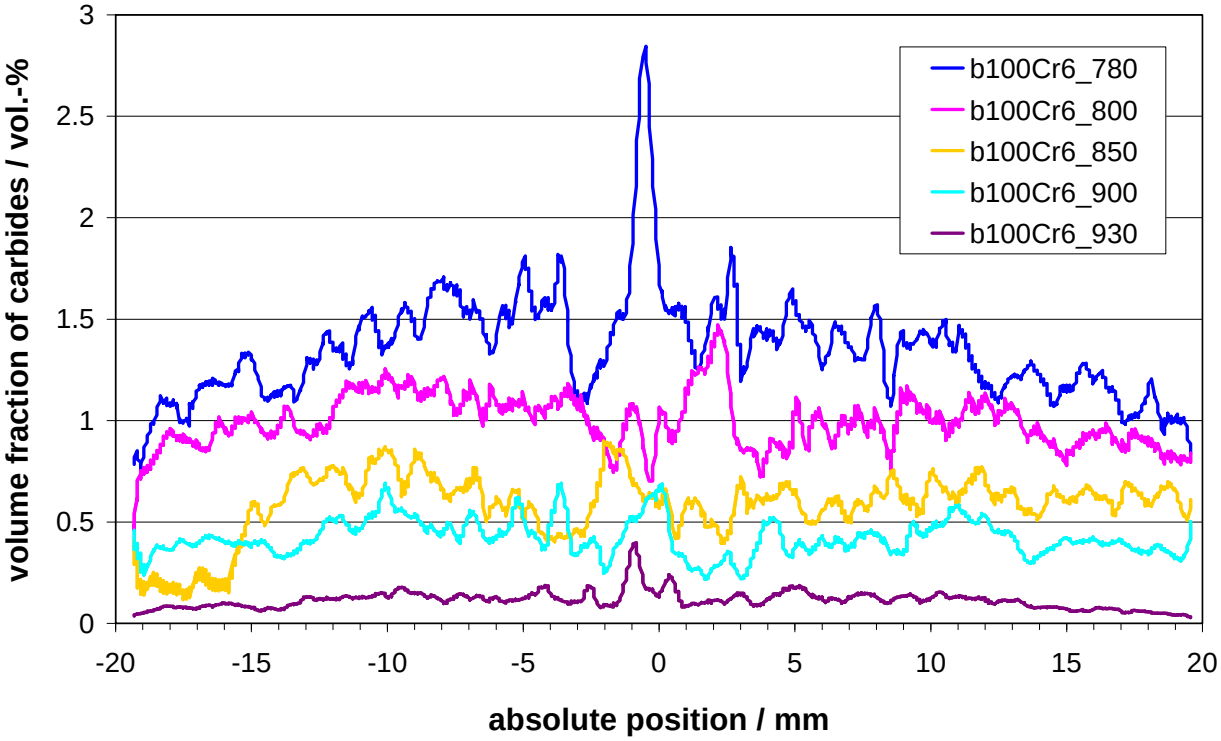

Figure 4-40 Trend of the volume fraction of the carbides per micrograph over the cross-section of the sample, presented as the floating average of 10 values for optical micrographs of samples of the bainitised steel 100Cr6, etched with 5 % nital

Figure 4-40 illustrates that there is a variation across the specimen thickness in carbide content, which, for the lowest re-austenitisation temperature (780 °C), shows a gradual increase from surface (0.8 vol.-%) towards the centre-line (1.5 vol.-%), before a spike (up to 2.8 vol.-%) at the centre-line itself. This variation is symmetric about the centre-line. With increasing re-austenitisation temperatures the overall carbide volume fraction decreases as does the degree of spatial variation, although the centre-line spike remains; in some cases this appears displaced to one side of the true centre-line, e.g. that for 800 °C. Above 800 °C the trace is essentially flat with a centre-line spike.

The spike in carbide volume fraction is consistent with centre-line segregation persisting from initial ingot/billet casting. On initial solidification, Cr partitions into the liquid phase and so the surface layer is Cr-depleted. As solidification proceeds there is a rise in Cr level until the last liquid to solidify is trapped at the centre-line giving a high level of Cr enrichment. This

will lead to extensive large carbide precipitation during cooling after solidification. The formation of Cr-rich carbides also appears to denude the adjacent regions in chromium and/or carbon so that the spike is bordered by areas showing lower volume fractions of coarse carbides, Figure 4-40.

After casting hot rolling compresses the profile as well as allowing diffusion processes to act, but it is insufficient to fully remove the spike. Away from the centre-line a periodic variation in carbide volume fraction is observed, which could be indicative of rolling through the ($\alpha+\gamma$) phase field. In this case, Cr partitions to the α-phase which is elongated into bands during rolling producing a periodic Cr content variation on top of that from solidification. Carbide precipitation will follow the variation in Cr level and this is shown by the 780 °C re-austenitisation sample. As the re-austenitisation temperature increases then the spatial variation is not as apparent (due to the lower absolute values compared to the background scatter in volume fraction), but a variation with a wavelength of ~ 1000 µm is still seen which is consistent with the Cr level variation from banding during ($\alpha+\gamma$) phase field rolling.

Due to these local inhomogeneities of the carbide volume fraction a direct correlation with the austenitising temperature is not possible unless a common position is taken and sufficient measurements are taken to account for banding and centre-line variations. However, there is a strong dependence between the two parameters and so these data could be combined with the texture analysis to characterise complex microstructures as obtained from the bainitic samples.

4.5.7.2.5 Correlation with properties for SEM micrographs

From the texture parameters measured at a separation of 1 pixel a correlation of the specific microstructure to the austenitising temperature was established using a neural network. The texture parameters have been measured together with the number and the volume fraction of carbides per image. In the first step 40 of the 143 micrographs have been chosen to train the neural network. The network was trained with the 11 texture parameters as the input values and the austenitising temperature as the output value. In the second step the number and the volume fraction of the carbides was used as well as the texture parameters as input values. In the third step the neural network was only trained with the carbide data. The correlation for these three analyses can be seen in Figure 4-41.

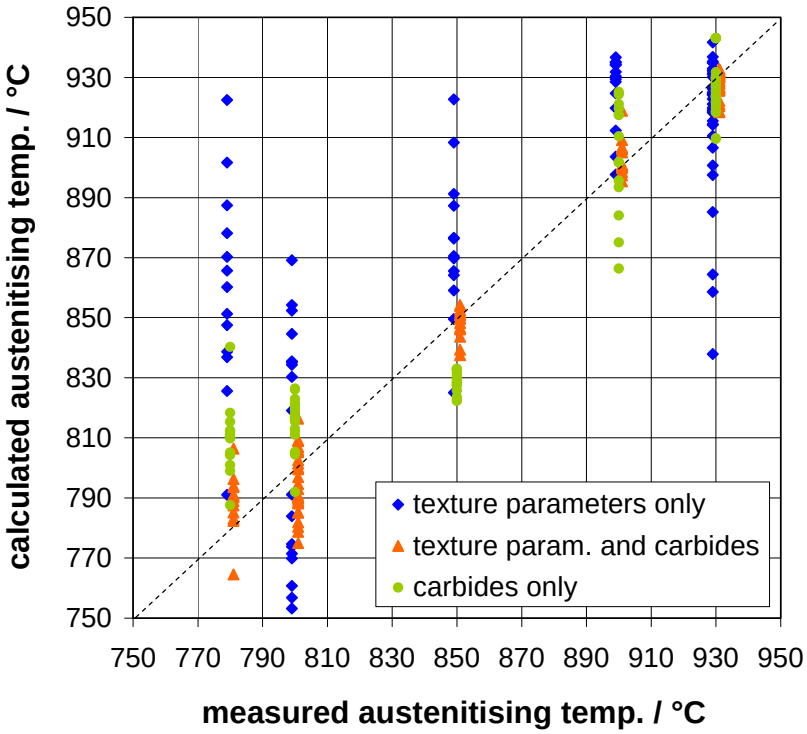

Figure 4-41 Correlation between the austenitising temperature applied during heat treatment and calculated from the carbide parameters and/or the texture parameters at a separation of 1 pixel determined from SEM micrographs presented in Figure 4-20 with and without using the number and volume fraction of the carbides; samples etched with 2 % nital; 103 micrographs analysed

For the analysis using the texture parameters only a large scatter of the values can be found. In addition, the means of these scattered distributions show a poor correlation with the measured re-austenitisation temperature. For the lowest temperature of 780 °C, all the calculated values are higher than the corresponding measured values. Also for 850 °C and 900 °C most of the calculated values are higher than the measured ones. For the 930 °C samples the values are too low.

Regarding the values calculated using the carbide volume fraction in addition to the texture parameters much less scatter in the values can be found, which now has a mean centred on the measured values indicating that the use of both sets of data can give good prediction of the re-austenitising treatment.

If only the carbide data are used to establish the correlation to the austenitising temperature, the quality lies between that of the aforementioned analyses. The range of scatter is larger

than for the calculation with texture and carbide data and the means no longer agree with the measured re-austenitisation temperatures. For the temperatures of 780 °C and 800 °C the calculated values are too high while for 850 °C they are too low. For the two highest temperatures the range of scattering lies well around the best fit line.

To quantify the quality of the correlation, the difference between the calculated and the nominal values of the austenitising temperature have been calculated. The mean value and the standard deviation describe the difference between the analysis with and without using the information of the carbides to train the neural network (Table 4-9).

As has already be seen in Figure 4-34, the analysis of the SEM micrographs by means of only the texture parameters gives a comparatively low mean value but a high standard deviation of the values. If the carbide information in terms of the volume fraction and the number of carbides per image (section 4.5.7.2.1) are included to the input values of the neural network, the mean value is significantly lowered to a value of -0.7. This indicates that the values scatter homogeneously around the best fit line. Also the standard deviation decreased from 59.7 to 8.5 indicating much better agreement if the analysis is done with the carbide information and the texture parameters. In Figure 4-41 this is indicated by the range of scatter that is significantly smaller if carbide data are analysed. For the correlation based only on the carbide data the mean value is 4.6 showing that the values do not always scatter homogeneously around the best fit line. The standard deviation is 18.2, comparably low, but about twice the value for the correlation based on both the texture parameters and the carbide data.

Table 4-9 Mean value and standard deviation of the difference between the calculated values and the nominal values of the correlation of the austenitising temperature for the SEM micrographs with a constant separation of 1 pixel regarding the analysis with and without the carbide information; samples etched with 2 % nital

	mean value	**standard deviation**
texture parameters only	4.0	59.7
texture parameters and carbides	-0.7	8.5
carbides only	4.6	18.2

4.5.7.2.6 Influence of the etchant on the texture parameters and correlation with properties for optical micrographs

Samples etched with 5 % nital

Since the optical microscope possesses a limited resolution and the carbides show relatively poor contrast to the surrounding matrix, the samples already presented in Figure 4-18 were etched with 5 % nital to obtain a high contrast. Representative micrographs with this etching are presented in Figure 4-42.

The same correlation as for the SEM micrographs with and without carbide data was established for the optical micrographs etched with 5 % nital. Again the texture parameters at a separation of 1 pixel were used to train the neural network, in one case together with the volume fraction and the number of carbides per image. The results of the two correlations are presented in Figure 4-43. The mean values and the corresponding standard deviations of the difference between the calculated and the nominal values are given in Table 4-10.

The correlation established using just the texture parameters yields values scattered around the value for the perfect correlation. The scatter for this etch at each temperature is greater than that for the samples etched using 2 % nital, although the mean of these scatter bands are closer to the measured re-austenitisation temperature. Only for 930 °C, the highest austenitising temperature, is the scatter band all below the actual measured value.

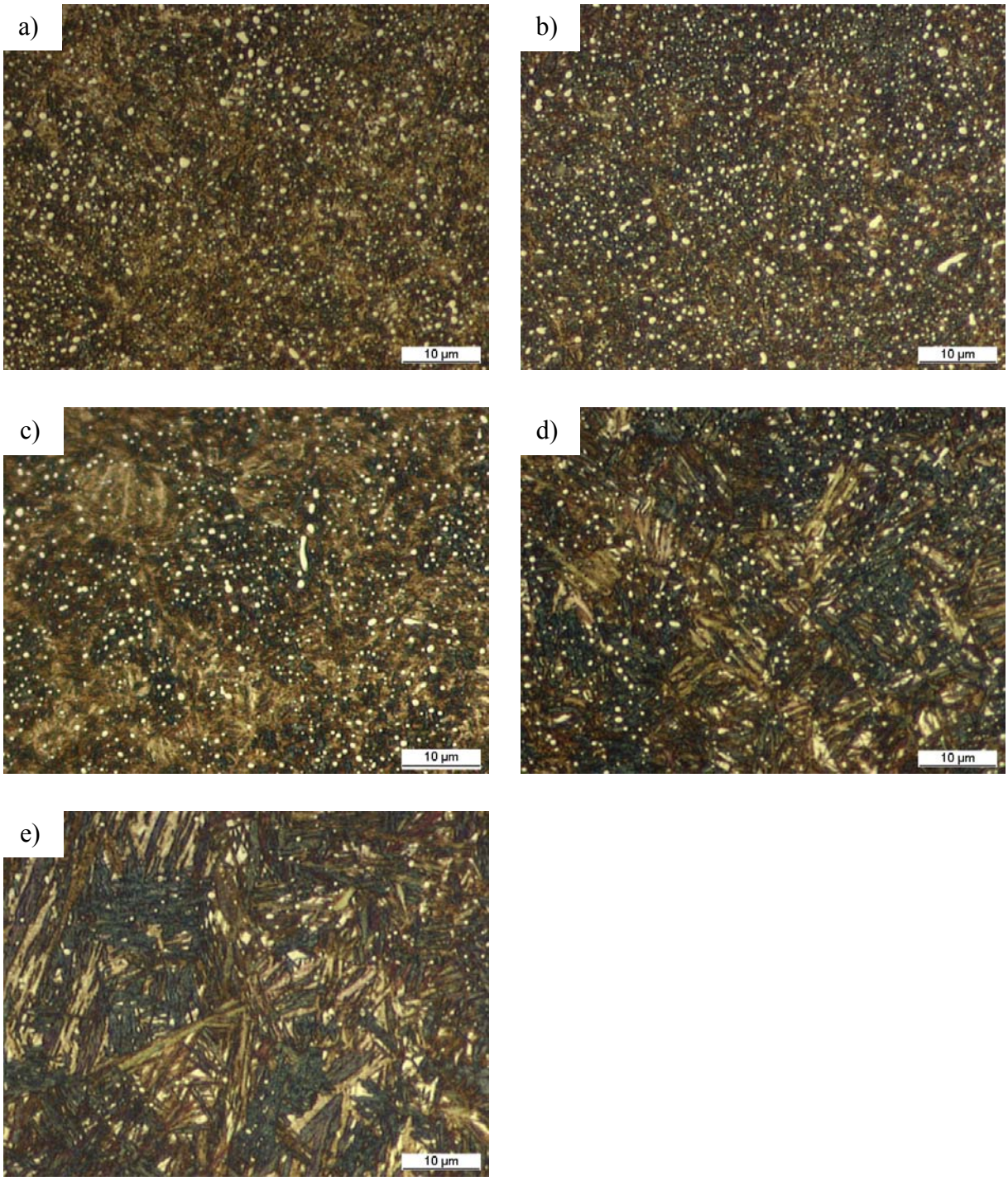

Figure 4-42 Optical micrographs of the bainitised samples of the tool steel 100Cr6, re-austenitised at different temperatures, T_A, etched with 5 % nital

a) 780 °C b) 800 °C

c) 850 °C d) 900 °C

e) 930 °C

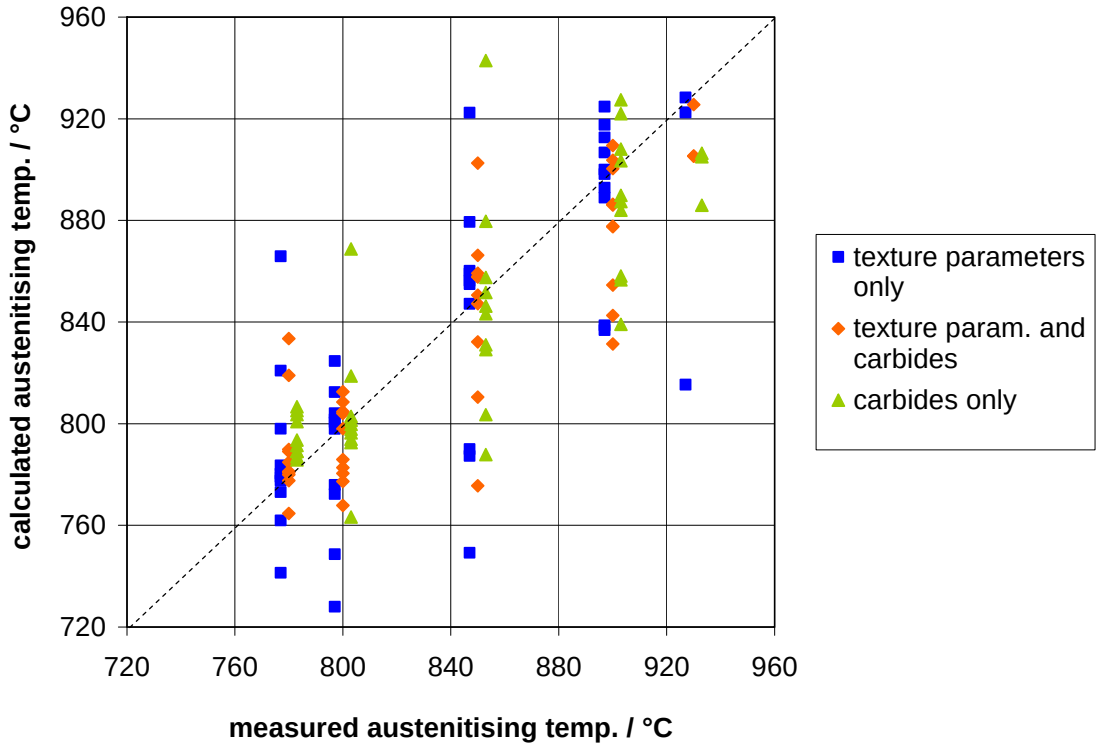

Figure 4-43 Correlation between the austenitising temperature applied during heat treatment and calculated from the texture parameters at a separation of 1 pixel determined from optical micrographs of the bainitised 100Cr6 samples (Figure 4-18) with and without using the carbide data; samples etched with 5 % nital; 43 micrographs analysed

The mean value of the difference between calculated and nominal values shows a negative value (-8.2) indicating predicted values, which are too low. The respective standard deviation quantifies the large scatter with a value of 39.2 is lower than for the 2 % nital etched samples, but the latter set contained a larger number of data points.

If the carbide information is included as input data, the correlation is improved compared with the texture-only analysis but is less good than the texture + carbide analysis for 2 % nital etched samples, Figure 4-41. Again most of the values scatter around the line for the perfect correlation apart from the values of the sample austenitised at 930 °C. The values calculated for this sample are again all lower than 930 °C. The range of scatter is decreased as has already be seen for the SEM micrographs. The standard deviation is reduced to 26.2 if the volume fraction of carbides is included to the analysis.

If only the carbide data are used to establish the correlation, the scatter is larger than that for the calculation with texture parameters and carbide data. This can also be seen in the standard deviation of 30.1 whereas the mean value of the difference calculated and nominal values is lowest for the three analyses with a value of -1.3.

Table 4-10 Mean value and standard deviation of the difference between the calculated values and the nominal values of the correlation of the austenitising temperature for the optical micrographs with a constant separation of 1 pixel regarding the analysis with and without the information of the carbides; samples etched with 5 % nital

	mean value	**standard deviation**
texture parameters only	-8.2	39.2
texture parameters and carbides	-7.0	26.2
carbides only	-1.3	30.1

Samples etched with Klemm's reagent

As an alternative etchant Klemm's reagent was tested. This is a colour etchant differentiating grains according to their orientation to the ground and polished surface [Wec82]. Representative micrographs of the samples etched with Klemm's reagent are given in Figure 4-44.

For the samples etched with Klemm's reagent a correlation of the texture parameters at a separation of 1 pixel and the carbide information to the austenitising temperature was established.

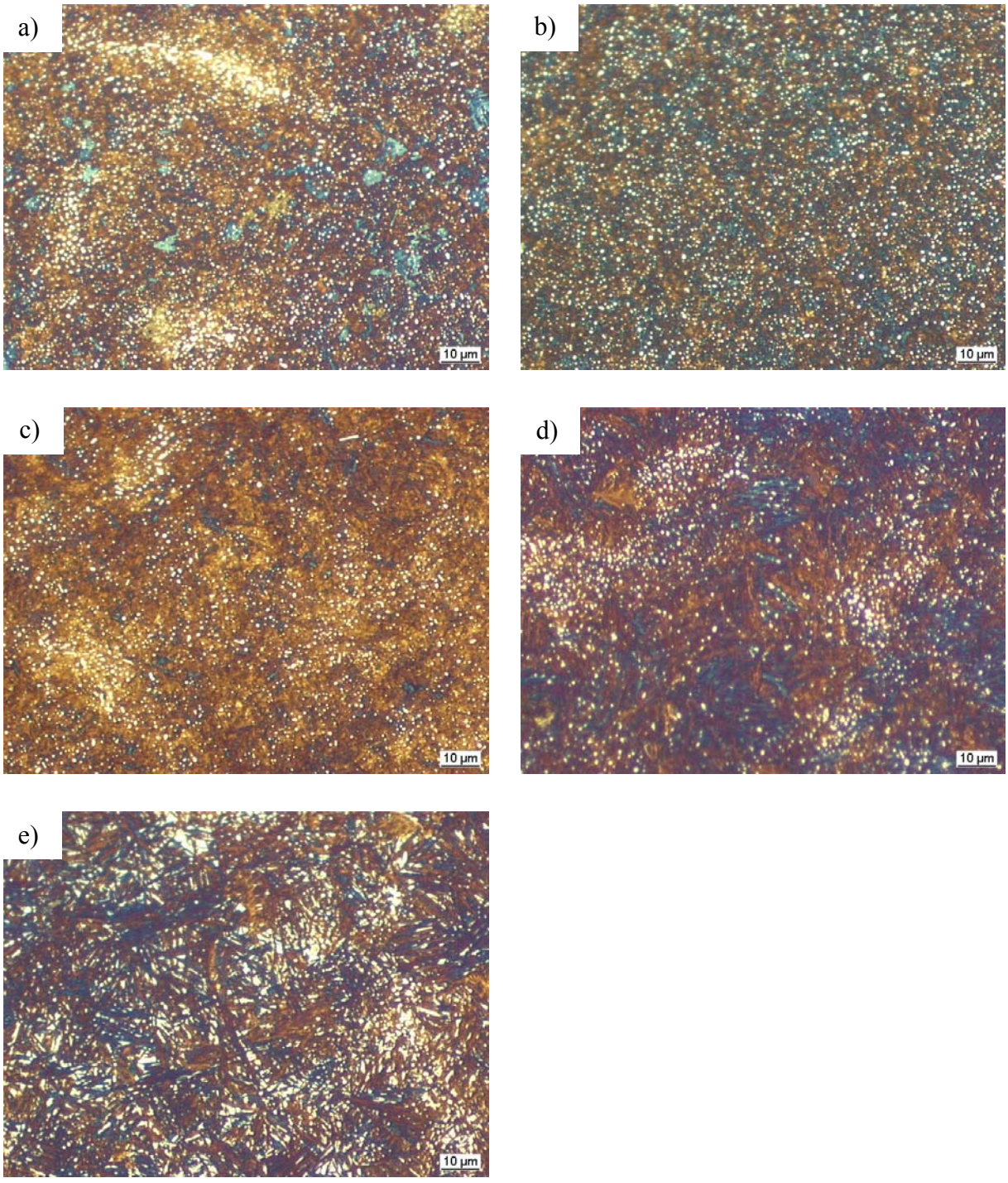

Figure 4-44 Optical micrographs of the bainitised samples of the tool steel 100Cr6, re-austenitised at different temperatures, T_A, etched with Klemm's reagent

a) 780 °C b) 800 °C

c) 850 °C d) 900 °C

e) 930 °C

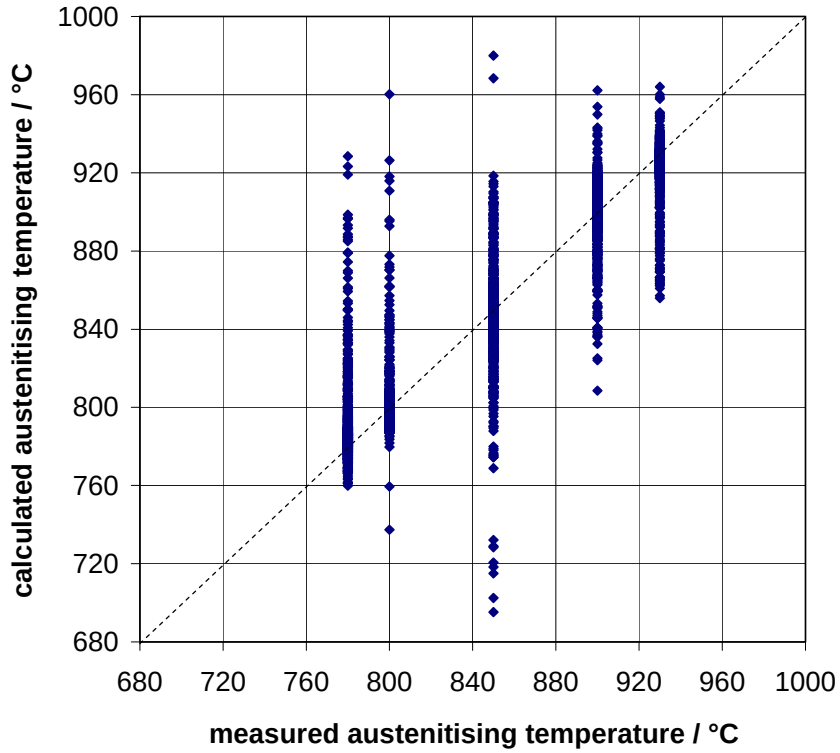

Figure 4-45 Correlation between the austenitising temperature applied during heat treatment and calculated from the texture parameters at a separation of 1 pixel determined from optical micrographs of the bainitised 100Cr6 samples etched with Klemm's reagent presented in Figure 4-44; 4307 micrographs analysed

The correlation shows very significant scatter in the values. Nevertheless the mean value of the difference between the calculated and the nominal values is with -0.2 very good and also the standard deviation with 22.8 comparably low. But as can be seen the maximal scattering is up to 150 °C. It can be seen that for the lower two austenitising temperatures most of the calculated values are higher than the measured values. For the highest temperature the calculated values are rather too low. Etching with Klemm's reagent, as for 5 % nital, gives poorer prediction compared with the use of a texture + carbide analysis for samples etched in 2 % nital.

4.6 Calculation of the lateral hardness distribution

The heat treated components (Table 3-3) show high hardness at the surface which decreases towards the component centre. Some typical hardness profiles of the investigated samples are presented in Figure 4-46.

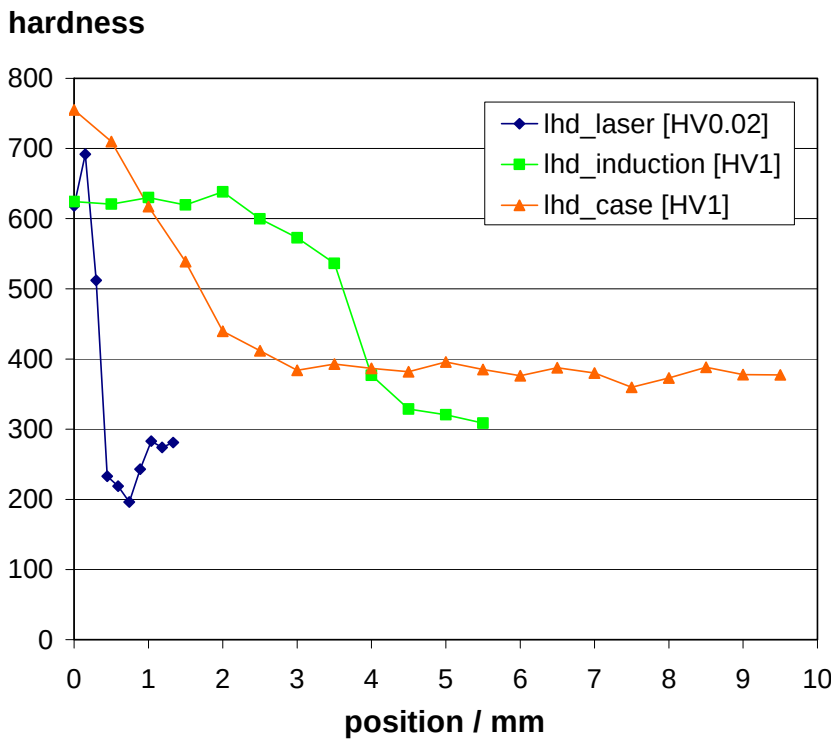

Figure 4-46 Comparison of the mechanically measured hardness profiles of the surface hardened steel components

Regarding the method of surface hardening and the materials, significant differences can be found in the hardness profiles. These differences in hardening depth and hardness are derived from modifications in the microstructure, which have been quantified using texture parameters.

All the 11 texture parameters were used in connection with a neural network to find a correlation between the local microstructure of the sample, quantified by the texture parameters, and the corresponding microhardness. This approach has been applied to different components made of different steels (Table 3-3).

4.6.1 Laser hardened steel component

Microstructure of the sample

The component of the steel 32CrB4 (material number 1.7076) was hardened at one edge by a laser beam. The rest of the cross-section was not changed due to this heat treatment and so showed the initial microstructure.

The overview image obtained by the Mosaix function is shown in Figure 4-47 (a) together with micrographs representing the initial microstructure in the core of the sample (b), a micrograph showing the microstructure in the heat affected zone (c) between the core microstructure and the laser hardened surface and the microstructure obtained by hardening using a laser beam at the surface of the sample (d).

As can be seen in the micrograph in Figure 4-47 (b), the initial microstructure of the sample consists of spheroidised alloy carbides in a ferritic matrix due to a soft annealing heat treatment before the hardening stage. To characterise the chemical composition of these carbides, these and the surrounding matrix have been analysed using EDS. Example spectrum positions are shown in Figure 4-48 with the corresponding results of the chemical analysis in Table 4-11. The soft annealing was preferred to increase the machinability of the component during fabrication but also to ensure adequate ductility in the practical use of the component. The sample shows a hardness of about 270 $H_{V0.02}$ for this initial microstructure in the core of the sample. For this microstructure the parameter Haram2 yields a value of 0.61.

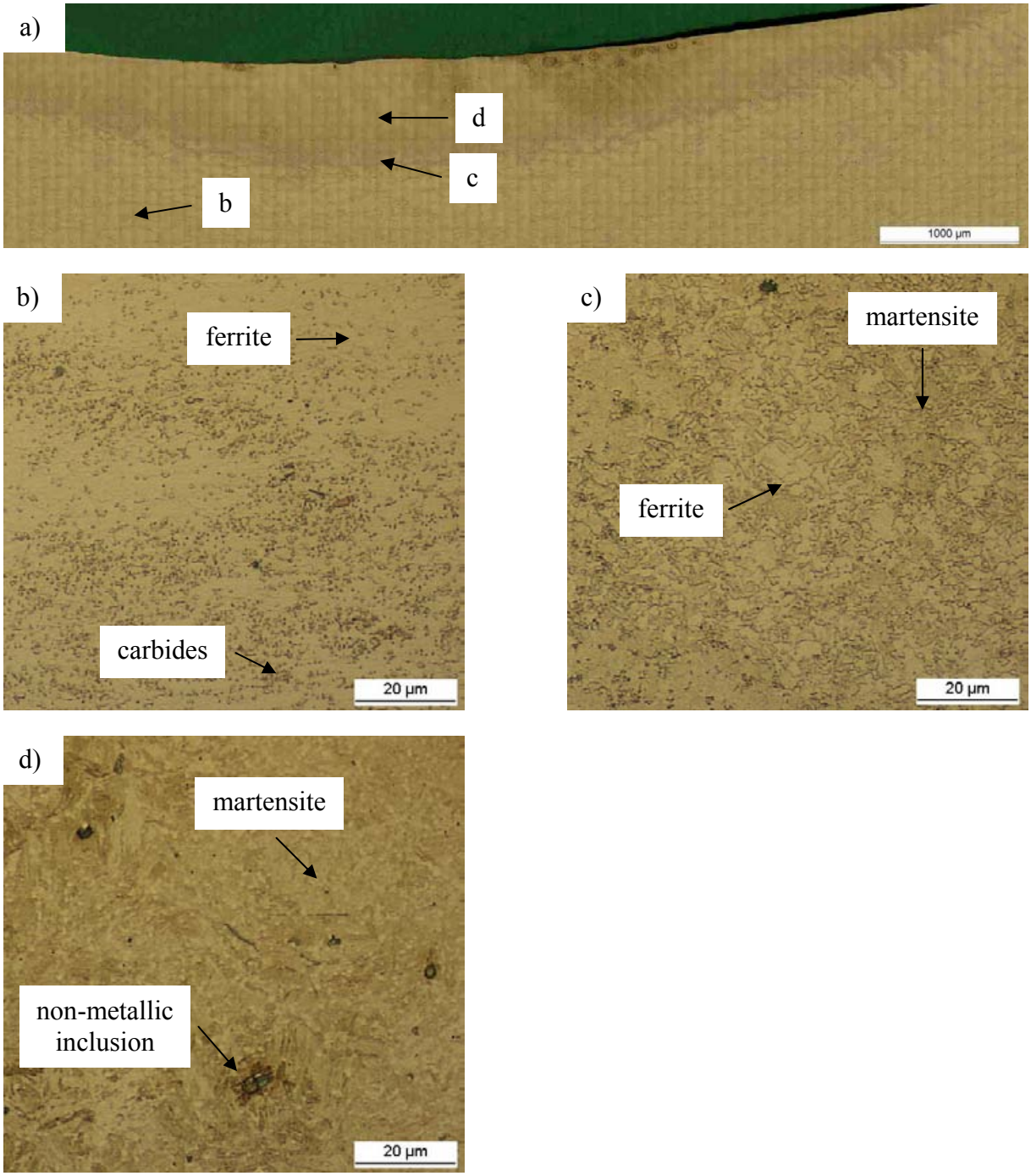

Figure 4-47 Micrographs of laser hardened sample lhd_laser of the steel 32CrB4, obtained by the Mosaix function of KS400, consisting of 1600 micrographs taken at a magnification of 500:1, etched with 2 % nital

a) overview image, obtained by the Mosaix function of KS400

b) micrograph of the initial microstructure obtained from the core of the sample

c) micrograph of the heat-affected zone

d) micrograph of the region hardened by a laser beam

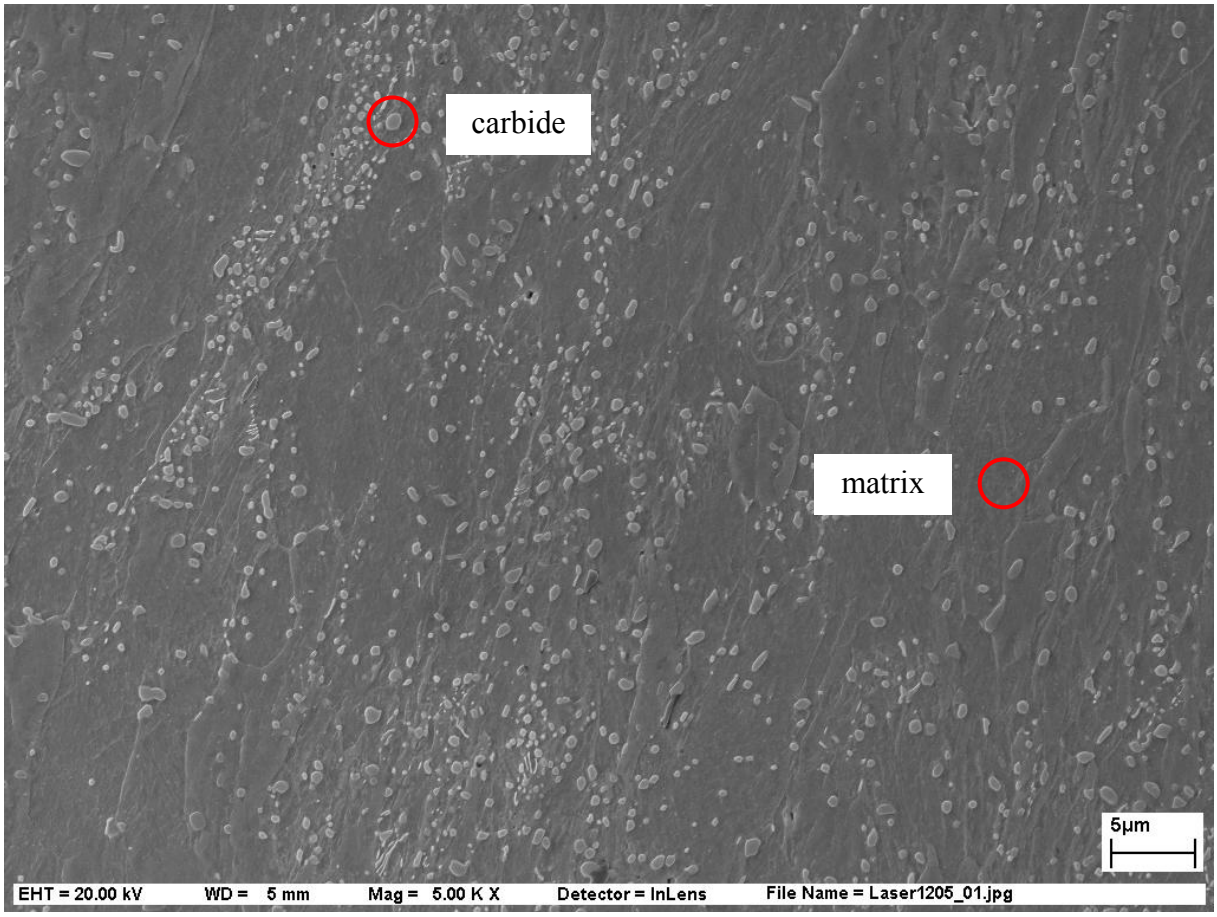

Figure 4-48 SEM micrograph of the initial microstructure in the core of the laser hardened sample lhd_laser with positions for the EDS marked, etched with 2 % nital, secondary electron image

In the heat affected zone shown in Figure 4-47 (c) between the laser hardened surface and the core microstructure the hardness decreases steadily with the distance from the hardened surface. This structure shows a reduction in the amounts of coarse carbides and ferrite as the hardened layer is approached. Both of these phases are replaced by bainite and eventually martensite. The degree of re-austenitisation and carbide dissolution increases through the HAZ towards the hardened region and so fractions of the initial microstructure remain between the transformed microstructure. This microstructural variation coincides with a variation in temperature during laser treatment, but the cooling rate is generally rapid as the base material provides a large heat sink. The parameter Haram2 increases to a value of 1.02 for the micrograph representing the heat affected zone, the hardness increases to 292 $H_{V0.02}$, although the values will vary through the microstructural gradient in the HAZ.

Table 4-11 Chemical analysis of a carbide and the matrix of the laser hardened sample of the material 32CrB4, gained from the EDS of the positions specified in Figure 4-48, together with the specified values after [Weg01], all values in wt.-%

element	position "carbide"	position "matrix"	specified values
Fe	82.72	96.30	balance
Cr	7.03	0.80	0.90 – 1.20
Mn	2.69	0.50	0.60 – 0.90
Si	0.21	0.32	≤ 0.40
B	0.39	0.00	0.0008 – 0.0050

The microstructure given in Figure 4-47 (d) shows a martensitic microstructure obtained by the quenching after full re-austenitisation and carbide dissolution by the laser beam increasing the carbon content of the austenite. Subsequent cooling transformed the austenite to martensite giving a high surface hardness between 530 and 760 $H_{V0.02}$ and the required wear resistance. The texture parameter Haram2 yields a value of 0.58 for the respective micrograph of the martensitic microstructure at the edge of the sample.

Measurement of the texture parameters

For the quantitative analysis of the microstructure the sample was scanned using a higher magnification. Using the Mosaix function of the software application KS400 about 1600 micrographs have been obtained at a magnification of 500:1 and merged into one single overview image. All the 11 texture parameters have been measured for each of the 1600 micrographs to be able to detect local variations in the microstructure by means of the texture parameters.

The trend of the texture parameter Haram2 is again presented in Figure 4-49 where the trend of the parameter is shown with varying distance from the surface along a trace perpendicular to the laser hardened surface of the sample. In this diagram again a very low parameter can be found at the surface of the sample showing the martensitic microstructure characterised by a

high hardness. This low value of the texture parameter is due to the microstructure consisting of a very fine needle-like structure with only small variations in the grey values.

With increasing distance and therefore increasing volume fraction of ferrite (and eventually carbides) in the microstructure, the values increase to their maximum of approximately 1.0. As the grain boundaries of the ferrite and martensite grains are developed, comparably high number of bright-dark transitions of adjacent pixels can be found yielding an increase in the texture parameter Haram2 compared to the martensitic microstructure. The hardness variation for a depth of up to 1.0 mm shows an initial rise to a maximum of just under 700 $H_{V0.02}$ before falling steadily to around 200 $H_{V0.02}$ at around 0.8 mm, Figure 4-46, which would correspond to a higher proportion of ferrite and bainite without coarse carbides. The base level of 280 $H_{V0.02}$ is reached at a depth of 1.0 mm.

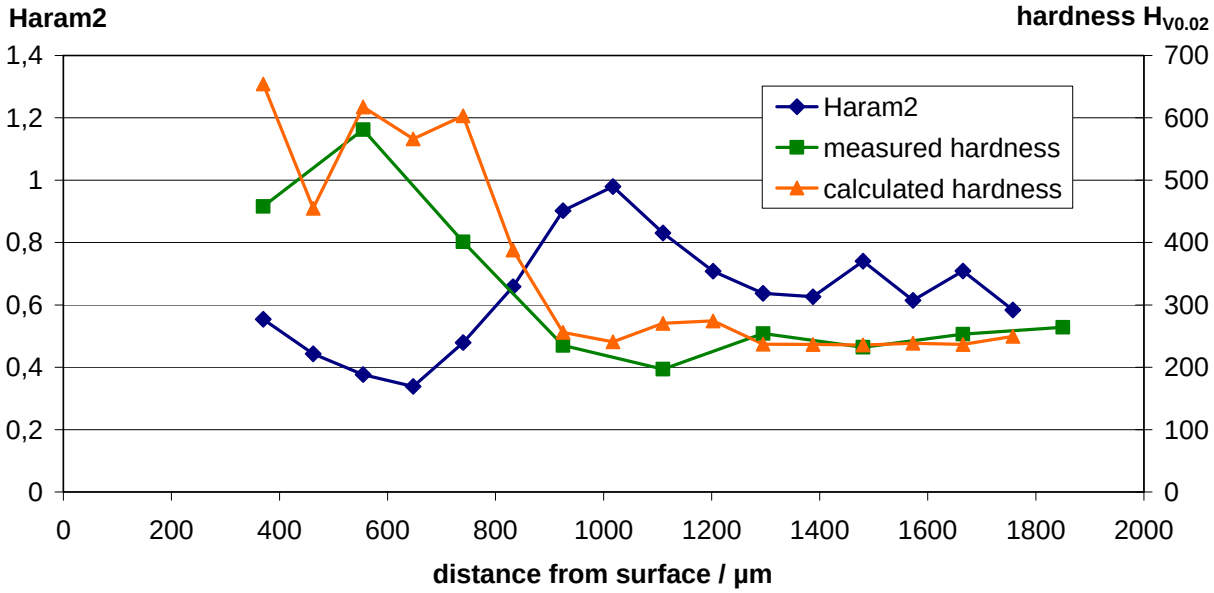

Figure 4-49 Trend of the texture parameter Haram2 perpendicular and with different distances from the surface of the laser hardened sample lhd_laser together with the respective measured and calculated microhardness values

For the base microstructure in the soft annealed microstructure the values of the texture parameter Haram2 decrease again to values between 0.6 and 0.8 with the hardness showing values of about 270 $H_{V0.02}$. As the microstructure consists of carbides in a ferritic matrix, a high number of bright-dark transitions of adjacent pixels can be found. As these transitions

are lower in their number as for the mixed microstructure consisting of martensite and ferrite, the parameter also yields lower values.

The variation described above for microstructure (which determines Haram2 values) and hardness is summarised in Figure 4-49 for one of the hardness traces. The overall trends in microhardness and Haram2 are inversely related, i.e. Haram2 starts around 0.6 then decreases as the hardness increases, increases through the large hardness decrease up to around 1 mm and then falls as the hardness rises to the base metal value. Although this variation is qualitatively correct, the relationship is not simple, e.g. the two Haram2 values of 0.8 correspond to microhardness values of 280 and 200 at different depths. The variation in hardness has been modelled using a neural network trained with the texture data and the corresponding Vickers microhardness $H_{V0.02}$.

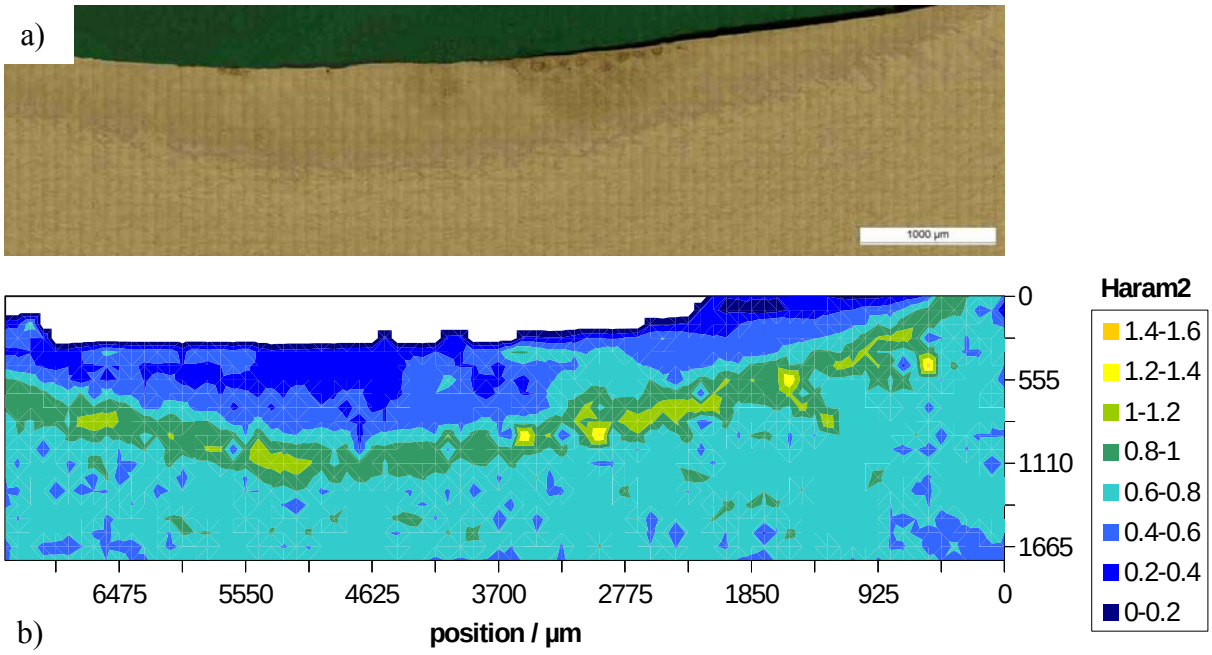

Figure 4-50 Overview of the laser hardened sample lhd_laser (a) (Figure 4-47) and corresponding texture parameter Haram2 mapped over the cross section of the sample (b); 1600 micrographs analysed

The texture parameters were measured for each of the 1600 positions representing a single micrograph. As an example the Haram2 parameter is shown in Figure 4-50. If compared to the corresponding micrograph in Figure 4-47 a good correspondence of the texture parameter and the local microstructure can be found. For the initial microstructure in the lower part of

the micrograph the texture parameter Haram2 gives values in the range between 0.6 and 0.8. In contrast to this the values in the hardened region show values between 0.2 and 0.6 for most of the area. For the heat affected zone showing a mixed microstructure of martensite and ferrite with spheroidised carbides the parameter is between 0.8 and 1.4.

For the correlation with the local microhardness this was measured at 5 traces with altogether 38 hardness indentations. The position of the traces on the sample is shown in Figure 4-51.

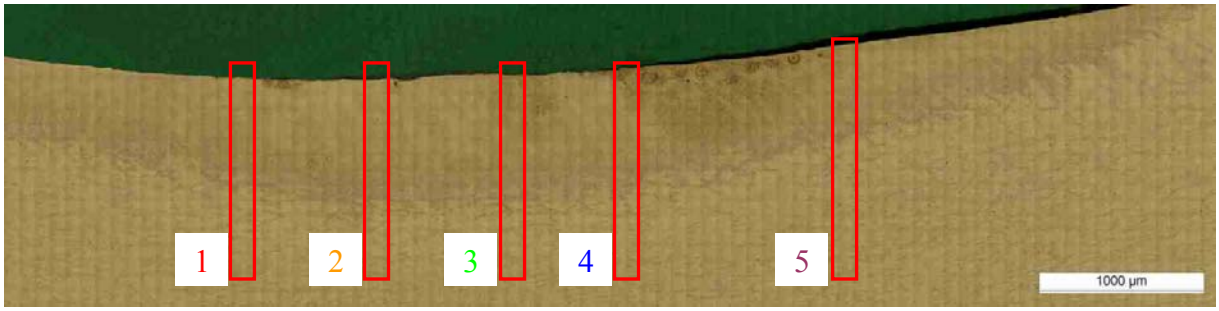

Figure 4-51 Overview of the sample lhd_laser already shown in Figure 4-47 with the regions marked where the 5 hardness traces are located and the trace number given next to the corresponding region

The hardness ($H_{V0.02}$) values for the traces 1-5 in Figure 4-51 are given in Figure 4-52. It can be seen that for all the 5 traces the hardness near the surface of the sample lies between 450 and nearly 700 $H_{V0.02}$. For all the traces but trace 1 it is obvious that the values of the hardness are increasing to the next measured position. With a further increase in depth the hardness values decrease significantly; to about 200 $H_{V0.02}$ at a distance of about 13 mm from the edge of the scanned area and are slightly increasing again with further increase of the distance to values between 250 and 280 $H_{V0.02}$.

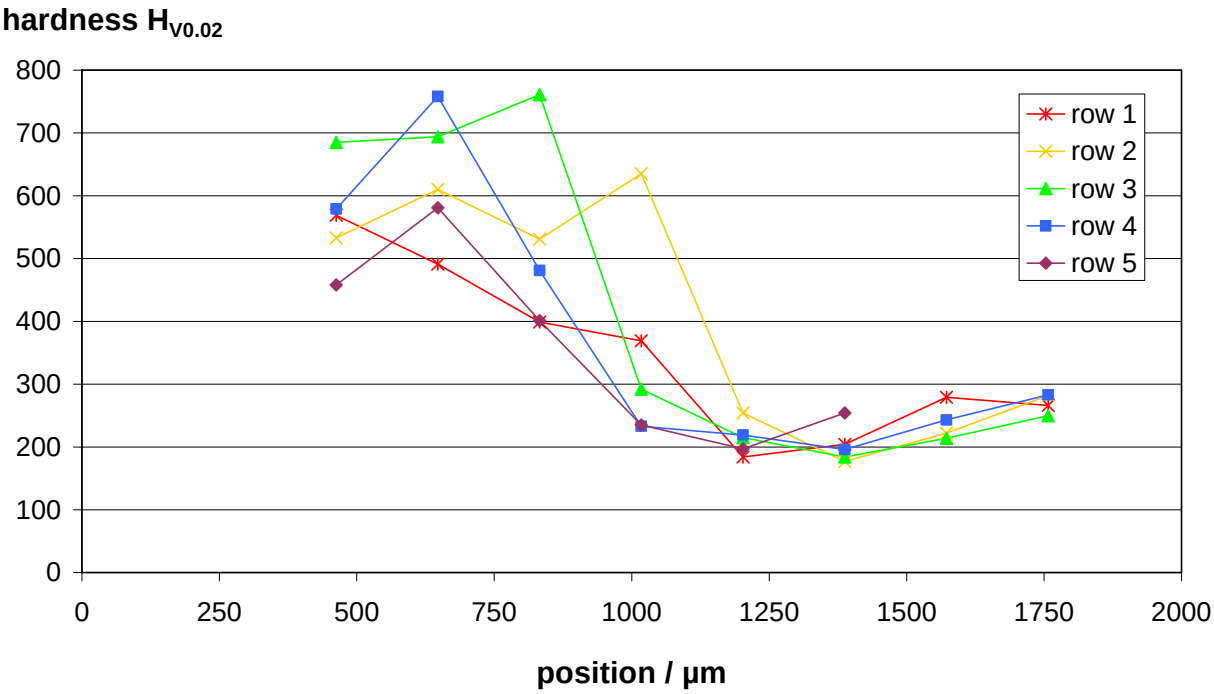

Figure 4-52 Trend of the hardness in $H_{V0.02}$ for the 5 traces designated in Figure 4-51 with the position measured from the edge of the scanned area

To be able to correlate the texture parameters of the specimen to the local microhardness, a neural network was trained with the 38 measured hardness values and the corresponding texture parameters. The distribution of the hardness for all the 1600 positions acquired and characterised by the texture parameters was calculated using the trained neural network and is presented in Figure 4-53.

The distribution shows very similar trends to the trends of the hardness presented in Figure 4-52 for the mechanical measurement. While for the core microstructure most of the values lie between 100 and 300 $H_{V0.02}$, a strong increase of the values can be found in the laser hardened layer. Here the hardness lies in the range between 400 and 900 $H_{V0.02}$. The change from the core microstructure to the hardened layer at the surface can be seen very clearly what could also be expected from the drastic differences in the microstructure.

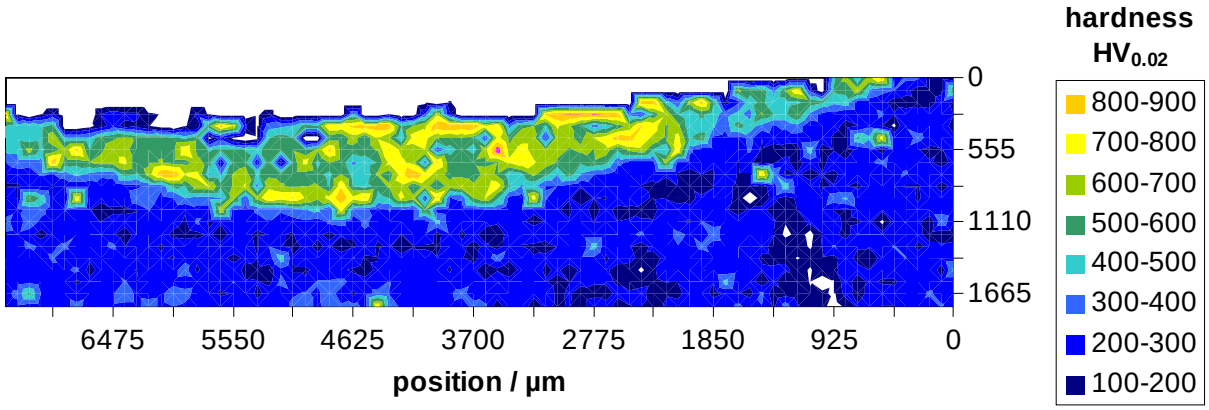

Figure 4-53 Mapping of microhardness of the laser hardened sample lhd_laser calculated from the texture parameters using a neural network trained with 38 hardness values and corresponding image information; 1600 micrographs analysed

4.6.2 Induction hardened steel component

To test the applicability of the texture analysis for induction hardened steel components a sample of the heat-treatable steel 42CrMoS4 was taken from a crank shaft. The surface of this component is hardened by induction heating to ensure the wear resistance needed for the later use as a bearing surface.

The investigated area was scanned at a magnification of 500:1 by the Mosaix function of KS400 and the texture parameters were measured for each of the 23,500 positions. The overview micrograph and five micrographs representing the microstructure of the five different areas are shown in Figure 4-54.

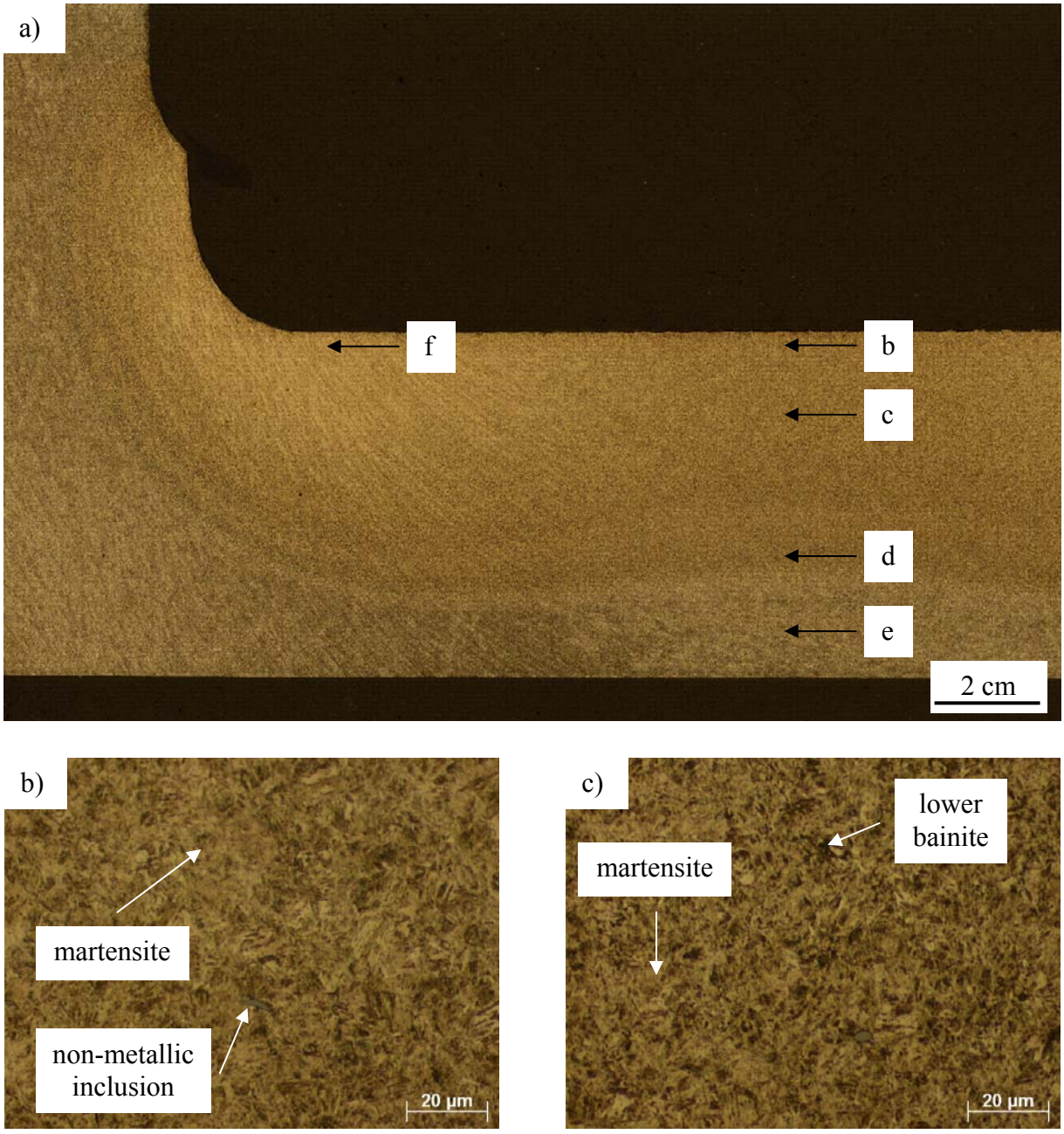

Figure 4-54 Micrographs of the induction hardened steel component lhd_induction of the heat-treatable steel 42CrMoS4 at different distances from the surface, etched with 2 % nital

a) overview of the sample obtained by Mosaix function of KS400 with a magnification of 500:1

b) micrograph from the induction hardened edge of the sample (0.5 mm from the surface) (624 H_{V1})

c) 1.5 mm from the surface (630 H_{V1})

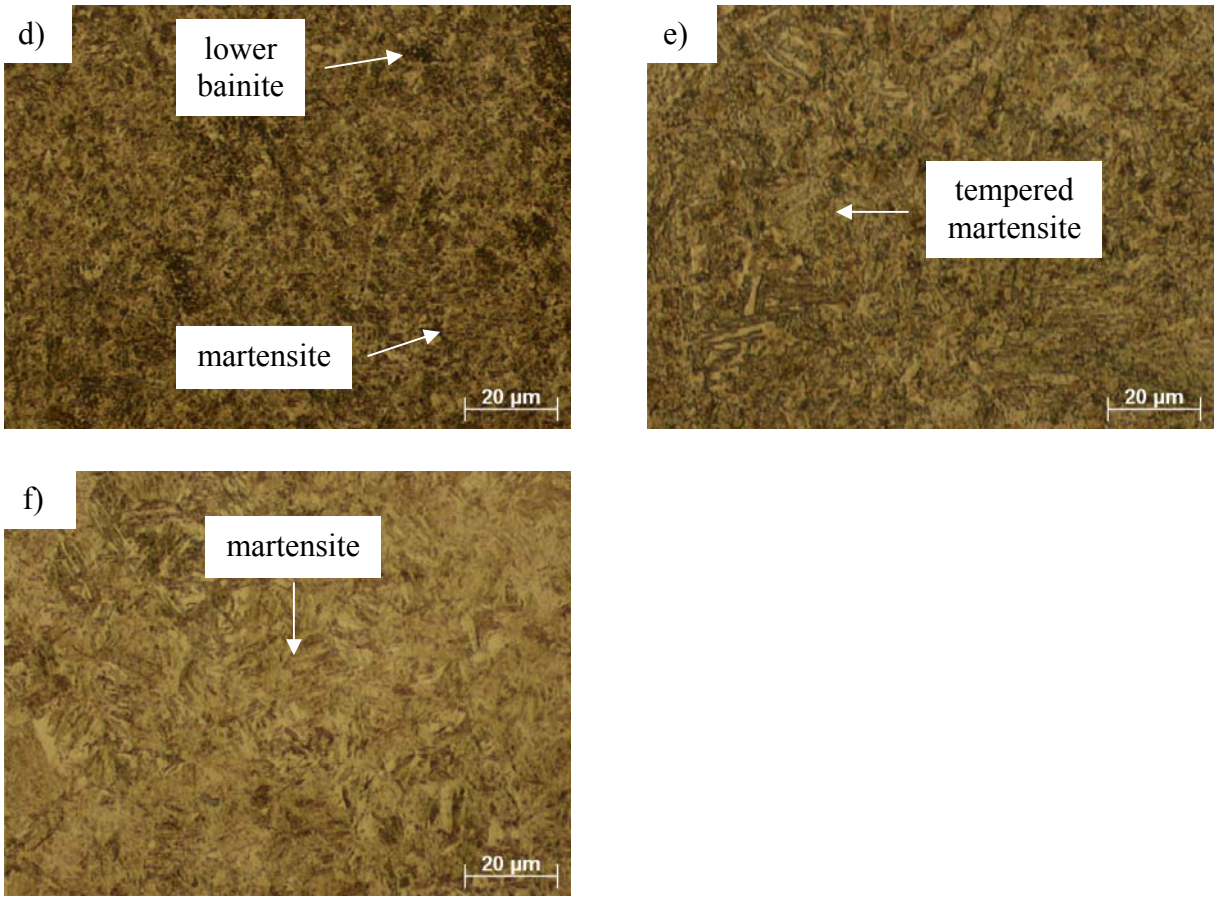

Figure 4-54 Micrographs of the induction hardened steel component lhd_induction of the heat-treatable steel 42CrMoS4 at different distances from the surface, etched with 2 % nital

d) 3.5 mm from the surface (573 H_{V1})
e) micrograph from the core (4.5 mm from the surface) (377 H_{V1})
f) micrograph from the inner diameter of the bend (0.5 mm from the surface) (627 H_{V1})

In the overview image, the area heated into the austenite phase field can clearly be seen outlined by the darker curving line closer to the specimen surface. The region is parallel to the bearing surface leading around the corner up the edge for about 5 mm. Beneath this region of the sample a change in the microstructure is obvious.

The micrograph in Figure 4-54 (e) taken from the core of the sample (4.5 mm from the surface) shows a microstructure containing large amounts of ferrite in a plate-like structure. Carbides can be seen in form of groups of small black globular particles that are too small to be resolved individually at this magnification. These carbides are likely to have precipitated

from the martensite supersaturated with carbon during tempering. This is the initial microstructure showing the quenched and tempered condition of the component before surface hardening. The hardness value of 377 H_{V1} is typical for a quenched and tempered condition of this material that is given with approximately 340 H_{V10} [Ros61].
Moving closer towards the surface of the component, the microstructure changes significantly (Figure 4-54 (d)). The difference is that at this position (3.5 mm from the surface) the microstructure becomes slightly finer and shows martensite and lower bainite. The hardness is with 573 H_{V1} considerably higher than for the core microstructure.
For a distance of 1.5 mm from the surface (Figure 4-54 (c)) the microstructure shows only slight changes from that shown in Figure 4-54 (d). At this position a martensitic microstructure with very fine needles can be found. The darker etching regions in between the martensite are lower bainite. The hardness increases again to 630 H_{V1}.
The micrograph in Figure 4-54 (b) taken at the induction hardened edge of the sample shows a martensitic microstructure that was formed due to the oil quenching after full re-austenitisation of this region by induction heating. The former quenched and tempered microstructure was completely transformed to austenite and later to martensite. This microstructure yields a hardness of 624 H_{V1}, which is marginally lower than values reported in the literature for this material in the fully martensitic state, 690 H_{V30} [Sch66a].
Compared to this the microstructure in the inner diameter of the bend, presented in Figure 4-54 (f), is much coarser than in the flat surface region of the sample. The matrix is again martensitic showing less lower bainite. The hardness is with 627 H_{V1} the same as for the position presented in Figure 4-54 (b).

The distribution of the texture parameters is given exemplarily by the parameter Haram2 in Figure 4-55. The distribution that can be found matches the overview image given in Figure 4-54 (a). A region with the same shape as the induction hardened area is obvious showing differences in the value of the texture parameter compared to the adjacent base metal region.
In the hardened region the parameter shows a value between 0.3 and 0.6 with the highest values in the inner diameter of the bend. In the flat surface area of the hardened region the parameter is lower showing values between 0.5 and 0.6. In the region representing the core of the component the parameter increases to values between 0.6 and 0.8.

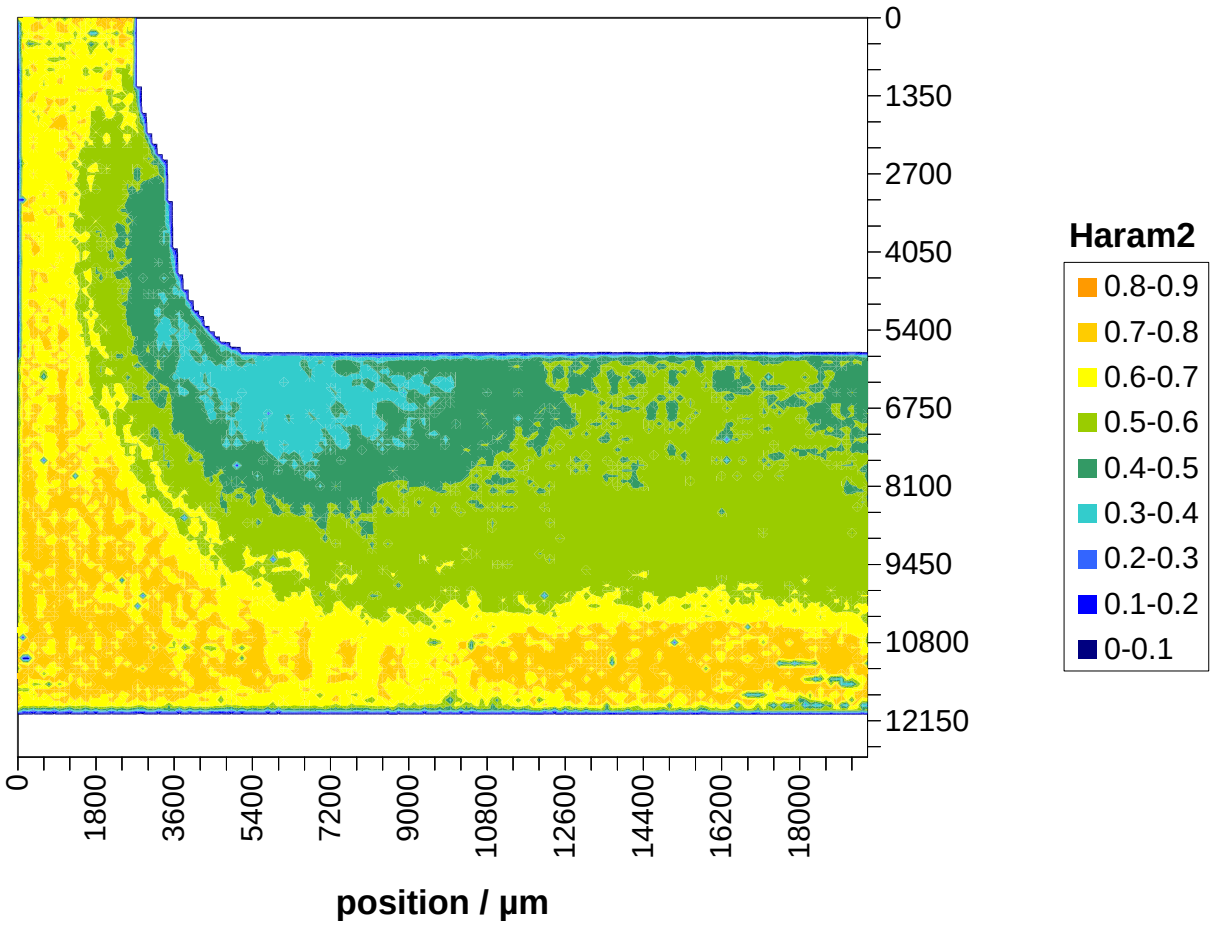

Figure 4-55 Mapping of the texture parameter Haram2 over the area of the sample lhd_induction shown in Figure 4-54; 23,452 micrographs analysed

For correlating the texture parameters with properties of the material, the Vickers hardness has been measured at 95 positions along 9 different traces. The positions of the traces are marked in the overview image in Figure 4-56.

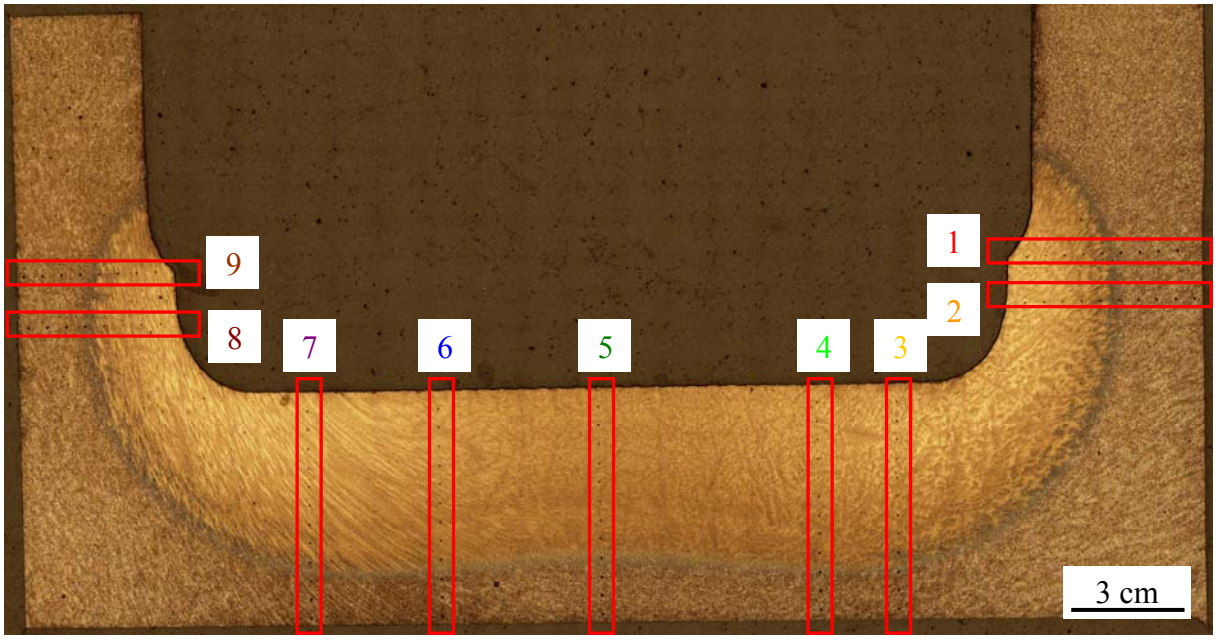

Figure 4-56 Overview of the sample lhd_induction with the positions of the hardness measurements marked, sample etched with 2 % nital

The hardness values for the traces measured are presented in Figure 4-57. All the traces show comparable values for the hardness within a distance of 0.5 mm from the hardened surface. The values are all within the range between 610 and 625 H_{V1}.

For the traces 1, 2, 8 and 9 a similar trend can be found. The values decrease with increasing distance from the surface very rapidly to a range of hardnesses between 310 and 380 H_{V1} for distances greater than 3 mm. The other 5 traces show only a very slight decrease of the hardness up to a distance of about 4 mm. Then a very distinct decrease follows with the hardness dropping to approximately the same range as for the other 4 traces.

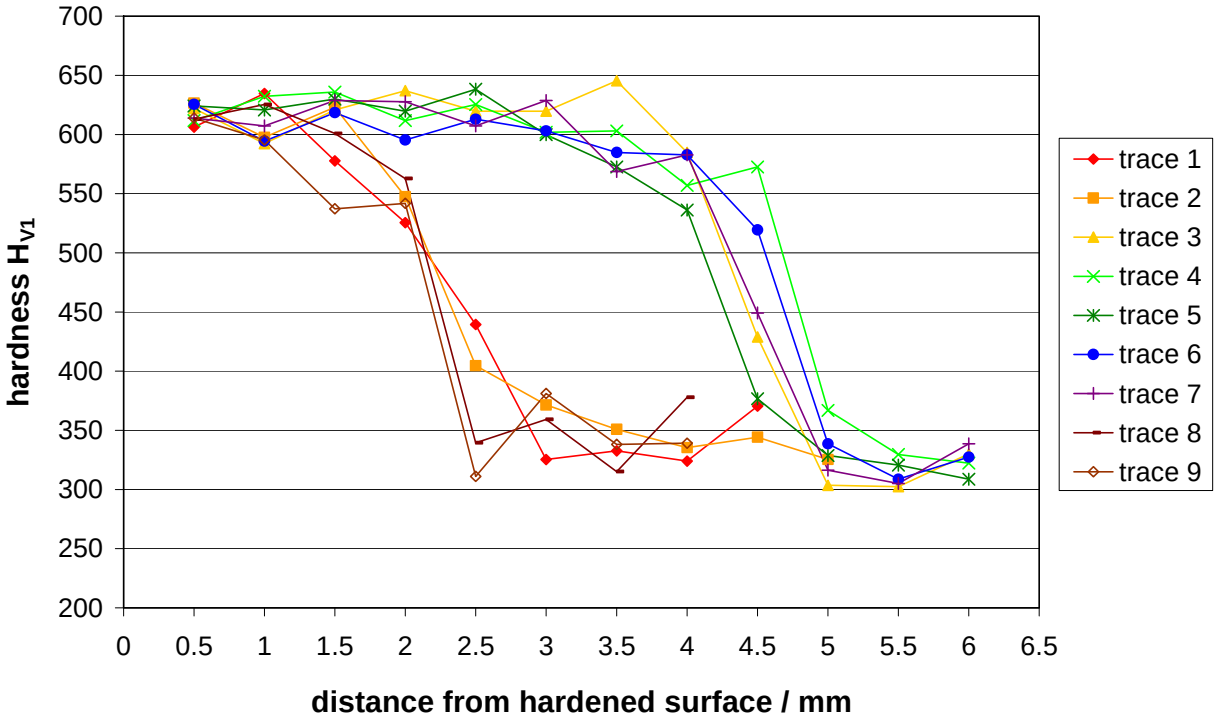

Figure 4-57 Trends of the hardness measurements for the sample lhd_induction of the traces marked in Figure 4-56

For comparison these hardness values are presented along with the texture parameter Haram2 and the hardness calculated from the 11 Haralick texture parameters in a neural network in Figure 4-58. As can be seen the measured hardness shows a plateau with values between 570 and 630 H_{V1} up to 4 mm from the surface. In this range the texture parameter Haram2 is increasing from about 0.37 to 0.49 showing also very small differences in the microstructure that influence the contrast of the micrographs, e.g. the slight decrease in the volume fraction of lower bainite from Figure 4-54 (c) to (b). The hardness calculated from this texture information shows good correlation to the measured values with hardness values between 600 and 690 H_{V1}.

With further increasing distance the measured hardness is decreasing significantly. The increase in the parameter Haram2 is steeper due to increased contrast in the microstructure. The calculated hardness shows a decrease similar to that of the measured values. Some single values of the calculated hardness are higher than the corresponding measured values.

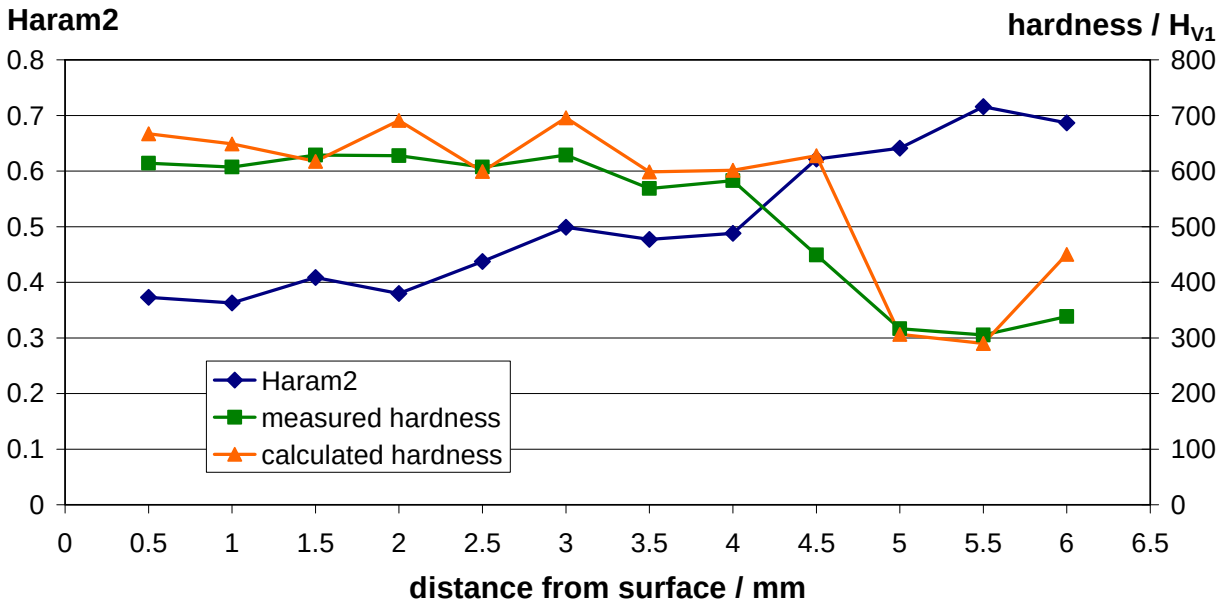

Figure 4-58 Trend of the texture parameter Haram2 perpendicular and with different distances from the surface of the induction hardened sample lhd_induction together with the respective measured and calculated hardness values

These hardness values were used together with the corresponding texture parameters to train a neural network to establish a correlation between the texture parameters with microhardness. From the information of the texture parameters measured for the 23,500 positions the distribution of the local hardness was calculated. This is presented in Figure 4-59.

The lateral distribution of the hardness shows a well defined area with a higher hardness than the surrounding matrix. In the hardened surface layer the hardness is between 500 and 800 H_{V1}, only in the middle of the hardened area close to the core material does the hardness dip to between 400 and 500 H_{V1}. This fits well with the physically measured values that show a hardness of about 610 to 625 H_{V1} at the surface of the sample. The core shows a hardness of about 200 to 400 H_{V1}. The measured values are in the range between 310 and 380 H_{V1}.
All these calculated values match with the measured values, except in the region of the edge of the sample where hardness values of up to 801 H_{V1} were calculated while the measured values are between 610 and 625 H_{V1}.

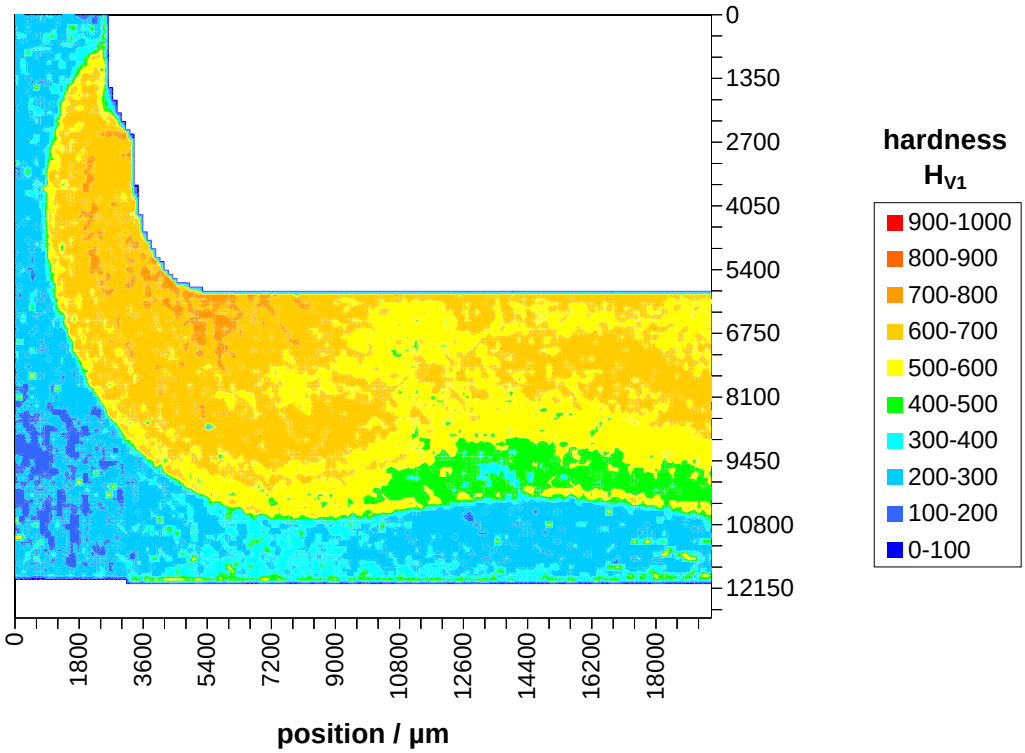

Figure 4-59 Mapping of local hardness of the induction hardened sample lhd_induction calculated from the texture parameters using a neural network trained with 95 hardness values and corresponding image information; 23,452 micrographs analysed

This correlation is presented for the hardness traces 5 to 9 in Figure 4-60 where the mechanically measured values are compared with the corresponding values calculated from the texture parameters using a neural network. The neural network was trained with the 11 texture parameters as input data and the corresponding hardness as output data. The mean value of the difference between the calculated and the measured values is -7.5, the corresponding standard deviation 74.6. Good correlation is seen for the higher hardness values of the hardened layer, whilst traces 5 and 6 yield calculated values that are almost always lower than the measured values.

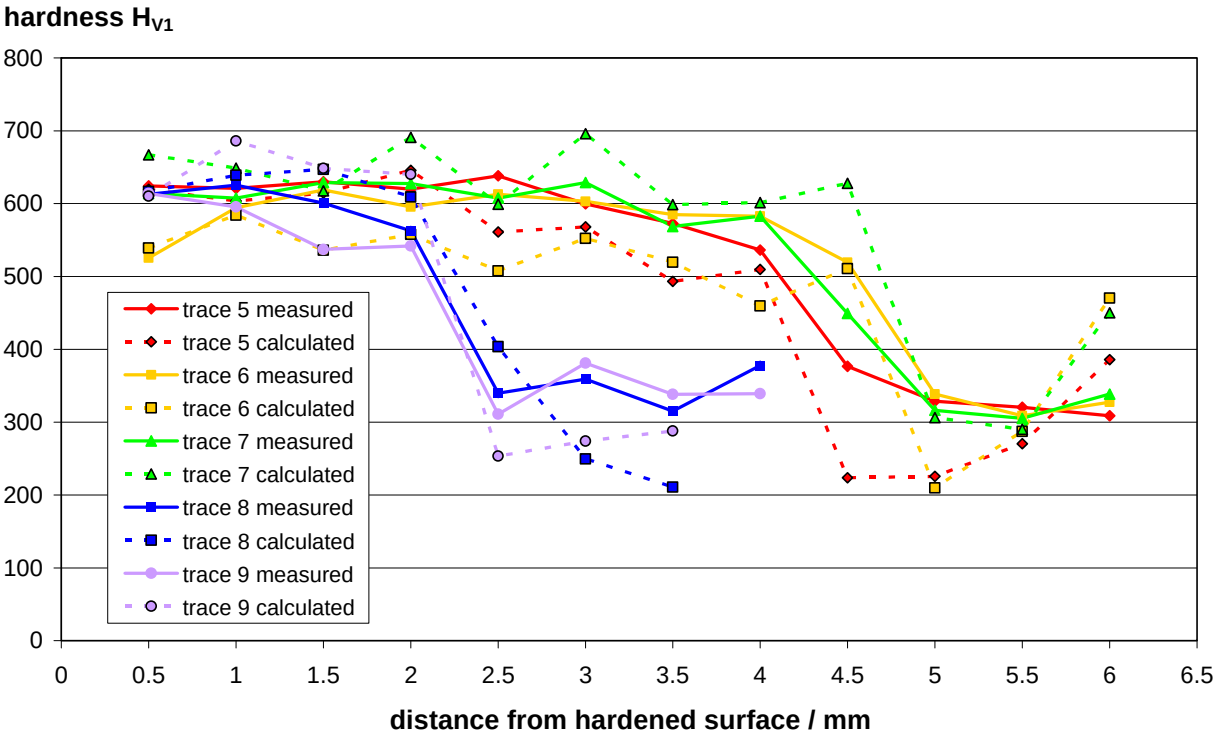

Figure 4-60 Trend of the measured and the calculated hardness of the induction hardened sample lhd_induction

4.6.3 Case hardened steel component

To check the practical advantage of the texture analysis, a component (cog) fabricated from 17CrNiMo4 was case hardened at the surface of the component. The cog as shown in the overview image in Figure 4-61 (a) is a part of a steering shaft.

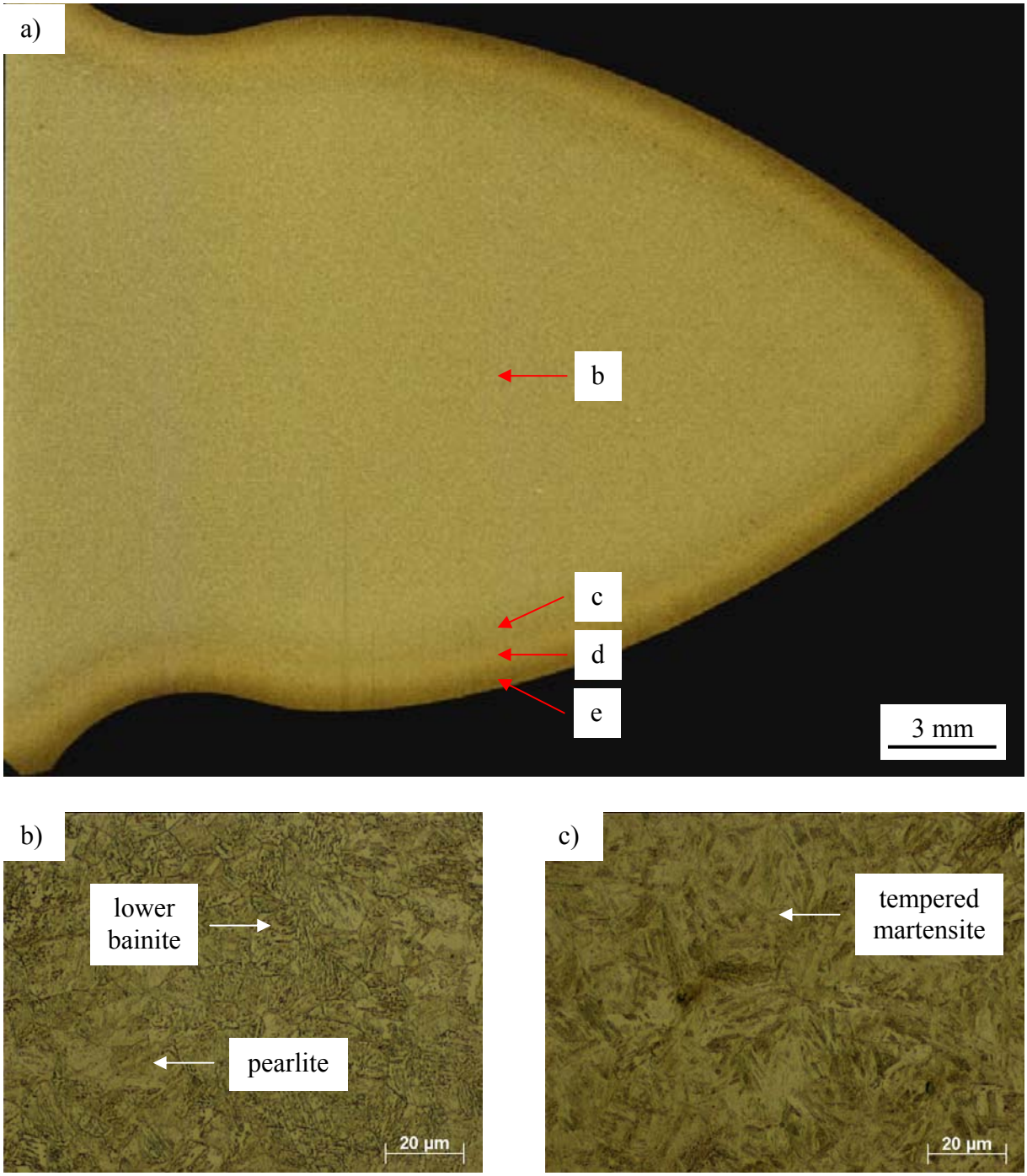

Figure 4-61 Micrographs of the case hardened component lhd_case of the steel 17CrNiMo4 at a magnification of 500:1, sample etched with 2 % nital

a) overview consisting of 34,400 micrographs taken by the Mosaix function of KS400, representing an scanned area of 800 mm²

b) core of the component (9.0 mm from the surface, 388 H_{V1})

c) transition region (2.0 mm from the surface, 539 H_{V1})

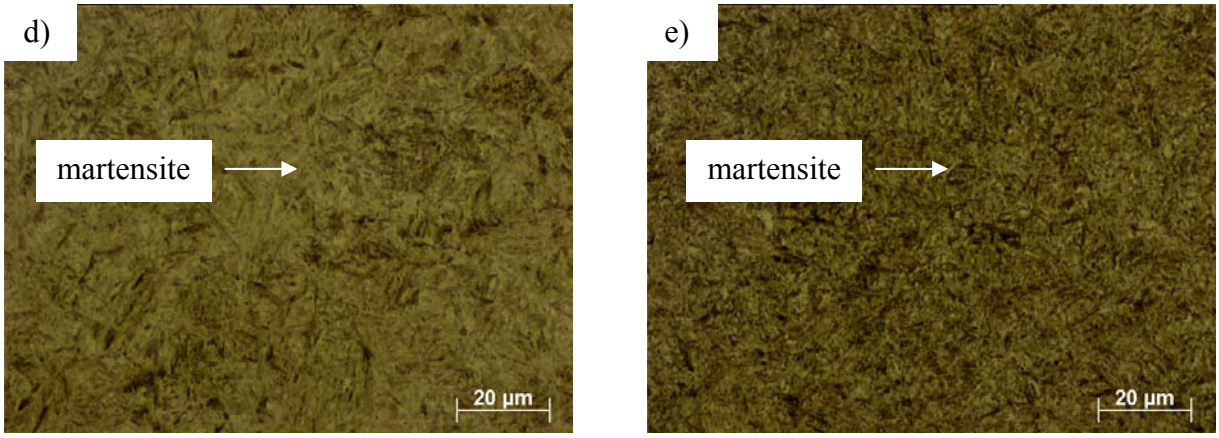

Figure 4-61 Micrographs of the case hardened component lhd_case of the steel 17CrNiMo4 at a magnification of 500:1, sample etched with 2 % nital

d) transition region (1.0 mm from the surface, 710 H_{V1})

e) hardened surface layer (0.5 mm from the surface, 755 H_{V1})

The core of the component (Figure 4-61 (b)) shows a microstructure consisting of bainite, pearlite and ferrite. As this cannot clearly be resolved at this magnification, a higher magnification micrograph from this region is presented in Figure 4-62 (a). The pearlitic regions appear darker due to the very fine lamellae of ferrite and cementite that cannot be resolved by optical microscopy. In the microstructure small dark spots can be found representing carbides that cannot be resolved at the applied magnification of 500:1. These can be attributed to the alloying with Cr and Mo that both show a high affinity for C and therefore tend to form alloy carbides [Sch66b]. Small regions of ferrite can also be found in the microstructure. This yields a hardness value of 388 H_{V1}.

In the transition region 2.0 mm from the surface (Figure 4-61 (c)), the microstructure is coarse and similar to tempered martensite. The strong etching attack of the martensite is indicative of carbide precipitation due to the tempering. The hardness is with 539 H_{V1} reasonably higher than in the core.

In Figure 4-61 (d) the microstructure in 1.0 mm distance from the surface is given showing a martensitic structure finer compared to that at 2.0 mm from the surface. The tempering effects are not present in this region, which is also borne out by the hardness of 710 H_{V1}; even higher than in the previously discussed micrograph.

The micrograph of the surface layer (Figure 4-61 (e)) also shows a martensitic microstructure that seems even finer than that at 1.0 mm distance from the surface. A micrograph from this

region at higher magnification can be found in Figure 4-62 (b). It is also obvious that the martensite is coloured darker and a large number of very small dark spots are visible. These effects can be attributed to the increased level of carbon in this region, which was increased by the case hardening of the component. This increases of the hardness of the martensite formed, can retain austenite, but also promote the precipitation of carbides in this region, the balance of which gives the measured hardness of 755 H_{V1}.

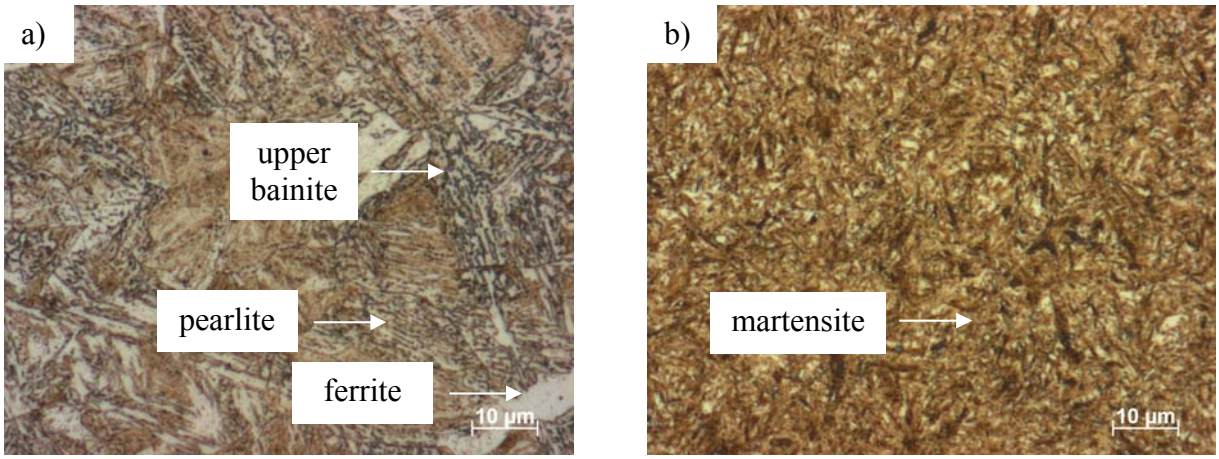

Figure 4-62 Higher magnified micrographs of the core (a) and the hardened surface (b) of the case hardened sample lhd_case, magnification 1000:1, etched with 2 % nital

For this component an area of approximately 800 mm² has been scanned using the Mosaix function of KS400 at a magnification of 500:1. This resulted in 72,252 micrographs for which the texture parameters have been measured for every single micrograph. The trend of the exemplarily chosen parameter Haram1 is shown in Figure 4-63.

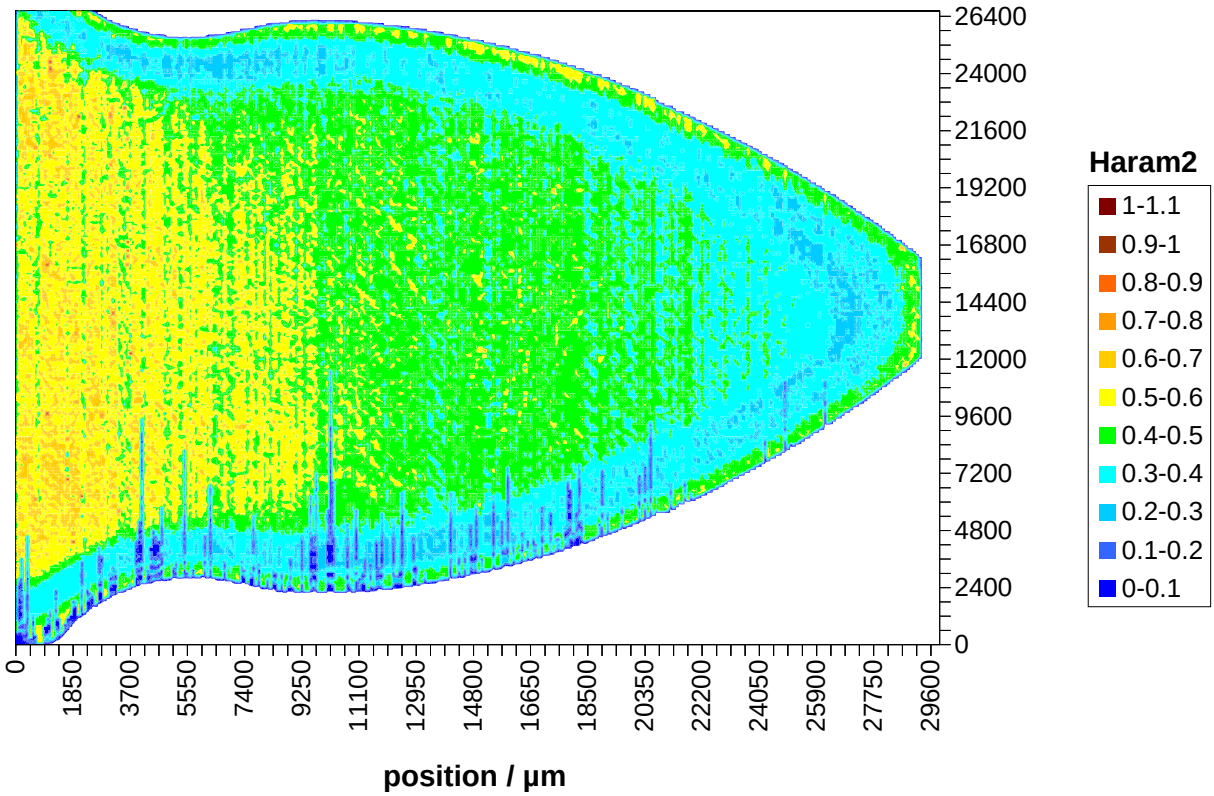

Figure 4-63 Distribution of the texture parameter Haram2 over the cross-section of the sample lhd_case shown in Figure 4-61; 72,252 micrographs analysed

It is obvious from the diagram that there is a very thin layer around the sample that shows values in the range of 0.4 to 0.5 for the parameter Haram2. This layer is about 500 µm deep in the region of the tip of the tooth and less at the other surface regions of the component. To the inside of the sample a region follows with the parameter being in the range 0.2 to 0.4. Following this region the parameter is again increasing to a range between 0.3 and 0.7 with very large local variations. Near the tip of the tooth the values are between 0.3 and 0.4; they are increasing steadily to the core to values between 0.7 and 0.8 near the core of the component.

There are several vertical lines in the lower part of the diagram showing very low values under 0.2. These values were measured due to insufficient focussing of the micrographs and can therefore be characterised as imaging artefacts. After refocusing when scanning over the sample surface the values were again in the same range as for the adjacent regions.

In horizontal direction a decreasing trend of the texture parameter Haram2 can be found from the core of the sample to the tip of the cog. This effect is due to a difference in the etching

response of the sample over the large area examined. In the region of the core of the sample the microstructure is etched more intensely and therefore shows higher contrast than in the region near the tip of the cog. As will be seen later (Figure 4-65) the hardness values are comparable in both regions as well as the microstructure. This effect can therefore be characterised as a preparation artefact.

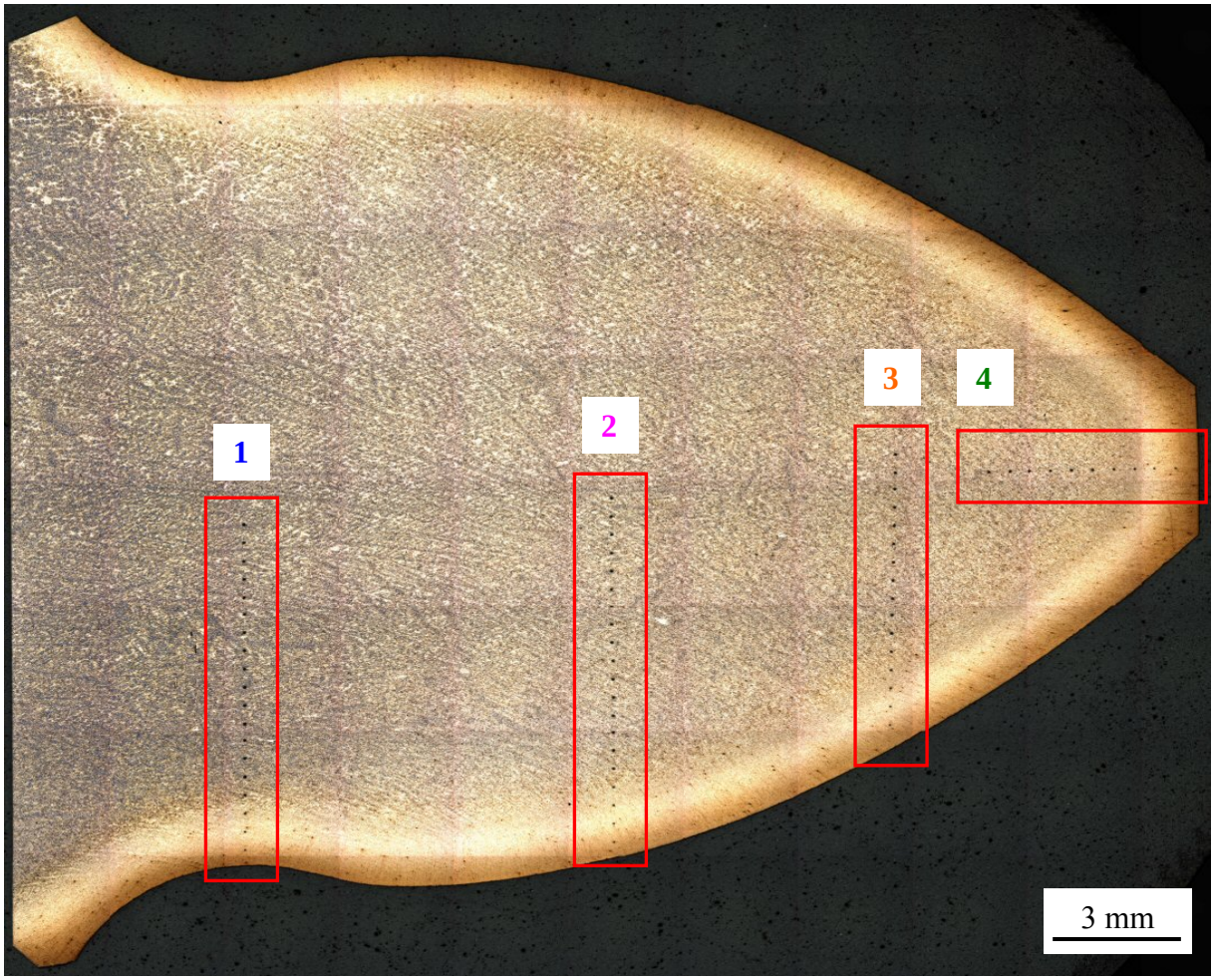

Figure 4-64 Overview of the sample lhd_case at a magnification of 25:1 with the hardness indentation of the 4 traces marked with the red boxes and the corresponding trace number, sample etched with 2 % nital

For this sample, micrographs have been taken and the corresponding Vickers microhardness has been measured. The position where the four traces of hardness indentations are placed and the corresponding trace numbers are shown in Figure 4-64. The trends in hardness that were measured are presented in Figure 4-65. Trace 1 to trace 3 were placed at the edge of the

sample leading to the inside of the component, whereas trace 4 was placed at the tip of the cog leading also perpendicular to the surface to the core of the part.

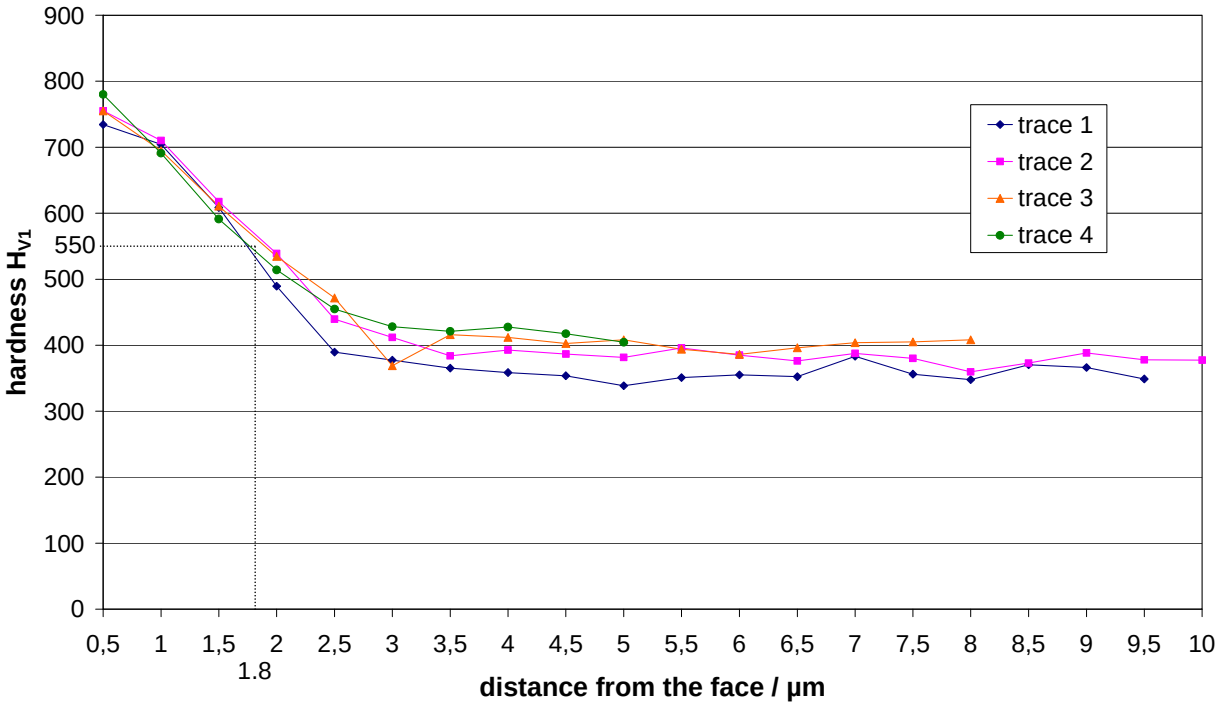

Figure 4-65 Trend of the hardness for the sample lhd_case along the four traces designated in Figure 4-64 together with the graphical determination of the depth of hardening

For all the hardness traces of the hardness indentations very similar trends in hardness can be found. While the hardness next to the surface is about 770 H_{V1}, it decreases with increasing distance from the surface. At a depth of approximately 3 mm from the surface, all the traces show values of about 360 to 430 H_{V1} which represents the core hardness of the component and therefore does not change with further increasing distance from the surface. For the trace 1 located near the root of the tooth a marginally lower hardness was measured in the core of the sample.

For the case hardened component the depth of hardening was estimated by means of the heat treatment parameters. From the carburising time t and the diffusivity D of carbon in austenite at the carburising temperature the distance x to the position with the C level in the midway between the surface and the core can be calculated after [Sta95] as

$$x = \sqrt{D \cdot t}$$ Eq. 4-7

With the carburising temperature of 950 °C and the carburising time of 12 hours (see also Section 3.1.2), a diffusion coefficient of carbon in austenite can be calculated as $35.1 \cdot 10^{8}$ cm^2 s^{-1} [Mil95]. Herewith a hardening depth of 1.23 mm can be calculated.

From Figure 4-65 the depth of hardness can be determined according to BS EN ISO 2639 [BSE02]. The required hardness of 550 H_{V1} yields a depth of hardening of 1.8 mm from the surface.

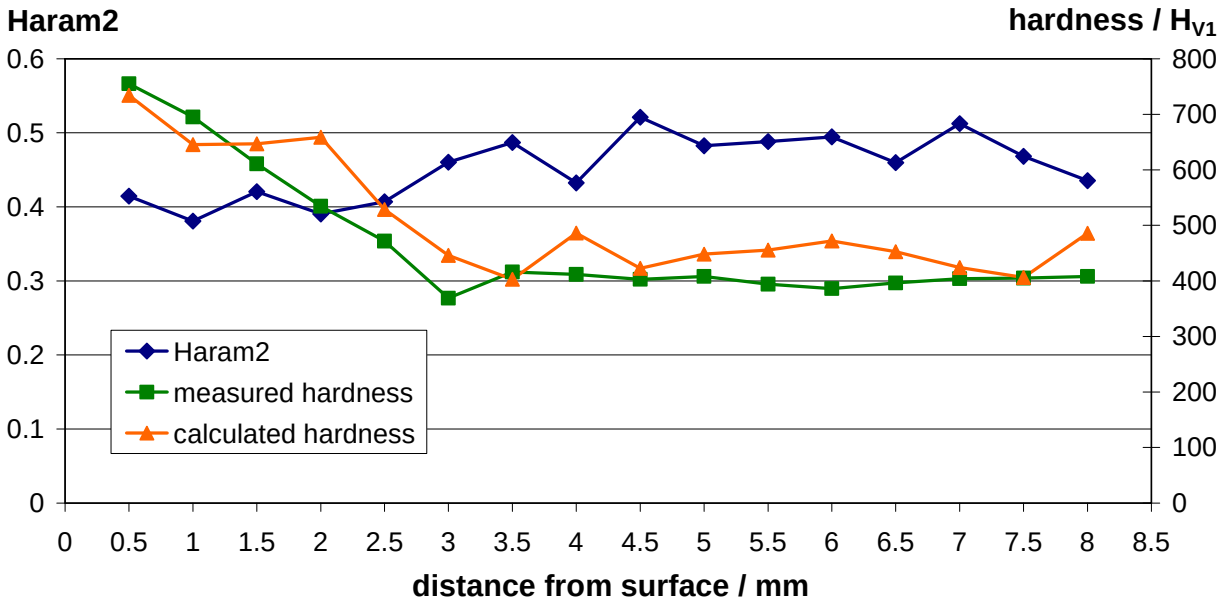

Figure 4-66 Trend of the texture parameter Haram2 perpendicular and with different distances from the surface of the case hardened sample lhd_case together with the respective measured and calculated hardness values

For comparison, variation of the texture parameter Haram2 is given with the corresponding measured hardness values of the trace 3 and the hardness values calculated using a neural network, Figure 4-66. This was trained with the 11 texture parameters after Haralick as input values and the corresponding hardness as output value.

For the measured hardness a continuous decrease can be found from the surface with 760 H_{V1} to 370 H_{V1} at a distance of 3 mm from the surface. For the texture parameter Haram2 an increase can be found in this area from 0.38 to 0.43. For increasing distance the hardness is increasing slightly but than shows constant values of approximately 400 H_{V1}. The texture

parameter yield values between 0.43 and 0.52. For the calculated hardness values a trend very similar to the measured values can be found with most of the calculated values being slightly higher than the measured ones.

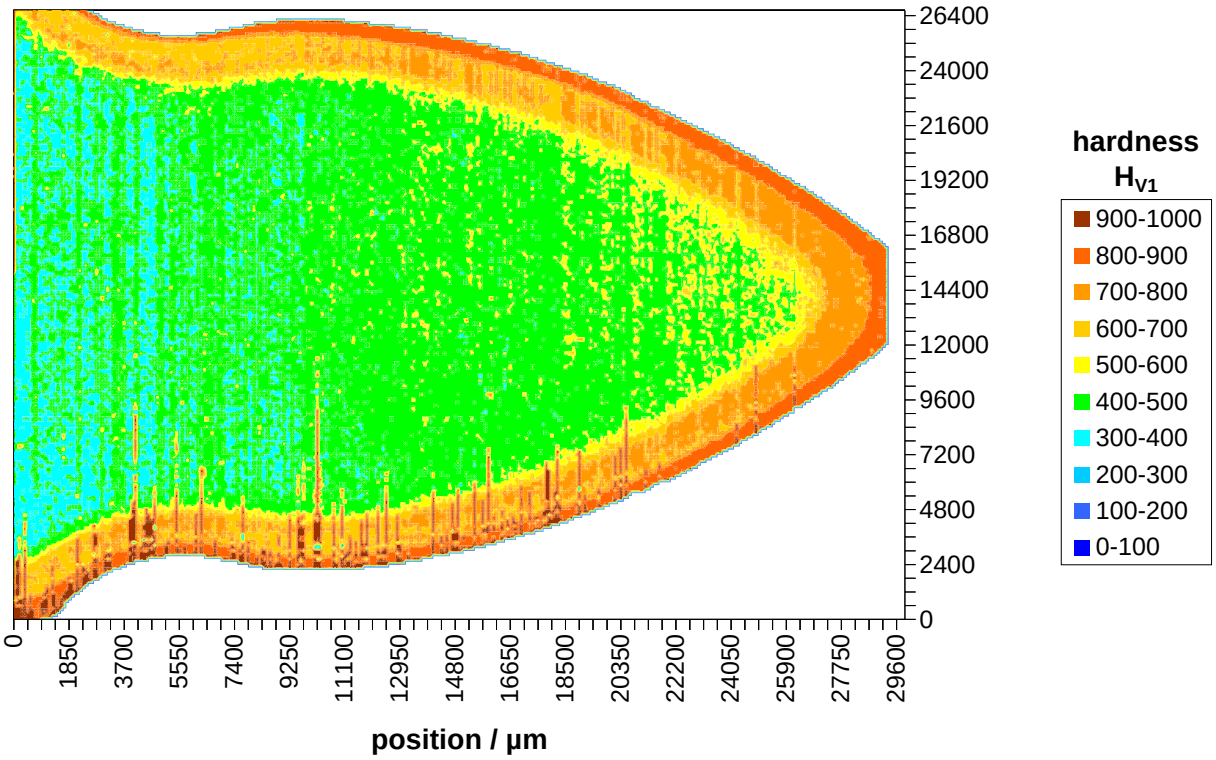

Figure 4-67 Mapping of hardness of the case hardened sample lhd_case calculated from the texture parameters using a neural network trained with 66 hardness values and corresponding image information; 72,252 micrographs analysed

The trained neural network gives a very clearly differentiated lateral distribution of the hardness. As can also be seen in the trend of the measured hardness values given in Figure 4-65 the surface of the sample shows a very high hardness of 800 H_V and more. The core shows a hardness of between 300 and 500 H_V depending on the position on the sample. Near the tip of the cog the hardness of the core is even higher with values between 500 and 600 H_V. The depth of the layer showing the highest hardness values of 500 and above is about 3 mm. This layer is leading all around the sample covering the complete surface.

To characterise the quality of the correlation the neural network was trained with the texture parameters and corresponding hardness values of the traces 1, 2 and 4 (see Figure 4-64). The

correlation was then calculated for trace 3 and is presented in Figure 4-68. The mean value of 40.5 shows that most of the calculated values are higher than the corresponding measured values. This is also obvious from the standard deviation that yields a comparably high value of 45.6.

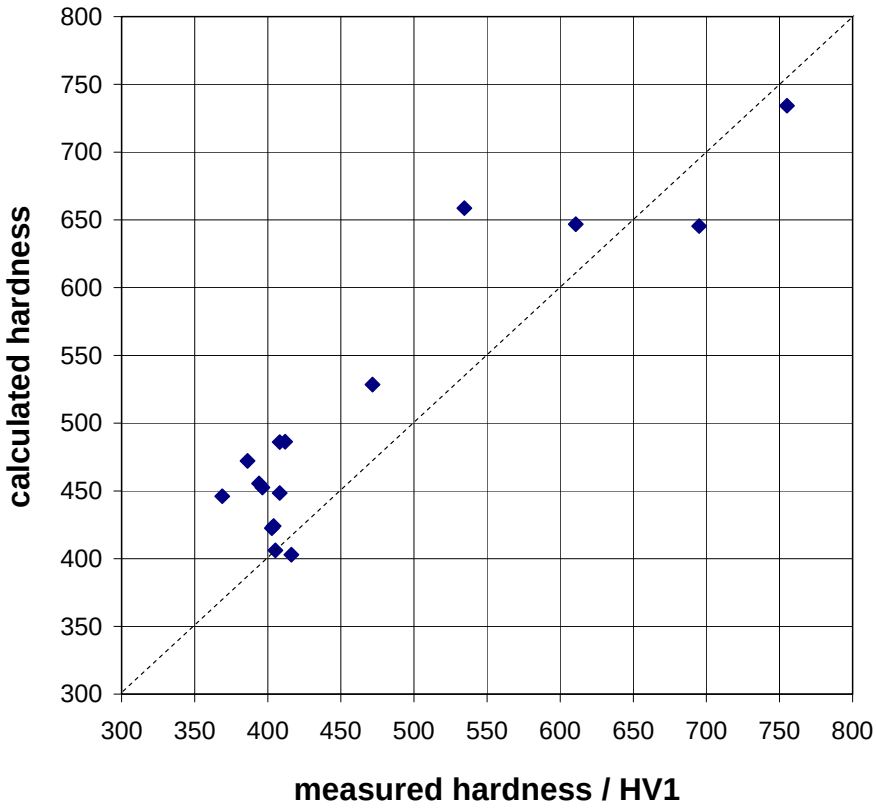

Figure 4-68 Correlation of the mechanically measured and the hardness calculated from the texture parameters, neural network trained with data of traces 1, 2 and 4, calculation for trace 3; 16 micrographs analysed

5 Discussion

5.1 Verification of values predicted by modelling methods

5.1.1 Characterisation of coarse, alloy carbides

Using thermodynamical calculations the equilibrium phase fractions of the hypereutectoid tool steel 100Cr6 were calculated for different austenitising temperatures in the range from 50 – 1000 °C. These values can be compared to the values measured for the pearlitic and bainitic samples, as a fast quench from the re-austenitising temperature should preserve the coarse alloy carbides present during re-austenitisation. The hardened microstructures should, therefore, show the volume fraction of alloy carbides present at the respective austenitising temperature. In a first step the calculated values have been compared with the values measured from SEM secondary electron micrographs.

For this analysis a large discrepancy was found between the predicted and the measured data (Figure 4-37). Up to an austenitising temperature of 850 °C the prediction shows higher values than measured for both the pearlitic and the bainitic samples. The predicted values are equilibrium volume fraction irrespective of size, whereas the measured values are limited by the resolution of the imaging system. The predicted carbide volume fractions are dominated by cementite, some of which will be incorporated into the pearlitic regions of the pearlitic samples and so can contribute to an underestimate the carbide proportion.

For the bainitic samples the volume fractions of coarse carbides were similar to those determined from the pearlitic samples, although the carbides cannot be masked by incorporation into pearlite. Thus, a significant part of these carbides must be too fine to be resolved by the magnification of 7,500:1 applied in the SEM [Bha02]. Dissolution during re-austenitisation reduces the volume fraction of carbides, but will also reduce their size, which will affect both pearlitic and bainitic samples.

For the higher austenitising temperatures of 900 °C and 930 °C investigated the predicted volume fraction of coarse carbides fell to 0 vol.-% while a reasonable amount can still be measured. As the prediction is based on the equilibrium condition the carbides are completely dissolved, while in technical conditions a reasonable amount is still left in the microstructure due to the non-equilibrium conditions after the one hour holding time. The finer carbides dissolve more readily, but the coarser carbides, which are resolvable, and it is this remnant that was measured.

If the measured volume fractions are compared between pearlitic and bainitic samples, quite similar values can be found while the bainitic samples yield slightly higher values. This might be due to the inhomogeneous illumination of the bainitic samples in the SEM, which in some cases makes it difficult to distinguish the carbides. In some cases probably objects might have been measured that are actually not carbides.

Another problem with the characterisation of the coarse alloy carbides is the inhomogeneous distribution of these carbides in the microstructure (Figure 4-40). As the difference in the carbide distribution not only depends on the heat treatment of the sample but also on the partitioning of the alloying elements, such as centre-line segregation, this cannot be used to characterise the microstructure of the sample, e.g. to establish a correlation with the respective austenitising temperature. If the measurement is done parallel to the centre-line of the sample at a constant distance the carbide volume fraction can be assumed to be nearly constant and therefore may characterise the heat treatment and processing parameters of the sample, particularly as the absolute volume fraction shows a direct correlation to the applied austenitising temperature of the sample.

5.1.2 Correlation of the conventional microstructural features with corresponding properties or processing parameters

To characterise the samples, the conventional microstructural features of the coarse alloy carbides, their maximum feret, their area, their form factor and their perimeter were measured. With these data additionally the volume fraction of carbides per micrograph was calculated. These data were then correlated with the austenitising temperature of the bainitised 100Cr6 samples using a neural network. The result of this correlation is shown in Figure 4-41 (carbides only).

The correlation shows a high mean value for the difference of the calculated and the measured values of 4.6 along with a high standard deviation of 18.2.

One of the reasons for this poor correlation is the low volume fraction of coarse alloy carbides, especially for the highest investigated austenitising temperatures, but also the significant variations in volume fraction from one micrograph to the other. These variations of the volume fraction are passed on to the neural network and therefore yield a poor correlation. As the volume fraction of carbides not only depends on the heat treatment of the sample but

also on the position on the sample surface (Figure 4-40), the standard deviation of the input data is increased, which is also passed on to the neural network to affect the correlation negatively.

5.2 Calculation of the cooccurrence matrix and the texture parameters after Haralick

5.2.1 Compression artefacts

To demonstrate the influence of the variation of separation in calculating the GLCM on the texture parameters, example images have been used (Figure 4-1). As can be seen from the figures representing the trend of the texture parameters in Figure 4-3, Figure 4-4 and Figure 4-8, the measured values do not show distinct extreme values but instead show ranges of distances with local extreme values.

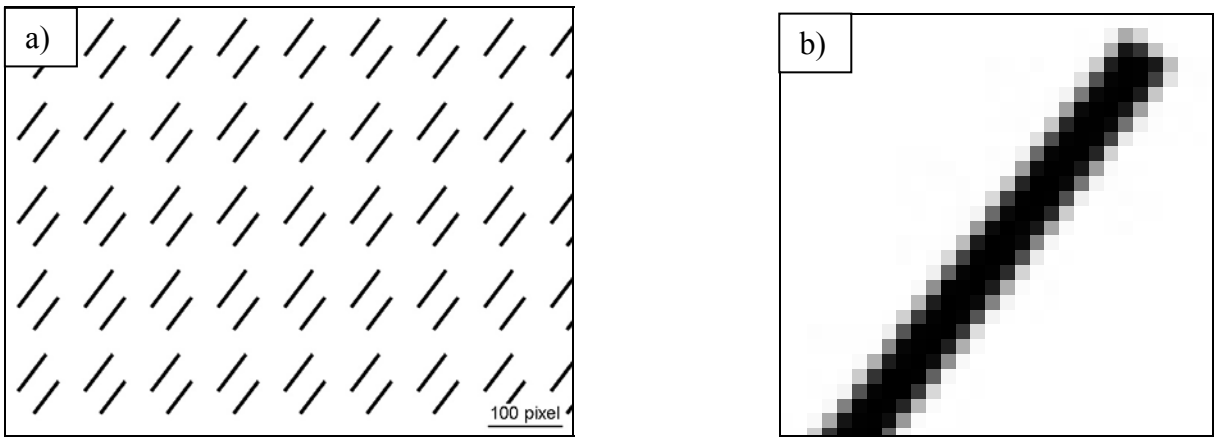

Figure 5-1 Example image with 5 pixel wide lines (a) from Figure 4-1 (a) and cut-out from this image (b)

Jpeg compression has been used to store the micrograph images. One of the effects of the Jpeg compression is the blurring of the images [Mee02]. The reason for this behaviour is the transform-based lossy compression of this algorithm that softens low frequencies and therefore causes a blurring of the image [Clu00, Bro04]. The effect can be seen in Figure 5-1 (b) showing a zoomed area from one of the example images. The edges of the dark areas representing sharp discontinuities in the grey intensities are blurred by the compression algorithm. This blurring in turn has significant influence on the corresponding GLCM, which

is shown schematically in Figure 5-2. Due to the blurring a shift from black-white transitions to transitions between different shades of grey values takes place. This again has significant influence on the texture parameters, e.g. the parameter Haram2 representing the contrast.

a)

		i		
		b	g	w
j	b	++	-	+
	g	-	-	-
	w	+	-	+++

b)

		i		
		b	g	*w*
j	b	+	+	-
	g	+	+	+
	w	-	+	++

Figure 5-2 Schematic GLCMs for the example image in Figure 5-1 (a) without compression and (b) with Jpeg compression and resulting blurring (i: grey value of examined pixel, j: grey value of neighbour pixel; b: black, g: grey, w: white)

\- very low, + low, ++ high, +++ very high number of neighbourhoods

For the texture measurements, all the images were stored using the Jpeg compression algorithm with a comparably low compression rate of only 10. This was done to minimise compression artefacts through blurring of the images, although a bigger file size had to be accepted. This in turn changes the distribution of the grey value distribution and therefore affects the texture parameters. As comparable settings have been used for all the investigations, the absolute values of single texture parameters may have been changed slightly and the occurrence of distinct local extreme values may be suppressed in favour of ranges showing extreme values.

5.2.2 Influence of the characteristics of the example images on the texture parameters

5.2.2.1 Area fraction of the needles

The example images have been created in analogy to the microstructure of hardened steels. In such a microstructure different phases may occur, as e.g. dark etching bainite in a martensitic matrix. Such an example is shown in Figure 4-7. The variation of the volume fraction of bainite in these micrographs can be expressed by the number of bainitic regions and their

respective size. This characteristic can also be found in the example images showing black needles on a bright background (Figure 4-1).

These two sets of images can be compared on the basis of the texture parameter variations. For both the parameters Haram2 (Figure 4-3) and Haram4 (Figure 4-8) an increase in the parameter value was determined for increases in both the area fraction of black needles in the example images and in the volume fraction of dark etching bainite in a martensitic matrix respectively.

For the parameter Haram2 the correlation to the area fraction of needles in the image is not linear (Figure 4-6) and is dependent on the system being studied so that an area fraction of 4 % for the bainitic samples corresponds to a Haram2 value of 3.6, whilst the same area fraction for the example images results in a value of only 1.8. A value of 2.8 also corresponds to area fractions of 2 % (bainitic), 5.5 % (example images) and 8.5 % (example images). This is due to differences in the object size. For the 5+10 pixel wide needles e.g. the GLCM shows an increased quantity of black-black transitions. So although the area fraction is increased the contrast is unchanged since the number of black-white transitions is nearly the same as for the 5 pixel wide needles. Regarding the micrographs this effect should determine the relation between object size and the volume fraction of objects, i.e. a higher number of smaller objects will increase the number of bright-dark transitions in the GLCM and therefore will affect the texture parameter Haram2. Haram4, however, is largely independent of article size and gives a more linear relationship between parameter value and area fraction within each set of images. However, there is no correspondence between the Haram4 values and area fraction between the image sets so that a bainitic area fraction of 4 % gives a Haram4 value of 16, whilst the same area fraction for the example images reduces this value to 8.

5.2.2.2 Influence of the angle between needles and the needle length on the texture parameters

For the orientation of the needles to each other, significant differences in the texture parameters can be found, especially with variation of the pixel separation used to calculate the corresponding GLCM. While for the parallel, long needles (5 pixel wide (Figure 4-1 (a)) and 5+10 pixel wide (Figure 4-1 (e))) very pronounced local extreme values can be found, this effect is reduced if either the length of the needles is reduced (5 pixel wide, short (Figure 4-1

(b))) or the needles are not parallel (5 pixel wide, not parallel (Figure 4-1 (c)) and 5 pixel wide, perpendicular (Figure 4-1 (d))).

For shorter needle lengths the number of black-white transitions is reduced giving a more homogeneous image and therefore GLCM, which in turn yields smaller differences in the texture parameters.

For non-parallel needles a similar effect can be found. As the distance between adjacent needles in the image is not constant, the number of black-white transitions varies for a given pixel separation. This yields a GLCM showing a comparatively low number of black-black transitions for a specific pixel separation compared to the very high number that can be found for parallel needles at the appropriate separation. Therefore, the differences in the texture parameters are much less than those for parallel needles.

5.2.2.3 Trend in texture parameters with variation of pixel separation

Example images

The variation in separation showed a significant influence on the absolute value of the texture parameters. This was found for all the texture parameters after Haralick. This was shown for the example images, given in Figure 4-1, in Figure 4-3, Figure 4-4 and Figure 4-8. A significant correlation between texture parameters calculated from the separation d_{calc} applied to calculate the GLCM and the structure of the images was found (Figure 5-3). Not only was a dependence of the absolute values on the image structure found but also local extreme values occurred depending on the needle-like structure of the images. For the images showing the 5 pixel wide and the 5+10 pixel wide parallel lines significant minima at about 35 pixels can be found for the parameter Haram2 (Figure 4-3), for the parameter Haram5 instead these local minima turn to maxima (Figure 4-4).

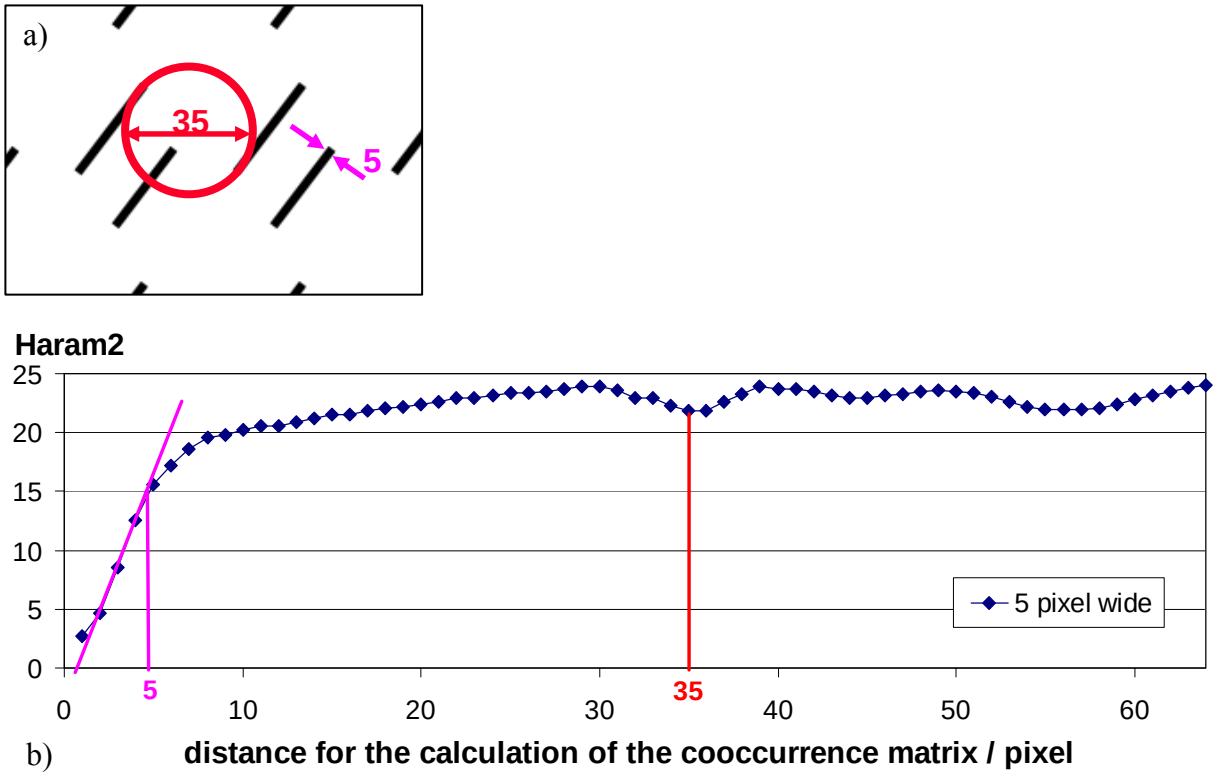

Figure 5-3 Influence of the structure size on the texture parameters after Haralick calculated at varying separation for the example of Haram2
a) example image with characteristic pixel distances marked in the image
b) influence of the variation of separation on Haram2

Regarding the example images these structure sizes can be correlated to the respective images. For the aforementioned images showing parallel lines these lines show a distance $d_{structure}$ of approximately 35 pixels. Four cases can be distinguished:

1) $d_{calc} << d_{structure}$:

   In this case a large number of white-white transitions are detected for pixels that lie both on the background and a high number of pixel neighbourships with black-black transitions inside the needles. But also a considerable number of black-white transitions can be found with one pixel lying in a needle and the adjacent one lying on the background. This leads to a rapid increase in Haram2 up to the width (5 pixels) of the needles in Figure 5-3.

2) $d_{calc} < d_{structure}$:

   For an increasing separation, d_{calc}, the number of black-black transitions is decreasing constantly since the probability that both pixels lie within a needle decreases as the

separation between the needles is greater than their width. The number of black-white transitions is therefore increasing, but at a slower rate, which is seen for Haram2 in Figure 5-3 between 5 and 30 pixels separation.

3) $d_{calc} = d_{structure}$:
   At this separation, a pixel (black) in one needle can have a neighbourship with one in an adjacent needle. The occurrence of black-black neighbourships reduces Haram2 over a range of 35 ± 5 pixels, as seen in Figure 5-3.
4) $d_{calc} > d_{structure}$:
   For these separations, the number of black-white transitions should be relatively constant, although there will be a fluctuation around the multiples of 35 ± 5 pixels, when adjacent pixels can be in separate needles. This is akin to coincident site lattices.

For the images showing non-parallel lines, there is a range of spacing values and so the extreme values for a specific separation d_{calc} used to calculate the GLCM is much weaker; distinct extreme values cannot be found in these cases (Figure 4-3). The difference between the images is the distribution of the widths of the lines in a distinct direction. If all the lines show the same width in a specific direction, this has very clear effect on the GLCMs. If the widths vary, the GLCMs show smaller differences with varying separations. The effects on the texture parameters are also lower.
For the image showing 5 and 10 pixel wide needles, Figure 4-1 (e), a linear increase with the distance can be found with a decrease in slope at about 5 pixels and again at about 10 pixels.
The use of Haram2 for real steel microstructures, e.g. bainite in martensite, will be affected as the features generally show range of both width and spacing values. These will smooth out the variation in Haram2 with pixel separation.

Optical and SEM micrographs

The comments above regarding steel structures are borne out by the texture investigations made on micrographs showing the complex microstructures of hardened steels, e.g. for the optical micrographs of the bainitised 100Cr6 (Figure 4-18). If the separation is varied for these images, a very homogeneous trend of the parameters can be found, e.g. for the parameter Haram2 in Figure 4-30. This is due to the very wide-spread width and distance distribution of bright and dark objects in the micrographs, i.e. no long range order can be

found for these microstructures. This causes very small variations in the GLCM, which, in turn, has little effect on the texture parameters with varying separation for the example images. The variation of the pixel separation used to calculate the GLCM and thereby the texture parameters provide only a small amount of additional information. A differentiation between the micrographs can be carried out for a constant distance of 1 pixel ($d_{calc} << d_{structure}$), which yields reasonable differences for the absolute values of the texture parameters calculated after Haralick.

A stronger dependence may be seen for more regularly spaced structures, such as pearlite or lamellar eutectics.

5.2.3 Relation of the texture parameters with the structure in the images

Example images

In the example images showing a needle-like structure a strong correlation of the texture parameters according after Haralick with characteristic parameters of the structure can be found. As already explained in Section 5.2.2.3, the trend of the texture parameters does show local extreme values and linear ranges with variation of the pixel separation used to calculate the GLCM. These separations can be directly correlated to specific features of the example images, such as the width of the lines or their spacing.

As an example using the parameter Haram4, representing the sum of squares or, in other words, the variance of the texture of the image, a correlation to the area fraction of the black lines in the example images can be established successfully (Figure 4-10). As the fraction of black pixels is increasing with the volume fraction of lines in the images, this broadens the distribution of the grey values and therefore the marginal-probability matrix of the GLCM (Figure 4-9), so that the texture parameter Haram4 increases.

Micrographs showing complex microstructures of hardened steels

This correlation was also verified for micrographs showing complex microstructures of hardened steels. For SEM micrographs of the bainitised 100Cr6 samples (Figure 4-20) the parameter Haram4 was correlated with the standard deviation of the grey value distribution of the specific micrographs. This standard deviation is directly linked with the distribution of contrasting phase fractions in the image, e.g. the volume fraction of dark etching phase as retained austenite in contrast to bright etching phases such as the carbides. Thus, this

conventional image analytical parameter may describe the distribution of the phases in the micrograph. The correlation between the texture parameter Haram4 and the respective standard deviation yields very good results (Figure 4-33).
Similar investigations have been made for the texture parameter Haram2 representing the contrast of the image. For this parameter a correlation with the volume fraction of bainite in a martensitic matrix of a plain carbon steel C45 with 0.45 wt.-% C after continuous cooling at different cooling rates (Figure 4-7) was established. As the volume fraction of bainite increases with decreasing cooling rate, the texture parameter Haram2 also increases (Figure 4-6). This is due to the large difference in the grey values of the bainitic microstructural features, which that appear dark in the optical micrographs and the martensite that etches less and therefore appears brighter in the micrograph.

To investigate the practical usefulness of the texture parameters, these were correlated with the processing parameter of re-austenitising temperature of the bainitised tool steel 100Cr6. The correlation of this temperature with the parameters Haram2, Haram4 and Haram5 is shown in Figure 4-25 for the micrographs given in Figure 4-18. This shows a dependence of the parameters on the austenitising temperature but no simple correlation with just the texture parameters could be found.
Nevertheless, for the Jominy end-quench specimen of the tool steel 100Cr6 calculation of the microhardness from the texture parameters after Haralick using a neural network could be achieved indicating that the microstructure can be characterised quantitatively with these parameters (Figure 4-11 and Figure 4-24). For single images even variations of the microstructure within a single micrograph could be made visible using the texture parameters (Section 4.5.3). Based on these results the experiments were continued not only for the samples heat treated to prove this method but also for samples with practical relevance (Section 4.6).
It was obvious that for the variation of the pixel separation (Figure 4-30), no distinctive local extreme values for texture parameters (such as seen for the example images showing needle-like structures (Figure 4-3)) could be found for the bainitised 100Cr6. The trend of the parameters of the hardened microstructure most closely resembles the trend of the parameter of the perpendicular needles. For both of these cases the variation in the texture parameter with pixel separation is very low. For both images the structures have different directions, i.e.

no distinctive texture over the whole image can be found. This in turn means that the micrographs showing the complex microstructure of hardened steels cannot be described quantitatively by a single texture parameter but the complete set of parameters has to be used to describe the images.

Although, for single parameters, no correlation to the different properties may be found, a neural network provides the opportunity to extract the data that are contained in the complete set of the 11 texture parameters after Haralick calculated with the image analysis software. The understanding of the relevance of the individual parameters, their relation to microstructural features and the refinement to a subset (<11 parameters) representing the same information as the complete set will need to be carried out in further work.

Several non-structural factors have been identified, which can affect the texture parameters significantly. It is desirable that only the microstructure influences the texture parameters, but, unfortunately, metallographical preparation, the imaging method determined by the type of microscope, the illumination technique, and also the settings of the microscope as the position of the diaphragms or the lamp voltage have all been found to be relevant. The absolute value of the texture parameter Haram2 determined from analysis of the SEM micrographs (Figure 4-32 (b)) is about 5-10 times higher than that for the light optical examination (Figure 4-30) of exactly the same samples.
In previous work [Fuc00], the influence of the microscope settings has been analysed. For the lamp voltage and the diaphragms a setting was found developing the microstructure in such a way to reveal even the finest resolvable structure whilst avoiding of artefacts.

5.2.4 Influence of the metallographical preparation on the texture parameters

The polishing of the samples turned out to bring significant differences in the analysis of the texture (Section 4.5.4). As this influences the texture parameters without a change in the microstructure a method had to be established for consistent and reproducible metallographical preparation.

Electrolytic preparation

Experiments with electrolytical polishing showed very inhomogeneous etching attack, especially when applied to large sample areas of 100 mm² and more as used for the evaluation of the lateral hardness distribution of locally hardened components. Even changing the relevant polishing parameters, such as the electrolyte or the polishing voltage, could not improve the results so that this method proved unsuitable for further analysis.

The inhomogeneous etching attack may be related to (i) local chemical inhomogeneities, (ii) local differences in the passivation of the sample surface after the preceding mechanical polishing and (iii) local differences in the flow rate of the electrolyte to the sample surface.

As the chemical inhomogeneities are most likely linked to differences in the microstructure this effect might offer an advantage in characterising certain microstructures. The passivation of the sample surface was minimised by electrolytically polishing the sample right after mechanically pre-polishing and cleaning them. The largest influence was still inhomogeneous flow of the electrolyte over the sample surface. This can be seen in Figure 4-29 (a) where a dark spot can be seen in the centre of the sample, which corresponds to the position where the electrolyte was pumped to the sample surface.

Mechanical preparation

For mechanical preparation a procedure was established to give reproducible and homogeneous polishing. Using a very detailed description of the grinding and polishing procedure (Table 3-7) with very strict implementation, the necessary homogeneity of polishing could be established (Figure 4-28) together with a negligible etching attack during this mechanical preparation. Due to this, this method was chosen for the preparation of the samples used to analyse large sample areas, as e.g. for the determination of the lateral hardness distribution.

5.2.5 Influence of image acquisition on the texture parameters

Focussing of the micrographs

During the investigations it turned out that good image quality is essential for reliable characterisation using the texture parameters after Haralick. One of the most important factors is the focussing of the samples as this determines the minimal resolvable detail size. Therefore efforts were made to optimise the focus of the samples as much as possible when taking the

micrographs. For single micrographs acquired from the optical microscope and from the SEM focus was adjusted manually to ensure the highest possible image quality. For the acquisition of larger surface areas as for the Jominy end-quench specimen or for the determination of the lateral hardness distribution of locally hardened samples an automatic focussing of the samples had to be used to acquire the large number of micrographs needed for the analyses. By adjusting the illumination and the step size to acquire images at different focus positions the results of the automatic focussing could be optimised regarding both focussing accuracy and process time.

For an optical micrograph the trend of the texture parameters after Haralick are shown in Figure 5-4 for a micrograph in the focus plane of the sample (Figure 5-4 (a)) and at defined positions from this plane (e.g. Figure 5-4 (b)). Here it can be seen that some parameters show virtually no dependence on the variation of the focus position, as e.g. Haram6, while others show significant changes in the values, as e.g. Haram7. Accurate focussing is therefore relevant to reveal the microstructure and to be able to calculate the texture parameters related to this structure.

The challenge lies in the depth of field being closely related to the applied microscopic magnification. As the microstructure of the investigated samples is very fine, a high magnification has to be used, which, in turn, results in a low depth of field. The correlation between the magnification applied in an optical microscope and the resulting depth of field, Δz, can be estimated by the Rayleigh equation [Tel97] with the refractive index, λ, of the medium between object and objective and the half angle, σ, of the most oblique light rays that enter the front lens as

$$\Delta z = \frac{\lambda}{n \cdot \sin^2 \sigma} \qquad \text{Eq. 5-1}$$

This correlation is also presented graphically in Figure 5-5 for the microscopic magnifications between 50:1 and 1000:1 of the utilised optical microscope.

a)

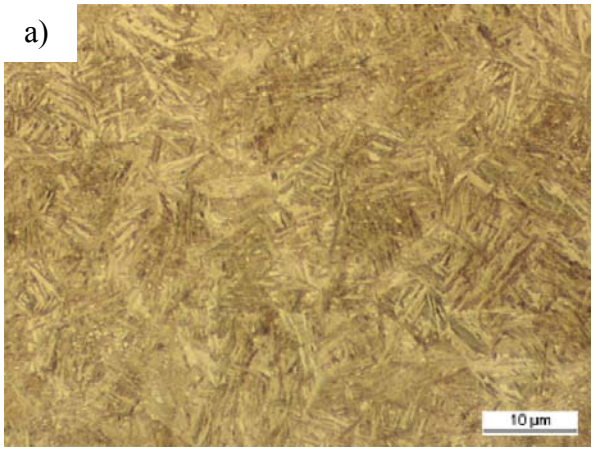

b)

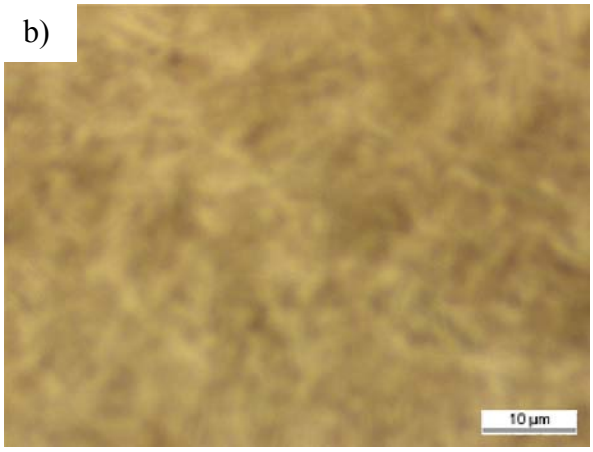

c)

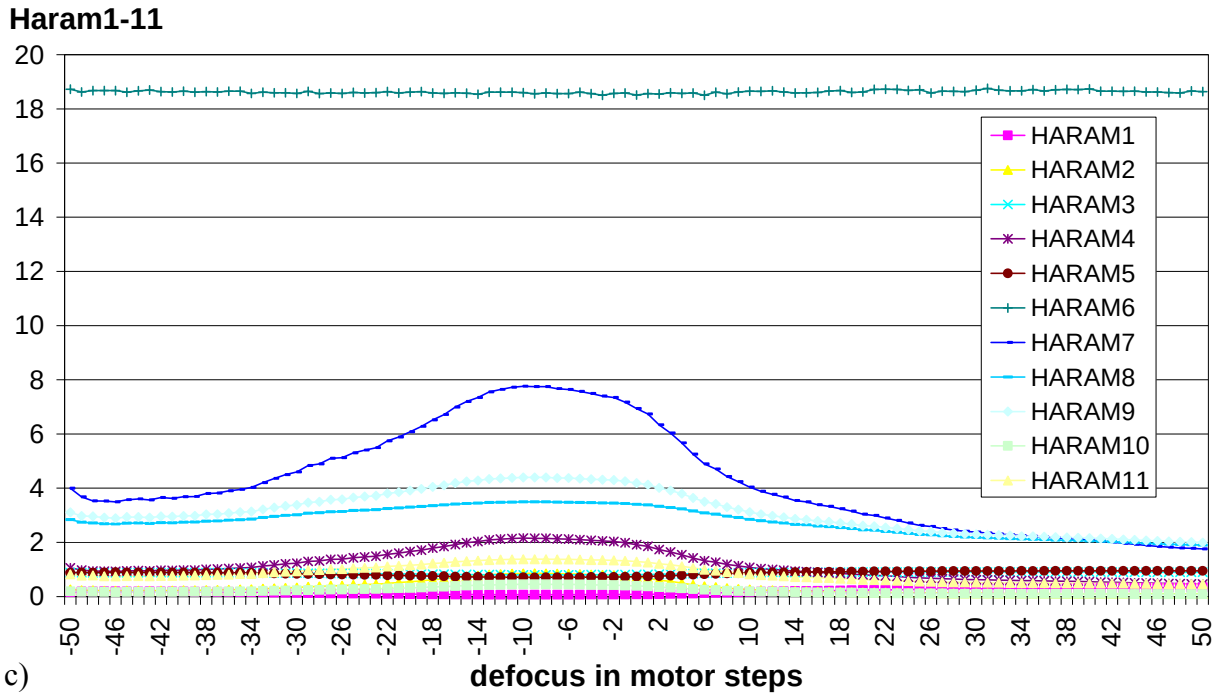

Figure 5-4 Influence of defocusing of the sample in the optical microscope on the texture parameters after Haralick at a separation of 1 pixel

a) micrograph in focus position (0 motor steps)

b) micrograph at 50 motor steps from focus position

c) trend of the Haralick parameters with variation of the focus position

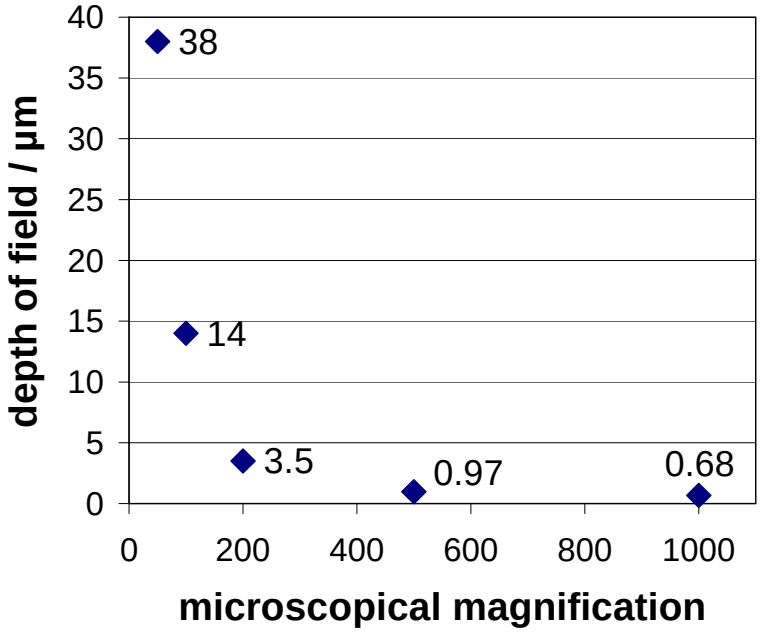

Figure 5-5 Correlation between the magnification of the utilised optical microscope and the resulting depth of field

As can be seen in Figure 5-5 the depth of field is only 3.5 µm for a magnification of 200:1. For higher magnifications the value continues to fall, but at a decreasing rate. For the very big areas analysed of the surface hardened samples this causes especially serious problems since the metallographical preparation, especially the polishing, results in rounding of the edges. This loss of flatness may be much more than 3.5 µm. Investigations showed that a difference of about 15 µm in height occurred over a length of 30 mm using standard metallographical procedures [Str04a]. This means that re-focussing the sample is essential during the acquisition of micrographs over these large sample areas if high microscopical magnifications are applied.

This can be seen in Figure 4-61 for the case hardened steel component. The images are acquired in this example from the lower to the upper part of the image and from the left to the right side using an autofocus function at every single position (Figure 5-6). As can be seen at the lower edge of the sample, some images are not in focus. The autofocus adjusts the z position of the scanning stage at each x-y actual position. This sometimes causes problems if the acquisition moves directly from the one edge of the sample to the other edge. If the differences in height are too big, the focus position might be out of the scanned z range. Then

for several images the autofocus cannot be found until the sample surface is again back in the range of the autofocus due to the topography of its surface.

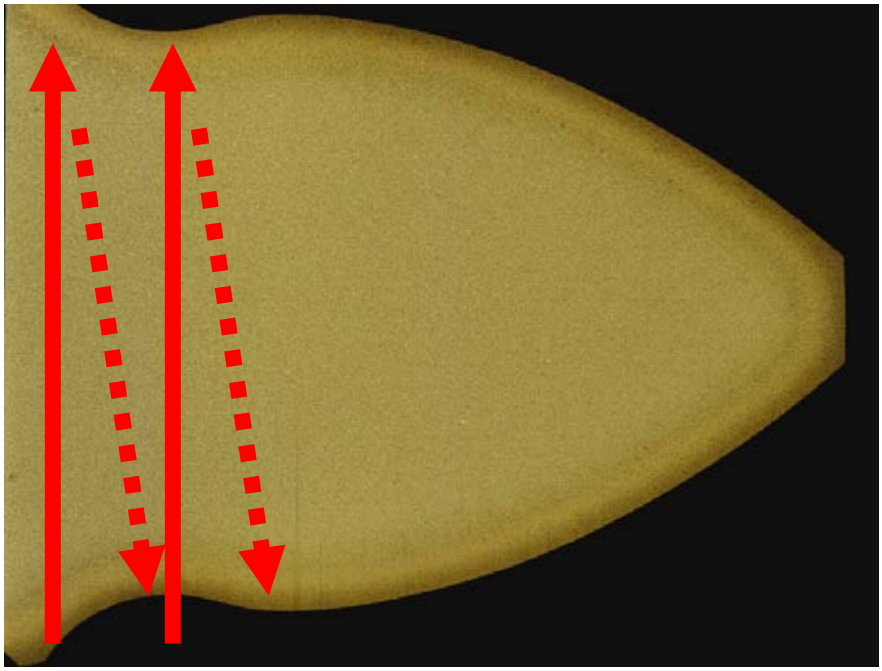

Figure 5-6 Schematic procedure of the image acquisition

The effect cannot only be seen in the micrographs but also in the measured texture parameters after Haralick, e.g. in Figure 4-63 for Haram2. Therefore, the correlation with the microhardness is affected (Figure 4-67) where the regions not in focus are characterised by very high hardness values. Therefore it is necessary to ensure a working autofocus for the image acquisition to prevent overestimation of the correlated (microhardness) values.

Differences in grey level intensities of SEM micrographs due to variations of local chemistry

In the SEM it turned out that the grey level intensities of the backscattered electron micrographs show a local variation with the microstructure, i.e. the surface topography [Joy97] but also small influences from the local chemistry. This can be seen clearly in Figure 4-16 and Figure 4-20. These differences in the grey value intensities cause differences in the texture parameters after Haralick.

For the correlation of the parameters with the re-austenitising temperature as a characteristic processing parameter, a significant scattering of the correlated data can be found (Figure 4-41). The standard deviation for this investigation is as high as 59.7.

As no enhancement was obvious to improve the homogeneity of the micrographs to visualise the microstructure, it was necessary to combine the texture information with additional microstructural features. For the combination of texture parameters with the area fraction of the coarse alloy carbides the correlation was found to improve significantly.

5.3 Correlation of texture parameters with mechanical properties or processing parameters

5.3.1 Direct correlation of a single texture parameter with mechanical properties or processing parameters

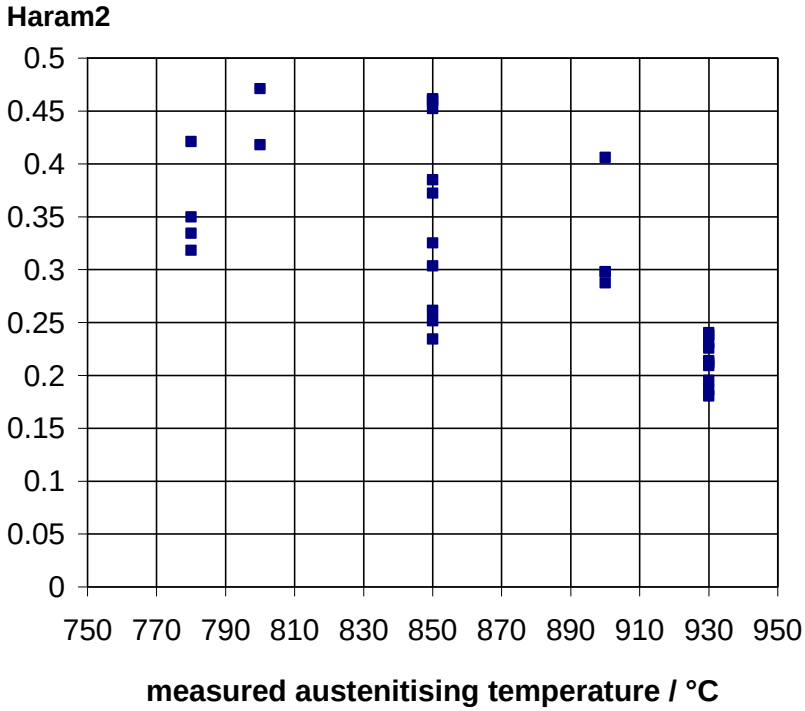

Figure 5-7 Correlation of the texture parameter Haram2 at a separation of 1 pixel with the measured austenitising temperature; 30 micrographs analysed

By Haralick a set of 14 texture parameters was defined [Har73] of which 11 have been used to characterise the complex microstructure of hardened steels. This complete set had to be used

to characterise the microstructure since for a single parameter the correlation to e.g. the respective re-austenitising temperature yields an overlap in the range of the values of the texture parameters. This is presented representatively for the parameter Haram2 in Figure 5-7. As this can be found for all the parameters the complete set has to be used since the combination of all the texture parameters increases the information content to be able to establish a correlation to the microhardness or the re-austenitising temperature due to a reduced overlap of the range of values of the microstructural feature data (Figure 4-24 and Figure 4-31).

5.3.2 Improvement of the correlation using the conventional quantification of microstructural features

Improvement of the correlation to the austenitising temperature for SEM micrographs

The correlation of the texture parameters with the austenitising temperature is not satisfactory due to a very high scattering of the correlated data. As this is a step backwards compared to the optical microscopical investigations with a standard deviation with 32.2 the characterisation of the coarse alloy carbides was investigated to improve the correlation. The scatterband of the carbide correlation was decreased significantly, i.e. the standard deviation was lowered from 59.7 to 18.2 (Table 4-9). To increase the correlation again, the data of both texture parameters and the information about the coarse alloy carbides was combined to characterise the micrographs. This yields a standard deviation of only 8.5 and therefore improved to a very good result of the correlation.

Improvement of the correlation to the austenitising temperature for optical micrographs

Similar investigations were also carried out for the optical micrographs of the same samples. In this case a standard deviation of 39.2 for the analysis based only on the texture parameters and 30.1 for the analysis based on the carbide are fraction was found. These values could be decreased to 26.2 for the combination of both data sets as training data for the neural network. The improvement is in this case is less significant than for the SEM micrographs.

It has also to be remarked that this improvement is only possible for hypereutectoid steels as these show coarse alloy carbides. For hypoeutectoid steels in the hardened condition the characterisation has to be based upon the complex microstructure of martensite and/or bainite since the amount of carbides is lower.

5.4 Factors influencing the quality of the correlation

Influence of the geometry of the neural network

The influence of the geometry of the neural network on the resulting correlation was investigated intensively in previous work [The98]. Here a feed-forward network was found to bring the best results.

In this work the topology of the hidden layer was varied from the standard 7 neurons to a matrix of 7x7 neurons for the texture parameters calculated at varied pixel separation to see the influence on the correlation (Figure 4-35). The determined differences in the standard deviation of the correlation have been marginal so that a network with only 7 neurons in the hidden layer can be used. The advantage of this smaller hidden layer is the reduction of calculation time for both training and calculation with the neural network. An increase in the quality of the correlation was not found for the additional neurons in the hidden layer, neither for the texture data at a separation of 1 pixel, nor for the texture data at varied separations.

Influence of the training data

To investigate the influence of the number of training data used to establish the correlation, the neural network was trained with various amounts of texture data measured for the laser hardened sample lhd_laser. The correlation of the complete data set with the local microhardness $H_{V0.02}$ is shown in Figure 4-53. These data sets consist of 38 hardness values measured from 5 traces over the sample surface together with the respective texture parameters. The neural network was also trained with the data of only one of the 5 traces, which is shown for the traces 2 and 4 in Figure 5-8.

For this variation of the training data a large discrepancy in the resulting correlation can be found. This is caused by the limited data measured at only 6 to 8 micrographs. The lack of redundancy in the training data causes a training of the neural network that is specific to the applied images. If these images do not show representative areas on the sample, e.g. artefacts that can only be found at this specific position, a proper correlation cannot be established for the remaining micrographs. Therefore the data of at least 5 redundant positions should be used for the training of the neural network to ensure the use of micrographs representative for the investigated sample.

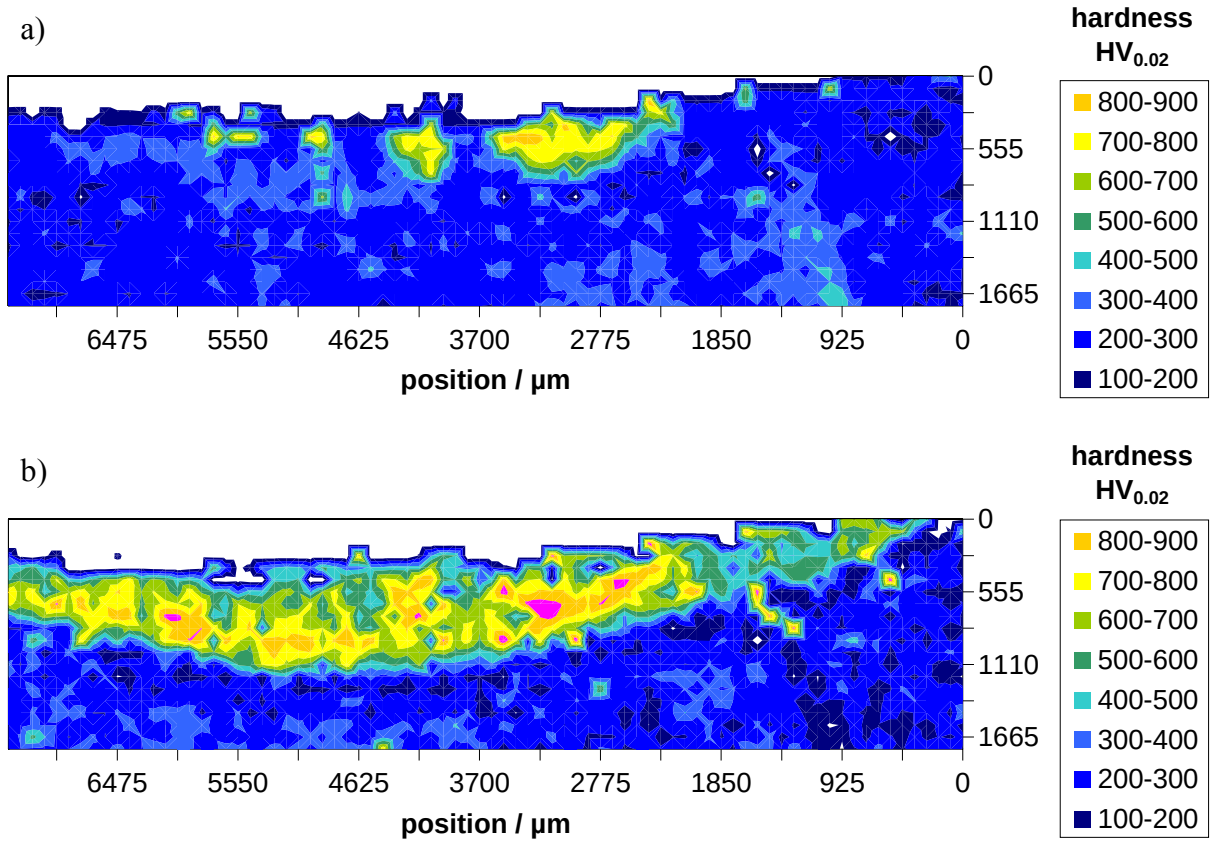

Figure 5-8 Lateral distribution of the local microhardness of the laser hardened sample lhd_laser calculated from the texture parameters using a neural network trained with hardness values and corresponding texture information of the hardness traces 2 (a) and 4 (b)

Overview of the factors influencing the quality of the neural network

For correlation of the texture parameters with the re-austenitising temperature of bainitised samples of the tool steel 100Cr6 different conditions have been used. Variations in:

(i) the etchant,

(ii) the pixel separation used for calculation of the GLCM,

(iii) the geometry of the neural network, and

(iv) the data sets used to train the neural network

yielded differences in the correlation with the re-austenitising temperature.

Both the mean value of the difference between the calculated values and the nominal values of the correlation and the respective standard deviation are given in Table 5-1 for the optical micrographs and in Table 5-2 for the SEM micrographs.

For the optical micrographs it can be seen that the variation of the separation used for calculation of the GLCM improves the correlation marginally compared to the evaluation with a fixed separation of 1 pixel. There is no relation to the increased data volume needed for the characterisation of a single micrograph as not just 11 parameters have been measured but 64 variations of each of these parameters. For this correlation with the separation varied between 1 to 64 pixels, if the size of the hidden layer is changed from 1x7 pixels to 7x7 pixels then the standard deviation even increases from 31.6 to 34.9.

Table 5-1 Overview of the mean values and standard deviations of the difference between the calculated values and the nominal values of the correlation of the re-austenitising temperature for optical micrographs using different etching conditions, neural network topologies and training data sets

reference and etching conditions	conditions	mean value	standard deviation
Table 4-6, 2 % nital	separation 1 pixel, input layer 11x1 neurons	-10.6	32.2
	separation 1-64 pixels, input layer 11x64 neurons	-8.0	31.6
Table 4-7, 2 % nital	separation 1-64 pixels, 1x7 neurons in hidden layer	-8.0	31.6
	separation 1-64 pixels, 7x7 neurons in hidden layer	-8.7	34.9
Table 4-10, 5 % nital	separation 1 pixel, texture parameters only	-8.2	39.2
	separation 1 pixel, texture parameters and carbides	-7.0	26.2
	carbides only	-1.3	30.1
Figure 4-45, Klemm	separation 1 pixel	-0.2	22.8

If the etchant is changed to 5 % nital, the standard deviation is much worse (39.2) than for the same investigation with the samples etched with 2 % nital (32.2). This is due to reduced development of contrast in the microstructure due to slight overetching. However, in contrast

to the etching with 2 % nital, the carbides are more clearly developed making automatic measurement of their features possible. If only these carbide data, i.e. volume fraction and number of carbides per image, are used to establish a correlation to the re-austenitisation temperature in the neural network, this correlation is slightly better (standard deviation 30.1) than the analysis based on the texture parameters of the 2 % nital etched samples. If both the texture parameters and the carbide data are combined to characterise the samples after 5 % nital etching, the correlation can be improved significantly showing a standard deviation of 26.2.

If the samples are etched using Klemm's reagent, the correlation can again be improved significantly. A standard deviation of only 22.8 could be achieved. The problem is that this etching is very sensitive to variations in the etching conditions and therefore produces local variations in the etching attack. Features such as the local chemical composition of both sample and etchant influence the etching response as well as local surface oxidation of the sample or turbulent flow in the etchant. These differences in the etching yield a large scatter of the values obtained from the texture parameters in the neural network. Deviations of as much as 150 °C can be found for the correlation. To eliminate these influences a large number of micrographs has to be analysed, i.e. over 4300 for this investigation, and the preparation has to be done very carefully. Both of these requirements are not practical except on a laboratory scale.

Table 5-2 Overview of the mean values and standard deviations of the difference between the calculated values and the nominal values of the correlation of the re-austenitising temperature for SEM micrographs with different training data sets

reference and etching conditions	conditions	mean value	standard deviation
Table 4-9, 2 % nital	separation 1 pixel, texture parameters only	4.0	59.7
	separation 1 pixel, texture parameters and carbides	-0.7	8.5
	carbides only	4.6	18.2

Compared to the correlations with optical micrographs the SEM micrographs gave a much worse correlation. The standard deviation is reduced from 32.2 to 59.7 for the analysis of the texture parameters after 2 % nital etching.
If only the carbide data are used to establish the correlation with the re-austenitising temperature, this yields a standard deviation of only 18.2, which is much less than for the comparable analysis using optical micrographs (30.1). This effect can be related to the higher magnification in the SEM and the insufficient contrast between carbides and matrix after etching with 2 % nital. In the optical microscope, carbides down to about 1 µm can be detected. In the SEM even smaller carbides can be resolved, which improves the characterisation of even small differences in the carbide volume fraction. The second difference is that even for the etching with 2 % nital the detection of carbides in the SEM is easier than in the optical microscope due to the higher resolution but also due to higher contrast with the surrounding matrix. If these data, the texture parameters and the carbide data, are combined for the analysis in the neural network, a standard deviation of only 8.5 is found, compared to 26.2 for the optical micrographs.

This method is therefore the one giving by far the best results. However the requirements for metallographic preparation for analysis in the SEM are greater than for the optical microscope. Additionally the time for analysis in the SEM is longer than for the optical microscope, and SEM is far more expensive, so that analysis using an optical microscope is preferred. This is a faster alternative giving reasonable good correlations with standard equipment as can be found in many metallographical laboratories.

5.5 Scanning of large sample areas

The scanning of large sample areas is one of the main demands of the texture analysis on the microscopical system. For the characterisation of a sample a number of measurements has to be done to ensure a reliable description of the sample. If local inhomogeneities in a sample are to be characterised, it is also essential to scan large areas to be able to determine the relevant differences in the microstructure.
This scanning system may be accompanied by different problems. One of these is the problem of automatically focussing the micrographs (section 5.2.5). With a careful metallographical preparation (section 5.2.4) this problem might be reduced.

As already mentioned in section 5.3.2, the correlation of the texture parameters with mechanical properties or process parameters may be enhanced if additional microstructural data is obtained to train the neural network, as e.g. the volume fraction of coarse alloy carbides in the respective micrograph. These additional data can contain extra information as e.g. local decarburisation of the sample. The metallographic preparation and the etching get in turn more significant as both the microstructure has to be revealed as well as a sufficient contrast between carbides and surrounding matrix has to be achieved. This preparation has also to be very homogeneous so as to decrease autofocus problems as well as the interference of the microstructure with preparation artefacts. Nevertheless, conventional microstructural data have been found to be valuable for the correlation and may improve this correlation significantly.

Another problem occurring for the scanning of large sample areas is the large amount of data that is measured. For the determination of the lateral hardness distribution e.g. the handling of 50,000 datasets and more might be interesting. With standard spread sheet software this may run into problems. Therefore algorithms have to be found to separate these data into smaller subsets that can be handled in a soluble manner.

5.6 Usefulness and limitation of texture analysis

The characterisation of microstructure is, undoubtedly, a very important technique to obtain information from a material and be able to predict properties from this information. For both quality control and material development this has proved to be a very powerful tool. With ongoing developments in material science the microstructures of modern steels are getting more and more complex, i.e. showing very fine mixed microstructures that are low in contrast. For such microstructures, accurate characterisation using conventional image analysis, e.g. grain size measurement or determination of phase fractions, is not readily achievable. Alternative characterisation techniques based on grey value statistics promise to solve this problem. The texture analysis after Haralick was used in this study to establish correlations between microstructure and processing / property parameters using neural network techniques.

It could be seen that different factors influence the quality of the correlation (section 5.4). These are the (i) metallographical preparation, (ii) the imaging technique, (iii) the variation of the separation between pixels used for calculation of the grey level cooccurrence matrix, (iv)

the geometry of the neural network and (v) the choice of representative data for training of the neural network.

Metallographical preparation

The most critical factor is the metallographic preparation of the sample. Investigations showed that using mechanical polishing produced the best results whilst electrolytical polishing gave severe inhomogeneities that are not linked to the microstructure. Etching, the final stage of metallographical preparation, reveals the microstructural features, which are the basis of the following texture analysis. Differences in the etching attack that are not related to the microstructure have therefore to be avoided. This means that metallographical preparation has to be done very carefully without producing artefacts in the microstructure.

If the etchant is changed the microstructural features that are developed may be different. As a standard etchant for steels 2 % nital was used, which reveals the general microstructure. If 5 % nital is used instead, the needle-like matrix of the hardened microstructure is overetched but the contrast between the coarse alloy carbide and the matrix is enhanced. This decrease in information that can be obtained from the microstructure can also be seen in the quality of the correlation of the texture parameters with the re-austenitisation temperature of the bainitised samples. The standard deviation increases from 32.2 to 39.2 for this change of etchant. Colour etching using Klemm's reagent instead of 2 % nital develops greater differences in the transformed microstructure, i.e. the difference between martensite and bainite. As this etchant produces severe artefacts, it is not reproducible and therefore not useful for the practical use of the texture analysis.

Imaging technique

The microscope system used to obtain the micrographs also has a big influence on the results of the texture analysis. As the lateral resolution of an optical microscope is limited by the wavelength of light, only the microstructural features above a critical size can be revealed and therefore influence the texture analysis. With an SEM more details can be revealed due to the higher resolution. This allows an enhanced characterisation of the micrographs since small differences in the microstructure can be differentiated. This is especially beneficial if the carbides are characterised. The correlation of these data is expected to be better than in the optical microscope. Nevertheless the characterisation of the microstructure only based on the

texture parameter yields a standard deviation of 59.7, which is much higher than for the optical samples. This is due to local inhomogeneities in the grey values due to variations in the local chemical composition or the surface topography. These effects yield a large scatter in the texture parameters that is not only related to the microstructure but also to sample preparation. To enhance the quality of the correlation the analysis would have to be done for a very large number of images as has also been seen for samples etched in Klemm's reagent.

One requirement of an imaging system is for automation of image acquisition. For the texture analysis a large number of micrographs is needed, i.e. at least 50 images to train the neural network with the texture parameters of representative microstructures. This necessitates the use of a scanning stage that moves the sample under computer control to acquire images from a large sample area. As magnifications of at least 500:1 are to be used, the depth of focus is very low. Hence, very careful metallographical preparation is needed to minimise height differences over the sample area; the sample has to be focussed before image acquisition to be able to reveal the microstructural features in the micrograph.

As the availability of optical microscopes is higher than that of SEMs, the study was mainly based on the analysis of optical micrographs. With modern automated microscopes and the corresponding software the acquisition of the required images and the measurement of the texture parameters after Haralick can be done within minutes. Due to the higher demands for metallographical preparation, the longer times to set up the system and the image acquisition times, data acquisition will take longer in the SEM than in the optical microscope. However, for the combination of the texture data with the carbide information the best correlation could be found using SEM.

Variation of the separation between pixels for the calculation of the GLCM

One approach to obtain additional information from the micrographs is the variation of the separation between pixels used for the calculation of the GLCM. For example images showing very regular structures with a very clear long rang order this variation reveals details about the size of and spacing between the structural elements. For micrographs of real microstructures, the structures are much less regular, so that these effects cannot be found. The additional information that can be obtained from the variation of the separation can

increase the quality of the correlation, e.g. the standard deviation for the texture parameters measured at a separation of 1 pixel is 32.2, but this decreases to 31.6 for the texture parameters measured at separations between 1 and 64 pixels. This variation increases the amount of data that has to be measured by a factor of 64. The increase of the measuring time is negligible, but the number of input nodes of the neural network has to be increased from 11 to 704 to be able to store the additional information from the variation of the separation. This increases the calculation times of the neural network for both training and calculation of the correlation. As the power of computers is increasing steadily this should not be a problem.

Geometry of the neural network

In previous studies [The98, Sch99, Fuc00, Fuc01] feed-forward neural networks have been shown to be able to establish a correlation between the texture parameters after Haralick and respective processing parameters or mechanical properties. To check the influence of the structure of the neural network the hidden layer was changed from 1x7 neurons to a matrix of 7x7 neurons. This changed the correlation insignificantly, the standard deviation increased from 31.6 to 34.9. A structure of the hidden layer of 1x7 neurons therefore gives better results with reduced calculation work.

Choice of representative data for the training of the neural network

For training of the neural network a representative set of data has to be used to establish the correlation. The network has to be trained with the texture parameters of all the variations in microstructure that occur in the sample. If the number of micrographs to train the neural network is reduced too much, this decreases the quality of the correlation (Figure 5-8). To avoid this methods have to be found to find representative information for the training of the neural network. For the calculation of the lateral hardness distribution several hardness traces were measured from the face of the sample to the core with the small enough distances between adjacent measuring positions to detect all the variations in the microstructure. By measuring several of these traces, differences in the metallographical preparation can be trained into the neural network so that these effects can be almost eliminated.

6 Conclusions and further work

The variation in Haralick texture parameters for a number of model and real (microstructural) systems has been investigated and related to processing and property data.

a) The individual parameters have been shown to be dependent on preparation and imaging conditions requiring specific procedures to be adopted for the application of this technique.
b) The variation of individual parameters with pixel separation can be related to characteristics in well-defined model images.
c) Individual Haralick parameters cannot, yet, be related to microstructural features in real microstructures nor be correlated with process and property parameters.
d) The use of a full set of Haralick parameters in a neural network gives a more successful correlation with processing and property parameters. The correlation is significantly improved by incorporation of standard microstructural data with the combined analysis giving better agreement than either of the datasets (texture parameters / carbides) individually.
e) Large samples (up to 25,000 micrographs) can be analysed automatically, successfully, although this is dependent on specimen preparation, especially flatness.

The further implementation of these techniques will require:

a) More detailed understanding of the variation of the individual Haralick parameters with image contrast, overall grey level, size and distribution of features in real microstructures.
b) Investigation of more regular, real microstructures, e.g. eutectics.
c) Correlation of absolute Haralick parameter values with image parameters (e.g. focus and overall grey level) and structural parameters in order to determine whether analysis of subsets can be used to deal with artefacts and reduce the need for such careful preparation and imaging.
d) Apply texture parameters to other data, e.g. ultrasonics, to determine the presence of defects that affect other properties, such as toughness.

7 References

[Aks01] Aksoy M., Yilmaz O., Korkut M. H. "The effect of strong carbide-forming elements on the adhesive wear resistance of ferritic stainless steel". Wear, 2001, 249, 639-646.

[Alj01] Al-Janobi A. "Performance evaluation of cross-diagonal texture method of texture analysis". Pattern Recognition, 2001, 34, 171-180.

[Any95] Anys H., He D. "Evaluation of Textural and Multipolarization Radar Features for Crop Classification". IEEE Transactions on Geoscience and Remote Sensing, 1995, 33 (5), 1170-1181.

[AST96] ASTM E112. "Standard Test Methods for Determining Average Grain Size". 1996.

[Atk77] Atkins M. "Atlas of continuous cooling transformation diagrams for engineering steels". Sheffield: British Steel Corp., 1977.

[Bal99] Balart M. J. "Structure-property relationships in high strength microalloyed forging steels". PhD thesis, University of Birmingham, 1999.

[Bar78] Bardes B. "Metals Handbook: Properties and Selection: Irons and Steels". Vol. 1, 9th edition, Materials Park: American Society for Metals, 1978.

[Bar95] Barbacki A. "The role of bainite in shaping mechanical properties of steels". Journal of Materials Processing Technology, 1995, 53, 57-63.

[Bee97] Bee J. V., Edmonds D. V. "A Metallographic Study of the High-Temperature Decomposition of Austenite in Alloy Steels Containing Mo and Cr". Materials Characterization, 1997, 39, 361-379.

[Ber89] Bergmann W. ""Werkstofftechnik – Teil 1: Grundlagen". 2nd edition, München: Carl Hanser Verlag, 1989.

[Ber99] Berg E., Kallel F., Hussain F., Miller R. K., Ophir J., Kehtarnavaz N. "The use of elastography to measure quality characteristics of pork semimembranosus muscle". Meat Science, 1999, 53, 31-35.

[Bha99a] Bhadeshia H. K. D. H. "Low Carbon Steels - The Calculation of Mixed-Microstructures & Their Mechanical Properties". Proceedings of International Conference on New Aspects of Microstructures in Modern Low-Carbon High-Strength Steels, Tokyo: Iron and Steel Institute of Japan. 1999, 75-79.

[Bha99b] Bhadeshia H. K. D. H. "Neural Networks in Material Science". ISIJ

International, 1999, 39 (10), 966-979.

[Bha99c] Bhadeshia H. K. D. H. "The bainite transformation: unresolved issues". Materials Science and Engineering, 1999, A273-275, 58-66.

[Bha01] Bhadeshia H. K. D. H. "Bainite in Steels". 2nd edition, London: The Institute of Materials, 2001.

[Bha02] Bhadeshia H. K. D. H. "Martensite in Steels". Lecture script, University of Cambridge, 2002.

[Bha04] Bhadeshia H. K. D. H. "Tempered Martensite" [online]. University of Cambridge. Available from: http://www.msm.cam.ac.uk/phase-trans/2004/Tempered.Martensite/tempered.martensite.html [Accessed 03 December 2004].

[Bis96] Bishop C. M. "Theoretical foundations of neural networks". In: Borcherds P., Bubak M., Maksymowicz A. "Proceedings of Physics Computing 96". Krakow: Academic Computer Centre, 1996.

[Bon04] Bonnevie E., Ferriere G., Ikhlef A., Kaplan D., Orain J. M. "Morphological aspects of martensite-austenite constituents in intercritical and coarse grain heat affected zone of structural steels". Materials Science and Engineering, 2004, A 385, 352-358.

[Bor95] Borgenstam A., Hillert M., Agren J. "Critical temperature for growth of martensite". Acta Metallurgica Et Materialia, 1995, 43 (3), 945-954.

[Bor96] Borgenstam A., Hillert M. "Bainite in the Light of Rapid Continuous Cooling Information". Metallurgical and Materials Transactions, 1996, 27A, 1501-1512.

[Bro04] Brown M. "JPEG Artefacts Test". Available from: http://www.nezumi.demon.co.uk/photo/jpeg/jpeg.htm. [Accessed 21 December 2004].

[BSE02] British Standard BS EN ISO 2639. "Steels – Determination and verification of the depth of carburized and hardened cases". Incorporating corrigendum 2, 2002.

[Byu01] Byun J., Shim J., Suh J., Oh Y., Cho Y. W., Shim J., Lee D. N. "Inoculated acicular ferrite microstructure and mechanical properties". Materials Science and Engineering, 2001, A319-321, 326-331.

[Cab04] Caballero F. G., Bhadeshia H. K. D. H. "Very strong bainite". To be published in: Current Opinions in Solid State and Materials Science.

[Cal99] Callister W. D. "Materials science and engineering: an introduction". 5th

edition, New York: John Wiley & Sons. 1999.

[Car97] Carl Zeiss Vision GmbH, "KS 400 Imaging System Release 3.0", User Manual Vol. 2, 1997.

[Che98] Tuceryan M., Jain A. K. "Texture Analysis". In: Chen C. H., Pau L. F., Wang P. S. P. „The Handbook of Pattern Recognition and Computer Vision". 2nd edition, Singapore: World Scientific Publishing Co., 1998.

[Clu00] Clunie D. A. "Lossless Compression of Grayscale Medical Images – Effectiveness of Traditional and State of the Art Approaches". In: Blaine G. J., Siegel E. L. "Medical Imaging: PACS Design and Evaluation: Engineering and Clinical Issues". Proceedings of The International Society for Optical Engineering, 2000, 3980, 74-84.

[Cun00] Cunat P. "Stainless steel properties for structural automotive applications". Metal Bulletin International Automotive Materials Conference. Cologne. 2000.

[Dau98] Daugman J. "Recognizing People by their Iris Patterns". Information Security Technical Report, 1998, 3 (1), 33-39.

[DIN76] DIN 50150. "Testing of steel and cast steel; conversion-table for Vickers hardness, Brinell hardness, Rockwell hardness and tensile strength". 1976.

[DIN87] DIN 50191. "Hardenability test by end quenching", 1987.

[Du04] Du C., Sun D. "Recent developments in the applications of image processing techniques for food quality evaluation". Trends in Food Science & Technology, 2004, 15 (5), 230-249.

[Dui00] Duin R. P. W. "Learned from Neural Networks". In: van Vliet L. J., Heijnsdijk J. W. J., Kielman T., Knijnenburg P. M. W. , Proc. ASCI 2000, 6th Annual Conf. of the Advanced School for Computing and Imaging, Lommel, Belgium, June 14-16, 2000.

[Dum03] Dumovic M. "Repair and Maintenance Procedures for Heavy Machinery Components". Welding Innovation, 2003, XX (1), 2-6.

[Edm98] Edmonds D. V. "Innovation in the processing of tonnage materials - examples from the steel and aluminium industries". Journal of Materials Processing Technology, 1998, 83, 1-13.

[Els02] El-Sesy I. A., El-Baradie Z. M. "Influence carbon and/or iron carbide on the structure and properties of dual-phase steels". Materials Letters, 2002, 57, 580-

585.

[EN92] EN 10027-2. “Designation system for steels – Part 2: Steel numbers”, 1992.

[Erd03] Erdogan M. “Effect of austenite dispersion on phase transformation in dual phase steel”. Scripta Materialia, 2003, 48, 501-506.

[Exn88] Exner H. E., Hougardy H. P. “Quantitative Image Analysis of Microstructures”. Oberursel: DGM Informationsgesellschaft mbH, 1988.

[Fer98] Ferro C. J. S. “Scale and texture in digital image classification”. MA thesis, West Virginia University, 1998.

[Fro99] From A., Sandström R. “Influence of Mixed Grain Size Distributions on the Toughness in High and Extra High Strength Steels”. Materials Characterization, 1999, 42, 111-122.

[Fuc00] Fuchs A. “Texturanalyse zur Ermittlung von Werkstoffeigenschaften aus Gefügebildern”. Diploma Thesis, University of Applied Sciences Aalen, 2000.

[Fuc01] Fuchs A., Bernthaler T., Stahl B., Klauck U., Reinsch B., Schneider G. “Bildanalyse komplexer Werkstoffgefüge durch Texturanalyse und Korrelation mit den Eigenschaften durch neuronale Netze”. Zeitschrift für Metallkunde, 2001, 92, 979-985.

[Ge99] Ge, A. X. “A Neural Network Approach to the Modeling of Blast Furnace”. Master thesis, Massachusetts Institute of Technology, 1999.

[Gir98] Girault E., Jacques P., Harlet P., Mols K., Van Humbeeck J., Aernoudt E., Delannay F. “Metallographic Methods for Revealing the Multiphase Microstructure of TRIP-Assisted Steels”. Materials Characterization, 1998, 40, 111-118.

[Gla72] Gladman T., McIvor I. D., Pickering F. B. “Some Aspects about the Structure-Property Relationship in High-Carbon Ferrite-Pearlite Steels”. Journal of the Iron and Steel Institute, 1972, 210, 916-930.

[Gog03] Gogotsi Y., Nikitin A., Ye H., Zhou W., Fischer J. E., Yi B., Foley H. C., Barsoum M. W. “Nanoporous carbide-derived carbon with tunable pore size”. Nature Materials, 2003, 2, 591-594.

[Guo03] Guo Z., Sha W. “Modelling the correlation between processing parameters and properties of maraging steels using artificial neural network”. Computational Computer Science, 2003, .

[Haa96] Haasen P. “Physical Metallurgy”. 3rd edition, Cambridge: Press Syndicate of the University of Cambridge, 1996.

[Hab68] Habraken, L., De Brouwer J. “De Ferri Metallographia I. Fundamentals of Metallography”. Düsseldorf: Verlag Stahleisen, 1968.

[Har73] Haralick R. M., Shanmugam K, Dinstein I. “Textural Features for Image Classification”. IEEE Transactions on Systems, Man and Cybernetics, 1973, Vol. SMC-3 (6), 610-621.

[Har74] Haralick R. M., Shanmugam K. S. “Combined Spectral and Spatial Processing of ERST Imagery Data”. Remote Sensing of Environment, 1974, 3, 3-13.

[Har91] Haralick R. M., Shapiro L. G. “Glossary of computer vision terms”. Pattern Recognition, 1991, 24 (1), 69-93.

[Hin99] Hinton G. “Supervised Learning in Multilayer Neural Networks“. In: Wilson R. A., Keil F. C. “The MIT Encyclopedia of the Cognitive Sciences”. Cambridge: The MIT Press, 1999.

[Hon00] Honeycomb R., Bhadeshia H. K. D. H. “Steels – Microstructure and properties“. 2nd edition, Oxford: Butterworth-Heinemann, 2000.

[Hor79] Hornbogen E. “Werkstoffe – Aufbau und Eigenschaften von Keramik, Metallen, Kunststoffen und Verbundwerkstoffen”. 2nd edition. Berlin: Springer Verlag, 1979, p. 221.

[Hor83] Hornbogen E. “Physical Metallurgy of steels” in Cahn R. W., Haasen P. (eds.) “Physical Metallurgy”. Part 2. 3rd edition. Amsterdam: North-Holland Physics Publishing, 1983, p. 1096.

[Hor92] Horstmann D. “Das Zustandsschaubild Eisen-Kohlenstoff und die Grundlagen der Wärmebehandlung der Eisen-Kohlenstoff-Legierungen”. 5th edition. Düsseldorf: Verlag Stahleisen mbH, 1992, p. 14.

[Irv57] Irvine K. J., Pickering F. B., Heselwood W. C., Atkins M. Journal of the Iron and Steel Institute, 1957, 195, 54-67.

[Ish95] Ishida M. “Calculation of the effect of alloying elements on the MS temperature in steels”. Journal of Alloys and Compounds, 1995, 220, 126-131.

[Jai96] Jain A. K., Mao J., Mohiuddin K. M. “Artificial Neural Networks: A Tutorial”. Computer, 1996, 29 (3), 31-44.

[Jon97] Jones S. J., Bhadeshia H. K. D. H. “Kinetics of the simultaneous decomposition

of austenite into several transformation products". Acta Materialia, 1997, 45 (7), 2911-2920.

[Jor99] Jordan M. I. "Neural Networks". In: Wilson R. A., Keil F. C. "The MIT Encyclopedia of the Cognitive Sciences". Cambridge: The MIT Press, 1999.

[Joy97] Joy D. C. "Scanning Electron Microscopy". In: Amelinckx S., van Dyck D., van Landuyt J., van Tendeloo G. "Handbook of Microscopy – Applications in Materials Science, Solid-State Physics and Chemistry". Methods II. Weinheim: VCH Verlagsgesellschaft mbH, 1997.

[Kar96] Karu K., Jain A. K., Bolle R. M. "Is there any texture in the image?". Pattern Recognition, 1996, 29 (9), 1437-1446.

[Key04a] "Effects on the martensite, pearlite and bainite formation" [online]. Key to Metals Task Force & INI International. Available from: http://www.key-to-steel.com/Articles/Art51.htm [Accessed 27 October 2004].

[Key04b] "Constant temperature transformation TTT curves" [online]. Key to Metals Task Force & INI International. Available from: http://www.key-to-steel.com/Articles/Art17.htm [Accessed 18 November 2004].

[Kin97] King H. W., Peters M. A. „Predictive equations for martensitic ant antoferromagnetic transformations in Fe-Mn-Al-Si alloys". Canadian Metallurgical Quarterly, 1997, 36 (2), 137-141.

[Kle04] Klein B. "Leichtbau im Automobilbau". v1.10 [online]. University of Kassel. Available from: http://www.uni-kassel.de/fb15/lbk/download/leichtbau/Leichtbau1_10.pdf [Accessed 28 October 2004].

[Kra99] Krauss G. "Martensite in steel: strength and structure". Materials Science and Engineering, 1999, A273-275, 40-57.

[Krö96] Kröse B., van der Smagt P. "An Introduction to Neural Networks". Lecture script. 8th edition. The University of Amsterdam, 1996.

[Kul03] Kulka M., Pertek A. "Microstructure and properties of borided 41Cr4 steel after laser surface modification with re-melting". Applied Surface Science, 2003, 214, 278-288.

[Kus02] Kusiak J., Kusiak R. "Modelling of microstructure and mechanical properties of steel using the artificial neural network". Journal of Materials Processing Technology, 2002, 127, 115-121.

[Kut99] Kutsov A., Taran Y., Uzlov K., Krimmel A., Evsyukov M. "Formation of bainite in ductile iron". Materials Science and Engineering, 1999, A273-275, 480-484.

[Lah96] Lahaye C. T. W. "Daily routine quantitative assessment of microstructure of steel by image analysis". Materials Characterization, 1996, 36 (4-5), 191-202.

[Lat01] Latala Z., Wojnar L. "Computer-aided versus manual grain size assessment in a single phase material". Materials Characterization, 2001, 46, 227-233.

[Lee99] Lee W., Su T. "Mechanical properties and microstructural features of AISI 4340 high-strength alloy steel under quenched and tempered conditions". Journal of Materials Processing Technology, 1999, 87, 198-206.

[Lee00] Lee E. H., Mansur L. K. "Fe-15Ni-13Cr austenitic stainless steels for fission and fusion reactor applications. II. Effects of minor elements on precipitate phase stability during thermal aging". Journal of Nuclear Materials, 2000, 278, 11-19.

[Les02] Leskovsek V., Ule B., Liscic B. "Relations between fracture toughness, hardness and microstructure of vacuum heat-treated high-speed steel". Journal of Materials Processing Technology, 2002, 127, 298-308.

[Lie98] Liedtke D. „Wärmebehandlung von Stahl – Härten, Anlassen, Vergüten, Bainitisieren". Merkblatt 450. Düsseldorf: Stahl-Informations-Zentrum, 1998.

[Liu01] Liu C., Zhao Z., Northwood D. O., Liu Y. "A new empirical formula for the calculation of M_S temperature in pure iron and super-low carbon alloy steels". Journal of Materials Processing Technology, 2001, 113, 556-562.

[Liu04] Liu D., Bai B., Fang H., Zhang W., Gu J., Chang K. "Effect of tempering temperature and carbide free bainite on the mechanical characteristics of a high strength low alloy steel". Materials Science and Engineering, 2004, A371, 40-44.

[Mar90] Marceau D. J., Howarth P. J., Dubois J. M., Gratton D. J. "Evaluation of the Grey-Level Co-Occurrence Matrix Method For Land-Cover Classification Using SPOT Imagery". IEEE Transactions on Geoscience and Remote Sensing, 1990, 28 (4), 513-519.

[Mat98] Materka A., Strzelecki M. "Texture Analysis Methods – A Review". COST B11 report, Technical University of Lodz, 1998.

[Mee02] Meesters L., Martens J. “A single-ended blockiness measure for JPEG-coded images”. Signal Processing, 2002, 82, 369-387.

[Mil95] Million B., Kucera J., Michalicka P. „The influence of silicon on carbon redistribution in steel weldments”. Materials Science and Engineering, 1995, A190, 247-252.

[Mod01] Modi O. P., Deshmukh N., Mondal D. P., Jha A. K., Yegneswaran A. H., Khaira H. K. “Effect of interlamellar spacing on the mechanical properties of 0.65 % C steel”. Materials Characterization, 2001, 46, 347-352.

[Mor03] Morito S., Tanaka H., Konishi R., Furuhara T., Maki T. “The morphology and crystallography of lath martensite in Fe-C alloys”. Acta Materialia, 2003, 51, 1789-1799.

[Mot56] Mott B. W. “Die Mikrohärteprüfung”. London: Butterworth Publications Ltd., 1956, p. 150.

[Mud02] Muddle B. C., Nie J. F. “Formation of bainite as a diffusional-displacive phase transformation”. Scripta Materialia, 2002, 47, 187-192.

[Nem03] Nemoto Y., Yamaguchi T., Horino T., Akatsu M., Yanagisawa T., Goto T., Suzuki O., Donni A., Komatsubara T. “Ferroquadrupole ordering and Gamma(5) rattling motion in the clathrate compound Ce3Pd20Ge6”. Physical Review B, 2003, 68 (18), art. no. 184109.

[Rip96] Ripley B. D. “Pattern Recognition and Neural Networks“. Cambridge: Cambridge University Press, 1996.

[Ros61] Rose A., Peter W., Strassburg W., Rademacher L. “Atlas zur Wärmebehandlung der Stähle”. Band 1. Teil II. Düsseldorf: Verlag Stahleisen, 1961.

[Sah02] Sahu P., De M., Kajiwara S. “Microstructural characterization of Fe-Mn-C martensites athermally transformed at low temperature by Rietveld method”. Materials Science and Engineering, 2002, A333, 10-23.

[San03] Sankaran S., Subramanya Sarma V., Padmanabhan K. A., Jaeger G., Koethe A. “High cycle fatigue behaviour of a multiphase microalloyed medium carbon steel: a comparison between ferrite–pearlite and tempered martensite microstructures”. Materials Science and Engineering, 2003, A362, 249-256.

[Sch66a] Schrader A., Rose A. “De Ferri Metallographia II. Structure of Steels.”,

Düsseldorf: Verlag Stahleisen, 1966.

[Sch66b] Schick H. L. “Thermodynamics of certain refractory compounds”. New York, London: Academic Press, 1966.

[Sch90] Schumann H. “Metallographie”. 13th edition, Stuttgart: Deutscher Verlag für Grundstoffindustrie, 1990.

[Sch99] Schmid J. “Quantitative Gefügeanalyse – Korrelation zwischen Textur-parametern und mechanischen Eigenschaften”. Diploma Thesis, University of Applied Sciences Aalen, 1999.

[Shi97] Shipway P. H., Wood S. J., Dent A. H. “The hardness and sliding wear behaviour of a bainitic steel”. Wear, 1997, 203-204, 196-205.

[Sin98] Singh S. B., Bhadeshia H. K. D. H. “Estimation of bainite plate-thickness in low-alloy steels”. Materials Science and Engineering, 1998, A245, 72-79.

[Smo01] Smolka B, Wojciechowski K. W. “Random walk approach to image enhancement”. Signal Processing, 2001, 81, 465-482.

[SNN00] University of Stuttgart, Institute for parallel and distributed, High performance systems (IPVR), “SNNS – Stuttgart Neural Network Simulator“. User Manual, Version 4.2, 2000.

[Sol04] Soltanian-Zadeh H., Rafiee-Rad F., Pourabdollah-Nejad S. “Comparison of multiwavelet, wavelet, Haralick, and shape features for microcalcification classification in mammograms”. Pattern Recognition, 2004, 37, 1973-1986.

[Som02] Dr. Sommer Werkstofftechnik. „Heat Treatment Database“. Issum-Sevelen: Dr. Sommer Werkstofftechnik GmbH, 2002.

[Spe72] Speich G. R., Leslie W. C. „Tempering of Steel“. Metallurgical Transactions, 1972, 3, 1045.

[Sta95] Stahl-Informations-Zentrum. “Einsatzhärten”. 2nd edition, Düsseldorf: Stahl-Informations-Zentrum, 1995.

[Str04a] Straub F. “Reinheitsgradbestimmung an hochreinen Stählen durch quantitative Gefügeanalyse von nichtmetallischen Einschlüssen mittels Licht- und Rasterelektronenmikroskopie”. Diploma Thesis, University of Applied Sciences Aalen, 2004.

[Str04b] Struers. „Material Safety Data Sheet – Electrolyte A3-I”. Available from: http://www.struers.com/resources/elements/12/24194/ELECTROLYTE%20A3-

I%20-%20US%20(M1201011%20-%202004-08-31).pdf. [Accessed 05 May 2005]

[Str04c] Struers. „Material Safety Data Sheet – Electrolyte A3-II". Available from: http://www.struers.com/resources/elements/12/24196/ELECTROLYTE%20A3-II%20-%20US%20(M1201003%20-%202004-08-31).pdf. [Accessed 05 May 2005]

[Suz63] Suzuki H. "The Relation Between the Structure and Mechanical Properties of Metals". National Physical Laboratory Symposium No. 15, 1963, Vol. II, p. 524

[Tel97] Telle R., Petzow G., Mücklich F. „Fundamentals of Light Microscopy". In: Amelinckx S., van Dyck D., van Landuyt J., van Tendeloo G. "Handbook of Microscopy - Applications in Materials Science, Solid-State Physics and Chemistry". Methods I. Weinheim: VCH Verlagsgesellschaft mbH, 1997.

[The98] Theuer J. "Quantitative Metallographie mit Bildverarbeitung". Diploma Thesis, University of Applied Sciences Aalen, 1998.

[The04] Thermo-Calc Software AB, "TCC – Thermo-Calc Software Users' Guide". User Manual, Version Q. Available from: http://www.thermocalc.com/Filer/Pdf/Manuals/TCCQ_UsersGuide.pdf. [Accessed 14 April 2005].

[Tom83a] Tomita Y., Okabayashi K. "Improvement in Lower Temperature Mechanical Properties of 0.40 Pct C-Ni-Cr-Mo Ultrahigh Strength Steel with the Second Phase Lower Bainite". Metallurgical Transactions, 1983, 14A, 485-492.

[Tom83b] Tomita Y., Okabayashi K. "Heat Treatment for Improvement in Lower Temperature Mechanical Properties of 0.40 Pct C-Cr-Mo Ultrahigh Strength Steel". Metallurgical Transactions, 1983, 14A, 2387-2393.

[Tom85a] Tomita Y., Okabayashi K. "Mechanical Properties of 0.40 Pct C-Ni-Cr-Mo High Strength Steel Having a Mixed Structure of Martensite and Bainite". Metallurgical Transactions, 1985, 16A, 73-82.

[Tom85b] Tomita Y., Okabayashi K. " Modified Heat Treatment for Lower Temperature Improvement of the Mechanical Properties of Two Ultrahigh Strength Low Alloy Steels". Metallurgical Transactions, 1985, 16A, 83-91.

[Ver84] Verein Deutscher Eisenhüttenleute. "Werkstoffkunde Stahl". Band 1, Grundlagen. Berlin: Springer Verlag, 1984.

[Ver96] Vermeulen W. G., Morris P. F., de Weijer A. P., van der Zwaag S. "Prediction

of martensite start temperature using artificial neural networks". Ironmaking and Steelmaking, 1996, 23 (5), 433-437.

[Ver02] Verma M. S., Pratt L., Ganesh C., Medina C. "Hair-MAP: a prototype automated system for forensic hair comparison and analysis". Forensic Science International, 2002, 129, 168-186.

[Vil91] Villars P. "Pearson's handbook of crystallographic data for intermetallic phases". Vol.3: In3PSe3-Zr. 2nd ed., Materials Park: ASM International, 1991.

[Wan00] Wang J., van der Wolk P. J., van der Zwaag S. "On the influence of alloying elements on the bainite reaction in low alloy steels during continuous cooling". Journal of Materials Science, 2000, 35, 4393-4404.

[Web95] Weber T., de Wit L., Saris F. W., Königer A., Rauschenbach B., Wolf G. K., Krauss S. „Hardness and corrosion resistance of single-phase nitride and carbide on iron". Materials Science and Engineering, 1995, A199, 205-210.

[Wec82] Weck E., Leistner E. „Metallographic instructions for colour etching by immersion – Part I: Klemm colour etching". Volume 77. Düsseldorf: Deutscher Verlag für Schweißtechnik (DVS) GmbH, 1982.

[Weg01] Wegst C. W. „Key to steel". 19th edition. Marbach: Verlag Stahlschlüssel Wegst GmbH, 2001.

[Wen96] Wenpu D., Zuobao F., Lang Y. "TEM Study of the Microstructure of HSLA100 Steel". Materials Characterization, 1996, 37, 169-175.

[Wes76] Weszka J. S., Dyer C. R., Rosenfeld A. "A Comparative Study of Texture Measures for Terrain Classification". IEEE Transactions on Systems, Man, and Cybernetics, 1976, SMC-6 (4), 269-285.

[Zha98] Zhang M., Kelly P. M. "Determination of Carbon Content in Bainitic Ferrite and Carbon Distribution in Austenite by Using CBKLDP". Materials Characterization, 1998, 40, 159-168.

[Zha02] Zhang J., Tan T. "Brief review of invariant texture analysis methods". Pattern Recognition, 2002, 35, 735-747.